

Development of Computational Methods for Standing Wave Microscopy

Ross Scrimgeour

Submitted in fulfilment of the requirements for
the degree of Doctor of Philosophy

Strathclyde Institute of Pharmacy and Biomedical Sciences

Faculty of Science

University of Strathclyde

April 1st, 2019

Abstract

Optical microscopy is an important tool in biomedical sciences and allows for the imaging of single cells, and has become vital and versatile tool for understanding cellular and subcellular processes. However, due to the wave nature of light, the spatial resolution is limited. As a result, most of the important biological process of a cell take place below 200 nm, which is beyond the resolution capabilities of conventional optical microscopy techniques.

In this work, I used multi-planar standing wave microscopy, an axial super resolution technique, where incident and reflected light from a mirror surface, create a standing wave. Multiple planes of lights are generated with a spacing of $\lambda/2n$, with an axial resolution of $\lambda/4n$, where λ is the excitation wavelength of light and n is the refractive index. When the multiple planes of light intersect a fluorescently labelled specimen, the result is an image with 3D information encoded in a 2D image. I showed that multi-planar standing wave images of healthy and *Plasmodium berghei* infected red blood cells had clear morphological deformations in the cell membrane. Furthermore, by applying a combination of noise filtering and segmentation techniques, 2D anti-nodal plane information was extracted. Next, I applied *a priori* knowledge to the standing wave red blood cells images to create a 3D reconstruction of the bottom concave surface.

To overcome, the limitations of single-wavelength standing wave (SW) microscopy a new method, which we call TartanSW multi-excitation, was applied to biological specimens. This reduced the modulation gap when compared with the use of a single-excitation wavelength. Furthermore, TartanSW multi-excitation and multi-emission both showed a unique spectral signature that reduced the ambiguity in the geometry of the specimen. Lastly, by utilising the phase difference between the different TartanSW multi-excitation wavelengths, I showed that in principle, the phase difference could be used to determine the axial height information from a 2D encoded standing wave pattern.

Contents

Chapter 1.....	1
1.1 Fundamental limits of resolution in optical microscopy.....	2
1.1.1 Resolution based on the point spread function	2
1.1.2 Abbe resolution limit.....	3
1.2 Overview of optical microscopy	5
1.2.1 The compound microscope.....	5
1.2.2 Enhanced contrast techniques.....	7
1.3 Fluorescence microscopy	8
1.3.1 Fluorophores	8
1.3.2 Epi-fluorescence microscope	11
1.4 Confocal microscopy	12
1.4.1 Confocal laser scanning microscope.....	13
1.4.2 Confocal Reflection Microscopy	15
1.4.3 Detection in CLSM.....	16
1.5 Total internal reflection fluorescence Microscopy	17
1.6 Super-resolution microscopy	19
1.6.1 Stimulated emission depletion microscopy.....	19
1.6.2 Structural illumination microscopy.....	20
1.6.3 Single molecule localisation	21
1.7 Interference microscopy	23
1.7.1 Standing wave microscopy.....	23

1.8	Image processing techniques	24
1.9	Red blood cells.....	25
Chapter 2.....		28
2.1	Introduction.....	29
2.1.1	Standing wave Microscopy	30
2.2	Experimental Methods.....	37
2.2.1	Fluorescently coated lens specimens	37
2.2.2	Red blood cell isolation and staining	38
2.2.3	Standing wave confocal laser scanning microscopy imaging of fluorescent specimens	40
2.2.4	Image pre-processing.....	41
2.2.5	Gaussian blur.....	42
2.2.6	Intensity Thresholding.....	43
2.2.7	Two-dimensional single-colour reconstruction	45
2.3	Results	47
2.3.1	Pre-processing and Gaussian blur application to lens specimen.....	47
2.3.2	Optimising the thresholding using SW lens specimen images	51
2.3.3	Two-dimensional SW reconstruction of a lens specimen and RBCs.....	54
2.3.4	SW imaging and two-dimensional of <i>P.berghei</i> infected red blood cells..	56
2.4	Discussion	62
2.5	Conclusion	65
Chapter 3.....		67
3.1	Introduction.....	68

3.2	Materials and methods	72
3.2.1	Preparation of fluorescently labelled specimens	72
3.2.2	Video-rate SW imaging of fluorescently labelled specimens	73
3.2.3	Polynomial and Cubic spline Surface fitting for 3D reconstruction of lens specimen.....	75
3.2.4	Analysis of lens specimen	76
3.2.5	Algorithm for 3D SW red blood cell reconstruction	78
3.3	Results	80
3.3.1	Simulations of SW PSF for high and low NA lens	80
3.3.2	SW imaging of fluorescently coated lens specimens.....	81
3.3.3	Comparison of threshold and edge detection images with standing wave theory	83
3.3.4	Comparison of polynomial and cubic spline 3D surface reconstruction of a simulated lens specimen	85
3.3.5	Video-rate SW imaging and computation 2D reconstruction of RBC.....	87
3.3.6	Comparison between video-rate SW microscopy and video-rate widefield epi-fluorescence microscopy.....	91
3.4	Discussion	94
3.5	Conclusions.....	100
Chapter 4	101
4.1	Introduction.....	102
4.2	Theory of TartanSW multi-excitation and multi-emission.....	107
4.3	Experimental methods	109
4.3.1	Fluorescently labelling of specimens	109

4.3.2	TartanSW multi-excitation and multi-emission imaging	109
4.3.3	Analysis of TartanSW lens specimen data	112
4.3.4	Difference Method for TartanSW imaging	114
4.4	Results	115
4.4.1	A comparison of simulated and experimental TartanSW multi-excitation	115
4.4.2	Simulated and experimental comparison used for TartanSW multi-emission	121
4.4.3	Confocal TartanSW multi-excitation and multi-emission imaging of red blood cells	126
4.4.4	Confocal TartanSW multi-excitation and multi-emission imaging of MCF-7 cells	129
4.4.5	Simulated Difference SW method	132
4.4.6	Application of the DiffSW method to experimental data	133
4.5	Discussion	136
4.6	Conclusion	141
Chapter 5	143
5.1	Introduction	144
5.1.1	Phase retrieval from known waveforms	146
5.1.2	Hilbert transform for phase retrieval	149
5.2	Methods	150
5.2.1	Lens preparation and confocal imaging	150
5.2.2	Phase method for three-dimensional reconstruction of line profile	151
5.2.3	Phase method for three-dimensional reconstruction of line profile	151

5.2.4	Phase difference method for 3D Reconstruction of 2D simulated TartanSW multi-excitation data	152
5.3	Results	155
5.3.1	A theoretical phase difference vs axial distance.....	155
5.3.2	A 3D phase difference reconstruction of simulated $f = 48$ mm lens specimen.....	157
5.3.3	A 3D phase difference reconstruction of simulated $f = 48$ mm lens specimen.....	162
5.3.4	Phase difference reconstruction method of experimental $f = 48$ mm lens specimen data.....	166
5.3.5	Phase difference reconstruction method of experimental $f = 48$ mm lens specimen data using a long pass filter as a substrate	169
5.4	Discussion	174
5.5	Conclusion	180
Chapter 6	182
6.1	Summary.....	183
6.2	Future work	185
Appendix I	– Gaussian Blur signal to noise calculation.....	202
Appendix II	– Standing wave 2D reconstruction.....	204
Appendix III	- Custom polynomial fit function	207
Appendix IV	– Standing wave surface fit comparison.....	210
Appendix V	– Lens analysis	215
Appendix VI	– Standing wave 3D reconstruction.....	218
Appendix VII	– Antinodal plane separation function	227

Appendix VIII – TartanSW multi-excitation simulation.....	235
Appendix IX - TartanSW multi-emission simulation	237
Appendix X – Difference standing wave simulation	239
Appendix XI – Phase difference reconstruction of a simulated intensity profile of a lens specimen.....	241
Appendix XII – Phase difference reconstruction of simulated 3D lens specimen	245
Appendix XIII – Phase difference reconstruction of an experimental lens specimen	249

Acknowledgments

First and foremost, I'd like to thank my supervisor Gail McConnell for the opportunity to study a PhD. I have learnt so much the last three and half years and appreciate all your guidance and support.

I'd also like to thank everyone in the Biophotonics group namely: Gill, Jana, Jan, Liam, Katrina and Lisa. And to the newer members of the group: Mollie, Shannon, Eliana and Jordan. All of you have kept me sane the office chats and supplying me with whisky and gin. I'd also like to thank Peter Tinning for many conversations and collaboration with the standing wave work.

I'd like to thank my friends and family, who have supported me through my PhD. In particular, my mum for her support over the PhD. My brother for his and general chat, and our trips to watch the rugby. I would like to thank Cara, who over the course of the PhD has offered her love, support and encouragement.

Declaration of Authenticity and Author's Rights

This thesis is the result of the author's original research, unless it has been explicitly stated in the text. It has been composed by the author and has not been previously submitted for examination which has led to the award of a degree.'

The copyright of this thesis belongs to the author under the terms of the United Kingdom Copyright Acts as qualified by University of Strathclyde Regulation 3.50. Due acknowledgement must always be made of the use of any material contained in, or derived from, this thesis.

Signed:

Date:

Publications

1. **Widefield standing wave microscopy of red blood cell membrane morphology with high temporal resolution**, *Peter W. Tinning, *[Ross Scrimgeour](#), and Gail McConnell, *Biomed. Opt. Express* 9, 1745-1761 (2018).

Conference Presentations

Poster Presentations

1. **Scottish Microscopy Group Symposium, Heriot Watt University, Edinburgh - three-dimensional reconstruction of multi-planar standing wave images of red blood cells**, [Ross Scrimgeour](#), David Li and Gail McConnell (2016).
2. **Microscience Microscopy Congress 2017, Manchester Central Convention Complex, Manchester - A computational method for two-dimensional quantitative analysis of standing wave images of red blood cells**, [Ross Scrimgeour](#), Peter Tinning, David Li and Gail McConnell (2017).
3. **European Light Microscopy Initiative, University College Dublin, Dublin - A computational method for 3D reconstruction of standing wave images of red blood cells captured at video-rate**. [Ross Scrimgeour](#), Peter Tinning and Gail McConnell (2018).
4. **Frontiers in Bioimaging, University of Strathclyde, Glasgow - A computational method for extracting 3D information from standing wave images of red blood cells**. [Ross Scrimgeour](#), Peter Tinning and Gail McConnell (2018).

Oral Presentations

1. **Invited Speaker: Photonex Europe, Biophotonics and Biomedical Microscopy, Ricoh Arena, Coventry – Spectral standing wave Microscopy – contour mapping the cell**. [Ross Scrimgeour](#), Peter Tinning, Jana Schniete and Gail McConnell (2018).

Chapter 1

Introduction

In this chapter, I briefly overview microscopy in general with a summary of super-resolution microscopy and interferometric techniques.

1.1 Fundamental limits of resolution in optical microscopy

In optical microscopy resolution is the smallest distance at which two separate point objects can be resolved [1]. Therefore, the resolution determines the smallest cellular and subcellular structures and processes that can be observed by an optical system [2]. Resolution can be quantified in several ways: either by the point-spread function (PSF) such as the Rayleigh, Sparrow criterion and the full-width half maximum (FWHM), or by the resolution criteria which was first experimentally demonstrated by Ernest Abbe in 1893 [1].

1.1.1 Resolution based on the point spread function

Two methods which use the PSF are the Rayleigh criterion and the Sparrow limit shown in Figure 1.1. The Rayleigh criterion was proposed by Lord Rayleigh and is defined as the first minimum of one object's Airy disk, which is overlapping with the maximum peak of the second object's Airy disk, then these two objects are said to still be resolvable [3]. The Sparrow limit is defined as two Airy disks, that are at a distance apart, which overlap to the extent where the resulting intensity profile between the Airy disks become flat, such that the dip in the sum of the intensity ceases to be visible between the two Airy disks [3]. Another common definition is the full-width half maximum (FWHM) resolution which is the difference between two points at half the intensity value of the Airy disk [4].

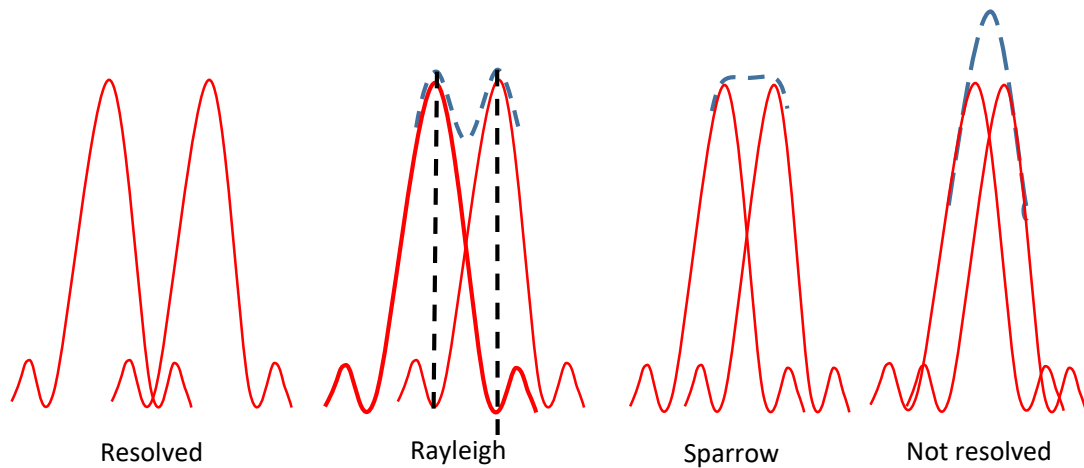


Figure 1.1- In red the PSF is shown for two-point sources and the blue dashed line is the sum of the intensities of the two PSF. (a) Two clearly resolved objects. (b) Two objects at the Rayleigh limit. The black dashed line shows the overlap of the maximum of one PSF with the first minimum of the second PSF (c) Two objects at the Sparrow limit and (d) two objects which cannot be resolved [3].

1.1.2 Abbe resolution limit

The fundamental theory for understanding the limit of resolution for the modern light microscope was first understood by the work of Abbe in 1873 [4]. In Abbe's formulation of the theory of imaging, Abbe's limit describes the smallest details of a periodic structure that can be imaged and resolved by an optical microscope. Consider the following setup: a specimen, an objective lens, the focal plane and the image plane. If the specimen is illuminated by a collimated coherent light source, the specimen acts as a diffraction grating and the objective lens acts as a transform lens which forms a Fraunhofer diffraction pattern of the object in the transform plane. The light waves then propagate beyond the transform plane of the objective lens and interfere to form an inverted image of the specimen [1], [3], [5]. Abbe made an important realisation that the objective lens cannot collect all the higher orders of the diffraction pattern. Thus, the numerical aperture (NA) of the objective lens defines the resolution limit [4]. In general, the Abbe limit for lateral resolution is given by:

$$d = \frac{\lambda}{2n \sin \theta} = \frac{\lambda}{2NA} \quad (1.1)$$

where, $NA = n \sin(\theta)$ is the numerical aperture of the objective lens, n is the refractive index of the medium between the coverslip and the objective lens and λ is the wavelength of the detected light. The axial resolution of an optical system is given by [6]:

$$d_z = \frac{2\lambda}{NA^2} \quad (1.2)$$

where, $NA = n \sin(\theta)$ is the numerical aperture of the objective lens and λ is the wavelength of light. It is clear when comparing Eqn. 1.1 and 1.2 that the resolution in the axial direction is poorer than in the lateral direction. For visible light the lateral resolution is approximately 200-300 nm, whereas in the axial direction the resolution is on the order of 700 nm [7]. Comparably, electron microscopy (EM) offers resolution below the diffraction limit of light. EM allows visualisation of cellular structures smaller than 200 nm, due to the De Broglie wavelength of electrons being much shorter than the wavelength of visible light, EM techniques have achieved a resolutions far below 50 nm [8].

EM has limited practical applications in biological studies, due to the preparation methods which is limited to fixed cells specimens and can cause shrinkage and alteration to the specimen presenting artefacts in the final images [9]. Therefore, there is much demand to produce better resolution with optical microscopes as many of the cellular features and processes take place below 200 nm [2], and to overcome the limitations of EM microscopes. Techniques have been developed throughout the years to improve resolution, including confocal microscopy which improves the lateral and axial FWHM resolution by a factor of $\sqrt{2}$ over a conventional microscope and allows for precise optical sectioning [10], [11]. In more recent years, microscope techniques using interference methods, such as 4pi microscopy [12] and standing wave microscopy [13], [14] have improved the axial resolution by a factor of five. Moreover, with the development of super-resolution techniques such as STORM [15], PALM [16], [17] and

STED [18], [19], it is possible to achieve a lateral resolution below 100 nm and an axial resolutions below 150 nm.

1.2 Overview of optical microscopy

The development of the first compound optical microscope is often accredited to the Dutch spectacle maker Zacharias Janssen in 1590 which was closely followed by Galileo Galilei in 1610 [3]. Robert Hooke between 1677-1682 described his observations using a compound microscope in his book *Micrographia*, which included famous descriptions and detailed drawings of his observations of fly's eye and plant cells [20]. Despite this, early compound microscopes suffered from technical problems that reduced the sharpness and quality of the images [1]. It was not until the late 19th century, when Zeiss and Abbe made rapid improvements with a multi-element lens system, using optical theory, that optical microscopes could be used for detailed studies of cells for the first time [1]. This formed the basis for the optical microscopes in use today.

1.2.1 The compound microscope

A compound microscope is a multi-lens system where a specimen is attached to a microscope slide and is illuminated with an incoherent light source by focusing the light through a condenser lens onto the specimen. The light is then passed through the objective lens which produces a magnified real image on the image plane. An ocular lens (eyepiece) will magnify the image further and form a virtual image which is then observed [3]. The objective lens is a crucial part of a microscope, as it can be changed to the desired NA and magnification. High NA objective lenses typically have numerical apertures of approximately 1.4-1.65 NA producing higher resolution images with a magnification of up to 100x. Objectives with a high NA require to be immersed in a medium between the objective lens and specimen, typically using an oil-based immersion fluid. Conversely, low NA and magnification lens are dry objectives i.e. the objective requires no immersion fluid and are imaged in air. [21]. Illumination is crucial

in optimising the performance of an optical microscope and the method of Koehler illumination is the standard method of illumination in optical microscopy, first introduced by August Koehler [21]. In an optical microscope there are two sets of conjugate planes, the image and aperture planes, both of which are shown in Figure 1.2. The image-forming light paths include the field diaphragm, specimen plane, intermediate image plane and the retina of the eye or a detector [5]. The aperture planes, which is the path of the illuminating light source planes, includes the lamp filament, the back focal plane of the condenser, the back focal plane of the objective lens, and the pupil of the eye which is also the location the Ramsden disc of light [5]. By precise alignment of the image and aperture planes, Koehler illumination produces an image that is evenly illuminated with an in-focus image formed at the detector or on the retina [21], [22].

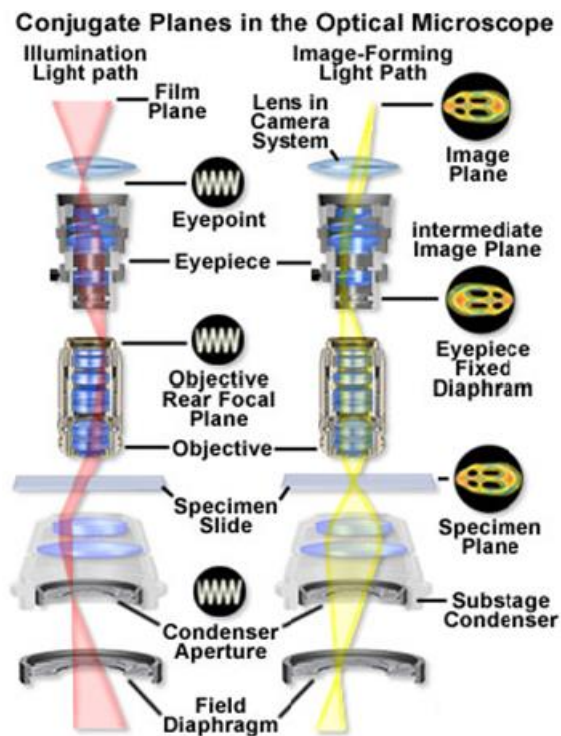


Figure 1.2- shows the light path of the illumination and image-forming conjugate planes in a microscope when setup for Koehler illumination [22].

1.2.2 Enhanced contrast techniques

Techniques have been developed to improve the image contrast and allow for observation of more cellular structures than can be observed in bright-field microscopy [7]. Three techniques which are popular are dark-field microscopy, phase contrast microscopy and differential interference contrast microscopy.

Dark-field microscopy is a technique which a specimen is illuminated at a high angle, such that the direct non-diffracted rays are not collected by the objective lens, with only the diffracted rays from the specimen being collected by the objective lens. As a result, the final image is produced by the diffracted light rays from the specimen. Therefore, higher contrast is produced in the final image which gives a more detailed view of the specimens fine structures e.g. lysosomes, bacterial flagella, diatom striae, and microtubules [21].

Phase contrast was first proposed by a Dutch physicist Frits Zernike in 1930's [23]. The principle of phase contrast microscopy is to place a condenser annulus before the condenser lens. Light is passed through the annulus creating a 'ring' shaped beam. The light which propagates through the specimen will be diffracted and collected by the objective lens. A phase plate is placed in the back focal plane of the objective lens, where the diffracted light is collected in different regions of the phase plate from the non-diffracted light, producing a further $\lambda/4$ phase shift. The light waves of the diffracted and non-diffracted rays interfere at the image plane. Therefore, the intensity change in the final image is dependent on the difference in phase shift introduced by the specimen [24].

Differential interference contrast microscopy (DIC) or Nomarski interference contrast (NIC) microscopy, is a simple technique that uses a Nomarski setup as a linear polariser. The light enters the Wollaston prism and is separated into two rays that are polarised 90 degrees relative to each other. The light is then transmitted through the specimen where the optical path length is changed by the thickness and refractive index of the specimen.

The light enters the objective lens and is focused onto the back focal plane where a second Wollaston prism recombines the light paths. However, the light cannot interfere as they are not oriented in the same plane. Therefore, an analyser is placed above the Wollaston prism before the eyepiece. Now, the light rays can interfere enhancing the contrast of the image [21], [25]. In essence, the DIC microscopy measures the gradient of the optical path difference with the largest optical path difference leading to the darker regions in the final image [25].

Even with techniques that enhance image contrast, such as phase contrast and DIC microscopy which allow for subcellular structures to be more easily identified, they are still fundamentally limited. The next significant development was the epi-fluorescence microscope which allows for greater specificity in identifying cellular structures and quantitative imaging of biochemical processes [1], [2].

1.3 Fluorescence microscopy

The first fundamental understanding of the phenomena of fluorescence was described in 1852 by G.G Stokes [27]. The first fluorescence microscope was developed between 1911 and 1913 by Otto Heimstaedt and Heinrich Lehmann to observe the autofluorescence in bacteria, animal, and plant tissues. In 1914, Stanislav Von Provazek used fluorescence microscopy to study dye binding in fixed tissues and living cells [28]. It was not until the early 1940s when immunofluorescence was developed by Albert Coons, a technique which allows for labelling with antibodies and fluorescent probes [29]. Nowadays, it is possible to label multiple different cellular structures with fluorescent probes to generate highly specific images of cells [30].

1.3.1 Fluorophores

Fluorescence microscopy is a technique that utilises fluorescent chemical compounds (referred to as fluorophores, fluorescent dyes and fluorescent proteins) and autofluorescence, both of which fluoresce when illuminated with the correct excitation

wavelength of light. A light source, typically a mercury lamp, light emitting diode or laser, illuminates the sample at the excitation wavelength of the fluorophore. Photons incident on the fluorophore transfer energy to the electrons in the ground state. The absorbed energy excites the electrons into higher orbitals. Electrons undergo a period of rapid non-radiative transition, which is known as the Stokes shift, before transitioning back to the ground state. Fluorescence occurs at the transition between an excited state and the ground state, at which point light is emitted at a longer wavelength than the excitation wavelength. This process is shown in the Jablonski diagram in Figure 1.3. The shift in wavelength between the excitation and emission peaks is referred to as a Stokes shift [26].

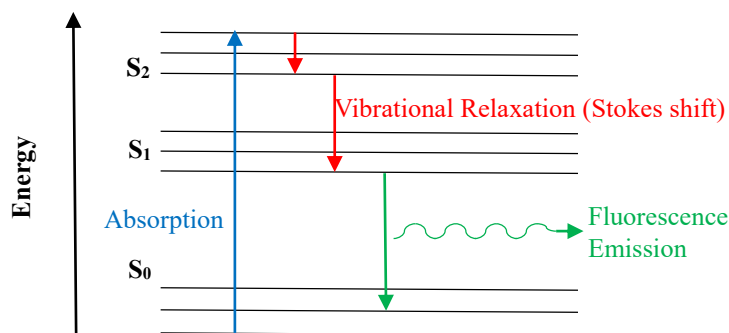


Figure 1.3 - A Jablonski diagram shows the molecules energy states during the excitation and emission of light in the fluorescence process. The S_0 state is the ground state, the lowest energy state. S_1 and S_2 are excited energy states [26].

The fundamental idea behind a fluorescence microscope is to study or investigate cells using the desired fluorophores or autofluorescence. Autofluorescence is a natural emission of light from biological substrates such as mitochondria and lysosomes [31], typically within the visible, UV or near infrared range when biological substrates are excited with light of the correct excitation wavelength [32]. Green fluorescent protein was first discovered in the 1960s by Shimomura [33]. By extracting the calcium dependent bioluminescent protein from the jellyfish *Aequorea Victoria*, which was given the name aequorin, it was observed during the isolation procedure the presence of a

second protein that emitted green light. This protein went on to be known as green fluorescent protein (GFP) [34]. Fluorescent proteins (FPs) variants have been created in recent years which produce a wide range of excitation (399-590 nm) and emission (511-649 nm) wavelengths, and if carefully chosen can provide a range of FPs for labelling of multiple cellular features of interest [35]. Fluorescent proteins have enabled non-invasive imaging in living cells and organisms of reporter gene expression, protein trafficking, and many dynamic biochemical signals [36].

The application of fluorescent labelling has now been developed to label specific cellular structures and processes with small organic dyes: Immunofluorescence utilises antibodies which are chemically linked to a fluorophore and labelled with specific antigens or proteins [29]. For example, immunofluorescence is routinely used for the imaging of microtubules in the cytoplasm of a mammalian cell [37]. Intracellular Ca^{2+} is vital to many different physiological processes [38], [39]. Therefore, the development of fluorescent calcium indicators as a method to quantify calcium release is important and has been achieved by changing their emission wavelength due to the binding of intercellular calcium ions [38], [40]. Lipid and membrane dyes, such as DiI, can be used to stain cytoplasm giving a uniform stain with low cytotoxicity [41], and the cell nuclei can be stained using dyes that attach to DNA such as DAPI [42]. As a result, the staining of the cell nuclei and internal cellular structures will allow for clear differentiation between cellular structures leading to higher specificity when imaging [41].

1.3.2 Epi-fluorescence microscope

In epi-fluorescence microscopy, a specimen is illuminated using an arc lamp, light emitting diode or laser. The typical setup is shown in Figure 1.4. The excitation light is passed through a filter cube with an excitation filter to select the correct excitation wavelength for the chosen fluorophore. The light is then reflected off a 45° dichroic beam splitter and passed through the objective lens onto the specimen. When a specimen is illuminated through the epi-fluorescence setup, the fluorophore is excited and emission light is emitted at a wavelength dependent on the fluorophore. Both the emission light and scattered excitation light is passed through the objective lens, and again back through the filter cube. The emission light is transmitted through the dichroic beam splitter which reflects the shorter wavelengths of the excitation light. An emission filter allows only the emission light to be transmitted before it can be observed through either the eyepiece or photodetector [26], [43].

Although epi-fluorescence microscopy has become a standard in modern day cell biology, it has several disadvantages. Epi-fluorescence microscopy causes images to produce out-of-focus planes of light, this ultimately leads to images with a high amount of fluorescent background, resulting in a fluorescent glow in the background which reduces the contrast of the final image [30]. A further constraint of epi-fluorescence microscopy is the phenomenon of photobleaching, a process where a fluorescent molecule loses its ability to emit light after being observed over an extended period of time. Photobleaching is a photochemical process and results in irreversible damage to the fluorescent molecule. In epi-fluorescence microscopy photobleaching is not just contained to in-focus planes, but the out-of-focus planes will also be susceptible to photobleaching. Therefore, photobleaching of the specimen will occur even when it is not being directly imaged [9], [11].

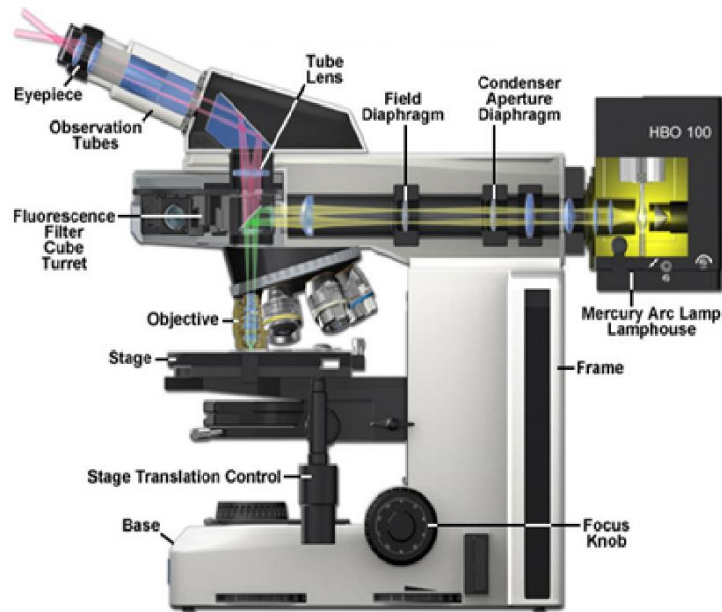


Figure 1.4- The layout of the excitation and emission light paths of an upright an epifluorescence microscope [43].

1.4 Confocal microscopy

Minsky first developed the concept behind confocal microscopy in 1955. It is a simple design that consists of an objective and a condenser lens with a pinhole aperture at either side, as shown in Figure 1.5. After the development of the confocal microscope by Minsky, very little interest was shown up until the late 1970's, due to the requirement of bright light sources and the computational power needed to handle the large 3D data sets [7]. However, since the development of epi-fluorescence microscopy it was apparent that emission from out-of-focus planes of light was also being collected during imaging, led to poor depth discrimination. With the continual popularity of epi-fluorescence microscopy, a technique was required that would eliminate the background fluorescence present in the images. The result was the development of the confocal laser scanning microscope (CLSM) [30].

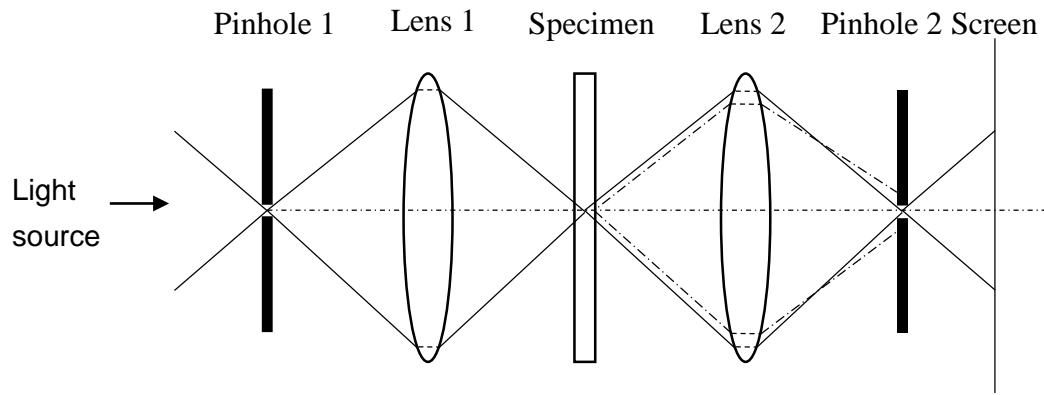


Figure 1.5 - A simplified ray diagram of Minsky setup. A light source is passed through the first pinhole aperture and a lens is used to focus the ray onto a specimen. Light is then transmitted and focused using a second lens and passed through a second pinhole aperture onto a screen. Only the light which is in focus (solid line) will pass through the aperture and out-of-focus light (dashed line) is rejected [9].

1.4.1 Confocal laser scanning microscope

In 1979, Brakenhoff and colleagues experimentally demonstrated a technique using a CLSM that produces an improved resolution at FWHM of 1.25 times over conventional microscopy using high NA oil immersion objectives lenses [44]. Then in the 1980's, two early commercial viable CLSM were developed alongside one another. Firstly, a system developed by Carlsson and Aslund in 1987 [11] and secondly a system by Amos, Fordham and White in 1987 [10], with the latter becoming the design of the standard CLSM [30].

The basic working setup of a CLSM system is shown in Figure 1.6. A laser light source is passed through a beam splitter which filters out any unwanted wavelengths of light, leaving only the desired excitation wavelength. Two mirrors are placed in the aperture plane which scans a laser across the specimen in the X and Y direction. Laser scanning is preferred over stage scanning, as stage scanning is slower due to the specimen needing to be translated [10]. Additionally, the movement of the stage will cause motion of the specimen affecting the image quality [7]. The light is then passed through two lenses, a scanning lens which focuses the light onto the image plane and then through a tube lens.

The light is transmitted through the microscope objective where it is focused onto the sample exciting the fluorophore. The emitted fluorescent light is passed through a microscope system back towards the laser source. A primary chromatic beam splitter reflects the light through another lens, focusing the light onto a second chromatic beam splitter. The beam diverges into separate paths, and a long pass filter is placed to filter out unwanted shorter wavelengths of light. A pinhole aperture stops any out-of-focus light from entering the photomultiplier tube [45].

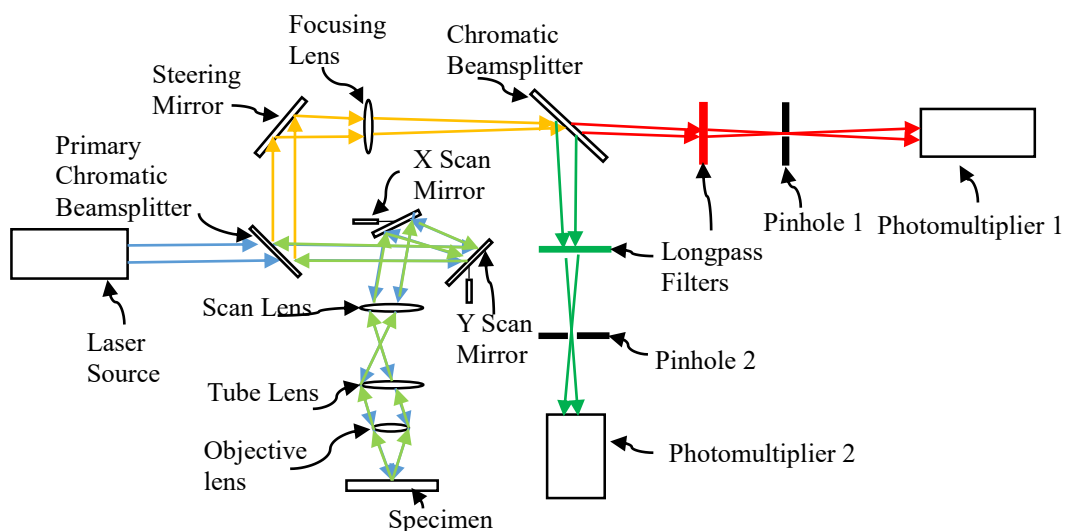


Figure 1.6 - A schematic diagram of a general confocal laser scanning microscopy (CLSM) which shows a laser beam being guided by two scanning mirrors. The emission light is collected again through the optical arrangement of mirrors and beam splitters onto the photomultiplier tubes.

One advantage of the confocal system is the factor of $\sqrt{2}$ improvement in both the lateral and axial resolution, although this is only a moderate enhancement of resolution over conventional microscopy [45]. The main advantage of the confocal arrangement is the improvement in the optical sectioning thickness [30]. The light from a laser is focused to a spot called the beam waist, when moving away from the focal spot the beam becomes wider at either side giving a characteristic hourglass shape as shown in Figure 1.7a.

Therefore, the beam will have excited the fluorophores in the out-of-focus planes as shown in Figure 1.7b. If the beam is focused onto a pinhole in the aperture plane, the out-of-focus light will be blocked by the pinhole, producing a thin optical section [46]. As a consequence, the pinhole size defines the thickness of the optical section, so a smaller pinhole will allow less out-of-focus light to reach the detector and produce a thinner optical section [47]. Moreover, there is greatly enhanced contrast in the confocal images, which allows for subcellular structures to be clearer and limits the glow from the out-of-focus fluorescent planes [10]. Precise optical sectioning in combination with scanning through multiple z depths of a specimen can be used to create a 3D image reconstruction of the specimen [46].

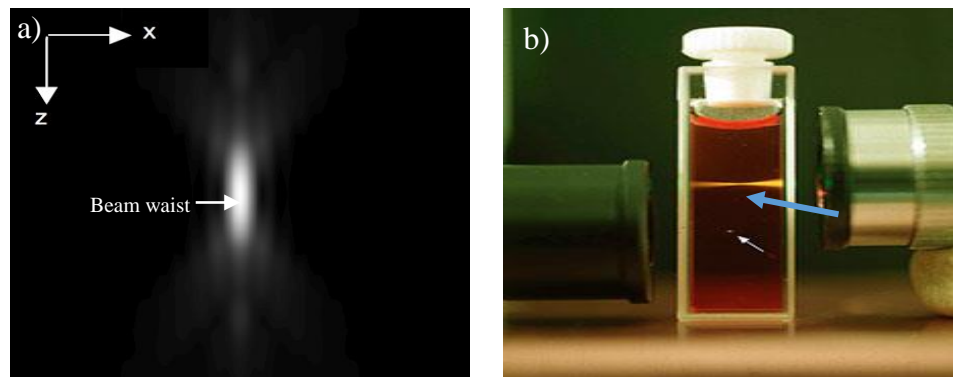


Figure 1.7- (a) The PSF of a laser beam in the x-z plane which shows the hourglass shape of the laser beam above and below the focal point. (b) A photograph by Brad Amos which shows single photon excitation (top) and two-photon excitation (bottom). The blue arrow points to the excitation of Safranin O and shows the excitation of the out-of-focus planes caused by single photon excitation.

1.4.2 Confocal Reflection Microscopy

Confocal reflection microscopy (CRM) is another method that is utilised in CLSM. CRM focuses a laser spot onto the specimen, where the reflections from the specimen features are passed through the confocal pinhole. Again, the out-of-focus light is rejected from above and below the focal plane just as in CLSM [21]. The advantage of CRM is that

it can be used to image live cells and unstained specimens. However, care must be taken as specimens are still susceptible to photodamage [48]. Imaging with CRM offers enhanced contrast over bright-field and dark field microscopy techniques [48]. However, CRM still does not offer the specificity of cellular structures that fluorescence probes can provide [48].

1.4.3 Detection in CLSM

To produce an image in CLSM, the ability to detect and maximise the number of photons that arrive at the detector that are converted from photons into an electronic signal is crucial [30]. Most of the photons when imaging will be lost through the transmission losses of the optical components of the microscope system and the scattered light from the specimen which will not be collected by the objective lens [7]. Photomultiplier tubes (PMT) are the most common detector in CLSM systems due to their performance in low light levels and fast response time [7]. Photomultiplier tubes absorb photons at the photocathode which in turn causes electrons to be ejected and multiplied through a voltage gradient by a series of electrodes called dynodes which then produces a voltage output signal [49].

One of the main factors that affects the photon efficiency at the detector is the quantum efficiency (QE) i.e. the proportion of photons that arrive at the detector that contributes to the output signal. Most modern PMTs have a QE of around 30%. Moreover, the noise level at the detector also affects the image quality this will include dark noise, which is the thermal generation of electrons, and multiplicative noise [7]. Therefore, it is important to reduce the source of external photons that can reach the detector and optimise the collection of fluorescent photons at the detector. By doing so, the signal-to-noise ratio can be improved resulting in higher image quality. Several ways this can be achieved is to either increase the pinhole aperture to allow more light to the detector or increasing the laser light incident on the specimen [21].

Lastly, in order to capture all the detail in an image the Nyquist criterion can be applied, which states that the sampling frequency must be twice the highest signal frequency [45]. Therefore, to capture the best image, the Nyquist criterion is applied and at least two pixels should span the diagonal of the Airy disk. Only the 100x objective lens meets this Nyquist requirement, hence additional magnification is required for lower magnification objective lenses [49].

1.5 Total internal reflection fluorescence Microscopy

Total internal reflection fluorescence (TIRF) microscopy or evanescent wave microscopy is a method developed for use in cellular imaging by Daniel Axelrod in the early 1980's [50]. Total internal reflection is a physical phenomenon that takes place when a light beam propagates through a medium of higher refractive index n_1 , and at the boundary with the medium of lower refractive n_2 , then the critical angle θ_c is given by,

$$\theta_c = \arcsin\left(\frac{n_2}{n_1}\right) \quad (1.6)$$

If light is incident at an angle greater than the critical angle, then the light is totally internally reflected. Although all the light is reflected, an electromagnetic evanescent wave is present beyond the surface boundary. The evanescent wave will propagate parallel to the substrate and the intensity of the evanescent wave decays exponentially [50]:

$$I = I_o \exp\left(-\frac{z}{d}\right) \quad (1.7)$$

where, z is the perpendicular distance from the substrate and d is the characteristic decay depth which is given by:

$$d = \frac{\lambda}{4\pi n_2} \left(\frac{\sin \theta}{\sin \theta_c} - 1\right)^{-\frac{1}{2}} \quad (1.8)$$

where, λ is the wavelength of the incident light and the incident beam angle is θ with the condition required that $\theta > \theta_c$.

There are two main types of TIRF microscopy that have been developed. One method, uses a glass or quartz prism that can be hemispherical or cubic [50], where a cell substrate is placed in contact with the prism with a layer of oil immersion in-between. A lens focuses the laser beam on to a prism which corrects the beam to the critical angle required for total internal reflection. The objective lens is placed below the specimen where it is used to detect the fluorescence caused by the evanescent wave. The second design utilises a high NA objective lens [51], and it is used in an epi-fluorescence setup. Using a high numerical aperture lens, typically above 1.45, angles of incidence above the critical angle can be achieved [52]. The fluorescent emission caused by the evanescent wave can then be detected back through the objective lens, and filtering of the excitation and emission wavelengths is done by using the appropriate dichroic filters cubes. The fluorescence output is dependent on the intensity of the evanescent wave, which drops off exponentially. Therefore, the fluorescence emission will drop off at the same rate. TIRF microscopy has a distinct advantage over epi-fluorescence microscopy, by allowing fluorescence imaging of regions near the substrate with an axial resolution of ≈ 100 nm [58]. However, TIRF does not offer improved lateral resolution and the axial resolution enhancement is only within a limited range of approximately 100 nm above the cell substrate [59].

TIRF microscopy has been used to study cellular substrates [50], one example used the fluorescence emission drop off to map of the cell contact points at distances from the substrate of 100-200 nm [53]. Additional studies could obtain visualisation of the plasma membranes near the cell substrate interface, a region which is typically obscured in epi-fluorescence microscopy by out-of-focus light [52].

1.6 Super-resolution microscopy

Thus far the microscopy techniques discussed have been of diffraction-limited resolution. In recent years, several methods have been developed to achieve super-resolution, such as stimulated emission depletion (STED) microscopy [18] and structured illumination microscopy (SIM) [54]. Furthermore, other super-resolution techniques rely on the localisation of single molecules. These methods include stochastic optical reconstruction microscopy (STORM) [15], photoactivated localisation microscopy (PALM) [16] and fluorescent photoactivated localisation microscopy (FPLAM) [17].

1.6.1 Stimulated emission depletion microscopy

Stimulated emission depletion microscopy was first proposed in 1994 by Stefan Hell and Jan Wichmann [18] and then demonstrated experimentally by Stefan Hell [19]. The basic principle of STED microscopy is to have an excitation laser and a second STED laser that suppresses the emission of the fluorophore at the edges of a diffraction limited spot of a CLSM laser, by the process of stimulated emission. Stimulated emission is a process, whereby photons with an energy that is the same as the energy gap between the ground and excited states, is depleted and emits light at the same wavelength as the incident laser beam [55].

To reduce the size of the point-spread function (PSF), a second laser (the STED laser) overlaps with the excitation laser beam. The STED beam profile has zero intensity in the centre, and a nonzero intensity around the edges (a toroidal shaped beam) and the wavelength is selected at the far edge of the emission spectrum of the fluorophore [8], [19]. With the combination of the excitation and STED beam, the effective beam spot size of the laser is reduced by the stimulated emission process, which suppresses the spontaneous fluorescence emission process and only emits light at the wavelength of the STED laser which is shown in Figure 1.8 [18]. The resolution of a STED microscope is given by:

$$\Delta r = \frac{\lambda}{2n \sin \theta \sqrt{1 + \frac{I_{max}}{I_s}}} \quad (1.9)$$

where, I_{max} is the power of the STED laser. If the intensity of the STED laser is increased so that $I_{max}/I_s \rightarrow \infty$ this implies “infinite” resolution; however, the resolution is limited by the laser power that can be generated and the laser power that can realistically be applied to a specimen without causing photodamage [56]. With the addition of a second STED beam, 3D STED can be achieved. The resolution is improved in the axial direction to approximately 150 nm and still obtain a 50 nm lateral resolution [39].

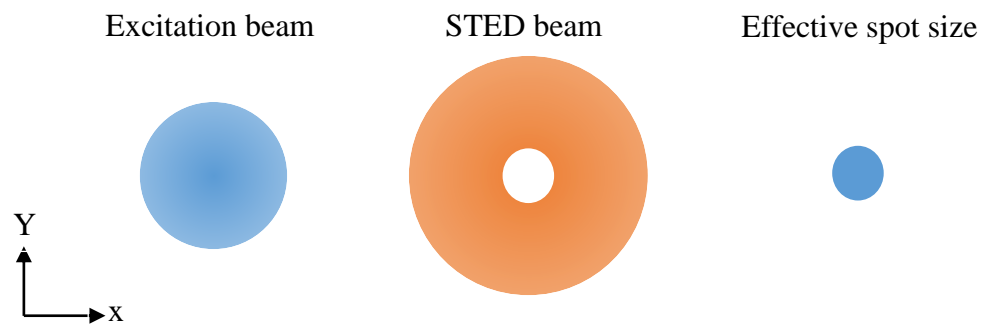


Figure 1.8 - The beam profiles for the excitation, STED and effective spot sizes. By overlapping the STED ‘donut shaped’ beam with the excitation beam, there is a reduction in spot size that illuminates the fluorophore [56].

1.6.2 Structural illumination microscopy

In the late 1990s a technique was proposed called structured illumination microscopy (SIM) [57], [58]. The concept uses an effect called a Moiré pattern. A moiré pattern consists of two overlapping grids that have either a different mesh spacing or angle, resulting in an interference effect. Therefore, using the moiré pattern it is possible to obtain information about the unknown structure if the pattern that illuminates the specimen is known. SIM is typically achieved by inserting a diffraction grating at the conjugate plane and projecting through the objective lens onto the specimen. The lateral

resolution enhancement using SIM is an improved of a factor of two, to approximately 115 nm [58].

SIM has also been reported to utilise a non-linear illumination approach to producing higher resolution images [54]. Under intense illumination, the emission of a fluorescent dye depends non-linearly on the intensity that it is being illuminated. As a result, the fluorescent emission will saturate, and the SIM intensity pattern now contains harmonics of higher spatial frequencies than in the original SIM method. SSIM can achieve a lateral resolution of <50 nm [54].

SIM has also been demonstrated to work for 3D imaging [59], [60]. In this setup, three illuminating laser beams are used: two beams illuminating in the lateral (x and y) direction and one in the axial (z) direction. Through this arrangement, an improvement in axial resolution to 250-350 nm can be achieved. Moreover, this has been extended to image with high specificity staining of cell features which allows for mapping of cellular structures. One such example managed to simultaneously image the DNA, nuclear lamina and the NPC epitopes of C2C12 cells by 3D-SIM [60]. SIM is particularly advantageous as it allows for 3D multi-coloured super-resolution imaging using standard biological staining dyes and procedures, which other super-resolution techniques do not allow [2].

1.6.3 Single molecule localisation

Single molecule localisation is a super-resolution technique that utilises the principle that a spatially isolated fluorophore position can be determined with a higher accuracy than the width of the point spread function if enough photons are collected [15]. Single molecule localisation detection was first demonstrated in 1989 at liquid helium temperatures [61], and later with fluorescence imaging with one-nanometre accuracy (FIONA) [62]. However, for this technique to be successful and improve resolution, the molecules must not be in close proximity to one another or they become difficult to

resolve [15]. Several techniques utilise an alternative approach by photoactivation and photoswitching of fluorescent molecules: these include FPALM, PALM and STORM, all of which were introduced in 2006 [15]–[17].

STORM was first demonstrated using a Cy3-Cy5 dye pair as an optical switch, and more recently using the Alexa Fluor 405-Cy5 and Cy3-Alex Fluor 647 [63]. It has been demonstrated that the cyanine dye, cy5, can be switched to and from its fluorescent bright and dark states reversibly, by using different wavelengths of light [15]. A series of images are built up by selectively switching the molecules on, using a green laser, and then switching the molecules off into their dark state, using a strong red laser [15]. Whereas, PALM utilises Photoactivated fluorescent proteins (PA-FPs). For example, PALM [16] uses Eos-based fluorescent proteins (EosFP, mEos, mEos2), and FPALM uses photoactivatable green fluorescent protein (PA-GFP) [17]. In both the PALM methods, a small number of molecules are activated using a laser at the activation wavelength of the PA-FPs and simultaneously imaged at the excitation wavelength. The imaging continues until the activated molecules are photobleached and the population of inactivated and the unbleached molecules are depleted. Both PALM and STORM reconstruct the final image by building up the fluorescent positions over the multiple images acquired. The result of the localisation of single molecules is that both these methods can achieve a lateral resolution of approximately 20-50 nm [2].

Three-dimensional-STORM has also been reported to improve resolution by a factor of 10 over the diffraction limit in both axial and lateral directions. One such example imaged the microtubules of a BS-C-1 cell [64]. This was achieved by deliberately introducing an astigmatism into the image by using a slightly cylindrical lens. Therefore, the PSF is distorted in the lateral direction x and y directions depending on the depth of focus. By fitting a Gaussian curve to the x and y PSF widths, the z coordinates can be unambiguously determined. Moreover, 3D imaging has been obtained using a dual-

objective lens approach in an interference PALM (iPALM) technique, which produces an axial resolution below 20 nm [65].

1.7 Interference microscopy

Interference is a phenomenon that occurs when two or more beams of light superpose. The resultant amplitude of the wave is dependent on the sum of each wave component. For example, if there are two waves with a relative π phase shift with respect to one another, the results in destructive interference. If there is no phase shift, constructive interference will take place [3], [5].

Interference reflection microscopy (IRM) is a technique which uses the basic principles of interference. The idea was first used in cell biology by Adam Curtis in 1964 [66], as a method to measure the gap between a glass slide and the cell to understand the structure of the cell where it had adhered to the substrate. Throughout the years, IRM has been used to study a wide range of cellular processes including cell adhesion and cell motility [67].

When cells are grown on a coverslip there is a gap between the slide and the cells of approximately 100-200 Angstroms [66]. Because of this gap, there is a reflection between the media in the gap and the glass interface. Further reflections occur between the cell membrane and the medium. This results in either constructive or destructive interference from the incident and reflected beams, with an intensity that is dependent on the size of the gap between the cell and the glass substrate. If the cell is not in contact, around 100 nm away from the substrate, it will appear bright as the gap between the cell and the glass is large enough that the reflected light will be in phase, thus constructively interfere. Intermediate distances are grey in intensity value [67], [68].

1.7.1 Standing wave microscopy

Standing waves (SW) were first experimentally demonstrated by Wiener in 1890 [5], and have been utilised in interference microscopy by Lanni in 1986 [13]. A SW can be created

by the interference of two counter-propagating coherent light sources at the specimen plane [12], [69]–[71], or by reflecting the incident light off a mirror surface [13], [14], [72]. In the study by Bailey et al, a fivefold axial resolution improvement was obtained over epi-fluorescence widefield and CLSM by optical sub-sectioning of fixed disassociated actin stress fibres of 3T3 cells [14]. Another study by Lanni et al [14] has been shown in the fixed 3T3 fibroblast cells stained with rhodamine labelled phalloidin, which allowed for the Lamella to be imaged. This was because the leading edge of the cell is very thin, therefore removing the contribution from additional anti-nodal planes. It was demonstrated that optical section comparable to CLSM could be achieved, but acquired at an acquisition time 10x faster than CLSM. [73]. Multi-planar SW microscopy has been shown to contour map specimens, and has been shown in 3T3-fibroblast stained with rhodamine labelled phalloidin [74]. Additionally, Amor et al [72], showed that the bottom concave surface of a red blood cell (RBC) adhered to a mirror surface, imaged with a upright CLSM, could reveal a precise contour map of the concave surface with an axial resolution of ≈ 90 nm.

It has previously been shown that a SW can be generated by the detection of narrow emission bandwidths, where an axial dependent spectral signature could be observed [75]. Amor et al, demonstrated that a modulated SW can be obtained, using three-narrow emission detection channels, which created a unique beating pattern dependent on the stokes shift between the excitation and the emission wavelengths [72]. Lambacher et al., noted that the beating effect was due to the presence of the excitation and emission SW [76], [77]. I have given a short overview of SW microscopy here, but I will expand on details of the SW literature in the upcoming Chapters.

1.8 Image processing techniques

The presence of noise due to the detector was briefly outlined in section 1.4.3. It is desirable to remove shot noise, which is captured during the image acquisition process. However, it is possible to use image processing tools to remove any noise present within

an image. Three common techniques used are mean, Gaussian and median filters [78]. Each filter involves an m by n mask which is convolved over each pixel in an image and is set to the value that depends on the operation over the mask region. A mean filter involves a simple mask that determines the mean value of the total pixels of the mask. A Gaussian blur filter is a Gaussian weighted mean filter with a matrix which is convolved along each pixel of the image. Gaussian filters are advantageous as weighted to the central pixel, thus limiting the effect of intensity pixels further away [79]. Furthermore, Gaussian filters are better suited at removing high frequency noise over low frequency noise than mean filters [80]. Median filters are typically better all-round filters and are particularly suited for shot noise with much better preservation of edge details. However, they are slower than mean and Gaussian filters [78].

Image intensity thresholding is a segmentation technique which separates an image based on an intensity cut off value i.e. threshold value. This is often a popular choice in microscopy for the purpose of segmenting cells, particularly when the difference between the intensity of the cell and the background is well separated [81]. Two standard methods are utilised; global thresholding where one threshold value is used as the intensity cut off such as the Otsu method [82], or local thresholding where a small local threshold intensity value is calculated over a small mask of m by n pixels of the image which is used to determining the intensity cut off [83]–[85]. Local thresholding is best suited when the image intensity of the objects which require to be segmented are not homogenous over the whole image [78], [83], [84]. I will present more detail about the computational techniques used in chapters 2 and 3, and how they were implemented for data extraction of multi-planar SW images.

1.9 Red blood cells

Adult mammalian red blood cells (RBC) are a type of cell which lacks a nucleus, mitochondria and other organelles. Red blood cells have a characteristic biconcave shape that permits increased manoeuvrability and faster diffusion of oxygen and carbon

dioxide across the plasma membrane [1]. Diseases such as sickle cell anaemia [87], [88], hereditary spherocytosis [87], [89], elliptocytosis [87] and plasmodium infected red blood cells (iRBC) [90], [91], all have been associated with morphology changes in the RBC membrane. A flickering phenomenon has been observed in RBC membranes which has been documented as early as 1890 [92]. Thermal processes or dynamic remodelling of the cytoskeleton and active membrane mechanisms was suggested as the possible process caused the flickering motion [93]–[95]. Many imaging modalities have been used extensively for the study of RBC morphology [96]–[98], such as quantitative phase imaging or differential interference contrast microscopy [99]–[101].

In the following Chapters, I will discuss the work carried out using multi-planar SW microscopy to create contour maps of model lens specimens, RBCs and MCF-7s. I will present computational methods to model the SW techniques used and extract 3D information encoded in the SW images.

In Chapter 2, I present a 2D reconstruction method which was used to extract anti-nodal planes information. I will characterise the 2D method using a model lens specimen. Then I apply it to both healthy and unhealthy RBC and observe the morphological difference in the RBC membrane.

In Chapter 3, I demonstrate the development of a 3D reconstruction method of 2D SW data captured using a widefield epi-fluorescence microscope over 1000 frames at video-rate (30.30 Hz). Two-dimensional information is extracted from the SW RBC images and by assigning axial height information, a 3D reconstruction was generated of the bottom concave surface of a RBC.

In Chapter 4, I present TartanSW multi-excitation and multi-emission techniques and include a mathematical model which is simulated for both TartanSW methods. Experimental model lens specimen data is presented and imaged using three different reflective substrates to characterise the TartanSW methods. This was extended to TartanSW imaging of RBC and MCF-7s. Finally, Difference SW (DiffSW) was applied to

TartanSW multi-excitation images and the simulated and experimental data were used to characterise the method which was then finally applied to MCF-7 TartanSW multi-excitation data sets.

In Chapter 5, I present a method for the reconstruction of TartanSW multi-excitation images by using the phase difference between each of the excitation wavelengths. I will show the theoretical approach and how phase angles were extracted from a 2D projection of the SW structure using a Hilbert transform. This was simulated for a radial profile and 2D image of a model lens specimen. It was also shown that the Hilbert transform introduces oscillations in the extracted phase angles, when a comparison of the extracted phase angles from the simulated data sets were obtained with and without a Hilbert transform. Lastly, the phase difference reconstruction method was applied to a line intensity data of an experimental SW lens specimen image.

Chapter 6 is a summary of the work present in the thesis, along with a description of possible future work.

Chapter 2

Development of a computational method to extract two-dimensional information from standing wave images of red blood cells

In this chapter, I discuss SW excitation of fluorescently labelled specimens which were imaged using an upright CLSM by simply placing a plane reflector below the specimen. Fluorescent anti-nodal fringes from the model lens specimens and red blood cells (RBCs) serve as precise contour maps which revealed 3D geometrical information. Then I compared the ability of SW multi-planar microscopy for the contour mapping of morphological differences in healthy and *plasmodium berghei* infected RBC. Finally, I characterised and demonstrated a computational method using the Gaussian blur *imgaussfit* and intensity thresholding *adaptthresh* MATLAB functions, which were used to extract both the positional and intensity information, to create a 2D reconstructions for both the model lens specimen and RBCs data sets.

2.1 Introduction

The aim of this work was to utilise multi-planar contour mapping of RBC specimens for both healthy and unhealthy cells and compare the ability of SW microscopy to capture morphological differences within the RBC cell membrane. Additionally, to develop a computational method which used noise filtering and intensity thresholding based segmentation techniques to extract the 2D positional (x , y) data along with their corresponding pixel intensities. It was an important first step to develop a method to reliably extract the 2D information from the SW images before 3D information could be extracted. The computational method was characterised using a model lens specimen and then applied to the SW images of healthy and infected RBCs.

2.1.1 Standing wave Microscopy

Standing waves, also known as stationary waves, were named as such because they appear to be stationary; the position of the maximum displacement (anti-nodes) and regions of minimal displacement (nodes) are at fixed points in space (Figure 2.1). In a stationary medium, there are two methods which can form a SW. Firstly, two counter propagating waves interfere with one another, or secondly an incoming light wave is incident onto a plane reflector, where the incident and reflected components interfere to create a SW [3], [5].

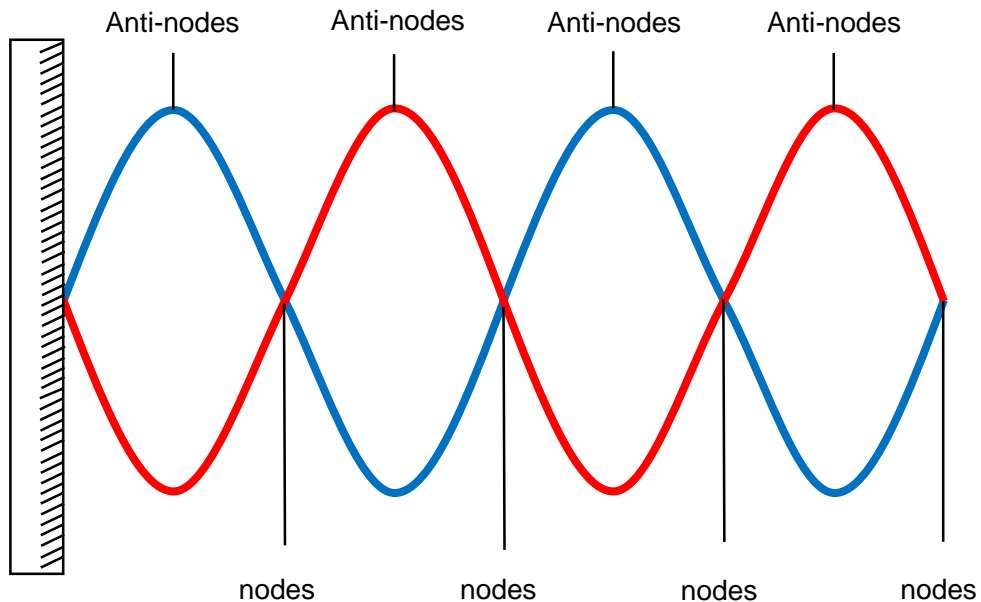


Figure 2.1- Standing wave formation due to reflection from a mirrored surface. The incoming wave (blue) reflects off the mirrors causing a π phase shift, as shown in red wave. This results in a standing wave, where at the mirrors surface there is zero displacement with each subsequent node occurring at half wavelength intervals. Points of maximum displacement are anti-nodes, the first anti-node occurs at a quarter wavelength from the mirrored surface, and again all subsequent anti-nodes are spaced at half wavelength intervals.

Standing waves were first experimentally demonstrated by Wiener in 1890 [5]. Wiener's experimental arrangement to detect SWs comprised of a glass plate, which was inclined at an angle to normal incidence, and a plane mirror which was illuminated at normal incidence (Figure 2.2). The glass plate was coated with a photographic film which was roughly $1/20$ of a wavelength thick. The photographic film blackened at the regions where the anti-nodal planes intersected the film but were transparent at the nodal points. Moreover, the regions of blackening corresponded to the electric field of the anti-nodal planes. Therefore, the photochemical process was dictated by the electric field vectors and not the magnetic field vectors [5]. Subsequent SW experiments, one by Drude with fluorescent films and another being Ives using photo-emissive films [102], again showed the response was caused by the electric field vector of the anti-nodal planes.

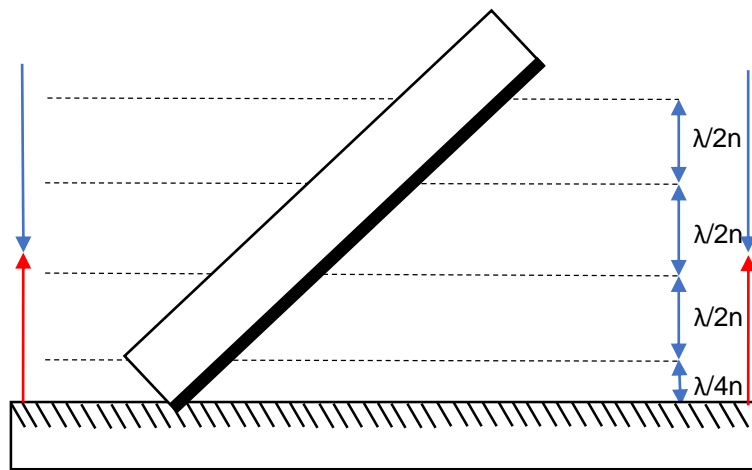


Figure 2.2 – Wiener's experimental setup for detecting the presence of SW anti-nodal planes. Where the anti-nodal planes intersect the photographic film, there was a blackening of the film. Blue lines show the incoming light and the red lines are the reflected light from the mirror [5].

Standing wave microscopy is a method of interference microscopy which was first described in 1986 [13]. In an approach by Bailey et al., demonstrated SW microscopy by using a plane reflector beyond the specimen, as shown in Figure 2.3a. By propagating a

Gaussian laser beam through an oil immersion objective lens and the specimen, the light is reflected normal to the surface of the reflector, and interference occurs creating a SW of light parallel to the focal plane. The most conventional method to create SW interference is to use a 4pi geometry arrangement. In the 4pi setup, light is passed through a beam splitter where the excitation light is separated into two different optical paths. For the illumination of a specimen at normal incidence, light is collimated by each of the opposing objective lenses. As a result, two counter-propagating coherent light sources interfere at the specimen plane, [12], [69] as shown in Figure 2.3b. In the study by Bailey et al, optical sub-sectioning of fixed disassociated actin stress fibres of 3T3 fibroblast cells was demonstrated using both setups, i.e. a reflector beyond the specimen and a dual-beam SW imaging [14]. As the SW intersects the specimen at the nodal and anti-nodal planes, fluorescence will be emitted at the anti-nodal planes and no fluorescent emission occurs at the nodal planes. Using the SW arrangement, a fivefold axial resolution improvement was obtained over conventional fluorescence microscopy and CLSM [14].

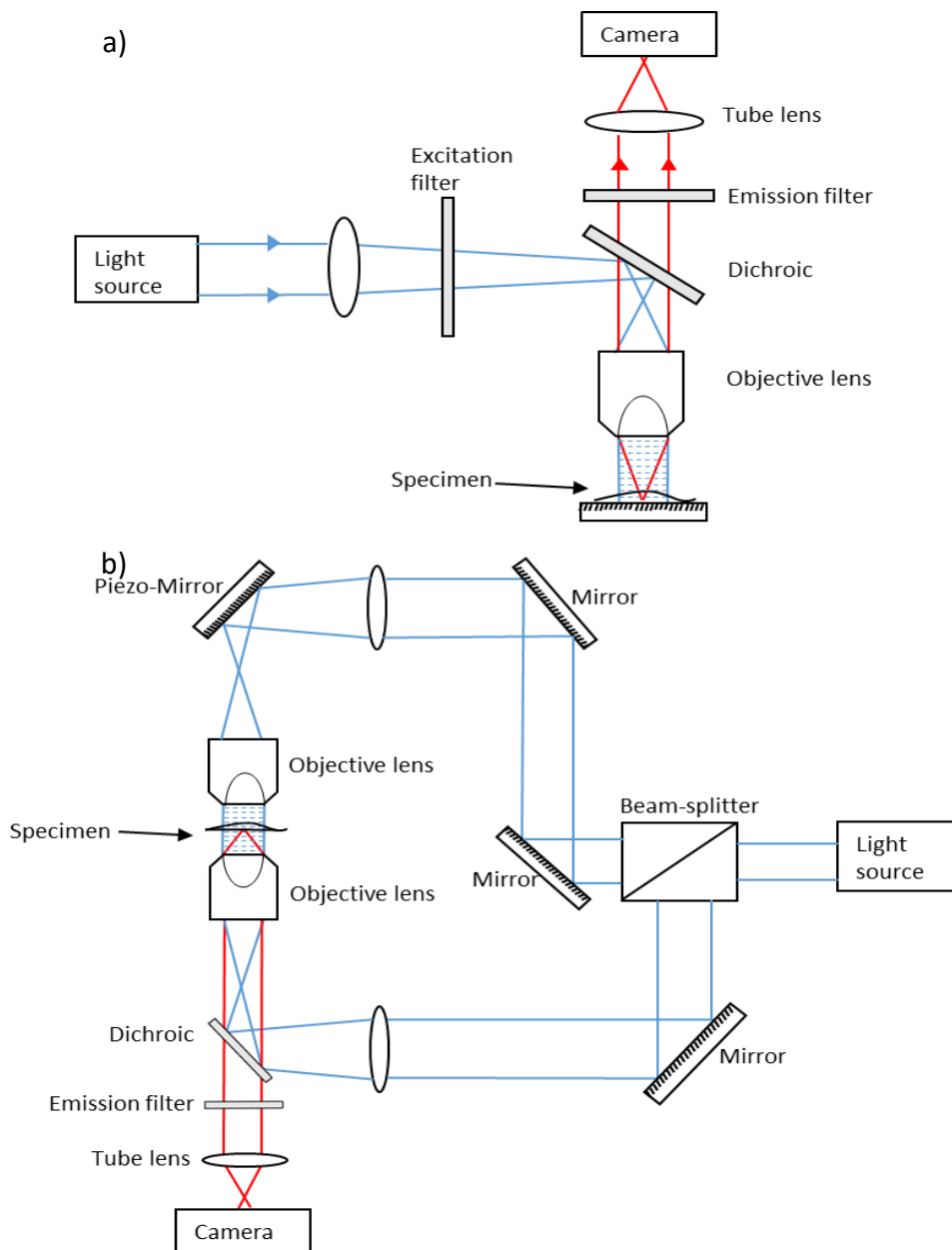


Figure 2.3 – A schematic diagram of the two methods used to create a SW in a microscope setup adapted from Lanni et al . The blue lines show the excitation optical path and the red lines show the emission optical path. a) A reflective substrate was placed below the specimen in an upright setup and SW was formed, as shown in Figure 2.2. b) A 4pi geometry setup with two counter propagating waves from opposing objective lenses, where the light interferes to create a SW. A specimen would be placed between each of the objective lenses.

The intensity of the SW field for two counter-propagating plane waves that interfere along the optical axis is proportional to [14]:

$$I(z)_{exc} = 1 - \cos(kz + \phi) \quad (2.1)$$

where, $k = 4\pi n/\lambda$ and λ is the wavelength of the excitation light, n is the refractive index of the immersion medium, z is the axial height and ϕ is the shift in phase relative to the specimen. If a beam of light is at normal incidence to the reflective substrate, or if two counter-propagating waves are propagating 180° relative to one another, the axial anti-nodal spacing is given as:

$$\Delta s = \frac{\lambda}{2n} \quad (2.2)$$

where, again, λ is the wavelength of the excitation light and n is the refractive index of the immersion media. The resolution of SW microscopy can then be estimated as half the nodal spacing and is given as $\lambda/4n$.

It has been demonstrated that SW microscopy was not only a method that could improve axial resolution, but could simultaneously obtain geometric information through the illumination of multiple axial planes [72], [103]. In a recent study by Amor et al. [72], the principle was demonstrated by coating the curved surface of a plano-convex lens specimen with a ATTO 532 fluorescent dye. Images were captured using an upright CLSM setup with the simple addition of a mirror below the specimen. This was carried out on an upright microscope, to allow the specimen to sit in-contact with the mirrored surface. The result was a concentric pattern of alternating bright and dark fringes caused by the SW planes intersecting the lens specimen at intervals of $\lambda/2n$. It was shown that the radial intensity of the fluorescent output of the concentric fringe pattern could be used to create a 3D reconstruction of the plano-convex lens. It should be noted that the accuracy of the location of the anti-nodal planes is measured as thickness of the plane, i.e. the FWHM, which is defined as $\lambda/4n$. Therefore, the FWHM is an important measure of accuracy. This is because, if we consider the location of an object or structure

fluorescing within a SW anti-nodal plane, the axial height of that object or structure can be determined based on the number of anti-nodal planes that have occurred from the mirrors surface. However, the accuracy of the axial height can only be determined within the axial thickness (FWHM) of $\lambda/4n$ of the anti-nodal plane.

The multi-planar SW principle was extended to the application of biological samples, specifically RBCs [72]. The RBCs were stained separately with DiI, DiO and DiI(5) and each placed onto separate mirrors. By doing so, details such as the bi-concave section of the RBC could be resolved due to the multiple fluorescent SW planes generated by the SW excitation pattern. Using different fluorescent dyes at different excitation wavelengths was advantageous, as DiO has an excitation peak at 488 nm which results in an axial resolution of ≈ 93 nm. In comparison, with DiI an axial resolution of ≈ 100 nm could be obtained at a 543 nm excitation. Thus, DiO allows for an improved axial resolution due to the shift towards a shorter excitation wavelength. In comparison, when the RBCs were adhered to a microscope slide only the outline of the RBC could be observed, thus showing no additional information about the RBC structure [72]. Therefore, by utilising the SW patterns as a 'contour map', additional axial information about the RBC geometry could be obtained, as was demonstrated by the SW imaging of the plano-convex lens specimen.

The multi-planar SW technique allowed for the observation of fine details in the 3D structure of a specimen which could not be observed when a conventional epifluorescence widefield or CLSM setup was used. In the resultant SW image, the anti-nodal planes contain the 3D information which was encoded in a 2D image. The 2D information was required to be extracted. However, extracting the relevant information was not trivial, as these features need to be well separated either spatially or by intensity [78]. Despite this, techniques to overcome difficulties in extracting the relevant data do exist. The first step, as discussed in this chapter, was to extract the anti-nodal information from the 2D projections. The multi-planar SW data which provided a contour

map of the specimen's structure has inherent advantages: Namely, that the specimens discussed in this Chapter have a concentric ring pattern, with each concentric ring corresponding to a different axial location. And more importantly for the propose of segmentation, the varying intensity of bright and dark concentric rings gave a basis to extract the information by using the SW intensity profile. Firstly, the computational method used noise filtering to remove much of the inherent noise fluctuations and left only the underlying SW signal. Then by using an intensity segmentation, such as local or global threshold, it was then possible to extract the anti-nodal information. For instance, the 2D pixel positional (x, y) data along with their corresponding intensity. This was firstly characterised using a model lens specimen and then was applied to the SW images of healthy and infected RBCs.

2.2 Experimental Methods

2.2.1 Fluorescently coated lens specimens

Uncoated silica plano-convex lenses, with a focal length of 48 mm and 72 mm with diameter of 6 mm (Edmund Optics), were cleaned using deionized water and then blow dried with compressed air to remove any contaminants. The lens preparation protocol described by Amor et al. was amended by replacing the APTMS coating with a solution of 0.01% mass concentration poly-L-lysine in H₂O (Sigma Aldrich) to allow the binding of 1,1'-Diocadecyl-3,3,3',3'-Tetramethylindocarbocyanine Perchlorate (DiI) to the lens surface. The specimens and poly-L-lysine solution were placed on a platform rocker for

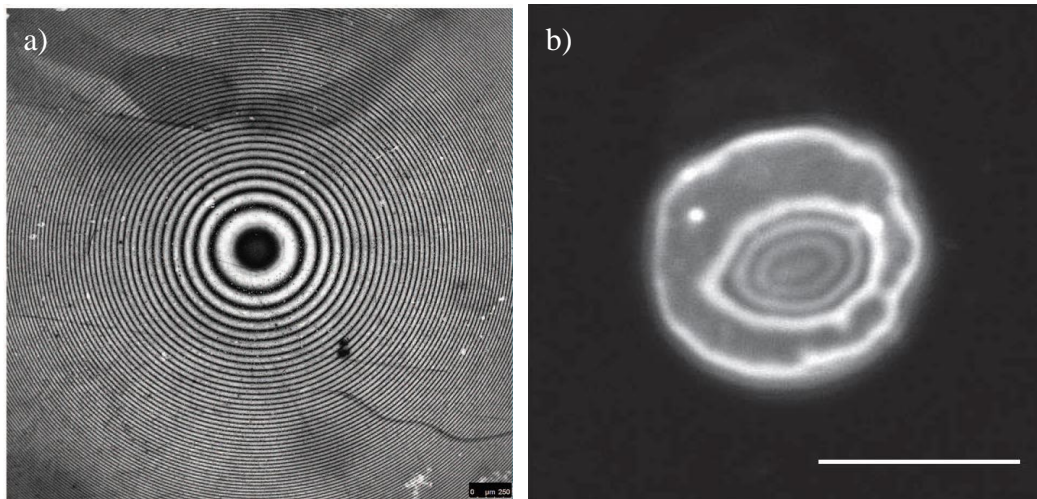


Figure 2.4 – The multi-planar SW images from Amor et al. [72]. a) A SW image of a plano-convex fluorescently coated lens specimen. b) A SW image of a fluorescently labelled RBC. Scale bar 5 μm . It was observed that the radial projection of the 3D geometry was encoded in a 2D image. The bright regions corresponded to the anti-nodal planes and dark regions correspond to nodal planes.

45 - 60 minutes to evenly coat the curved surface of the lenses in the solution, after which the lenses were thoroughly washed in deionised H₂O and blow dried.

A fluorescent layer was applied to the lens specimen in order to compare the theoretical and experimental SW anti-nodal spacing's and FWHM in the same manner as carried out in the work of Amor et al [72]. To deposit a monolayer of Dil on the curved surface of the lens specimen, a 30 µM solution was prepared by diluting 560 µL of a 1 mg/mL stock solution of Dil (Invitrogen) in 20 ml of dimethyl sulfoxide (DMSO) (Sigma Aldrich, UK).

I coated the lens specimen with Dil, which was also used to label the RBCs and has been used extensively in RBC membrane studies [72], [104], [105]. Specimens were labelled through direct application of the dye allowing the two lipophilic hydrocarbon tails to diffuse laterally into the membrane after which it fluoresces brightly and it is reported to not cause toxicity to the specimen [106]–[108].

The lens specimens were placed in a glass Petri dish with the curved surface submerged in the dye solution and gently rocked overnight. The Petri dish was wrapped in aluminium foil to prevent photo-damage to the dye during this period. The following day the specimens were washed three times in deionized water, then dried using compressed air and kept out of direct light until imaging.

2.2.2 Red blood cell isolation and staining

Blood specimens were obtained on the day of the experiments by cardiac puncture of a single mouse, which was rendered unconscious through CO₂ exposure, and the collected blood was immediately mixed in 1 ml centrifuge tubes (Star Labs) with acid citrate dextrose (ACD), an anti-coagulant. The ACD comprised of 1.32 g trisodium citrate (Fisher Scientific), 0.48g citric acid (Arcos Organics) and 1.40 g dextrose (Fisher Scientific) and was made up in 100 ml of distilled water. Cardiac punctures were performed by technical staff from the University of Strathclyde's Biological Procedures Unit in accordance with

UK Home Office guidelines and approved by the University of Strathclyde Ethics Committee.

For the study of infected red cells (iRBC), mice were infected with GFP-tagged *P. berghei* and treated with phenylhydrazine (Phz). Blood was obtained through cardiac puncture at the schizont stage and further enriched magnetically to produce higher parasitaemia by Dr Katie Hughes at University of Glasgow [109].

The method which was used to isolate and stain both the iRBC and RBC has been adapted from the protocol described by Amor et al [72]. The mouse blood and ACD suspension was spun down at 2000 rpm for 10 minutes with the supernatant removed and the pellet resuspended with 500 μ L of 4% bovine serum albumin (BSA) (Sigma) in phosphate-buffered saline (PBS) (Gibco). This process was repeated another three times so only a suspension of RBCs remained.

Red blood cells were fluorescently labelled by adding 200 μ L of the RBC suspension to 790 μ L 4% BSA in PBS along with 10 μ L of a 1 mg/mL stock solution of Dil. The solution was then incubated at 37 °C for 60 minutes whilst being gently shaken to ensure even distribution of the dye. After this, they were spun down and resuspended a further four times to remove all excess dye.

Silver broadband mirrors (Thorlabs) were prepared for imaging by first being thoroughly cleaned in ethanol (purity > 99.8 %, Sigma). Then to promote specimen adhesion to the mirrors they were coated with a solution 0.1% mass concentration poly-L-lysine (Sigma) and incubated at 37 °C for 45 – 60 minutes whilst being gently rocked. The preparation was washed with PBS and sterilised using UV light. 5 μ L of the RBC suspension was pipetted onto the mirrors under a coverslip (VWR, thickness = 1.5) 10 minutes prior to imaging.

2.2.3 Standing wave confocal laser scanning microscopy imaging of fluorescent specimens

Standing wave CLSM was carried out on the specimens using a Leica SP5 DM6000 CLSM. An argon laser provided the 488 nm and 514 nm excitation wavelengths and a HeNe laser provided the 543 nm excitation source. Fluorescence emission was collected by a Leica SP[®] spectral detector. SW images were obtained by placing a specimen which was either in contact or adhered to a mirrored surface below the objective lens, as shown in the configuration of the setup in Figure 2.5.

The model lens specimen images were acquired using a HCX PL APO CS 10.0x0.40 DRY UV objective lens, with an image size of 2048 x 2048 with a line average of 3 applied to the image to reduce the noise present in the image. A scan speed of 100 Hz was used.

Imaging of the healthy RBCs was conducted using a HCX PL FLUOTAR 100.0x1.30 oil objective lens objective lens. Images were captured at a 543 nm excitation wavelength with detection at 555-655 nm. For imaging of the iRBC, an excitation wavelength illumination was provided at 543 nm with a HCX PL FLUOTAR 100.0x1.30 oil objective lens. Fluorescent emission was detected between 550-700 nm. The GFP expression parasite images were obtained using an excitation from a 488 nm argon laser and emission detection at 500-540 nm. Infected red blood cells were imaged at slower scan speed of 100 Hz to allow for longer pixel dwell time, the image size was reduced to 1024 x 1024 pixels as not to increase the overall scan speed of the image acquisition. As a

result, a similar signal-to-noise could be obtained without compromising the image quality.

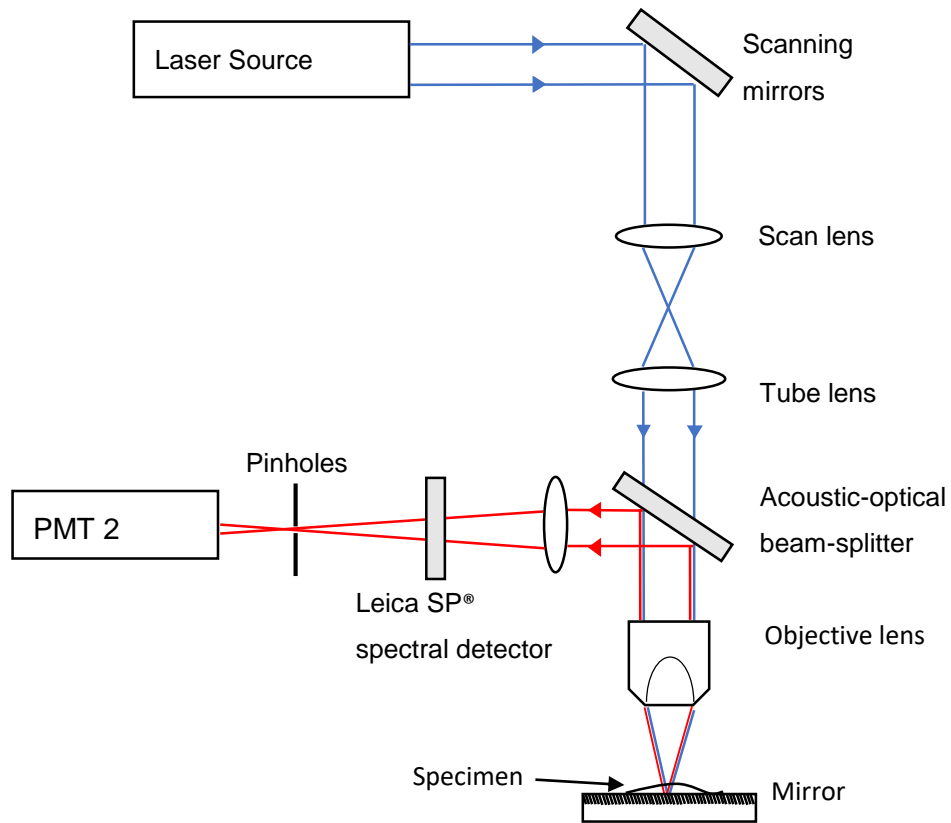


Figure 2.5 – Schematic diagram of experimental setup of the Leica SP5 DM6000 CLSM. The excitation (blue) light reflects off a dichroic mirror, which was located at the specimen plane, to generate a SW due to interference. The SW of light caused fluorescence emission (red), where SW anti-nodes intersected the specimen, was then propagated upwards through the lens and was separated using a Leica SP[®] spectral detector. The fluorescence signal was then detected by a PMT.

2.2.4 Image pre-processing

The purpose of image pre-processing was to crop and linearly contrast adjust the image before being imported into MATLAB to produce the 2D reconstruction. The images were opened in FIJI [110], as a .TIFF format and each image was cropped to contain only the

RBC of interest. To improve the contrast of the lens specimen and RBC SW images, the contrast and brightness was adjusted linearly in FIJI. This helped differentiate between the anti-nodal and nodal planes before the images were import into MATLAB.

2.2.5 Gaussian blur

The SW images had high frequency noise present. As a result, it made it difficult to process the SW images using the intensity thresholding techniques. Therefore, it was desirable to remove as much of the high frequency noise components from the image. This was achieved by application of a Gaussian blur. A Gaussian Blur was used as a low pass filter to remove the high frequency noise components whilst preserving the characteristic low frequency anti-nodal and nodal interference pattern of the SW. A 2D Gaussian blur is given as:

$$G(x, y) = \frac{1}{2\pi\sigma^2} e^{-\frac{x^2+y^2}{2\sigma^2}} \quad (2.3)$$

where σ is the standard deviation of the Gaussian function, x is the distance from the origin in the vertical axis, y is the direction from the origin in the horizontal axis. In practice, I used MATLAB's *imgaussfit* function, which applied a Gaussian blur to the normalised contrast adjusted SW images. Before application of the Gaussian blur, the images were read into MATLAB using the *imread* function. A Gaussian blur with standard deviation (std. dev.) values of $\sigma = 0, 1, 2, 3, 4, 5, 10$ and 20 were applied to the lens specimen image. To compare the effectiveness of the noise reduction for each std. dev., a Gaussian blur was applied to the SW images and the signal-to-noise ratio was calculated using:

$$SNR = \frac{\mu_{signal}}{\sigma_{signal}} \quad (2.4)$$

where, μ_{signal} is the mean of the signal and σ_{signal} is the standard deviation of the signal. In practice, due to the sinusoidal nature of the signal of the radial line plot, if a mean value was calculated over the whole signal, the signal structure would be averaged out.

Thus, a local mean was selected as it should retain as much of the underlying structure of the signal. This was achieved by utilising a local moving average and std. dev., with the moving average calculated over a 21 pixel range for each pixel, using the *movmean* and *movstd* functions in MATLAB. The result of the *movmean* (μ_{signal}) and *movstd* (σ_{signal}) was then used to calculate the signal-to-noise for each pixel using Eqn. 2.4. Lastly, the signal-to-noise for the image was calculated by taking the mean value of the signal-to-noise ratio for each pixel (Script Appendix I). This was repeated for every Gaussian blur std. dev value applied to the image.

2.2.6 Intensity Thresholding

Intensity thresholding was used to extract the SW anti-nodal planes in the SW image. A global threshold technique called the Otsu method was applied to the $f = 48$ mm single colour lens specimen SW image by using the *greythresh* function. A range of local adaptive intensity threshold values were applied to SW images using the inbuilt function *adapthresh* in MATLAB. This technique used a mean local intensity threshold which was based on the Bradley technique [84], an extension of the Wellners Method [83]. These methods use a local mean to determine the threshold value, where the mean value is calculated over a $m \times n$ pixel kernel in the image. The advantage of local intensity thresholding was that the threshold value set was dependent on the local pixel neighbourhood value. Specifically, this technique utilised a kernel which moves around the surrounding image and calculated the local mean value. If the pixel value was less than the local mean threshold it was set to black (0), if it was greater than the threshold value it was set to white (1). The global Otsu threshold was compared with a local threshold over a range of values from 0.5 to 0.9 which was applied in increments of 0.1, and between 0.55-0.65, which was applied in the increments of 0.01. The kernel (filter) size selected was the largest pixel distance between an anti-nodal and nodal plane in the SW images. This reduced the likelihood of under segmenting the SW anti-nodal planes in the SW image. A comparison of the experimental threshold data to a ground truth was

determined using a simulated 2D lens specimen. To simulate the lens, *a priori* knowledge of the lens specimen geometry was utilised, given that a hemisphere could be understood as shown in Figure 2.6.

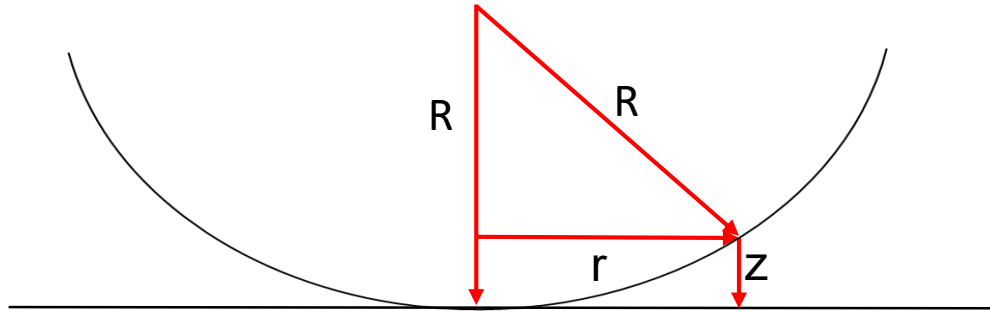


Figure 2.6 – A diagram which shows the lens specimen geometry. The red lines represent the geometry for the lens and how the radial distance (r) and height from the mirror (z) at any point along the surface of the mirror relates to the radius of curvature of the lens specimen.

Using Pythagoras's theorem, the radius of curvature of the lens was related to the height from the mirror and the radial distance at which that point occurred and was given by [72]:

$$R = \sqrt{r^2 + (R - z)^2} \quad (2.5)$$

where R was the radius of curvature, r was the radial distance and z was the axial height above the mirror. From this expression, I rearranged Eqn. 2.5 and solved for z , thus giving

$$z = R - \sqrt{R^2 - r^2} \quad (2.6)$$

Now using the known I substitute Eqn. 2.3 into Eqn. 2.1 for the axial height this then gives us a representation of the spherical intensity pattern of the simulated lens specimen, thus giving:

$$I(r) = 1 - \cos(k(R - \sqrt{R^2 - r^2})) \quad (2.7)$$

Applying a scaling factor for the pixels per micron, data points were generated for eight SW anti-nodal peaks which allowed for the direct comparison between the simulated and the experimental data sets. The simulated threshold image was created by determining all the data points with a normalised intensity value of less than 0.5, and setting them to 0 intensity, as they corresponded to nodal planes. Next, all normalised intensity values ≥ 0.5 were set to an intensity value of 1. Then the percentage between the total number of threshold pixels with a value 1 compared with the total number of pixels of the simulated data set was then calculated. For experimental data sets, SW lens specimen images were imported into MATLAB and the thresholding procedure was applied and the total number of pixels in an image was calculated. Again, the total number of pixels with a value 1 in an image was calculated as a percentage of the total number of pixels in an experimental SW lens image. The percentage values were then compared between the experimental threshold images and the simulated theoretical lens specimen to quantify the accuracy of the threshold procedure.

2.2.7 Two-dimensional single-colour reconstruction

To create a single colour 2D reconstruction of the lens specimen and RBC SW image (Algorithm shown in Appendix II), the pre-processed images were cropped and contrast adjusted using FIJI and read into MATLAB using the *imread* function. The *x* and *y* coordinates of each pixel were stored in two matrices and calibrated using the image scale. The image intensities were normalised between 0 and 1. A Gaussian blur was applied using the *imgaussfit* function and an intensity threshold was applied using the *adaptthres* function. The threshold image was compared to the raw SW image to extract the correct intensity values and *x* and *y* coordinates for each pixel within the threshold anti-nodal plane. The intensity values and the *x* and *y* coordinate values were translated into vectors and plotted using the *imshow* function which created an image of the 2D reconstruction. The procedure of the 2D reconstruction steps was shown below in Figure 2.8.

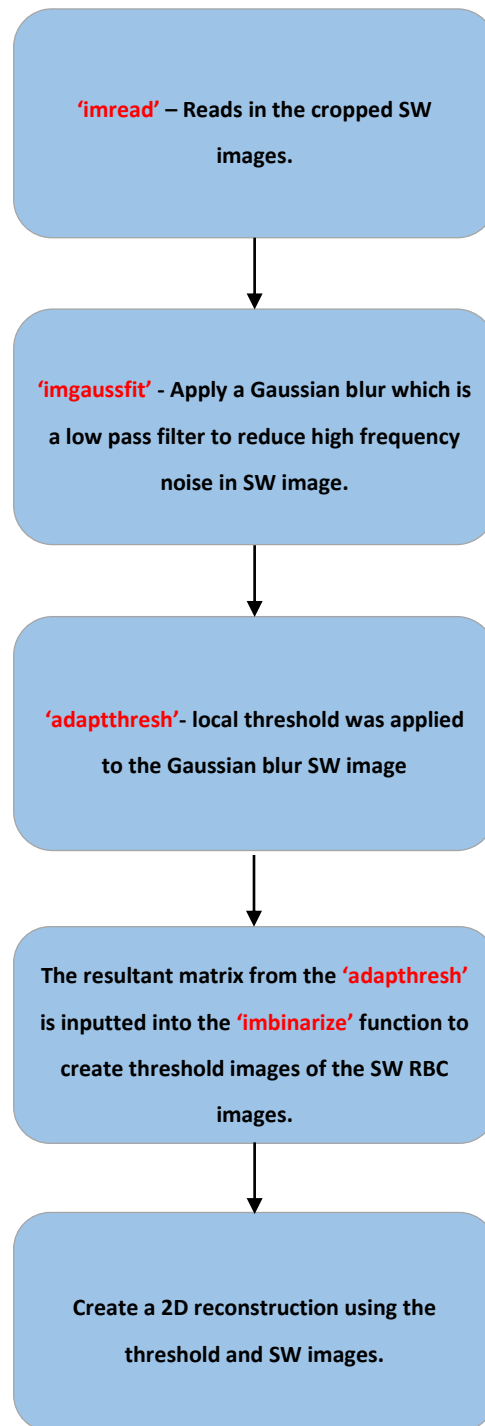


Figure 2.7 – A flowchart of the key steps to create a 2D reconstruction of the lens specimen and the RBC and iRBC SW images. The MATLAB functions used are shown in red.

2.3 Results

2.3.1 Pre-processing and Gaussian blur application to lens specimen

specimen

A SW image was captured for a fluorescently coated $f = 48$ mm model lens specimen at an excitation wavelength of 543 nm, with the fluorescent emission wavelengths captured between 550-650 nm. Firstly, FIJI was used to linearly adjust both the brightness and contrast of the lens specimen images. A concentric ring pattern was observed in Figure 2.8a, where the bright fringes corresponded to the regions where the excitation SW intersected the specimen, and as a result generated fluorescent emission. The concentric ring pattern varied periodically across the field of the 2D image, and increased at distances farther away from the centre of the lens. An intensity plot of a single pixel thick line was shown in Figure 2.8b. I observed a sinusoidal profile of the normalised fluorescence intensity of the SW lens specimen. Note the noise present in the SW profile in Figure 2.8b

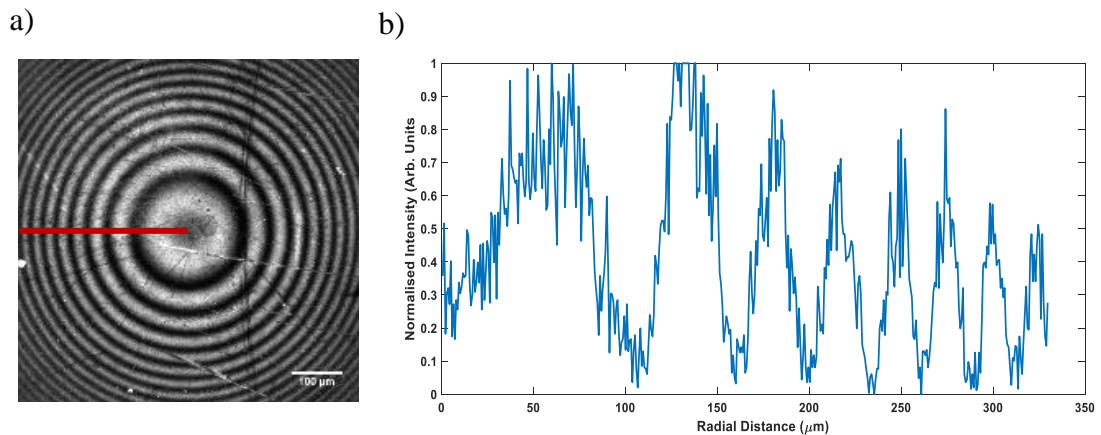


Figure 2.8– a) Dil labelled $f = 48$ mm lens specimen with a concentric ring pattern where the axial anti-nodal planes intersect the lens specimen. b) A radial plot of a one-pixel thick line through the specimen i.e. the red line. I observed the oscillating pattern due to the SW.

Because of the presence of random noise in the SW images, a Gaussian blur was applied with MATLABs *imgaussfit* function to the raw images with std. dev. values of $\sigma = 0, 5, 10$ and 20. In Figure 2.9a, the effect of the increased std. dev. resulted in greater smoothing of the images, when a higher σ was applied. Consequently, at very high σ values the blurring effect becomes more dominate in the image, particularly at the edge of the image. Next, the radial intensity profiles were extracted from the centre of the image to the far-left hand side of the image (which was shown with the red line overlay in Figure 2.9a) and plotted as radial distance against normalised intensity. The intensity profiles in Figure 2.9b, for each σ values showed a characteristic oscillation with high frequency noise being removed at $\sigma = 5, 10$ and 20 values. However, at values of $\sigma = 10$ and 20, attenuation of the fluorescent signal occurred at larger radial distances. This was particularly evident at $\sigma = 20$, where the attenuation became more prominent in the centre of the image. This resulted in only three distinct peaks, with the signal levelling off at higher radial distances i.e. at the edges of the SW image, which led to loss in SW structure.

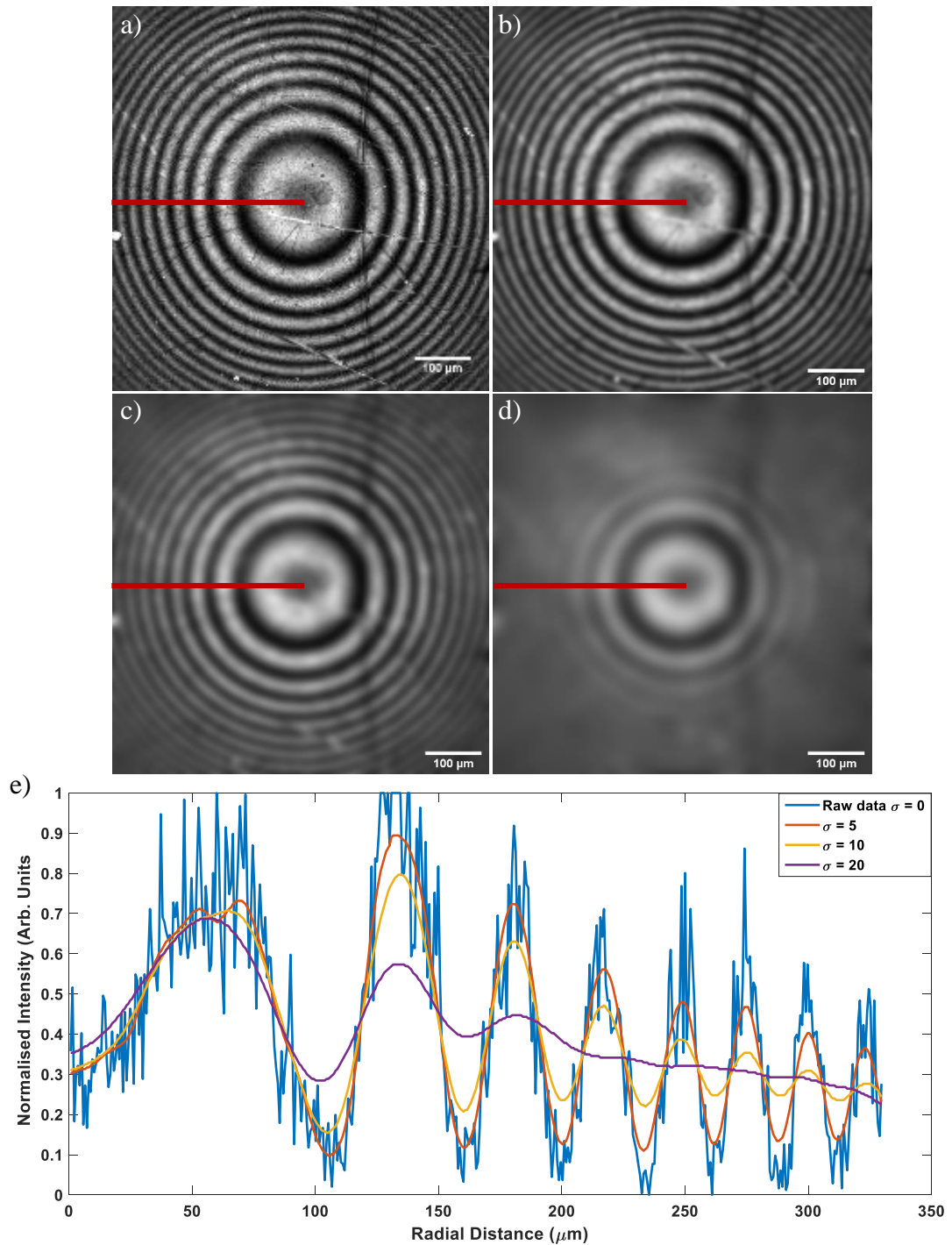


Figure 2.9 - Application of a Gaussian blur with varying standard deviation to the Dil stained lens specimens SW images. a) $\sigma = 0$, b) $\sigma = 5$, c) $\sigma = 10$, d) $\sigma = 20$. e) A radial plot of the lens specimen for each of the σ Gaussian blur applied are shown in a-d).

Next, a smaller range of std. dev. values between $\sigma = 0$ to 5 in increments of 1, were applied to the SW image, as was shown in Figure 2.10. When the value of σ was incrementally increased, there was a reduction in high frequency noise which resulted in a smoother signal with slight attenuation. In other words, much of the noise components were removed leaving only the characteristic sinusoidal SW profile.

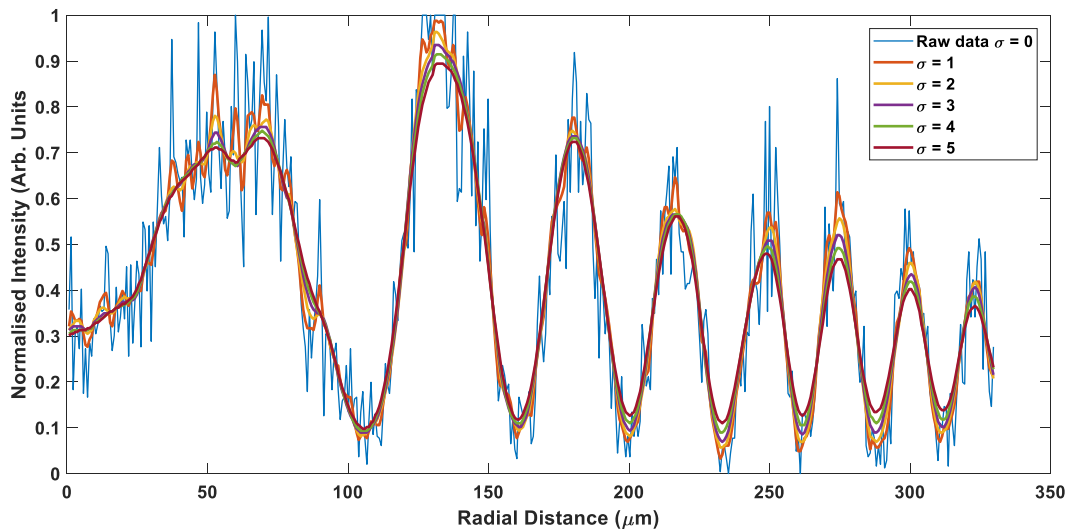


Figure 2.10 - A Gaussian blur applied to the $f = 48$ mm lens specimen between $\sigma = 0$ to 5 in increments of 1. The application of increased std. dev. gradually reduced the overall noise in the SW signal, but with the effect of attenuation to the SW signal.

Now, to compare the signal-to-noise ratio, Eqn. 2.4 was used to calculate the signal-to-noise for each σ value applied to the SW image for each of the corresponding radial intensity profiles (Figure 2.9e and Figure 2.10). In table 2.1, the signal-to-noise ratio was calculated over the full range of σ values with a 17x increase in signal-to-noise over the full range, but at the expense of the SW structure. However, over the optimised $\sigma = 0$ to 5 range, a 3x increase signal-to-noise was reported without significant loss to the overall SW structure.

Table 2.1-Table of the signal-to-noise ratio calculated for each Gaussian blur std. dev. (σ) applied to the pre-processed lens specimen SW specimen images.

Std. Dev. (σ)	Signal-to-noise ratio	Standard error
0	2.86	± 0.07
1	4.75	± 0.18
2	6.36	± 0.32
3	7.54	± 0.48
4	8.21	± 0.54
5	8.85	± 0.57
10	13.60	± 0.85
20	48.93	± 2.56

2.3.2 Optimising the thresholding using SW lens specimen images

Intensity thresholding was used to separate the nodal and anti-nodal planes. The raw SW $f = 48$ mm lens specimen had a Gaussian blur of $\sigma = 5$ applied. To characterise the local mean threshold, sensitivity values which ranged from 0.50 – 0.90 in increments of 0.1 were applied to the image and compared with Otsu global threshold. Figure 2.11a shows the global threshold applied to the SW image. The resultant global threshold images captured very little of the anti-nodal planes, particularly in regions away from the centre of the image. Conversely, the application of a local threshold captured much of the anti-nodal planes as the threshold sensitivity applied was increased (Figure 2.11c-f) over a filter size of 51 by 51 pixels. In addition, all the local threshold images showed the characteristic radial anti-nodal pattern comparable to the SW image captured in Figure 2.8a. Above a 0.7 sensitivity, an excessive amount of the image was removed via the

threshold process which included the nodal plane regions particularly in the corner of the images (Figure 2.11 d-f). As expected, when the sensitivity of the threshold values was too low (sensitivity value of 0.5), the threshold image appeared to extract less of the anti-nodal planes, but performed better than Otsu global thresholding, as was demonstrated in Figure 2.11 a-b. Qualitatively, it was then possible to infer that a sensitivity value 0.7 resulted in too much thresholding, and a 0.5 sensitivity value of was too little. However, a sensitivity value of 0.6 resulted in a very good representation of the SW lens image. Therefore, an optimal sensitivity value lies between the local threshold sensitivity range of 0.55 and 0.65.

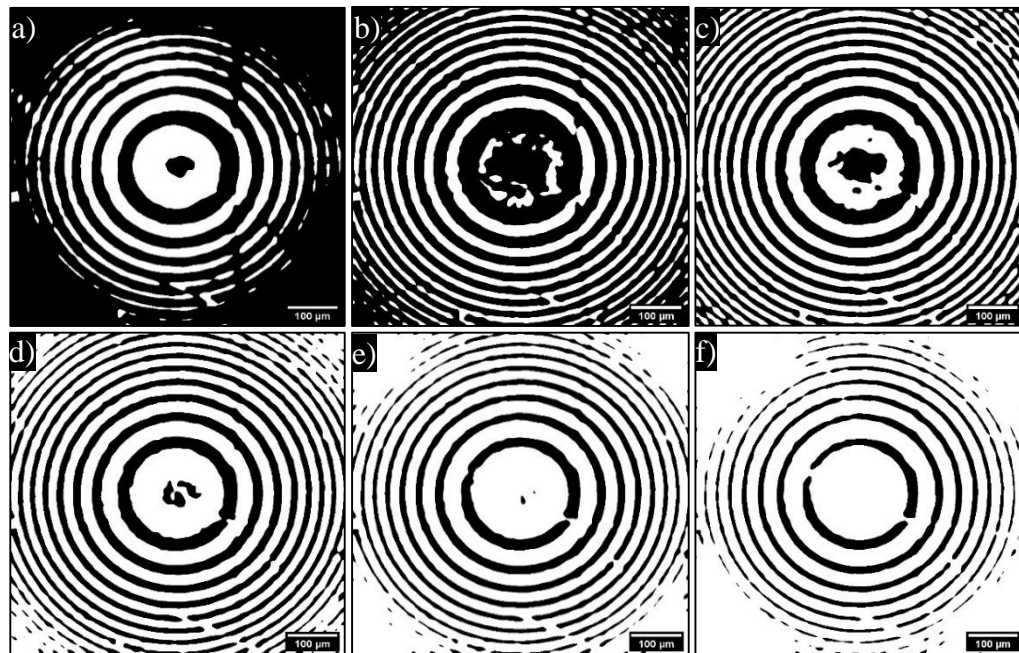


Figure 2.11 - Dil stained lens specimen with the application of global and local thresholding techniques. a) Global thresholding of the lens specimen using the Otsu method. Local mean thresholding was applied with a filter size of 51 x 51 to the SW lens specimen at threshold values of b) 0.5 c) 0.6 d) 0.7 e) 0.8 and f) 0.9.

Local mean threshold was now applied with sensitivity values between 0.55 to 0.65 in increments of 0.01, with a filter size of 51 x 51. The anti-nodal plane percentage was plotted against local mean sensitivity values in Figure 2.12. This theoretical anti-nodal

percentage represents the amount of the anti-nodal planes which had been captured at the FWHM width for each anti-nodal plane. The dashed line was an overlay of the anti-nodal plane percentage information and was determined theoretically from the simulated SW image of $\approx 50\%$. Note that the theoretical value was obtained from the theoretical threshold image, where the intensity values were ≥ 0.5 , and not from the application of a local mean threshold to the theoretical simulated lens specimen. From Figure 2.12, it was possible to extract the point at which the experimental data intersects the theoretical anti-nodal percentage. The point of intersection was determined to be at ≈ 0.60 sensitivity, this offers the best extraction of the SW anti-nodal plane information based on the fluorescence intensity of SW data, using a local mean threshold with a 0.60 sensitivity and a filter size of 51×51 .

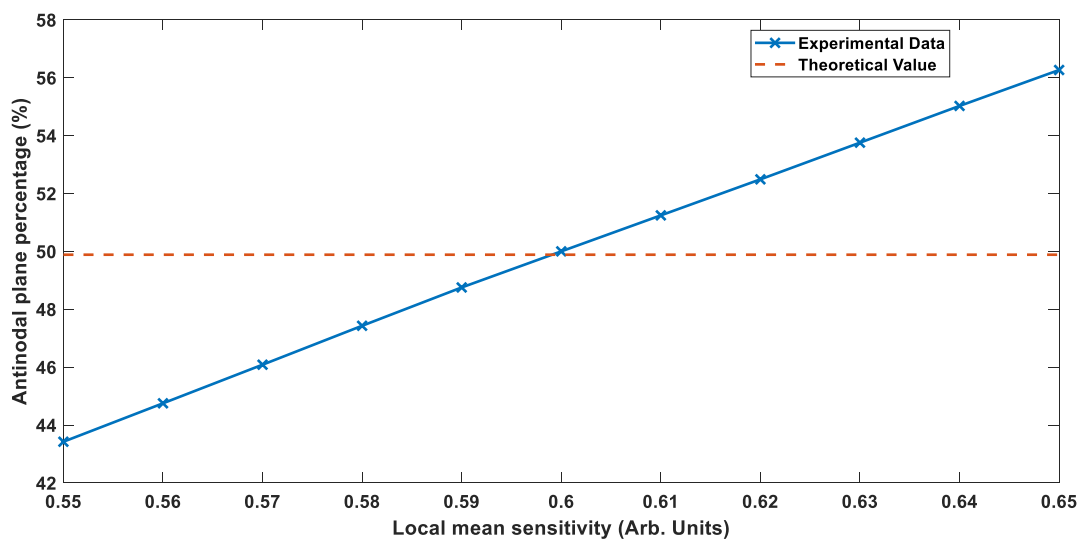


Figure 2.12 – A plot of anti-nodal plane percentage against local mean sensitivity. The dashed line was the theoretical value of the anti-nodal plane percentage and was present to determine the point of intersection between experimental and theoretical results.

2.3.3 Two-dimensional SW reconstruction of a lens specimen and RBCs

A single colour $f = 48$ mm lens specimen was imaged using a 543 nm excitation light source. Figure 2.13a shows a SW image of the lens specimen with a concentric fringe pattern which is characteristic of the SW anti-nodal planes intersecting a fluorescently coated lens specimen. The 2D reconstruction was created for the lens specimen. A Gaussian blur was applied with a standard deviation value of $\sigma = 5$. Note this gave the best balance between signal-to-noise ratio and retained much of the detail in the SW image. The values for the Gaussian blur std. dev., and the local adaptive threshold sensitivity and pixel neighbourhood size, were obtained quantitatively using the optimised conditions obtained in sections 2.3.1 and 2.3.2. A local adaptive thresholding technique was applied to obtain as much of the SW anti-nodal planes as possible. In this instance, I applied a sensitivity of 0.60 and local neighbourhood size of 51 by 51 pixels to extract the anti-nodal plane information based on fluorescence intensity. Now that the anti-nodal and nodal planes were clearly separated, a 2D reconstruction of the lens specimens was created by application of the method described in section 2.2.7. A comparison of Figure 2.13b with Figure 2.13a showed that the pixel value intensity at each pixel location resulted in an accurate representation of the positional and intensity information of the SW concentric fringe pattern. Furthermore, the pixel intensities were consistent with the raw SW image. Notice the saturated fluorescent dye spot regions and areas of poor binding which were present in both the raw SW image and the 2D reconstruction.

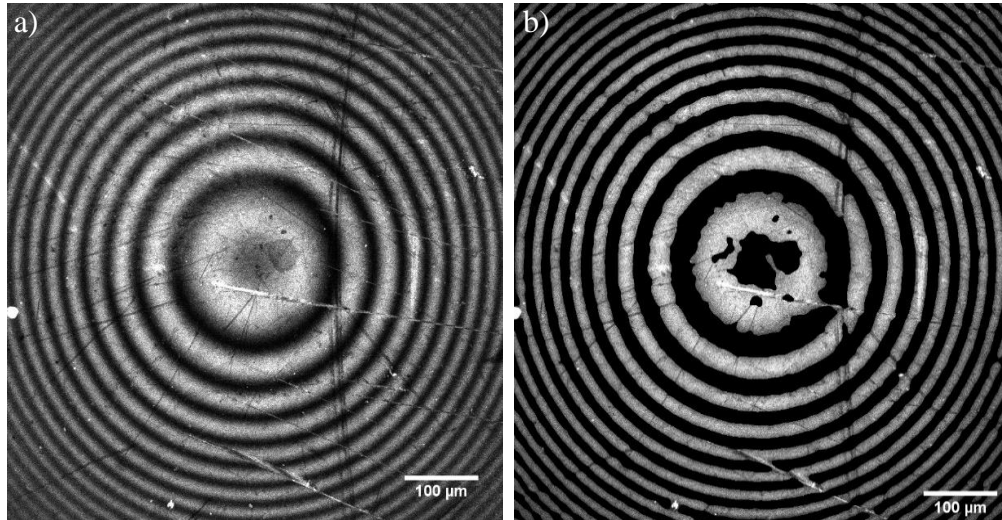


Figure 2.13 – a) A single colour SW image Dil coated $f = 48$ mm lens specimen. A threshold value of 0.60 was applied to the Gaussian blur image. b) The 2D reconstruction of the $f = 48$ mm SW image which showed the intensity values mapped back on to the threshold image from the raw SW image.

This method was further extended to a biological specimen by imaging RBCs using the SW technique. Figure 2.14a and c, shows the raw RBC image where the SW anti-nodal planes intersect the concave surface closest to the mirror creating a concentric ringed fringe pattern. I observed the structural differences between the healthy RBC. For example, the RBC in Figure 2.14a has more elliptical concave surface than the RBC in Figure 2.14c. A Gaussian blur of $\sigma = 5$ was applied to the raw RBC image in Figure 2.14a and c). In Figure 2.14b and d, using the optimised parameters threshold parameters, the RBC threshold image demonstrated clear separation of the anti-nodal and nodal planes. As before, the threshold image was used to extract the pixel intensity values by storing the position and intensity of each anti-nodal region from Figure 2.14a. Figure 2.14 b and d, shows the 2D reconstruction of the anti-nodal planes which intersect the RBC specimen. As expected, only the positional values of the anti-nodal plane with their

corresponding intensity values are extracted. Notice that regions where bright spots were observed in the raw image could also be seen in the 2D reconstruction.

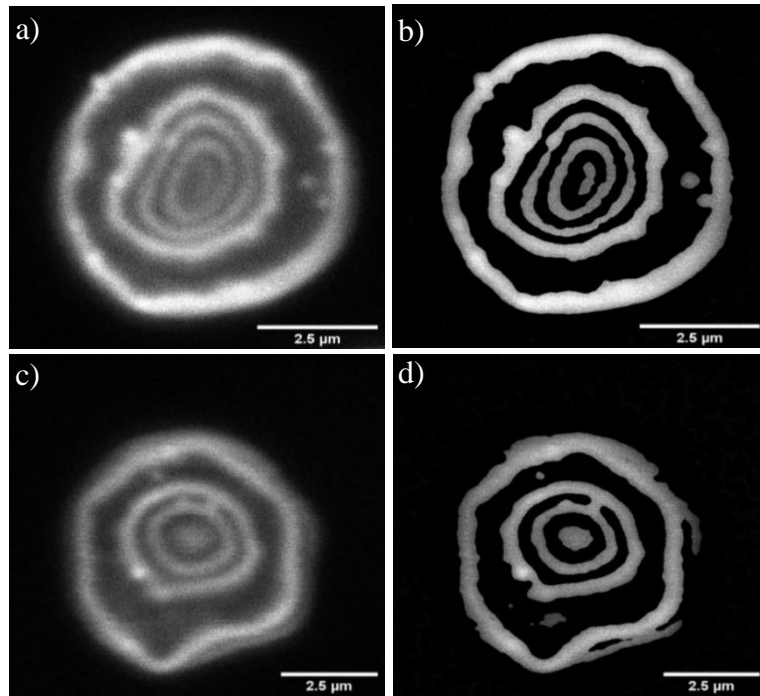


Figure 2.14 - Single colour SW images and 2D reconstruction of a Dil stained red blood cell that has been cropped and the contrast adjusted in ImageJ. A Gaussian blur of $\sigma = 5$ applied to a) and c) The threshold image with a local mean threshold sensitivity value of 0.60 with a filter size of 51 x 51 applied to the Gaussian blur image b and d) are 2D reconstruction of a SW RBC.

2.3.4 SW imaging and two-dimensional of *P.berghei* infected red blood cells

P. berghei was used as a model for the SW imaging of unhealthy RBCs to compare the SW structure pattern with healthy RBCs. Firstly, I checked the autofluorescence of Phz which was used to increase parasitaemia, as it had been known to cause autofluorescence [111]. As a result, I first captured uninfected Phz treated RBC and imaged them using a 40x/1.3 NA oil immersion objective and compared the Phz treated

RBC with non-treated Dil stained RBCs adhered to a mirrored surface. Phenylhydrazine autofluorescence was tested at the three excitation wavelengths used for Dil iRBC imaging of 488 nm, 514 nm and 543 nm. Each wavelength was individually set at the same power for both the untreated and treated RBCs. To compare the intensities, 10 RBCs were taken as regions of interest (ROIs) in each image and the mean intensity over the 10 ROI's were calculated and shown in Table 2.2. In Figure 2.15, the intensities in the 543 and 514 nm excitation channels showed little autofluorescence. Thus, there was a large difference in the overall intensity between the treated and non-treated RBC images. The autofluorescence was more apparent with a 488 nm excitation wavelength due to the decreased of the fluorescence signal from the Dil membrane stain.

Table 2.2 – A comparison of the relative intensity of change between untreated Dil stained and the Phz treated RBCs not stained with Dil.

Excitation Wavelength (nm)	Intensity Untreated (Arbitrary Units)	Intensity Phz treated (Arbitrary Units)	Relative change (fold increase)
543	64.1 ± 6.0	1.64 ± 0.04	38.0
514	62.9 ± 5.4	2.63 ± 0.06	22.9
488	39.0 ± 2.8	4.86 ± 0.37	7.02

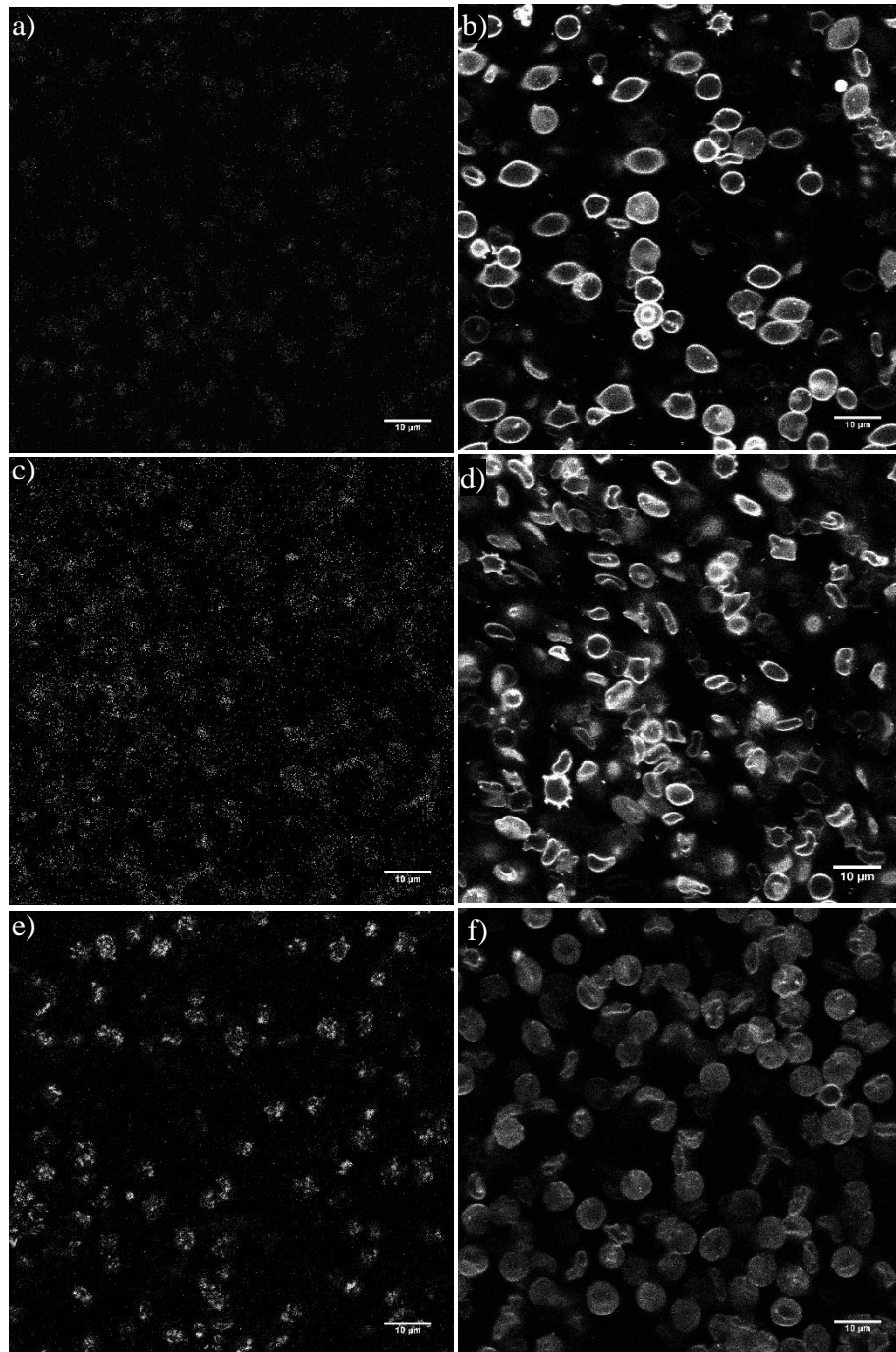


Figure 2.15– Autofluorescence images of RBCs treated with Phz imaged at excitation wavelengths of a) 543 nm, c) 514 nm and e) 488 nm. The treated Phz images have been contrast stretched to use the full dynamic range of the images. RBCs stained with Dil but not treated with Phz were imaged at wavelengths of b) 543 nm, d) 514 nm and f) 488 nm.

Infected RBCs were captured using a HCX PL APO CS 100x1.30 oil immersion objective lens on a Leica SP5 DM600 CLSM. Figure 2.16 shows an image of a RBC which was infected at the schizont stage. I observed protrusions from the cell membrane of the iRBC and noticed that there was no longer a concentric ring pattern which was characteristic of healthy RBC SW images. Instead there were three distinct regions near the mirrored surface, this suggested a deformation in the iRBC membrane most likely due to the presence of the parasite within the RBC.

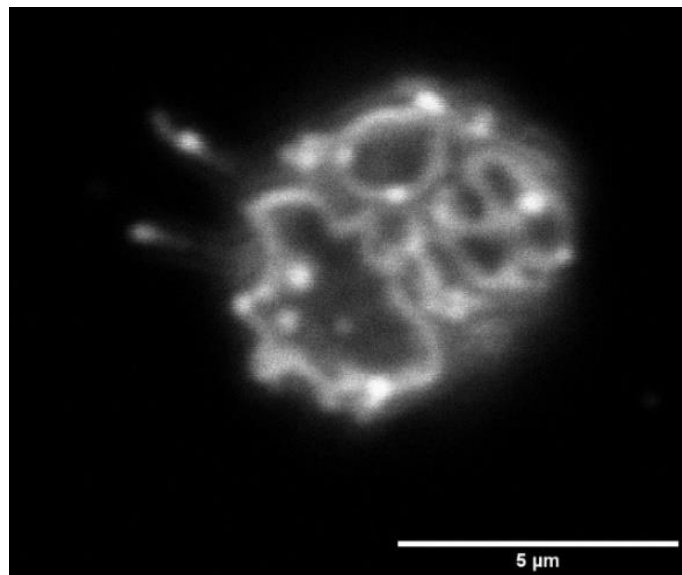
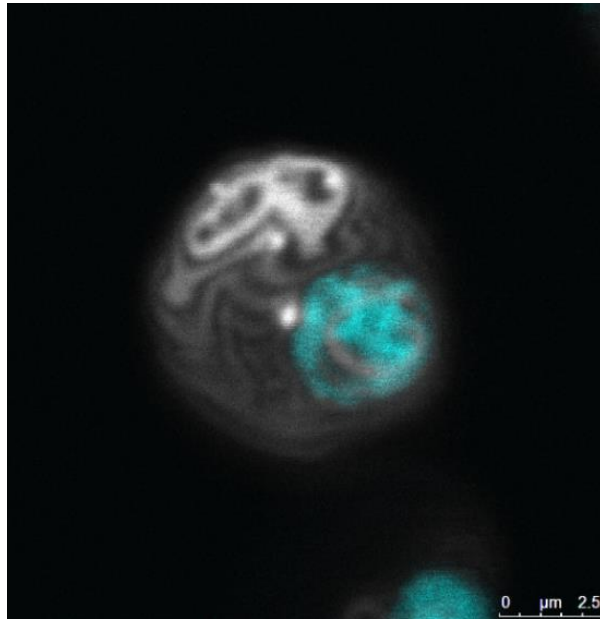


Figure 2.16 – RBCs infected with P. berghei at the schizont stage. An SW image of the iRBC had shown protrusions and morphological changes and loss of the concave shape in the iRBC structure.

Next, to confirm the presence of a parasite within the RBC membrane was the cause of the deformation observed in the SW images, I captured SW images with both the Dil labelled iRBC, at an excitation wavelength 543 nm, and the GFP tagged parasite at 488 nm with the GFP emission collected at 500-540 nm. The plane of focus was adjusted such that it brought the out-of-focus parasite into focus. I observed an overlap of the parasite within the cell membrane in the x and y positions. It was observed that there was rounding of the cell membrane where the parasite was located as shown in Figure 2.17.

There was also deformation in RBC membrane and lose in the characteristic bi-concave surface, as was previously observed.



*Figure 2.17 - A mature schizont *P. berghei* iRBC with the parasite GFP tagged (cyan) and the RBC membrane was stained with Dil (greyscale). The cell membrane of iRBC showed deformation due to the presence of parasite.*

After successfully carrying out imaging of *P. berghei* iRBCs, I investigated if the GFP labelled parasites were detected within the same iRBC, because when focusing on the parasite, I moved the plane of focus away from the mirror surface. To investigate this, I utilised the 488 nm edge of the Dil excitation spectrum and the emission was detected over 550-650 nm. The GFP emission detection was adjusted to collect between 495 – 525 nm to limit the bleed through of the Dil emission. Thus, I was able to detect the fluorescence emission from the cell membrane and parasite simultaneously. Figure 2.18a, showed the SW image for an iRBC, where I observed the Dil stained cell membrane. Now I moved the plane of focus, and in grey I observed that cell membrane was almost identical to Figure 2.18b, and there was clear localisation of the parasite in cyan within the cell membrane of the iRBC.

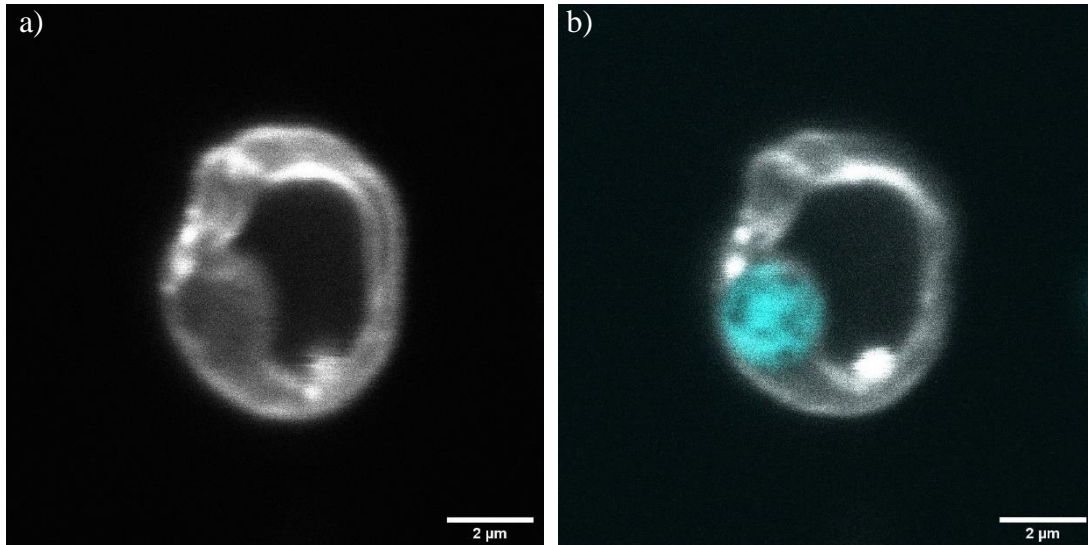


Figure 2.18 – SW images of mature schizont stage iRBC. a) The red blood cell membrane of the infected RBC closest to the mirror surface at 514 nm excitation b) 488 nm excitation of both the membrane in grey and the GFP Parasite now in focus within the cell membrane.

Finally, I utilised the methods developed for the 2D reconstruction of healthy RBC. I applied a Gaussian blur with a std. dev. of $\sigma = 5$ to each image. In Figure 2.19a, I applied a local mean threshold with a sensitivity of 0.60 and a filter size of 61 x 61. In Figure 2.19b, a local threshold with a sensitivity of 0.60 and a filter size of 41 x 41 was applied. I did observe clear banding structure with rejection of much of the background and nodal regions. This was an important step, as it allowed for only the anti-nodal plane information to be extracted, which has the geometric information encoded within it, whilst removing much of the unwanted background and nodal plane signals. This was particularly important as the parasitic invasion of the RBC caused deformation to cell membrane [90]. Therefore, only the anti-nodal plane information revealed the geometric structure.

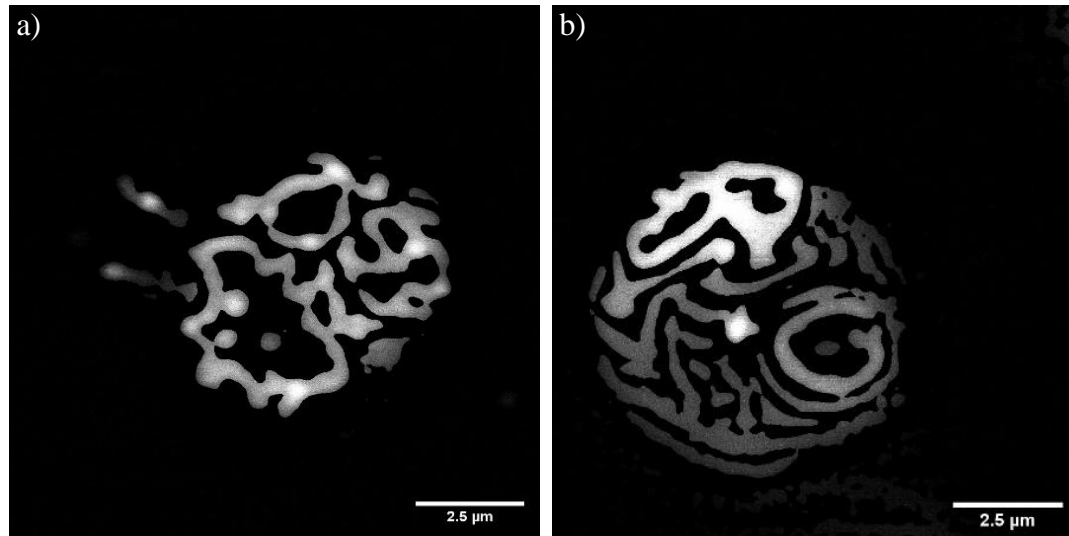


Figure 2.19 – Two-dimension reconstruction of SW images of Dil stained *P. berghei* iRBCs shown in a) Figure 2.16 and b) Figure 2.17. In both cases, I observed clear separation between the anti-nodal planes and the rejected background and nodal regions of the iRBCs.

2.4 Discussion

RBC SW imaging has been carried out by Amor et al [72], which demonstrated precise contour mapping of the concave surface of a RBC closest to the mirror surface. Repeating this experiment, I observed banding structure due to the concave nature of RBC. Currently, no SW study thus far has demonstrated the use of SW for the contour mapping of unhealthy RBCs. Therefore, I investigated malaria as a model for SW imaging of unhealthy RBCs using GFP tagged *P.berghei*. Before imaging, I sought to confirm that autofluorescence would not affect the imaging of the iRBC. It was suspected that the treatment of Phz which was used to increase parasitaemia could cause increased autofluorescence in RBCs, due to the breakdown of hemoglobin by-products which were also autofluorescent [111]. However, at the 543 nm and 514 nm excitation wavelengths I observed very little autofluorescence with a 39 and 28.9 fold increase between the Dil stained and non-Dil stained Phz treated RBCs. Therefore, Phz treatment did not impact

imaging of iRBCs at the excitation wavelengths that I was interested in using for SW imaging.

P. berghei was selected at the schizont stage which is the final stage of the parasite asexual reproduction cycle, before they rupture the RBC membrane and the merozoites go on to invade new RBCs [90], [112]. When applying the SW method to iRBCs, I observed the loss of the characteristic concave structure with partial or full rounding of the RBC membrane. This was consistent with previous studies, that the result of parasite invading the RBC changes the morphological properties of the RBC [90], [91], [113], [114], and that the morphology changes were likely to be comparable across *Plasmodium* species [115]. Additionally, it must be noted that in Figure 2.17 the parasite may not have fully matured to the schizont stage. Thus, a smaller parasite has caused deformation to the bottom edge of the RBC. It was clear that the invasion of the parasite caused deformation to the RBC which the SW method could detect.

Quantitative phase methods have been used to investigate healthy and unhealthy RBCs and extract quantitative information about the cell morphology [33], [100], [116]–[118]. However, the set-up for quantitative phase methods and analysis of the data is not trivial, and may require specialised optics and additional setup to the microscope [99], [101]. SW microscopy on the other hand, was an easy-to-implement technique, although data analysis techniques are required to be developed. Additionally, SW allowed for quick inspection which could then be used to make assumptions about the RBC geometry. Furthermore, SW images showed clear morphological differences between the healthy RBCs and the *P. berghei* iRBCs.

Standing wave multi-planar technique allows for contour mapping of 3D structures with super-resolved sections [72]. However, the drawback of this technique was that the 3D information was encoded within a 2D image. Overcoming the challenge of quantification and decoding the information present in the SW images was an important step and was required to be addressed to take full advantage of the multi-planar SW images. For this

technique to be applicable to arbitrary geometrical structures, I required a computational method to extract the 2D positional and intensity values of the pixels within the anti-nodal planes. The approach to solving this problem was to use techniques already available in the MATLAB image processing toolbox to provide the computation tools for anti-nodal plane extraction.

Noise plays a role in making it difficult to extract information using segmentation techniques. The application of noise filtering techniques is common in preprocessing to reduce the noise present within an image. I applied a Gaussian blur at different std. dev. values which reduced the noise present in the image, as shown in Table 2.1. In particular, an improvement in the signal-to noise which was measured at very high sigma values. However, it was observed that there was an increase in smoothing and loss of the distinct details of the anti-nodal pattern as the std. dev. value of the Gaussian blur was increased. This was to be expected, as larger the std. dev. becomes, the values within the smoothing kernel becomes larger, which resulted in blurring of the edge structures and reduction in the image contrast [79], [119]. In the situations where the std. dev. was too large, and because of the projection of the 3D lens surface in 2D, I noticed the loss of the higher frequencies near the edge of the SW images. This was the result of the Gaussian blur, which in-effect filtered out higher frequency components and resulted in loss of the SW structure. Therefore, a choice has to be made based on the observation of the amount of smoothing present in an image and the improvement in the signal-to-noise ratio, without the loss of fine details and overall SW structure. This could be done by inspection.

Intensity thresholding method was suitable at segmenting cellular features that had a high intensity difference and were spatially separated [81]. Therefore, intensity thresholding was a suitable method for detecting the high intensity SW anti-nodal planes from the low intensity nodal planes and background. Initially, global thresholding was achieved by application of the Otsu method [82] and was compared with standard mean local thresholding technique [84]. Global thresholding was not suitable for our SW image

data sets, as the emission light intensity was not homogeneous over the whole image. The cause of this variation of the light intensity over the image was due to the inhomogeneous binding of the fluorescent dye over the whole lens surface and the drop off in intensity farther away from the mirror surface. Therefore, utilising local adaptive thresholding was advantageous, as they were well-suited to varying levels of light intensity over the image. This was achieved by generating a local threshold value for a small region of pixels within an image [83], [84]. Thus, local thresholding produced SW threshold images with anti-nodal planes separated from the nodal planes. The result was a concentric fringe pattern that resembled the raw SW image.

Finally, in MATLAB by utilising the threshold image to extract only the anti-nodal plane intensity and positional data (x,y) , a 2D reconstruction of the lens specimens, healthy and infected RBCs could be obtained. However, Dil causes problems with dye spots being present within the RBC membrane, this will require further image processing to improve segmentation of the anti-nodal planes. Additionally, iRBC have a complicated membrane structure which leads to ambiguity of the axial height of the SW banding structure. As a result, it would be difficult to make assumptions about the cell geometry. Whereas, healthy RBCs have a more predictable morphology that require less assumptions about the cell geometry to extract the axial height information. In future, the 2D reconstruction method could be used as the first step in the development of a method to assign 3D information to healthy RBCs to produce 3D reconstruction using SW microscopy.

2.5 Conclusion

In this chapter, I have discussed the work carried out on the 2D SW images. Standing wave RBC imaging of *P. berghei* has demonstrated, in principle, the ability of SW technique to be used to contour map and investigate the cell morphology of both healthy and infected RBCs. The aim of this experiment was to develop a set of computational techniques which could be utilised to extract the 2D position (x,y) and pixel intensity

information of the SW anti-nodal planes. By using a Gaussian blur and image segmentation techniques, I was able to extract the anti-nodal plane information whilst rejecting both the nodal and background signal. Using the raw SW and threshold images, I was able to extract the pixel intensities from the images and create a 2D reconstruction of lens specimens, RBC and iRBC specimens.

Chapter 3

Three-dimensional reconstruction of video-rate widefield standing wave RBC images

In this chapter, I developed a computational method to create a 3D reconstruction of a fluorescently labelled healthy RBC captured with a widefield epi-fluorescence setup at video-rate. Furthermore, it was demonstrated that by extending the method outlined in chapter 2, the lateral (x,y) and intensity information from the SW images anti-nodal planes could be extracted. Through development of a custom algorithm, I removed images where the anti-nodal planes were in contact. This was suspected to be caused by dye clumps. Using *a priori* knowledge of the healthy RBC biconcave surfaces, axial height information was assigned to the boundaries of the anti-nodal planes. Using the axial height information, cubic interpolated concave surface of the RBC was calculated, which created a 3D reconstruction and improved the visualisation of the RBC. I showed that from the healthy RBC SW images presented in this Chapter, 981 images out of 1000 acquired could be reconstructed in 3D. The SW RBC technique was compared to standard widefield epi-fluorescence imaging and showed that the SW technique not only reveals more topographical information which could be reconstructed, but that the specimen does not undergo any increase in toxicity or rate of photobleaching over the image acquisition time.

3.1 Introduction

Multiple-planar SW microscopy allows for 3D information to be encoded into a 2D image. In this case, images of healthy RBCs were captured with a widefield epi-fluorescence microscope. In this Chapter, my aim was to develop a method for the 3D reconstruction of SW RBC images, using inbuilt and custom MATLAB functions combined with the 2D reconstruction code developed in chapter 2. By using *a priori* knowledge of the RBC, axial information was assigned to produce a 3D reconstruction. For SW RBC images where the anti-nodal planes appeared in contact, a method was described to segment these images. The code was then implemented to obtain a 3D reconstruction of widefield SW microscopy images of healthy RBCs which were captured at 30.30 hz over 1000 frames.

Lastly, photo-bleaching and photo-toxicity rates were compared between SW widefield imaging and standard widefield epi-fluorescence imaging.

In Chapter 2, the SW equation (Eqn. 2.1) described the intensity of the SW propagation along the axial height direction relative to a mirrored surface. However, this did not account for the dependence of the axial intensity profile due to the NA of the objective lens. Therefore, an additional term was required to describe the widefield SW axial intensity distribution.

In widefield epi-fluorescence SW microscopy, a specimen is illuminated with an intensity profile that is proportional to $1 - \cos(kz)$ [14], [73]. This will produce an oscillatory field within the depth of focus where fluorescence will only be generated within the anti-nodal regions at a thickness of $\lambda/4n$, where λ is the excitation wavelength and n is the refractive index. In conventional widefield epi-fluorescence microscopy, the detection PSF can be approximated to $\text{sinc}^2\left(\frac{NA^2}{2n\lambda_{em}}z\right)$ [120]. Thus, when the detection PSF is combined with the axial modulation of the excitation field, this acts as a modulation on the widefield detection PSF [121]. Therefore, an expression for the effective PSF for widefield SW microscopy is a convolution between the SW structure (Eqn.2.1) and the conventional widefield detection PSF, which results in an widefield SW intensity profile which is proportional to [103], [120]:

$$PSF(z) = 1 - \cos(kz) * \text{sinc}^2\left(\frac{NA^2}{2n\lambda_{em}}z\right) \quad (3.1)$$

where λ_{em} is the peak emission wavelength, NA is the numerical aperture of the objective lens, $k = 4\pi n/\lambda$ and z denotes the coordinate along the z axis [122], [123]. Depending on the wavelength of excitation, the resolution using SW microscopy could be significantly below the axial diffraction limit. This expression in Eqn. 3.1 was used to characterise the effect of the NA on the anti-nodal and FWHM values of the SW. This was important, as these assumptions were used to generate a model for 3D reconstruction of the SW RBC images.

Red blood cells undergo flickering and movement [93]–[95], and rare diseases which have been associated with membrane morphology changes include sickle cell anaemia [87], [88], hereditary spherocytosis [87], [89], elliptocytosis [87] and malaria infected RBC [90], [114], [115]. These clear morphological changes between healthy and diseased RBC makes the use of optical microscopy a powerful tool for research or diagnosis. Whilst SW microscopy allows the observation of axial and lateral movements in the plasma membrane that cannot be seen using standard widefield epi-fluorescence microscopy or, in real time, using CLSM SW microscopy. However, the SW images have multiple planes of 3D information encoded in a 2D image which can make the visualisation and extraction of meaningful data difficult.

It was difficult to extract 3D information for multiple reasons, firstly, SW microscopy provided a contour map of lens specimens and RBCs, which projected the 3D information onto a 2D plane [10]. As a result, this produced a periodic structure which had a varying spatial frequency component that was dependent on the radius of curvature of the lens specimen i.e. when a SW intersects a fluorescently coated lens specimen the succession of anti-nodes becomes more rapid across the field of view, as shown in Figure 3.1a. Furthermore, due to the single wavelength of fringes, *a priori* knowledge of the specimen geometry would be required to reconstruct the specimen through a purely mathematical approach. This was only applicable for the model lens specimen, where the precise geometry was known. Another approach was to use a specimen, such as a RBC, where the general bi-concave structure was known even though the precise knowledge of the geometry was not. Therefore, assumptions about the resultant SW RBC image could be made and the axial information could be assigned to each anti-nodal plane.

Before assigning the axial information to the SW RBC image, segmentation of the 2D projected anti-nodal planes was required, as was demonstrated in Chapter 2. This was successful for data which had high contrast in intensity and low noise. Any high frequency noise that was present was removed through a Gaussian blur. Then by

application of local mean intensity thresholding, positional (x, y) and intensity data was extracted for the 2D SW RBC anti-nodal plane information. However, to assign axial information to the segmented SW image was challenging, as each segmented anti-nodal plane was required to have no points that were in contact between different anti-nodal planes with no breaks present within the anti-nodal plane ring. Additionally, the known axial height information was required to be assigned to a known location on the segmented 2D SW anti-nodal planes.

There were two known properties that could be used to assign axial information to the segmented SW image. As the anti-nodal planes of the SW occur at locations of maximum intensity, by finding these points of maximum intensity, distance values of $m\lambda/2n$ could be assigned, where m , is a multiple integer of each successive anti-nodal plane. Another method would be to use the FWHM boundary values at the edge of the segmented anti-nodal planes. The FWHM was extracted by detecting the FWHM locations using Canny edges detection [124]. This would require an expression that defines the propagation of these axial reference points away from the mirrored surface. An expression was derived from our knowledge of the anti-nodal spacing and the FWHM of each plane. I then determined the axial position for each lower plane edge (z_1) and each upper plane edge (z_2) using the following equation:

$$z_1 = \frac{3\lambda}{8n} + \frac{\lambda(m-1)}{2n} \quad (3.2)$$

$$z_2 = \frac{\lambda}{8n} + \frac{\lambda(m-1)}{2n} \quad (3.3)$$

where m is the plane number above the mirror. I aimed to use the 2D segmentation method, alongside Eqn.3.2 and Eqn.3.3 to create a 3D reconstruction of a SW RBC captured on a widefield epi-fluorescence microscope.

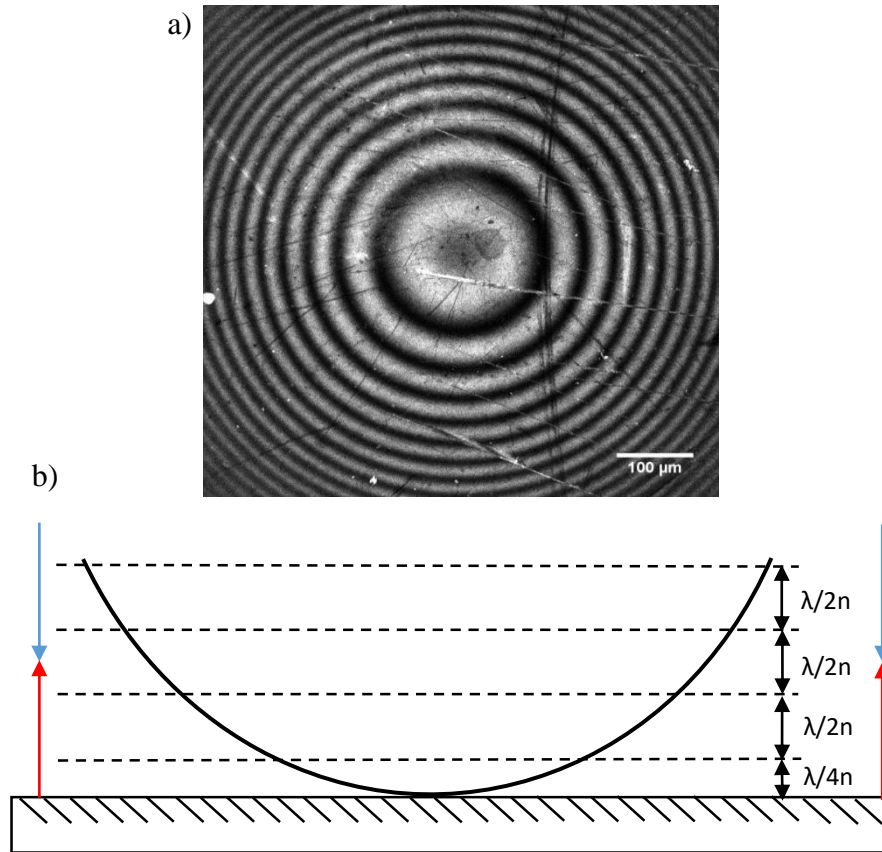


Figure 3.1 – a) A fluorescent $f = 48$ mm lens specimen SW image captured using an excitation wavelength of 543 nm. This shows the 3D information encoded in a 2D image. b) A diagram of how the SW planes intersect the specimen in 3D which results in the image in a).

3.2 Materials and methods

3.2.1 Preparation of fluorescently labelled specimens

Len specimens were prepared as described in Chapter 2.2.1 in order to compare our theoretical and experimental SW anti-nodal spacings and FWHM in the same manner as carried out in the work of Amor et al.[72].

I coated the lens specimen with DiI, which was also used to label the RBC and has been used extensively in red blood cell membrane studies [72], [104], [105]. The RBC were stained using the method presented in chapter 2.2.2. Other membrane dyes, such as DiO, DiA and Di-8-Anepps were investigated, but it was found that these were unsuitable as they were either internalised by the RBC or photobleached too rapidly for practical use with the widefield and confocal set up, irrespective of whether or not a SW was present.

3.2.2 Video-rate SW imaging of fluorescently labelled specimens

Widefield SW imaging of the fluorescently labelled specimens was carried out by Peter Tinning (University of Strathclyde) using an upright epi-fluorescence microscope (Olympus BX50) with a 100X/1.4 oil immersion objective lens (UPlanSApo, Olympus) for the RBC and with a 10x/0.4 dry objective lens (UPlanSApo, Olympus) for the lens specimens. Specimens were illuminated using a pE-4000 multi-LED system (CoolLED) coupled to the microscope.

Fluorescence emission was collected > 561 nm using a CMOS camera (Hamamatsu ORCA-Flash 4.0LT) with a binning $n = 2$ and an exposure time of 33 ms. 9x extra magnification was added before the camera to increase the size of the specimen and reduce the number of RBC present in the field of view. Signals were recorded using the WinFluor imaging and electrophysiology analysis software [125]. A schematic diagram of our experimental setup can be seen in Figure 3.2.

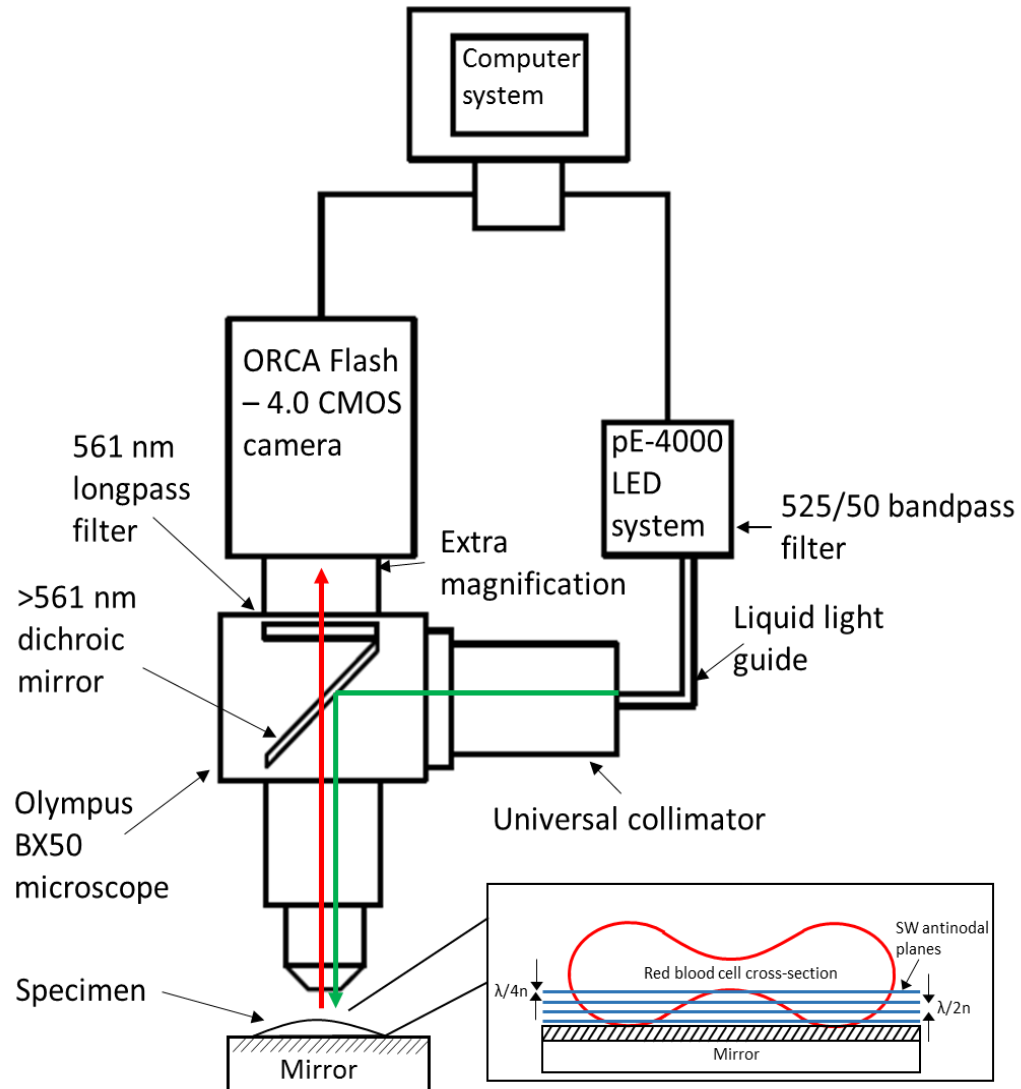


Figure 3.2 Schematic diagram of the experimental setup for the standing wave method and implemented using the BX50 microscope system. The excitation light is reflected off a broadband mirror and interferes to generate a standing wave. The standing wave of light causes fluorescence emission at the standing wave anti-nodes that intersect a fluorescently coated specimen which then propagates upwards through the lens, dichroic mirror and long pass filter to be detected by the CMOS camera.

3.2.3 Polynomial and Cubic spline Surface fitting for 3D reconstruction of lens specimen

A polynomial model was used for the interpolation of simulated lens data set axial values using a custom MATLAB function called *CustomPolfit3D* (Appendix III). The custom function was used to create a surface fit for a 2nd, 3rd and 4th degree polynomial equations. In principle, to create the polynomial surface model in MATLAB I define a vector for a 2nd degree surface polynomial which is given as:

$$P(x, y) = 1 + c_1x + c_2y + c_3x^2 + c_4xy + c_5y^2 \quad (3.4)$$

where, x and y is the Cartesian coordinates and c_n is the coefficients of the polynomial. Now, given that $\mathbf{V} = P(x,y)$, the polynomial can be expressed in matrix form:

$$\mathbf{V} = \begin{bmatrix} 1 & x_1 & y_1 & x_1^2 & x_1y_1 & y_1^2 \\ 1 & x_2 & y_2 & x_2^2 & x_2y_2 & y_2^2 \\ \vdots & \vdots & \vdots & \vdots & \vdots & \vdots \\ 1 & x_n & y_n & x_n^2 & x_ny_n & y_n^2 \end{bmatrix} \quad (3.5)$$

Writing in a more compact form and then solving in a pseudoinverse least squares method, over a range of the known x , y and z values, the coefficients can be determined by:

$$\mathbf{C} = \text{pseudoinv}(\mathbf{V}) * z \quad (3.6)$$

where, \mathbf{C} is the polynomial coefficients and z is the known axial height at corresponding x and y values. Now, that the polynomial equation coefficients have been determined, by interpolation for values x_q and y_q , the unknown height values, z_q , were calculated using the following equation:

$$z_q = \mathbf{V} * \mathbf{C} \quad (3.7)$$

where, matrix \mathbf{V} in Eqn. 3.5 was filled with the x_q and y_q and the solving using the known coefficients \mathbf{C} , z_q was interpolated to determine the unknown axial locations.

In practice, this method was applied to simulated lens specimen data using Eqn. 2.3, which was outlined in chapter 2.2.6. Firstly, a matrix of x , y and z Cartesian coordinates, which correspond only to the anti-nodal plane locations, (x , y , and z values which correspond to nodal planes were removed i.e. simulated SW normalised intensity values < 0.5) was used to determine the polynomial coefficients \mathbf{C} , using Eqn. 3.6. To generate the surface fit for the simulated lens specimen, the full range of x and y coordinates, including the nodal plane values, were interpolated to determine the axial height, z , using Eqn. 3.7. Now, the *surf* MATLAB function was used to generate a surface reconstruction of the lens specimen and a *Scatter3* plotted the simulated lens specimen using the x , y and z Cartesian coordinates.

A piecewise cubic (3rd order polynomial) continuous curve was used for interpolation. In other words, a cubic interpolation fits data point-to-point in the form of a 2D 3rd order polynomial equation. This was done using the *griddata* function in MATLAB, where the known positions x , y and z were used to create an interpolated function. Using x_q and y_q query points, unknown axial heights (z_q) were then determined at points along the interpolated cubic piecewise function.

To simulate a non-ideal specimen, a Gaussian function was created using the *fspecial* function in MATLAB. A matrix size of 71 x 71 and Std. dev. of $\sigma = 20$ was added to a region of the simulated x and y values lens data. This resulted in a distorted region. Surface reconstructions of the simulated non-ideal lens specimens were created using the polynomial and cubic as described above. The full algorithm for polynomial and cubic spline fitting comparison is shown in Appendix IV.

3.2.4 Analysis of lens specimen

The SW images of the plano-convex lens specimens were taken to confirm that the anti-nodal FWHM and spacings as shown in Figure 3.4, using LED illumination, were comparable to the theoretical values. The images were cropped in FIJI to only contain

eight anti-nodal planes. A MATLAB script (Appendix V) was created to analyse the radial signal by taking an average around the centre of the image, which reduced the noise and made it easier to extract the anti-nodal spacing and FWHM. This was done using the custom function *radialavg* [126], which rotates around a 2D matrix and calculates the radial average around a unit circle of a 2D matrix. In this case, the 2D SW image as shown in Figure 3.3.

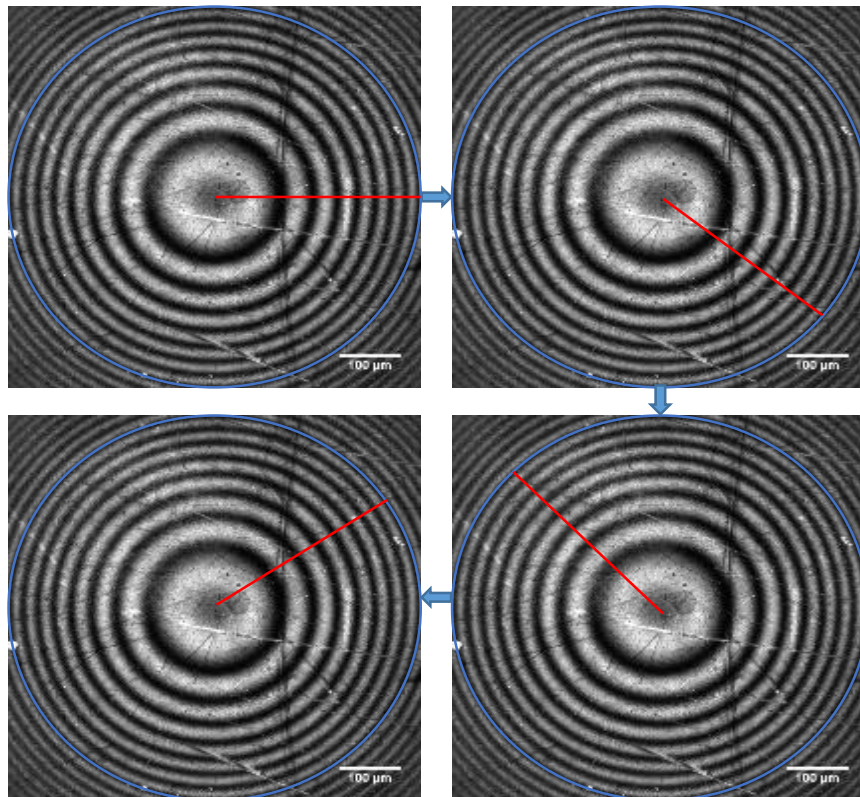


Figure 3.3 – Shows how the radial average code works. The blue circle represents the outline of the unit circle. The red line represents the intensities stored at each location. The image above only shows four locations of the line intensity points. In reality, n number of radial locations can be determined. Each corresponding pixel value in each line profiles were averaged to generate an average line intensity over the full rotation of the unit circle.

To determine the peak intensities for each anti-nodal plane, I used the *findpeaks* function to store the positions as a vector. Then by subtracting each anti-nodal position, the anti-nodal spacing was calculated and then the average experimental anti-nodal spacing was calculated. The average FWHM values were determined using the *findpeaks* function. Again, the average experimental FWHM was calculated. (The MATLAB Scripts in Appendix V).

3.2.5 Algorithm for 3D SW red blood cell reconstruction

All computational reconstruction was done using MATLAB R2017a on a desktop computer running 64-bit Windows 7 operating system with a 7th generation Intel core i7-770 3.6GHz quad-core processor and 64 Gb 2400 MHz DDR4 RAM. The script for 3D reconstruction is in Appendix VI.

The raw SW RBC movies were exported from WinFluor [125], and converted to a .TIFF stack. In FIJI, the images contrast was adjusted and then cropped to contain only the RBC of interest. The SW red blood cell images had high frequency noise present due to the instrumentation noise which was reduced by applying a Gaussian blur (MATLAB function *imgaussfilt* with a standard deviation of $\sigma = 2$). I utilised a local thresholding method *adapthresh* set to a 25 by 25 kernel size with a sensitivity of 0.60. Local threshold was used as the intensity profile was not homogenous across the image. The values for σ and the local threshold sensitivity were chosen as they provided the most accurate FWHM and anti-nodal spacings, when applied to the $f = 30$ mm lens specimen, and resulted in the highest number of reconstructions when applied to the RBC datasets.

Resolution is important in microscopy as it dictates the smallest distance between features of interest that can be resolved. The ability to achieve 3D reconstructions of the SW movies was limited by the lateral resolution available with widefield microscopy. As the shape of the RBC changed over time, anti-nodal planes could appear to be in contact with one another, if the separation between planes was less than the lateral resolution

of the microscope. To achieve anti-nodal separation, firstly the contrast of the threshold image was inverted such that the nodal regions were represented as '1's and the anti-nodal regions were '0's. The background region around the RBC was removed such that only the nodal planes were present, and by using the *bwmorph* function, thinning was applied to the nodal regions to reduce them to one-pixel thick lines. Radial lines were taken at one-degree intervals using the *imrotate* function, which rotates a 2D matrix around a centre point and stored the coordinates of each nodal plane into $n = 3$ columns, as the data sets presented here were mostly only ever 3 nodal planes. At the points where there was a discontinuity where less than 3 coordinates were detected, the planes had to be assigned to the correct column. This was achieved by comparing each value to the last value in each column and determining which number was numerically closest. In order to fill in the missing column values, any column values which were equal to zero were then assigned the value NaN (not a number). Through cubic interpolation, the NaNs were then replaced by an interpolated value to obtain a complete nodal plane, with any of the outliers removed using the *isoutlier function*. The completed planes were then dilated into a 3-pixel thick line, using *bwmorph*, and subtracted from the original anti-nodal plane threshold image. The result was a threshold image in which all the anti-nodal planes have been separated (the anti-nodal plane separation function is shown in Appendix VII). Once the planes were separated, I then extracted the boundaries of each of the SW anti-nodal planes using Canny edge detection [124]. The positions of the anti-nodal plane boundaries were indexed, and the values of the x and y Cartesian coordinates stored in a matrix. Now, each of the anti-nodal planes FWHM were uniquely labelled. This was done by using the *bwlabel function*, which determined if there were 8 adjacent pixels with the intensity value of 1. Now, the boundary values were assigned an axial location using Eqn.3.2 and Eqn. 3.3. Using the *griddata* function, the known x , y and z values were mapped to a 3D surface and the axial positions for all remaining data points were then determined using the cubic interpolation method. By extracting all the intensity values from the anti-nodal planes in the SW RBC images, a custom colourmap

was created and assigned the intensity to the correct coordinate. The final 3D reconstruction was created using the scatter3 and surf MATLAB functions and was stored as a .TIFF stack which was converted to an .AVI movie.

3.3 Results

3.3.1 Simulations of SW PSF for high and low NA lens

To understand the effect of a low and high NA objective lens on the SW intensity profile. I compared a 0.4 and a 1.4 NA objective lens, which was used for imaging the lens and RBC specimens, respectively. The simulation was set for an axial height range of $z = 1$ to 1650 nm, equivalent to eight SW anti-nodal planes, with the excitation wavelength of 549 nm and peak emission wavelength of 570 nm for the SW PSF simulation. In Figure 3.3a, the SW profile of the low NA objective lens showed that there was very little intensity drop over the eight SW anti-nodal planes. As a result, I would expect to observe many anti-nodal planes within the depth of field when imaging a lens specimen. Conversely, from Figure 3.3b, I could see that a 1.4 NA had a large effect on the emission drop of the SW structure, with the intensity drop offs completely at ≈ 600 nm. This was because of the convolution between the SW excitation illumination and the emission PSF. Therefore, the intensity of the SW fringes detected beyond an axial range of 600 nm was negligible. Any contribution from these out-of-focus SW fringes would produce background fluorescence, but as the intensity out-of-focus fringes relative to the in-focus fringes was considerably lower, it would have a minimal effect on the observed SW fringe pattern. Therefore, it was assumed that only 3 anti-nodal planes would be observed at one time within the depth-of-focus when imaging with a 1.4 NA objective lens for SW RBC imaging.

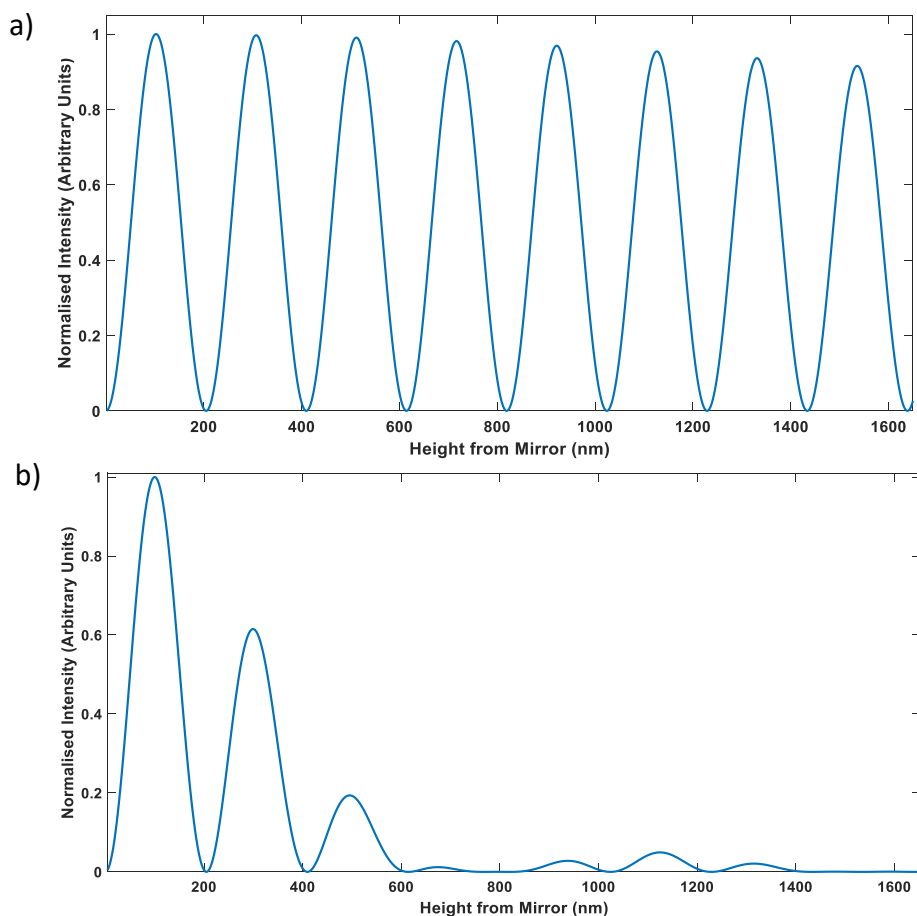


Figure 3.4 – Simulated SW PSF using eqn. 3.1 at a 549 nm excitation wavelength and a peak emission wavelength of 570 nm. a) A 0.4 NA objective lens and b) a 1.4 NA oil immersion objective lens.

3.3.2 SW imaging of fluorescently coated lens specimens

To confirm that the interference patterns observed in the images (captured by Peter Tinning) resulted from SW excitation, and to verify that the experimental anti-nodal spacing's and FWHMs were comparable to the theoretical values, fluorescently labelled lens specimens were imaged with the widefield setup image in air, as shown in Figure 3.5a. As expected, an alternating pattern of the SW intersecting the lens specimen was observed. Now, 4% BSA in PBS was pipetted under the lens specimens to replicate the conditions that a SW would form when SW RBC imaging was carried out. An interference

pattern was observed, and as was predicted, the refractive index change between the mirror and lens specimen resulted in a reduction in the FWHM and anti-nodal spacing (Figure 3.4b). I used my lens analysis MATLAB script, which had taken a radial average for each image and the average experimental anti-nodal spacings and FWHMs (Figure 3.5c and d) were determined and compared with the theoretical PSF calculated values using Eqn. 3.1. As a result, more anti-nodal peaks were observed within the same axial range for 4% BSA in PSA than in air (Figure 3.5b and d). In Table 3.1, I showed that the experimental and theoretical values were in good agreement with theory with a percentage error less than 3.00%.

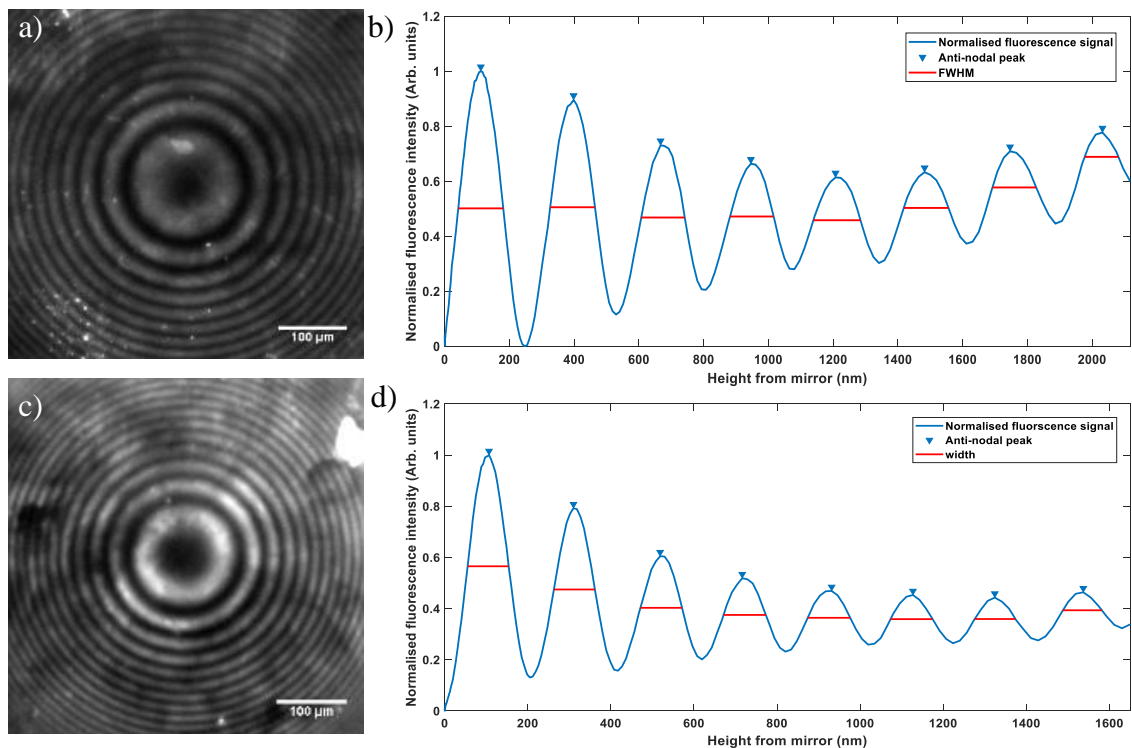


Figure 3.5 - SW images of a $f = 30$ mm fluorescently coated lens specimen. a) A 2D SW image of a fluorescently coated lens specimen (placed on a mirror and imaged using a widefield setup). b) The radial averaged plots of the anti-nodal axial locations of a). c) A 2D SW image of a fluorescently coated lens specimen where 4% BSA in PBS ($n=1.34$) was placed between the lens and the mirrored surface. d) The radial intensity profile of the lens specimen in c).

Table 3.1 – A Comparison of experimentally determined anti-nodal spacings and FWHM obtained from lens specimen imaging and the theoretically determined values calculated using Eqn. 3.1, where the peak excitation wavelength was 549 nm, and the peak emission wavelength detected was 570 nm.

Widefield SW imaging lens specimen comparison		
Refractive index	1.34	1.00
Theoretical Anti-nodal spacing (nm)	204	275
Measured Anti-nodal spacing (nm)	204 ± 3	274 ± 4
Percentage difference (%)	0.34	0.10
Theoretical FWHM (nm)	102	137
Measured FWHM (nm)	100 ± 1	138 ± 1
Percentage difference (%)	2.30	0.55

3.3.3 Comparison of threshold and edge detection images with standing wave theory

To extract the anti-nodal planes, a local threshold was applied to the SW images and edge detection was used to extract the FWHM regions of the SW planes. This was achieved by application of a 0.60 local mean threshold with a pixel size of 25 by 25 for the widefield SW images. A 2D reconstruction was created as described in chapter 2.2.3. The widefield threshold SW lens image for the first 8 anti-nodal planes and the 2D reconstruction is shown in Figure 3.6. To confirm that the extracted data using this

method was in agreement with theory, the 2D reconstruction of the lens specimen was analysed using a radial average as in section 3.3.2. I calculated that 2D reconstruction of the widefield SW lens image (Figure 3.6b) had an anti-nodal spacing which was 279 ± 4 nm with a percentage difference of 1.82% when compared to the theoretical value of 274 nm. To show that the edge detection coincided with the edges of the threshold anti-nodal planes, the threshold image is overlapped with the edge detection images in red. It was observed that the canny edge detection extracts the edge of the anti-nodal planes at the FWHM boundaries. Using the radial average on the threshold image, the FWHM spacing was calculated. I then confirmed that the extracted FWHM using the edge detection was 138 ± 2 nm. The theoretical FWHM value was 137 nm, giving a percentage error of 0.55%, which was in good agreement with theory.

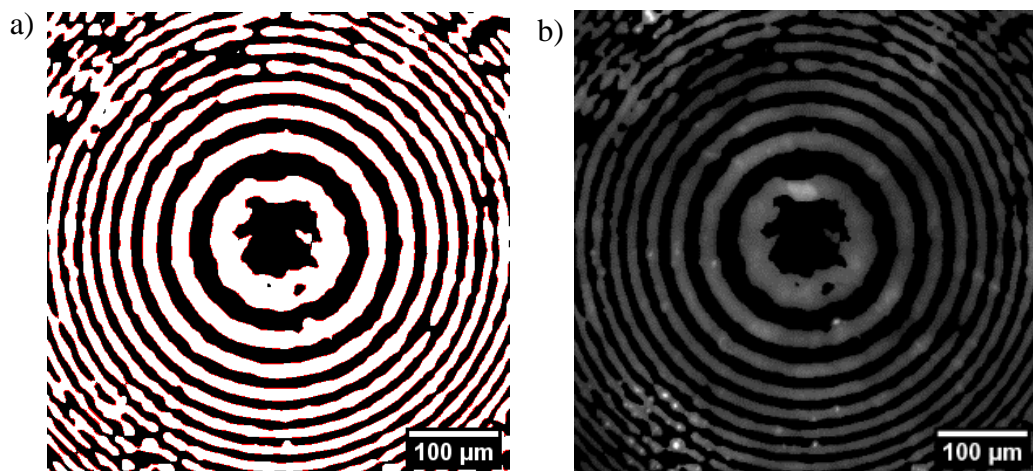


Figure 3.6 – A $f = 30$ mm lens specimen with the application of - a) A local mean threshold of a 0.60 sensitivity and a region size of 25×25 pixel. In red is the overlap of the canny edge detection on the threshold SW image. b) A 2D reconstruction utilising the intensity and positional values extracted from the threshold and original SW images.

3.3.4 Comparison of polynomial and cubic spline 3D surface reconstruction of a simulated lens specimen

To test the best fitting method for surface reconstruction, I simulated the SW 3D x , y and z positions of a lens specimen with a radius of curvature $R = 24.87$ mm, at a height of 2.5 microns. The addition of a Gaussian function was added to simulated lens specimen to the x and y position values to create a deformation in the surface. A 71×71 Gaussian function with a std. dev of 20 was applied with an additional scaling factor of 70 was to the Gaussian function to make the deformation more prominent. In Figure 3.7, I observed the effect the 2nd, 3rd and 4th order polynomial surface fits and a cubic interpolation fitted to the deformed lens surface. With the application of higher order of polynomial fits to the deformed surface, it was noticed that oscillation become prevalent. Table 3.2, shows the coefficient of determination (R^2) values which increased for each higher degree of polynomial fit applied to the deformed surface and a R^2 value of 1.00 for each polynomial fit for an ideal simulated lens dataset. The cubic fit piecewise procedure was applied to the simulated datasets and I noticed that the fitting procedure fits from data point to data point. The result was no oscillations and the deformed surface being well interpolated. Cubic interpolation created a surface that accurately represented the simulated lens specimen even with the presence of deformations.

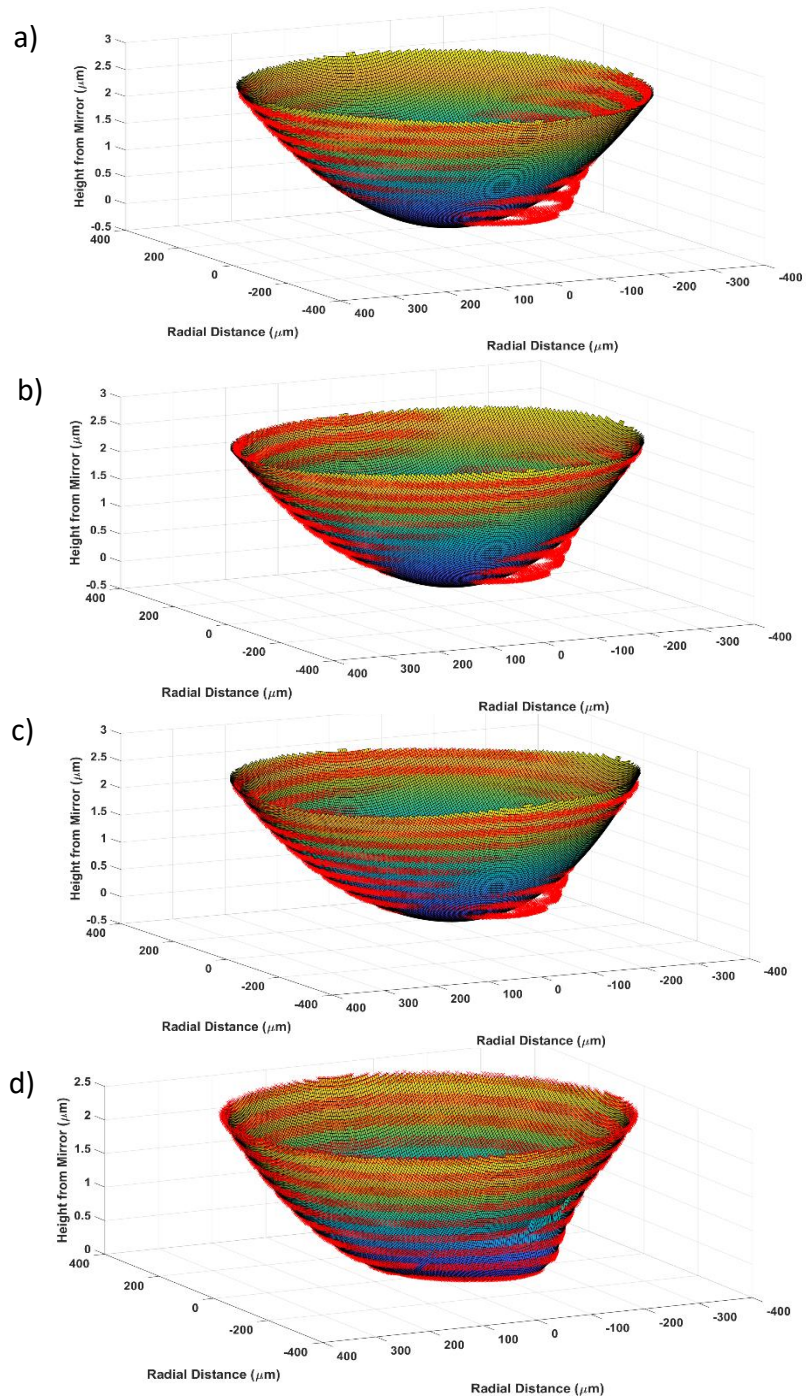


Figure 3.7 – A scatter plot (red data points) which shows the simulated data points of the anti-nodal planes positions for a $f = 48$ mm lens specimen and surface plot 3D reconstructions using a) 2nd, b) 3rd and c) 4th order polynomial fits and d) cubic interpolation.

Table 3.2 - Shows the coefficient of determination for a 2nd, 3rd and 4th order polynomial fit applied to a simulated $f = 48$ mm lens specimen for both ideal and Gaussian deformed data sets.

Polynomial fit degree	Ideal lens R ²	Gaussian deformation R ²
2 nd	1.000	0.982
3 rd	1.000	0.987
4 th	1.000	0.990

3.3.5 Video-rate SW imaging and computation 2D

reconstruction of RBC

Using the optical setup shown in Figure 3.1, it was possible to carry out upright widefield SW imaging of the bottom surface of a fluorescently labelled RBC at speeds in excess of video-rate (Images were captured by Peter Tinning in Figure 3.8). By carrying out this technique, images of rapid membrane fluctuations and changes in real time were observed, which would not be observable using point scanning methods, due to the limited temporal resolution available. Using the video-rate data obtained from the resolution measurements, and the imaging of the fluorescently coated lens specimens in 4% BSA in PBS, it could be concluded that a lateral resolution of 290 nm and an axial resolution of 100 ± 1 nm could be achieved.

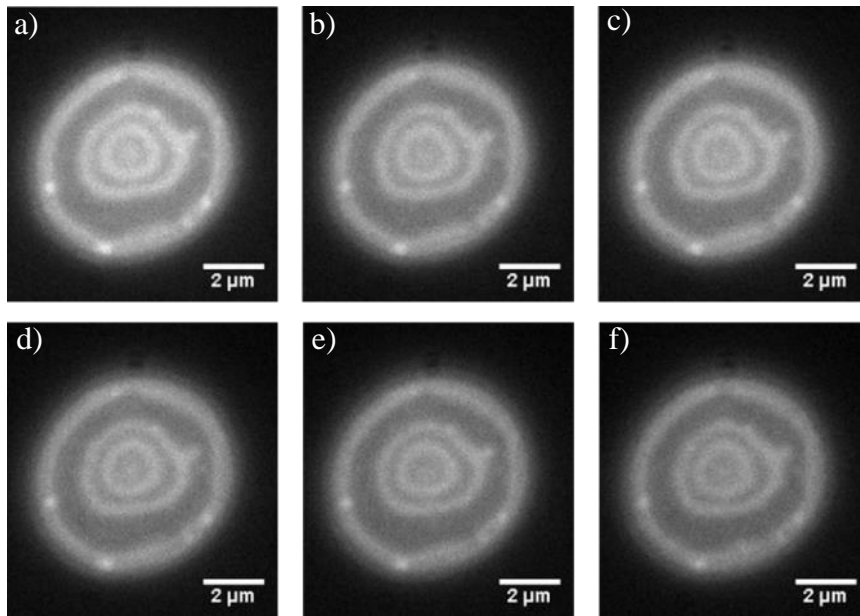


Figure 3.8- Single frames taken from the video-rate SW (captured by Peter Tinning) movie of the bottom half of a red blood cell labelled with the membrane dye Dil using a camera binning $n = 2$. The frames presented as a-f are frames 1, 200, 400, 600, 800 and 999.

Using the computational script I created, which was described in section 3.2.5, I was able to isolate the anti-nodal planes from the background by local adaptive thresholding of the SW RBC images. Then a 2D reconstruction of the SW movie was created by mapping the original intensities to the threshold images (Figure 3.9) and stored the subsequent anti-nodal x and y coordinates for each frame. This resulted in a video showing only the RBC anti-nodal planes.

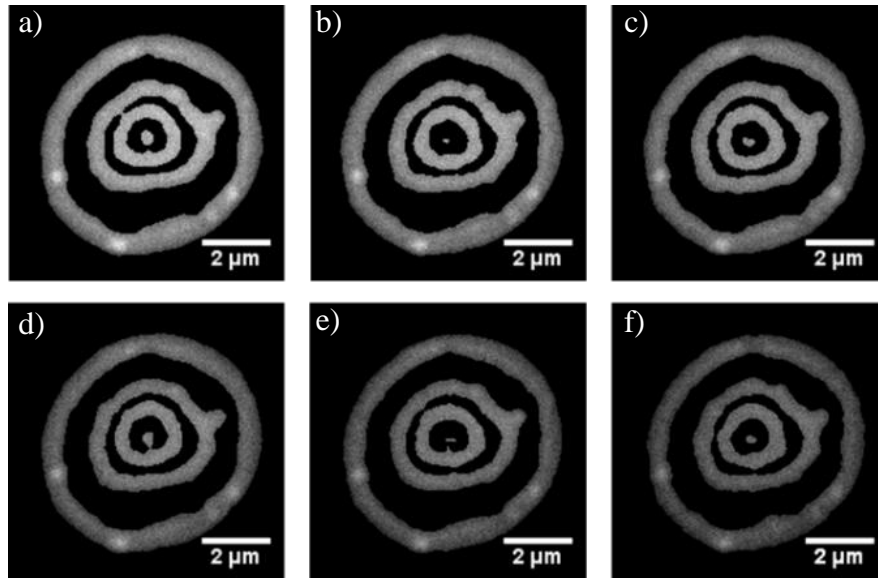


Figure 3.9 - 2D reconstruction of the SW movie with the original intensity values applied to the isolated anti-nodal planes. The frames presented as a-f are frames 1, 200, 400, 600, 800 and 999.

However, I observed that the anti-nodal planes were in contact in some frames of the movie. As a result, a method was required to extract and separate the anti-nodal planes. By applying a custom segmentation method, the threshold images of the video-rate SW were firstly inverted, thus leaving only the nodal regions as shown in Figure 3.10b. I had observed that the gaps in the nodal planes exist where the anti-nodal planes were connected. By implementing thinning and skeletonisation, a gap was observed which could then be cubic interpolated, as described in methods section 3.2.5, and resulted in a complete nodal ring. I then separated anti-nodal planes (Figure 3.10a) that appeared to be in contact by subtracting the completed nodal ring in Figure 3.10c with one another. The result was separated anti-nodal planes in Figure 3.10d. The results of the key steps of the process shown in Figure 3.10 was applied to frame 503 of the SW movie.

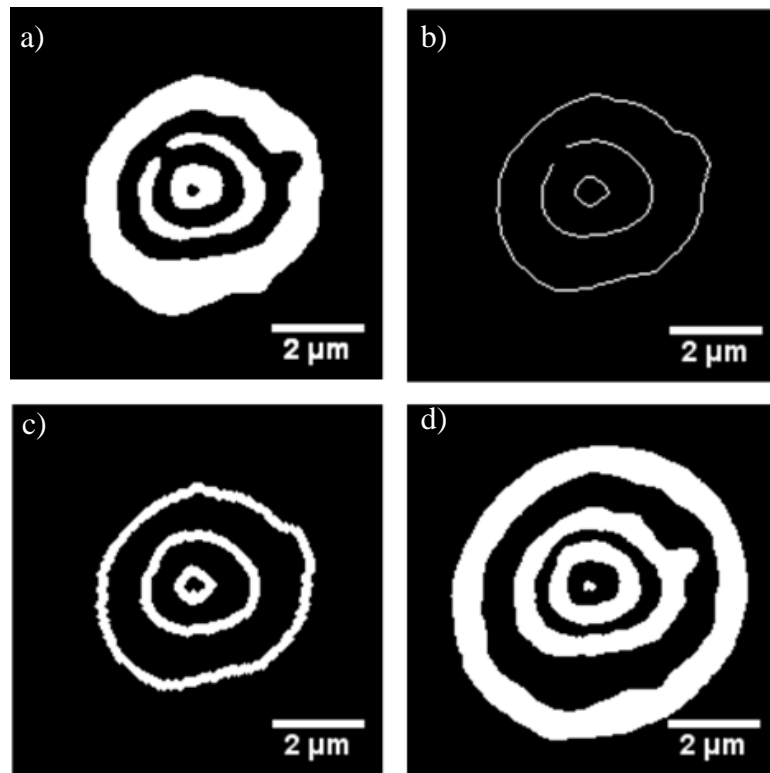


Figure 3.10 - Key steps of the anti-nodal plane separation for frame 503 of the SW movie. a) Threshold image has been inverted and resulted in a binary image of the nodal regions. b) A skeletonized image of the nodal regions. c) The resultant cubic interpolated nodal planes which have been dilated by three pixels. d) The anti-nodal planes have been separated by subtracting c) from the anti-nodal plane threshold image.

Using Eqn. 3.2 and Eqn. 3.3, the theoretical axial positions were applied to the segmented edge detection regions. I then interpolated each axial height for the pixels between each SW plane edge. The 3D surface and the anti-nodal plane intensities were shown in Figure 3.11, which aids in our understanding of the 3D membrane structure of the specimen and allows for the observation of morphological changes in the lateral and axial directions in real time.

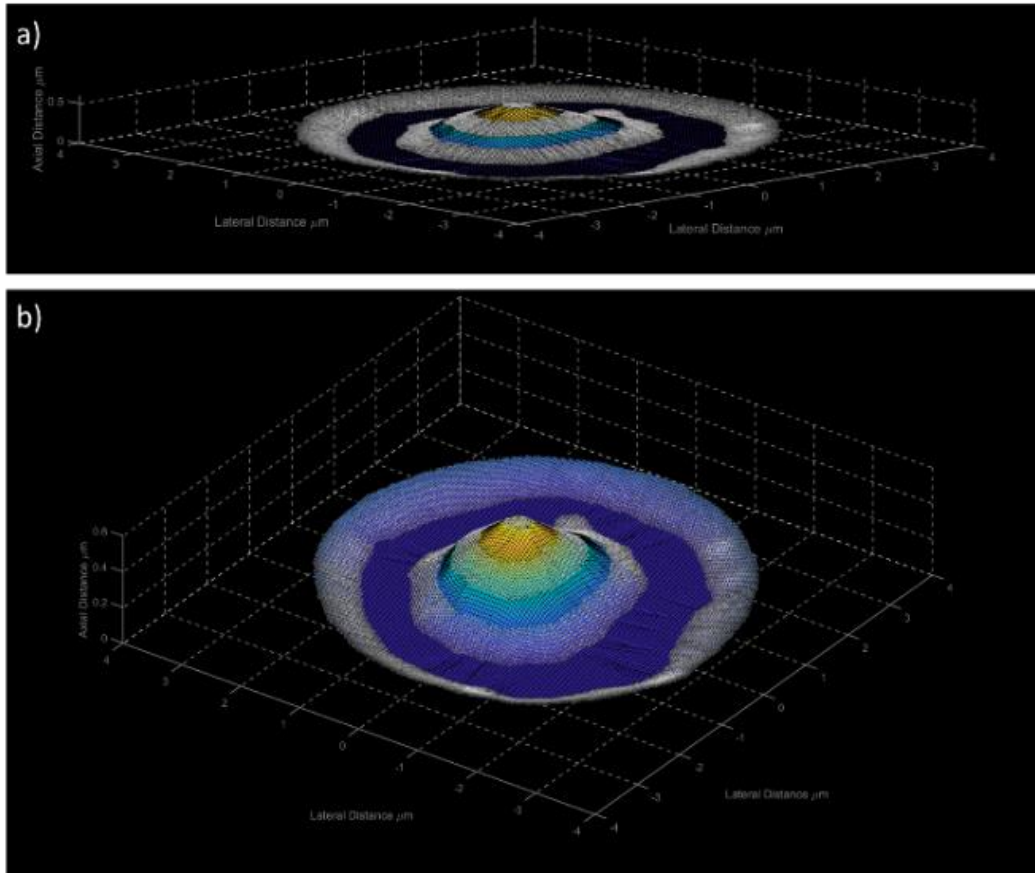


Figure 3.11 - A 3D reconstruction the first frame of the SW movie where a) where the aspect ratio has not been altered and b) the aspect ratio of the z axis has been increased to 13.33 for easier visualisation.

3.3.6 Comparison between video-rate SW microscopy and video-rate widefield epi-fluorescence microscopy

After successfully carrying out video-rate SW microscopy and generating 2D and 3D reconstructions of the 2D SW RBC movies, the effect of the SW imaging technique on the rate of specimen photobleaching was investigated and compared to that of widefield epi-fluorescence microscopy recorded at video-rate. SW imaging of was carried out for 10 RBCs using the method described in section 3.2.2. To investigate the photobleaching rates, I cropped and contrast adjusted the SW movies and created a MATLAB script to

obtain a normalised 2D reconstruction for each image. As before, the MATLAB script applied a local threshold to isolate the anti-nodal planes and the average intensity of all the non-zero intensity pixels was calculated. The intensity was outputted for each time point. This process was repeated but with the RBC on standard microscope slides rather than a mirror, to image the cells using standard widefield epi-fluorescence illumination rather than with a SW. The average normalised intensity along with the standard error of the mean for each time point ($n = 10$) for SW microscopy can be seen below in Figure 3.11a, and for widefield epi-fluorescence imaging in Figure 3.11b.

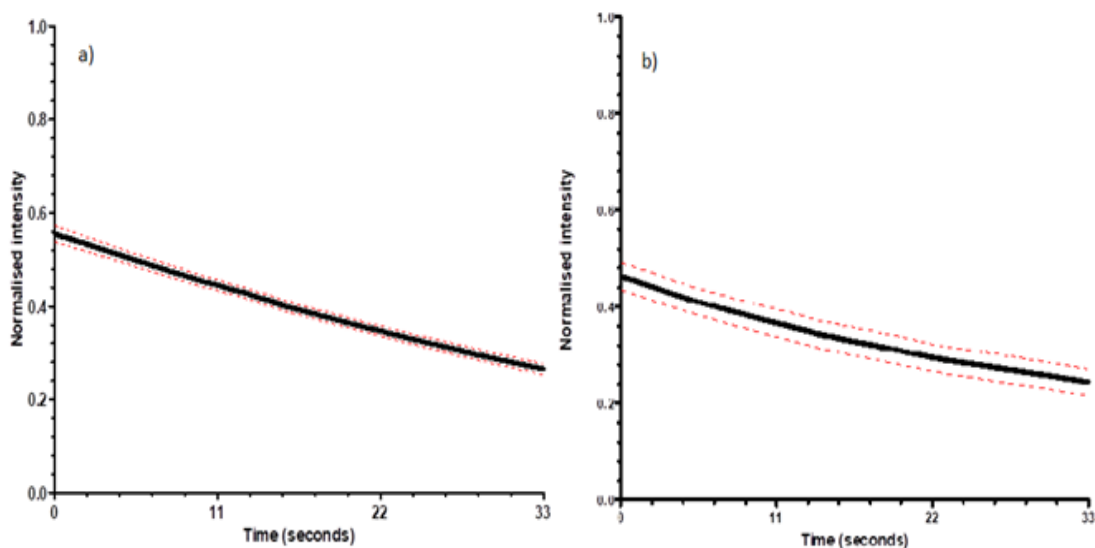


Figure 3.12 - Average normalised intensity (solid line) and the standard error of the mean (red dashed line) from a) SW movies and b) widefield imaging of RBC ($n = 10$) excited using a 550 nm LED with an illumination power at the specimen plane of 1.71 ± 0.01 mW.

When comparing the data using both techniques, the measured average intensity decrease observed across the 1000 frames when using SW imaging was 51.89 ± 2.28 % and for standard widefield epi-fluorescence imaging it was 47.78 ± 4.78 %. Peter Tinning, compared (and generated Figure 3.12) these rates and applied a student t-test after which it was found that there was no significant difference between the average photobleaching rates obtained with each technique ($P > 0.05$).

The average initial normalised intensity values when using each technique was compared. The SW imaging provided an initial normalized intensity of 0.55 ± 0.02 which was significantly larger than that with widefield microscopy using the same power at the specimen plane ($n = 10$, $P < 0.05$ compared to an initial intensity using widefield imaging of 0.46 ± 0.03). This was attributed to the increased brightness of the SW images compared to the widefield epi-fluorescence images was due to the multiple in-focus fluorescent planes being present in the SW images. In widefield epi-fluorescence microscopy there was only a single plane in-focus with the rest of the image being composed of out-of-focus fluorescence.

It was also explored what the effect of SW imaging technique had on RBCs over longer timescales. As before, RBCs were adhered on to a mirror or a microscope slide. The specimens were imaged using an LED with a camera exposure time of 100 ms and captured an image every 15 seconds for a duration of 30 minutes, by Peter Tinning (Figure 3.13 and Figure 3.14). The six-time point images were shown for both a SW setup as shown in Figure 3.13, and a widefield epi-fluorescence technique as shown in Figure 3.14.

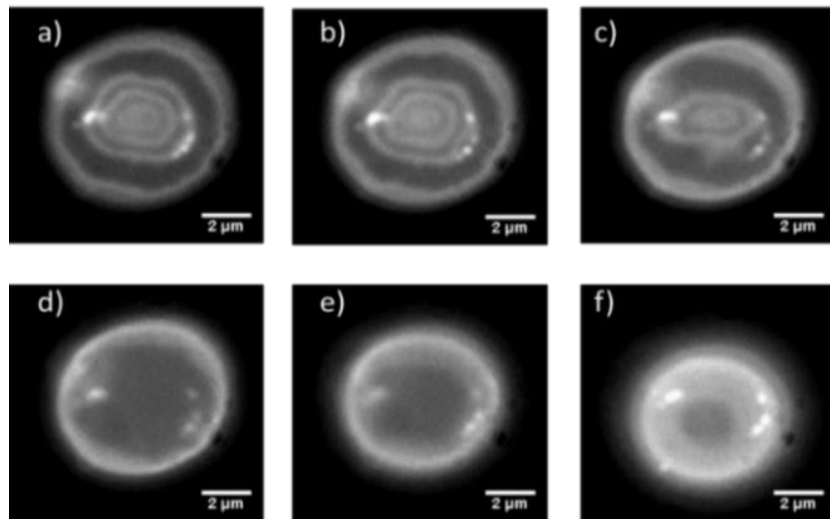


Figure 3.13 Cropped and contrast adjusted SW images of a RBC. The frames presented as a-f are at time points 15, 360, 720, 1080, 1440 and 1800s.

As was observed from the above Figure 3.13, SW microscopy reveals a greater amount of topographical information of the RBC when compared with widefield epi-fluorescence imaging. It was also apparent that both RBC appear to flatten and undergo membrane deformations at approximately the same rate regardless of which imaging technique was used.

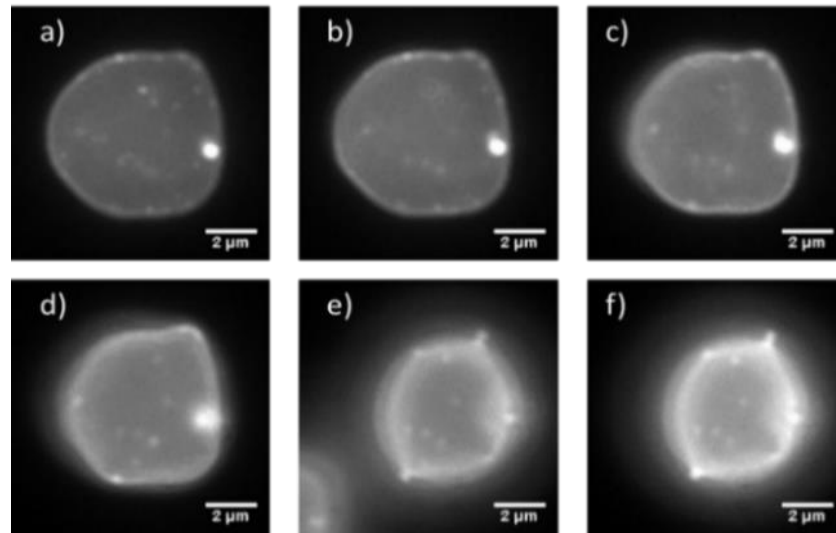


Figure 3.14 - Cropped and contrast adjusted widefield epi-fluorescence images of a red blood cell. The frames presented as a-f are at time points 15, 360, 720, 1080, 1440 and 1800 seconds.

3.4 Discussion

As with chapter 2, all previous applications of SW microscopy have utilised lasers sources for excitation [14], [72], [75], [122], [127]. However, here an LED source was used for illumination. Thus, it was important to confirm that the experimental anti-nodal spacing and FWHMs were comparable to the theoretical values, when the SW was generated using LED illumination. To do this, the model fluorescent lens specimen imaging experiments carried out by Amor et al. was repeated, but with media of different refractive indices between the specimen and the mirror. It was found through these experiments that I was able to obtain, in all media, anti-nodal spacings and FWHMs

which were not significantly different from the theoretical values with a percentage error of less than 3%. This was important as modest assumptions about the anti-nodal FWHM positions was required for the 3D reconstruction.

The contour mapped 3D structures were encoded in the 2D image. Thus, it was an important aspect to be able to extract meaningful data axial information from the video-rate data. Therefore, I developed a computational method which extracts and segments the 3D anti-nodal information (The anti-nodal spacing was confirmed using a lens specimen). However, for the RBC this did require some assumptions to be made based on a healthy RBC membrane morphology for both the nodal and anti-nodal regions. It should also be noted that the SW fringes mirror-side of the cell are very good (flat and equi-distant), but that the apical surface of the cell is more problematic to image with this method because the quality of the SW fringes degrades away from the mirror surface, as the simulation of SW structure had shown when using the high 1.4 NA objective lens a large drop off in intensity. As a result, the assumption was made that there were only ever three nodal planes.

In specific circumstances, the method used for anti-nodal separation was unsuccessful and fewer than the full 1000 frames could be reconstructed in 3D. This occurred when images contained bright spots between the anti-nodal planes, which I believed was due to free dye clumps, so I was unable to assign axial heights to these objects. The other situation was one where any planes were broken, which often arose from either the incorrect interpolation of the nodal regions, or due to the lack of data points caused by multiple anti-nodal contacts.

The script was capable of automatically removing images which had too few or too many object edges compared to number of assumed nodes. Any subsequent frames missed by the automated method had to be removed manually from the 3D reconstruction movie and in the data presented here this only amounted to three frames of 984. To check for the best surface model for reconstruction, a simulated ideal lens data with deformations

was created. I observed oscillations in the polynomial interpolation, particularly at higher order polynomial fits, this is known as Runge's phenomenon. Polynomial interpolation for 3D reconstruction was limited to fitting to ideal surfaces where no deformations in surface morphology exist. In reality, cellular structures are complex. Therefore, polynomial fitting would not be suitable as it would create artefacts in the reconstruction. In contrast, the piecewise cubic interpolation fits data point to data point which created a 3D reconstruction which resembled the extracted x , y and z data. As a result, the accuracy of reconstruction relied on the accuracy of the FWHM axial locations extracted from the threshold SW image.

Through the application the computational method, and subsequent removal of incorrectly-reconstructed frames, I was able to generate movies that contained up to 981 frames from the 1000 raw SW movies. Using the computational technique described, I was capable of taking a widefield SW movies acquired at 30.30 Hz and output 2D reconstructions in approximately 10 seconds for the full thousand frames and 3D reconstruction in approximately 10 minutes for 981 frames. The CPU RAM required was 64 GB, however, it could be possible to split the SW movies into a smaller subset of frames and process them individually to reduce memory consumption.

As this study was conducted over a time period it was investigated whether the SW technique caused any further photo-toxicity to the specimen compared to widefield epifluorescence imaging. The RBC appeared to decay at a similar rate and in a manner that resembled the decay observed previously over 12 minutes under periodic focused laser illumination [128]. For computational reconstruction, is only limited by the experimental conditions and it appeared that SW fringes could be observed clearly at 360s and start to disappear at 720s in the time-lapse experiments. Therefore, as long as there was a clear spatial separation of SW fringes in the RBC images, a reconstruction could be obtained for imaging times up to 720s. In the study of Wong et. al, [128], it was found that membrane damage occurred even at low laser powers as the result of reactive

oxygen species being generated via photo-hemolysis. This process has been hypothesised to be due to interactions between the reactive oxygen species and the membrane proteins, band 3 and spectrin [128], which has also been reported in studies using widefield illumination [129], [130]. However, it was shown that in the SW RBC video-rate experiments no photo-toxicity effects over the 33 second duration could be observed. Photobleaching rates are comparable over the 33 seconds with both widefield and SW illumination. Photobleaching is a limitation for the computational method. This occurs when the amount of photobleaching observed reduces the fluorescence intensity, such that the intensity thresholding cannot distinguish well enough between background and the anti-nodal planes.

Interference reflection microscopy (IRM) has also been used previously to image RBCs allowing the specimens to be imaged without using a fluorescent probe, and results in images that resemble those obtained when using the SW technique [131], [132]. However, the Curtis model of IRM has been shown to be inconsistent with membrane topography measured by other methods. For example, Gingell, et al. [133] measured the thickness of the space between coverslip and the membrane of chick fibroblasts by including a cell impermeable fluorescent dye in the extracellular space and found by total internal reflection fluorescence microscopy (TIRF) excitation that there was close contact (shown by dye exclusion) over almost all the area of the cell facing the coverslip and not just in the 'close contact zones' or 'focal adhesions' seen in IRM. They also remarked that a dark peripheral band was seen in IRM of some cells, which had no counterpart in the TIRF image. They speculated that the IRM image was influenced not by the membrane topography but by the thickness of the cytoplasm in that region. More recently, Iwanaga et al. [134] used a standing-wave method similar to ours, in which the highly hydrophobic dye Dil was used to stain the cell membrane specifically, and, again, there was no evidence for the 'close contacts' that were interpretations of the dark zones in IRM. These authors raised the cell membrane ingeniously on silica microsteps away from the reflecting layer and showed that the contrast changes were as expected if the

membranes followed the steps faithfully and were excited at the anti-nodal planes in the SW pattern, demonstrating that their method, which they called 'Fluorescence Interference Contrast' (but which was in fact a SW method like ours), was a reliable method for studying membrane topography, whereas IRM was not. Not only is IRM ambiguous, in that it cannot be assumed to report membrane position, but it is also affected by scatter so that absolute values for axial distances and resolutions cannot be obtained from the observed contrast in IRM images. The SW method provides an unequivocal axial ruler related to the wavelength and refractive index of the medium and, since it involves a specifically localized fluorophore, it reports the position of the membrane unaffected by cytoplasmic contents. Additionally, this resulted in an easier theoretical model for understanding the fringe pattern observed in a SW image, which would allow for less assumptions about the specimens to create a 3D reconstruction.

Many super-resolution microscopy techniques can provide a spatial resolution improvement both axially and laterally, something which would not be possible in SW microscopy. There will be circumstances where SW microscopy would not be a suitable technique, such as when very high lateral resolution would be required. Even with this limitation, video-rate SW microscopy was carried out and which allowed for observation of rapid membrane fluctuations and the morphology of RBCs. This is an advantage for researchers looking to investigate membrane flickering and the biomechanical characteristics of RBC [93], [95], [135], or the behaviour of diseased or healthy RBC undergoing morphological changes [87], [136]–[139]. The high temporal resolution of our technique has allowed us to observe rapid membrane changes in real time which appears to indicate that the entire membrane is in motion with whole-cell vibrations being observed and small movements taking place at the concave surface. Though the ability to observe whole cell movements with super-resolved axial sections, demonstrates that our technique may also have applications in cell tracking or motility studies. The motion observed in the concave surface resembles the movements which occur at the boundary between the concave section and the outer membrane [94],

though the majority of this boundary inhabits a nodal plane. I was unable to observe the very small membrane dimpling, which are on the order of approximately 40 nm, that have been observed in other studies using quantitative phase imaging [138]. This was to be expected, as the dimples are not large enough to cross the boundaries between an anti-nodal or nodal plane, as small axial movements (~100 nm) within the planes could not be resolved.

It should be noted that some other super-resolution microscopy techniques may require the use of specific dyes [15], [16], [140], [141], whereas SW microscopy was compatible with standard fluorescent membrane dyes commonly employed in widefield epi-fluorescence microscopy. Another advantage of utilising SW microscopy was that it could be performed using a typical widefield epi-fluorescence microscope with the only change required for specimen preparation being the replacement of a microscope slide with a mirror. Whereas some other super-resolution techniques may require the use of specialist microscopes [19], [59], [65], [142].

It is also common to find that super-resolution techniques typically sacrifice temporal resolution in order to increase spatial resolution [143], [144], whereas SW was able to improve the widefield axial resolution by a factor of approximately 8 and maintain high temporal resolution imaging of live cell specimens in 3D. This was not possible in the work carried out by Amor et al. as they utilised a scanning confocal microscope for imaging [72]. The ability to carry this out on a widefield epi-fluorescence microscope also allows for the possibility of multiple RBC to be investigated simultaneously which could be an advantage for diagnosis or studies requiring a high data throughput.

Lastly, the computational technique for a 3D reconstruction of RBC was not applied to the *P.berghei* iRBC, this was primarily due to the structure of the iRBC. In the computational method above, I assumed a concave structure for a healthy RBC. However, iRBC the geometric structure was far more complex, due to the presence of the parasite in the cell membrane. Thus, the limitation of this computational method

was that the known geometric direction was required. However, this was not possible using a single excitation wavelength SW approach as this leads to ambiguity of directionality was observed with the cell membrane of SW iRBC images, as shown in Chapter 2. Development of additional SW techniques would be required and characterised on model specimen before the application to the unknown geometry of cells. Furthermore, the application of SW microscopy with a single-wavelength was also limited when a complete topographical map of the specimen would be required, because of the contribution of nodal planes in the final image, which resulted in periodic bands of missing information. In the next chapter, I will discuss the TartanSW approach as a possible method to overcome the limitations of single excitation wavelength SW imaging.

3.5 Conclusions

In this chapter, I described a new computational method for extracting data from SW movies or images. Using existing segmentation techniques, which firstly extracted the 2D anti-nodal plane information. Video-rate widefield SW RBC data sets were captured at 30.30 Hz over 33 seconds which captured 1000 frames, and by application of a 3D reconstruction method, it was possible to create a 3D reconstruction of 981 out of the 1000 frames. This method meant that 3D data encoded in the 2D SW RBC images could be extracted and a 3D visualisation of the bottom concave surface of the RBC in contact with the mirror was produced. In future, this could allow for further quantitative analysis to be carried out on the RBC membrane 3D morphology over time. However, the limitation of the single wavelength SW approach was that it required *a priori* knowledge of the specimen, which would make it difficult to reconstruct complex or unknown cellular structures. This would require a SW technique that could encode additional information about the directionality to gain further insight the 3D shape of the specimen.

Chapter 4

TartanSW multi-excitation and multi-emission SW imaging of lens specimens, MCF-7s and red blood cells

In this chapter, I report three new multi-wavelength SW techniques called TartanSW multi-excitation, TartanSW multi-emission and DiffSW. I developed a theoretical model for the TartanSW method which considered the contribution of both the excitation and emission SW. I simulated the TartanSW method over an axial range of 0-5 μm in MATLAB, and then compared it with a $f = 48$ mm fluorescently coated lens specimen on a bare aluminum microscope slide. I observed a similar spectral signature between the experimental and simulated data for both TartanSW techniques. Furthermore, it was noticed that when the simulated model SW data was compared with the experimental lens specimen SW data had, the resulting spectral signature and intensity modulation observed was different depending on the reflective substrate used. I confirmed that there was an improvement in the modulation gap reduction when using TartanSW multi-excitation over single wavelength SW excitation. Next, I demonstrated that TartanSW techniques could be applied to biological specimens by imaging both RBCs and MCF-7's (grown on mirrors and stained with Dil by Peter Tinning, University of Strathclyde). Lastly, the DiffSW method was applied to TartanSW multi-excitation images with a theoretical model I generated in MATLAB. The simulated DiffSW data was compared to the experimental DiffSW images obtained using the TartanSW multi-excitation CLSM image of a $f = 48$ mm lens specimen. I demonstrated that the DiffSW resulted in an axial resolution improvement of ≈ 45 nm over TartanSW multi-excitation.

4.1 Introduction

I aimed to provide a theoretical model for TartanSW multi-excitation, multi-emission and DiffSW microscopy, which I simulated in MATLAB. This was done as to understand the TartanSW and DiffSW methods spectral signatures observed and how they compared to the experimental TartanSW and DiffSW data. Firstly, TartanSW multi-excitation was modelled alongside the experimental lens specimens data, and due to the SW anti-nodal location being dependent on the excitation wavelength, this resulted in an modulation gap reduction over single wavelength SW. Secondly, I utilised the emission SW to further

map the geometry of lens specimens which had taken advantage of the intensity modulations that were dependent on the difference between the excitation wavelengths and the narrow emission detection band. This demonstrated that the spectral signature would help gain further axial information about the specimen geometry without *a priori* knowledge. A simulation of the theoretical TartanSW multi-emission model was required as a method to compare the experimentally obtained model lens specimen with the theoretical SW model. Lastly, the difference method which was a post-acquisition technique to improve the resolution of SW imaging was achieved by application of image processing of the TartanSW multi-excitation images. Again, it was simulated and compared to the theoretical model. Once characterised, the TartanSW and DiffSW techniques were applied to biological specimens (which was done alongside Peter Tinning, University of Strathclyde), to verify the application of TartanSW and DiffSW in biological specimens and that the observed spectral signature was similar to the theoretically modelled TartanSW data.

All previous work in SW microscopy had adopted a single wavelength approach which was used to excite the fluorophore bound to the structure of interest [14], [72]–[74], [120], [122], [123], [145]. Lanni et al. used SW imaging to optically sub-section, with a plane thickness and axial resolution of $\lambda/4n$ [13], [14], [123]. More recently multi-planar SW imaging, which periodically intersects a fluorescent stained specimen, was used to produce a precise contour map of the geometry of a lens specimen and RBCs with a single excitation wavelength [72]. The main disadvantage with single wavelength multi-planar excitation SW was the inherent modulation gap of $\approx 50\%$, due to the nodal regions of the axial structure of the SW pattern containing no information about the specimen, as shown in Figure 4.1a. To overcome this issue, multiple excitation wavelength SW images were obtained separately. This was advantageous, as the three different wavelengths would correspond to different axial locations, due to the anti-nodal plane positions being dependent on the excitation wavelength ($\lambda/2n$). Therefore, the multiple excitation SW approach could reduce the overall information loss, when compared to single

wavelength SW imaging, revealing more information about the specimen as shown in Figure 4.1b.

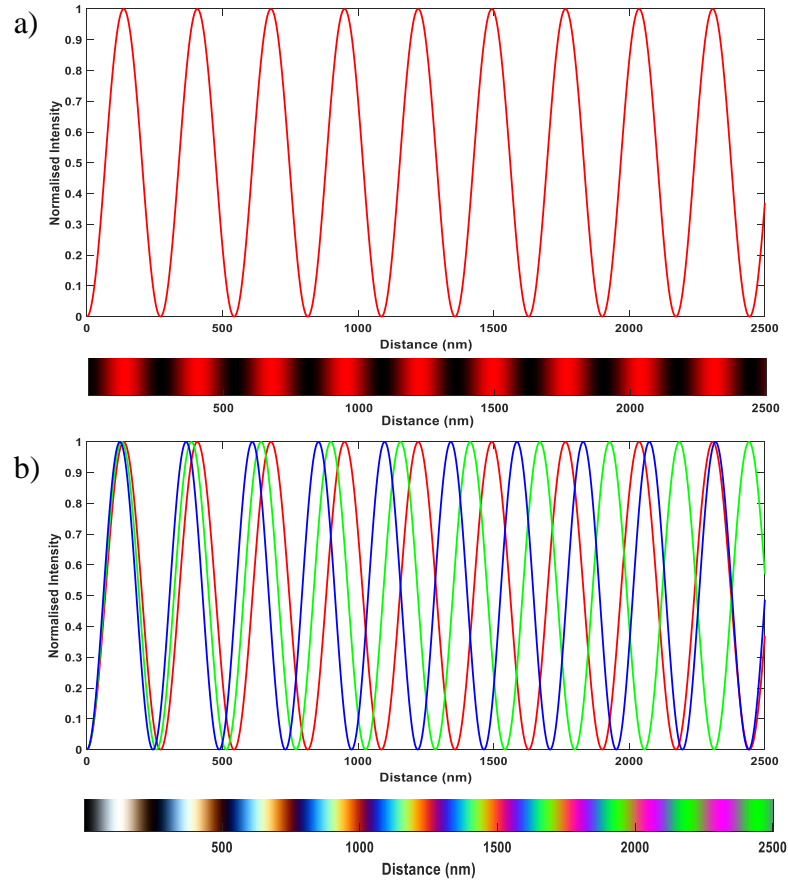


Figure 4.1-This diagram shows the principle of the modulation gap reduction using TartanSW multi-excitation. a) A single wavelength at 543 nm was used and there was clear periodic structure with an information gap of 50%. b) Three excitation wavelengths at 488 nm, 514 nm and 543 nm have been pseudo-coloured in blue, green and red, respectively. The spectral separation observed was a result of the relative positions of the anti-nodal spacing locations changing due to their wavelength dependence. Thus, a reduction in the information gap of 44% could be theoretically obtained over a single-excitation wavelength i.e. a reduction of the black nodal regions in the colour map in b).

Drexhage conducted experiments which utilised highly reflective gold and silver coated microscope slides, on top of which was a stair like succession of CdC₂₀ layers which were coated with a monolayer of fluorescent dye [146], [147]. By illuminating the fluorescent dye layers with light at the excitation wavelength of the fluorescent dye, the resultant fluorescence emission intensity observed was dependent on the intensity of the electric field of the SW [146], [147]. Lambacher et al. utilised this approach for fluorescence interference contrast microscopy (FLIC) and mapped fluorescence intensity as a function of height of fluorescent labelled cell, by creating a Si mirror with stepped SiO₂ layers at known heights values. Additionally, it was observed that the fluorescence emission self-interference generated an emission and excitation SW simultaneously, and as a result, this created a modulation in the fluorescence intensity [147].

Elsayad et al. demonstrated using laser-scanning in reflection method with fluorescently labelled cells grown on a dielectric surface, that with the application of a narrow detection bandwidth of < 10nm, an axial distance-dependent spectral signature could be obtained [75]. Finally, work by Amor et al. [72], utilised the effect of the emission SW to create a modulation in the fluorescence intensity. Their approach was to capture images with a CLSM of a fluorescently coated lens specimen. By application of an emission detection at 5 nm bandwidth centered at 550 nm, 560 nm, 570 nm and 580 nm. A modulation was detected due to the presence of both the excitation and emission SW. To confirm the presence of a emission SW, a laser line filter was placed below the specimen instead of a mirror, which resulted in suppression of the excitation SW with only the presence of a 580 nm emission SW. Moreover, by subtracting the excitation SW from the emission SW resulted in a modulation identical to the moiré pattern obtained experimentally at 580 nm. As a result, it was demonstrated that the modulated field amplitude was the difference between the stokes shift of the excitation and emission SWs [72].

I set out to utilise the method presented by Amor et al. and use three different 5 nm narrow band detection channels to create an intensity modulation that occurred at different axial locations. By encoding multiple spatially modulated intensity patterns, which was dependent on the detection wavelength, it could be utilised to gain further spatial information not available when using a single detection channel. Additionally, I aimed to use the both TartanSW multi-excitation and multi-emission methods to remove axial ambiguity that was inherent in single colour SW microscopy without *a priori* knowledge of the specimen. This was achieved by using three pseudo-coloured red, green and blue channels for each of the multiple emission and excitation wavelengths, which may reveal directionality about the specimen. Figure 4.2 demonstrated the principle of the SW plane ordering, where a convex and concave with the resulting anti-nodal plane order. The intensity variation, which resulted in the pseudo-colour ordering, was due to the SW intersecting different axial locations. This is created by shifting the anti-nodal positions using multiple excitation wavelengths (multi-excitation), or the modulation in the intensity by using multiple emission detection wavelengths (multi-emission). The result, in both of these cases, was the colour ordering observed was dependent on the specimen geometry.

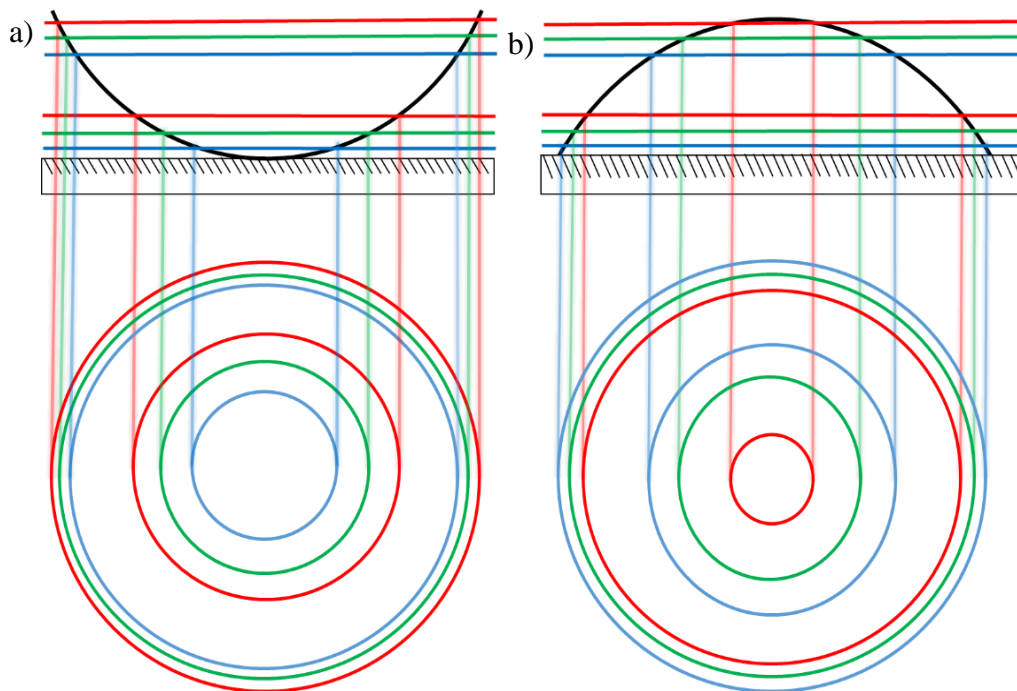


Figure 4.2 – A simplified diagram to demonstrate how the intersection of multiple wavelengths used in TartanSW could be utilised to remove ambiguity of direction in single wavelength multi-planar SW microscopy. Here two different geometrical setups are shown above a) a convex surface and b) a concave surface. The concentric rings below each of the geometric shapes demonstrate how the projection of the three wavelengths onto the 2D lateral plane results in colour ordering changes.

4.2 Theory of TartanSW multi-excitation and multi-emission

A theoretical expression for the TartanSW multi-excitation and multi-emission was required which would describe the axial intensity profile due to the presence of both the excitation and emission SW. Here, the assumption was made that when a 0.15 NA objective was used for TartanSW imaging of the lens specimen, the effect of the objective lens was negligible over the small axial region imaged. This was because, the full axial PSF range of a 0.15 NA objective lens was much larger than the small axial region imaged. The fluorescence emission, due to the excitation SW, was observed at the spatial

frequency of the excitation wavelength. Thus, as stated in previous chapters, the excitation SW is given as,

$$I_{exc}(z) = I_o \left(1 - \cos \left(\frac{4\pi}{n\lambda_{exc}} z \right) \right) \quad (4.1)$$

where z is given the axial height, λ_{exc} is the excitation wavelength, n is the refractive of medium and I_o is the constant intensity. Secondly, there was the presence of a secondary SW, due to the fluorescence emission which was reflected from the mirrored surface [76], [77], [147], [148]. Modelling the emission interaction was done by considering each fluorophore as a randomly oriented oscillating dipole emitter [148, 150]. As fluorescence is a spontaneous process, the fluorescent emission would be incoherent with the other fluorophores that have also been excited within the focal volume. As a result, interference of the emission is only considered to occur between the direct and reflected rays of each individual fluorophore, which in this chapter is considered to occur at normal incidence to the mirror surface and can be expressed as:

$$I_{emis}(z) = I_o \left(1 - \cos \left(\frac{4\pi}{n\lambda_{emis}} z \right) \right) \quad (4.2)$$

where, λ_{emis} is the emission wavelength and z is the axial height from the mirrored surface. The constant intensity amplitude, I_o , is unknown. However, the intensity for both excitation and emission SW in Eqn. 4.1 and 4.2 will be proportional to $1 - \cos\left(\frac{4\pi}{n\lambda_{exc}} z\right)$ and $1 - \cos\left(\frac{4\pi}{n\lambda_{emis}} z\right)$, respectively. To account for the range of emission wavelengths, I then integrated over the detection bandwidth, as a result eqn. 4.2 becomes:

$$I_{emis}(z) = \int_{\lambda_{emismin}}^{\lambda_{emismax}} 1 - \cos \left(\frac{4\pi}{n\lambda_{emis}} z \right) d\lambda_{emiss} \quad (4.3)$$

Now, Eqn. 4.3 gives an expression for the emission SW. The full contribution of both the excitation and emission SW could be determined and is calculated by a convolution between the excitation and emission waves [72], [76], [77] As a result, the effective intensity pattern observed is proportional to:

$$I(z) = \left[1 - \cos\left(\frac{4\pi}{\lambda_{exc}}z\right) \right] * \int_{\lambda_{emismin}}^{\lambda_{emismax}} \left[1 - \cos\left(\frac{4\pi}{\lambda_{emis}}z\right) \right] d\lambda_{emiss} \quad (4.4)$$

4.3 Experimental methods

4.3.1 Fluorescently labelling of specimens

A fluorescently coated lens specimen was prepared as in chapter 2.2.1 and stained with Dil as a method to characterise TartanSW multi-excitation and multi-emission methods. Again, RBCs stained with Dil were prepared, as in previous chapters, and adhered to a poly-L-lysine coated aluminum mirror (Laser 2000).

MCF-7s, an established breast cancer cell line, was used as a method to characterise the TartanSW in eukaryotic cells and was prepared by Peter Tinning (University of Strathclyde). MCF-7s were grown on an aluminum mirror (Laser 2000) and transferred into a glass Petri dish using tweezers. HEPES buffered saline (HBS) containing (in mM): NaCl 140, KCl 5, MgCl₂ 2, HEPES 10, D-glucose 10 and CaCl₂ 2, pH 7.4 buffer was added until the mirrors were completely covered, gently rocked. Next, the buffer was exchanged for 4 ml of new HBS buffer and used to cover the mirrors. To stain the MCF-7s, 20 μ l of 1mg/ml Dil in DMSO was added to the 4 ml of HBS buffer and the Petri dish was covered and gently shaken for 1 hour at 37°C. To remove any excess dye, it was washed off after incubation by exchanging the HBS buffer at least twice. Now, the stained cells were stored at 37°C and incubated in a six well plate with HBS buffer and covered with aluminum foil until they were ready to be imaged.

4.3.2 TartanSW multi-excitation and multi-emission imaging

TartanSW multi-excitation was carried out on Dil labelled specimens with three different excitation wavelengths which were selected using the following criteria: the three excitation wavelengths selected must be within the spectrum of the dye excitation and were sufficiently spectrally separated from each other. This maximises the modulation gap reduction, due to the phase dependence of each SW on the excitation wavelength.

As a result, the excitation wavelengths selected were 543 nm, 514 nm and 488 nm with fluorescent emission detected over a 100 nm range between 550-650 nm.

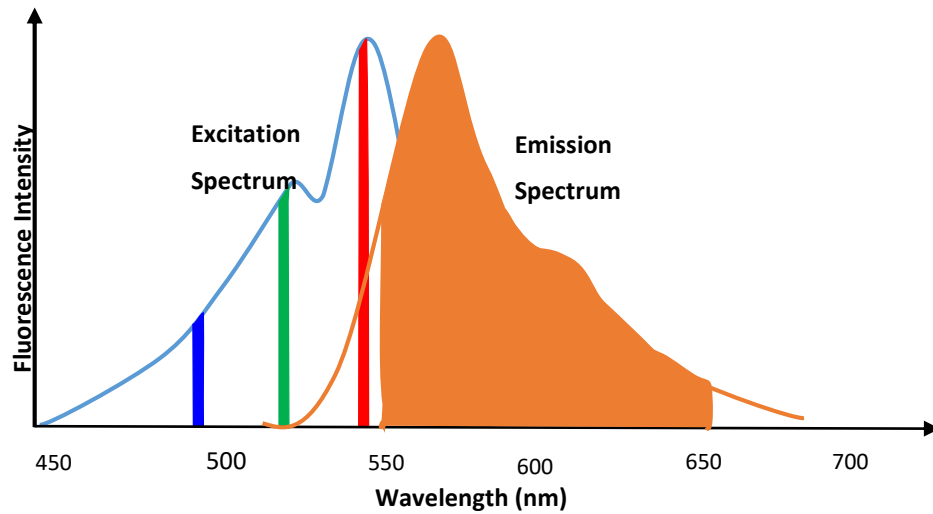


Figure 4.3 – A representation of how the Dil spectrum was utilised for TartanSW multi-excitation. The red (543 nm), green (514 nm) and blue (488 nm) were the lasers used within the dye excitation spectrum and in orange was the emission spectrum represents the 100 nm fluorescent emission detection.

TartanSW multi-emission was excited at a wavelength of 514 nm and fluorescent emission was collected simultaneously on three different PMT channels at 5 nm detection bandwidths, using the Leica SP5 spectral detector (Figure 4.4). The detection channels were set to 567-572 nm, 592-597 nm and 617-622 nm for the lens specimens and MCF-7 cells. The RBC used an excitation wavelength of 514 nm, however, I shifted the emission detection bands to a more efficient region of Dil's emission spectrum to 550-555 nm, 565-570 nm and 575-580 nm, respectively. For RBC imaging, a high magnification (100x) objective lens was required and consequently, the image brightness was reduced.

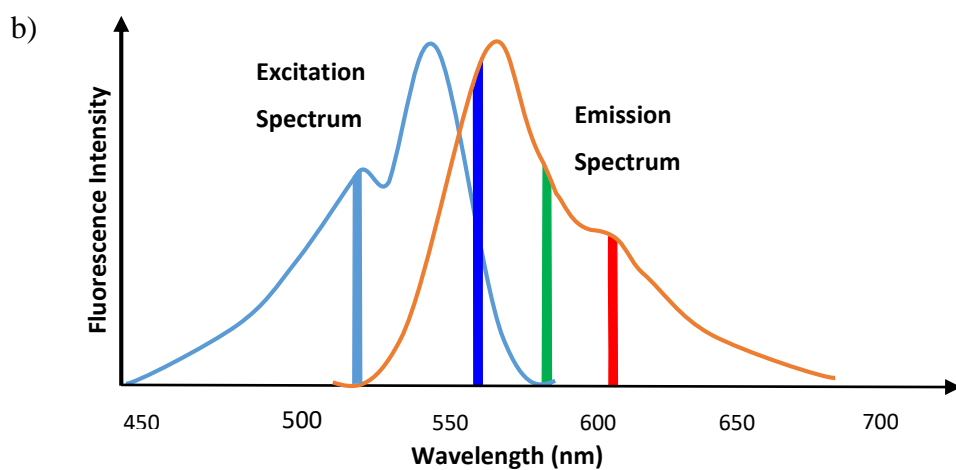
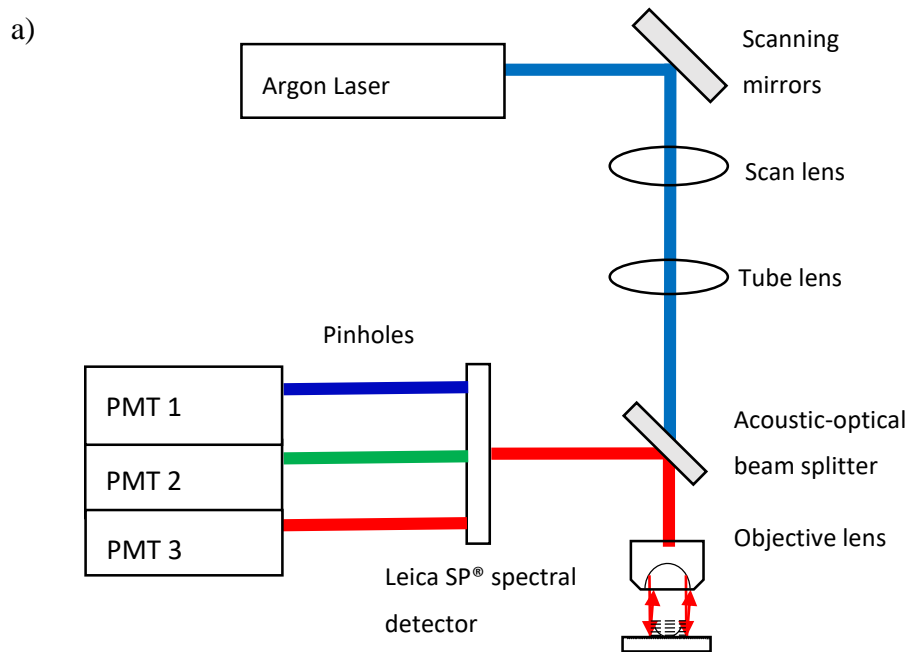


Figure 4.4 – a) A schematic diagram of the Leica SP5 used for TartanSW multi-emission where a single excitation wavelength is used to excite the specimen with a mirror below the specimen. Emission was detected simultaneously at three different PMTs with 5 nm detection bandwidths. b) A diagram which represented how the wavelengths selected were applied to the excitation and emission spectrum of the Dil.

TartanSW multi-excitation and multi-emission imaging of fluorescent labelled specimens were captured using a Leica DM600 confocal microscope. The $f = 48$ mm lens specimen was placed under a HCX PL FLUOTAR 5.0x 0.15 dry objective lens and imaged using three different plane reflectors, these included: a dielectric mirror (BB1-E02, Thorlabs), an aluminum mirror (TFA-20C03-10, Laser 2000) and a bare aluminum microscope slide (TS-AL-134, Dynasil) with no protective coating. Images were captured at an image size of 2048 x 2048 pixels with a scan speed of 100 Hz. A 3-frame average and a digital zoom of 2.01x was applied to the image.

MCF-7s were grown on an aluminum mirror (Laser 2000) and imaged in a buffer medium of HBS with 4% BSA with an HCX APO L U-V-I 40.0x0.80 water objective lens. TartanSW multi-excitation images were captured at 4096 x 4096 pixels and imaged with a scan speed of 100 Hz and a 3-line average. TartanSW multi-emission images were captured at 2048 x 2048 pixels with a scan speed of 100 Hz and a 3-line average.

Finally, RBCs adhered to an aluminum mirror (Laser 2000) were imaged using a HCX PL FLUOTAR 100.0x1.30 oil immersion objective lens. Images had a frame size of 512 by 512 pixels at a scan speed of 200 Hz with an 8.9x digital zoom, using a 3-line average. For TartanSW multi-emission RBC imaging, an image size of 1024 by 1024 at a scan speed of 100 Hz with a 10.6x digital zoom, using a 3-frame average. Once the images were captured, they were stored as .tiff files and the metadata was stored as a .lif file format.

4.3.3 Analysis of TartanSW lens specimen data

In FIJI, the lens specimen TartanSW image was cropped and a Gaussian blur of $\sigma = 2$ was applied to remove noise. In MATLAB, a radial line profile was taken from the centre of the TartanSW image outwards, and by using Eqn. 2.6, the radial distance was translated to axial height. As a result, an intensity profile was plotted against axial height (Height from Mirror) over the range of $z = 5 \mu\text{m}$. An axial range of $5 \mu\text{m}$ was selected as to characterise the spectral signature over a large axial distance. The modulation gap was

calculated by using the *findpeaks* function in MATLAB, where only anti-nodal planes (peaks) that have a normalised intensity of above 0.1 and a peak separation of 100 nm were detected. From this, the measured FWHM was determined and the minimum FWHM boundary from the shortest wavelength (488 nm) and the maximum FWHM of the longest wavelength (543 nm) were extracted. This was repeated for nine anti-nodal planes, as to keep the comparison consistent over a known range across all the SW images. To calculate the modulation gap, the nine 543nm and 488 nm FWHM boundaries values were subtracted and the result for each boundary was added together to determine the total contribution of the TartanSW multi-excitation method. Next, the total contribution was subtracted from the total distance over the tenth nodal plane. The percentage of information gain between the TartanSW multi-excitation modulation gap and a single wavelength of the 543 nm were subtracted from one another. The 543 nm wavelength was used as the comparison; as the previous SW DiI single excitation wavelength imaging was carried out using a 543 nm excitation wavelength.

The TartanSW multi-emission was analysed using the theoretical amplitude modulation, λ_{mod} , and was calculated using the following equation [72]:

$$\frac{1}{\lambda_{mod}} = \frac{1}{\lambda_{emis}} - \frac{1}{\lambda_{exc}} \quad (4.5)$$

where, λ_{emis} is the emission detection wavelength and λ_{exc} is the excitation wavelength. For a SW, the theoretical spatial frequency, λ_{SWmod} , of the intensity modulation is given by [72]:

$$\lambda_{SWmod} = \frac{\lambda_{mod}}{2n} \quad (4.6)$$

where, n is the refractive index of the immersion medium. The spatial modulation of the experimental data was obtained using a line profile from the centre of the TartanSW lens image. The TartanSW multi-emission intensity plots were obtained from the experimental images in MATLAB, and from these plots two different minimal intensity values of the intensity modulation were determined manually extracted. This was

calculated subtracting the two intensity modulations from one another, and as a result I obtained the experimental spatial frequency of the modulation intensity.

4.3.4 Difference Method for TartanSW imaging

DiffSW images were obtained by the application of post-acquisition image processing of the TartanSW multi-excitation images. In MATLAB, the theoretical DiffSW was simulated for the 543 nm, 514 nm and 488 nm excitation SWs and the emission detection was simulated over a range of 550-650 nm, with an axial range of $z = 0-5 \mu\text{m}$, using Eqn. 4.4. The DiffSW was simulated and by calculating the absolute difference between the 514 nm and 543 nm, and the 488 nm and 514 nm excitation wavelengths. Mathematically, the difference method intensity (I_{diff}) was calculated by taking the modulus of the difference between the short and long excitation wavelengths and is given by:

$$I_{diff} = |I_{SWshort} - I_{SWlong}| \quad (4.7)$$

where, $I_{SWshort}$ is the intensity of the shortest excitation wavelength used and I_{SWlong} , is the intensity of the longest excitation used. In practice, this was achieved in FIJI by taking each channel and using the image calculator in FIJI, a composite image was created as a colour merge of the green-red channel, which was pseudo-coloured red, and blue-green channel, which was pseudo-coloured green. The two composite images were merged to create the final red-green DiffSW image. The resolution of the DiffSW method was calculated by selecting a line profile from the centre of the lens specimen image outwards over a range of $z = 0$ to $5 \mu\text{m}$. The *findpeaks* function was used in MATLAB to extract the FWHM values at minimum peak separation of 50 nm with normalised peak intensity of 0.05. Once the peaks were detected, the FWHM was extracted for each anti-nodal peak and the mean FWHM was calculated to obtain the resolution.

4.4 Results

4.4.1 A comparison of simulated and experimental TartanSW multi-excitation

In the first instance, I simulated TartanSW multi-excitation in MATLAB to characterise the multi-excitation method using the code in Appendix VIII. The three excitation wavelengths selected were 543 nm, 514 nm and 488 nm over an axial range of $z = 0$ -5 μm and were simulated using eqn. 4.1. The resulting profile shown in Figure 4.5a. It was noticed, as each excitation SW propagates away from the mirror surface there was a gradual separation between each of the excitation wavelengths. As a result, the anti-nodal planes coincide at different locations, which indicated more information about a specimen could be obtained. Each of the excitation wavelengths were assigned a pseudo-colour of red, green, and blue from the long to short wavelengths. Now, the simulated normalised intensity profiles were combined in MATLAB to generate a spectral representation of the axial intensities at different axial heights. As was shown in Figure 4.5a, for the first anti-nodal plane, the overall fringe structure was white due to little spectral separation between each of the excitation wavelengths. This was expected, as the SW propagates, each of the excitation SWs become more out-of-phase wave with respect to one another over the axial range. Once the relative phases were fully out-of-phase, such that the nodal plane of one excitation wave overlaps with another anti-nodal plane position, the spectral signature reversed in order until the waves were in-phase.

Now for comparison, I considered the effect of the emission contribution over a detected emission wavelength of 550 – 650 nm, which was calculated using Eqn. 4.4. There was a reduction of intensity, with an observable modulation in the intensity, particularly within the first three fringes of the 514nm and 488 nm excitation channels, as shown in Figure 4.5b. Again, it was observed in Figure 4.5 that the spectral signature colour map changed over the axial distance, due to the relative phase relationship of the excitation

wavelengths. An overall modulation gap reduction of 34% was calculated for the theoretical profile in Figure 4.5b.

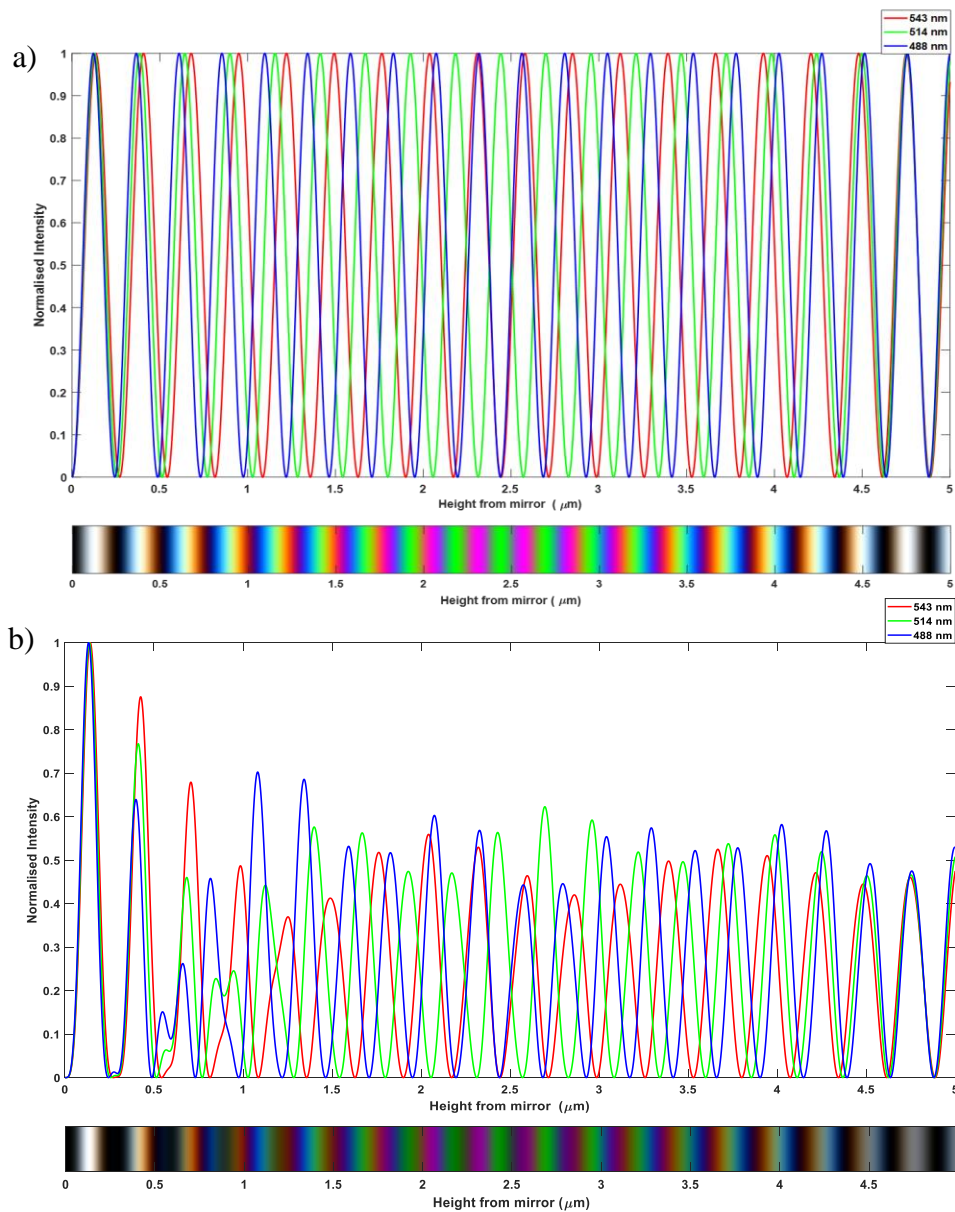


Figure 4.5 – Simulated TartanSW multi-excitation using only Eqn. 4.1 for an excitation wavelengths of 543, 514 and 488 nm over an axial range $z = 0\text{--}5 \mu\text{m}$ shown in a). b) A representative of the pseudo-colour channels overlapping with the resultant spectral signature.

Next, I sought to confirm that the spectral pattern simulated could be produced experimentally. A $f = 48$ mm Dil stained lens specimen was imaged using three excitation wavelength at the 543 nm, 514 nm and 488 nm laser lines, with mission detection captured between 550-650nm. TartanSW multi-excitation was repeated using three different substrates: a bare aluminum coated microscope slide, a dielectric mirror and an aluminum mirror. All images were contrast adjusted and cropped with a Gaussian blur of $\sigma = 2$ applied to the image.

Firstly, to best replicate the simulated data, I used a bare aluminum microscope slide which has no spacing between the reflective aluminum substrate and the lens specimen. In Figure 4.6a – c, is each of the excitation image and the resulting merged RGB image is shown in Figure 4.6d. A radial SW pattern was observed where each wavelength intersects the fluorescently labelled lens specimen. Furthermore, a spectral signature was observed with a radial dependence on the radius of curvature of the lens specimen. The experimental spectral signature observed resembled the theoretical spectral signature in Figure 4.5b. Additionally, a radial line intensity plot was taken from the centre of the radial image and converted to height from the mirror. A comparison between the simulated TartanSW in Figure 4.5a and b and the normalised intensity plot shown in Figure 4.6e, demonstrated that a modulation effect was present due to the emission SW. This was particularly evident in the blue and green channels, where there was a clear reduction in the intensity of the third and fourth, and fifth and six fringes in both the simulated (with emission contribution in Figure 4.5b) and the experimental data. Finally, the experimental modulation gap reduction was calculated to be 42%.

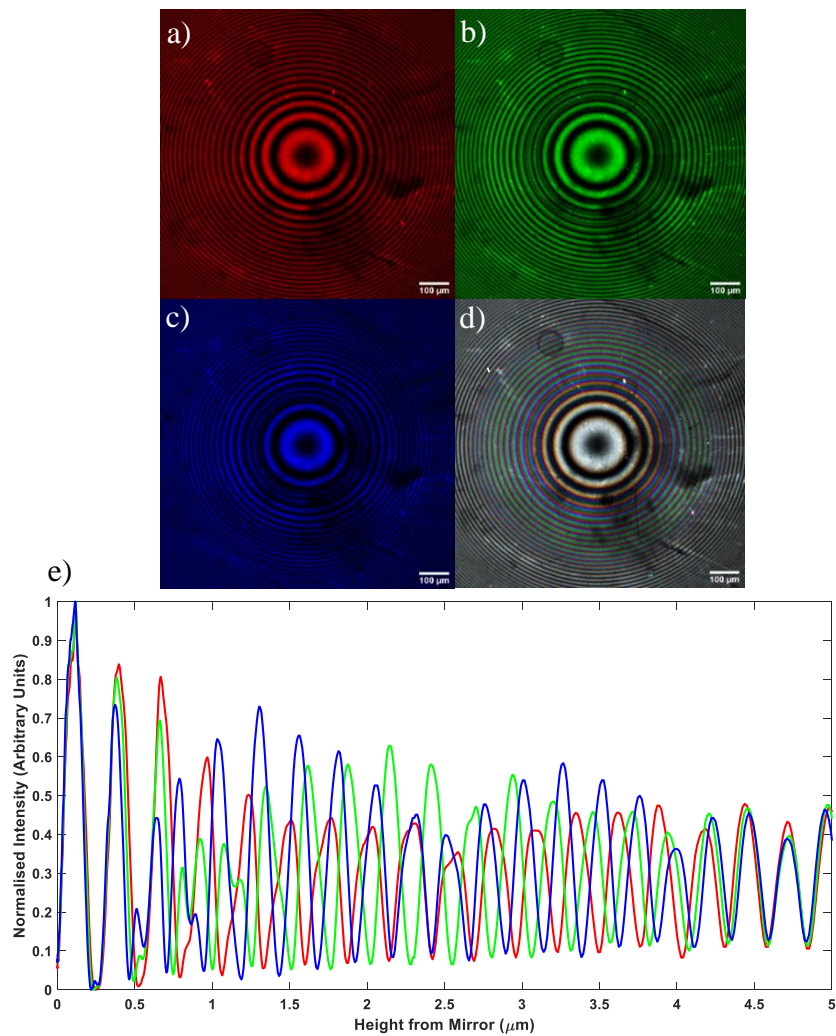


Figure 4.6 – A TartanSW multi-excitation image of a $f = 48$ mm len specimen imaged on a bare aluminum microscope slide. Emission wavelengths were detected between 550-650 nm, with the images captured at different excitation wavelengths of a) 543 nm, b) 514 nm and c) 488 nm. d) An RGB image of images a-c resulted in a spectral signature. e) A normalised intensity profile from the centre of the image out towards the left edge of the image. The radial distance was converted to axial height from the mirror for each excitation wavelength using Eqn.2.6.

To demonstrate the effect of the TartanSW multi-excitation on an aluminum mirror (Laser 2000) and dielectric mirror (Thorlabs), an $f = 48$ mm lens was imaged using each mirror. The composite RGB merged images were shown in Figure 4.7a and c, respectively. It was observed that the spectral signature was different for each of the reflective substrate used.

The TartanSW multi-excitation images captured on an aluminum mirror were shown in Figure 4.7a. The spectral signature captures using the aluminum mirror appeared to be shifted relative to the simulated (Figure 4.5b) and the experimentally obtained lens specimen imaged on a bare aluminum microscope slide (Figure 4.6). A normalised line intensity profile of the aluminum mirror shown in Figure 4.7c, demonstrated that the shift of the anti-nodal plane corresponded to the anti-nodal plane closest to the mirror surface. This was observed with respect to the intensity profiles of the simulated and bare microscope slide in Figure 4.5b and Figure 4.7c, respectively. The axial shift was estimated for each of the excitation wavelength of 543 nm, 514 nm and 488 nm. To do this, the normalised intensity values at $z = 0$ was acquired from Figure 4.7b and used to estimate the axial shift from the equivalent normalised intensity values of the second anti-nodal plane in Figure 4.6e. The axial shift for each excitation wavelength was 295 nm, 295 nm and 298 nm, with an average axial shift of 296 ± 1 nm. Lastly, a modulation gap reduction of 48% was calculated when an aluminum mirror was used.

The TartanSW multi-excitation image obtained, using a dielectric mirror. (Figure 4.7c) showed a different spectral signature than the simulated TartanSW multi-excitation in Figure 4.5b. However, due to the spectral signature each of the axial offsets was different for each excitation wavelength used. As a result, it was more difficult to calculate the axial offset, as there were no obvious directly comparable points in the dielectric intensity profile (Figure 4.7d) compared to the bare aluminum microscope slide intensity

profile (Figure 4.6e). The axial offsets were estimated to be 215 nm, 316 nm and 331 nm for the 543 nm, 514 nm and 488 nm excitation wavelengths.

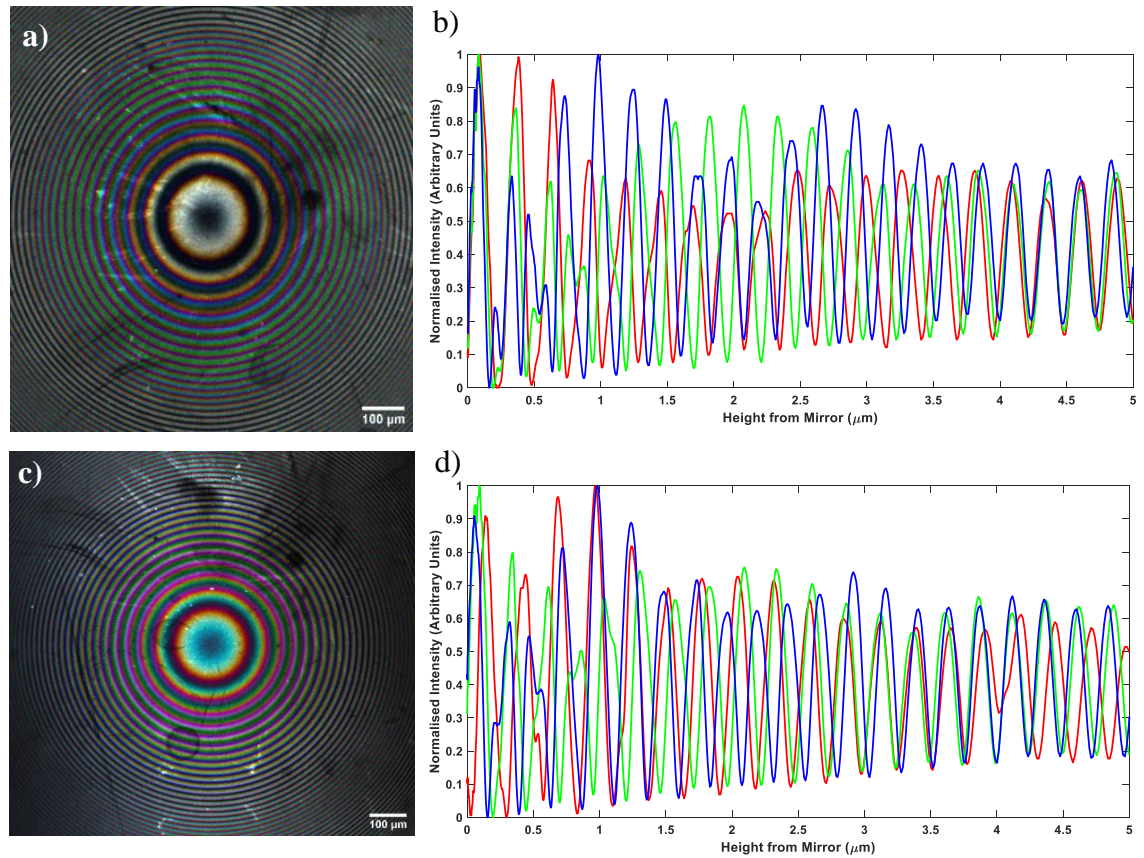


Figure 4.7 - TartanSW multi-excitation images of a $f = 48$ mm lens specimen which used excitation wavelengths of 488 nm, 514 nm and 543 nm, which were pseudo-coloured blue, green and red, respectively. a) An aluminium mirror (Laser 2000) RGB composite image and b) the normalised intensity profile of the lens specimen. c) Thorlabs dielectric mirror RGB composite image and b) the normalised intensity profile of the lens specimen.

4.4.2 Simulated and experimental comparison used for TartanSW multi-emission

TartanSW multi-emission was a technique that was utilised to create an intensity modulation caused by the presence of both the excitation and the emission SW. To characterise TartanSW multi-emission, I simulated the effect of an excitation wavelength of 514 nm and with three different emission wavelengths at 567-572nm, 592-597 nm and 617-622 nm, which were pseudo-coloured blue, green and red, respectively (Appendix IX). In Figure 4.8a, a beating pattern was observed which was dependent on the difference between the excitation and emission wavelengths. The theoretical intensity modulation was calculated, using Eqn. 4.5 and Eqn. 4.6, which gives values of 2637 nm, 1898 nm and 1509 nm. The normalised intensities for each channel was then overlapped to create a representation of the spectral signature, due to the beating modulation over the three emission detection wavelengths.

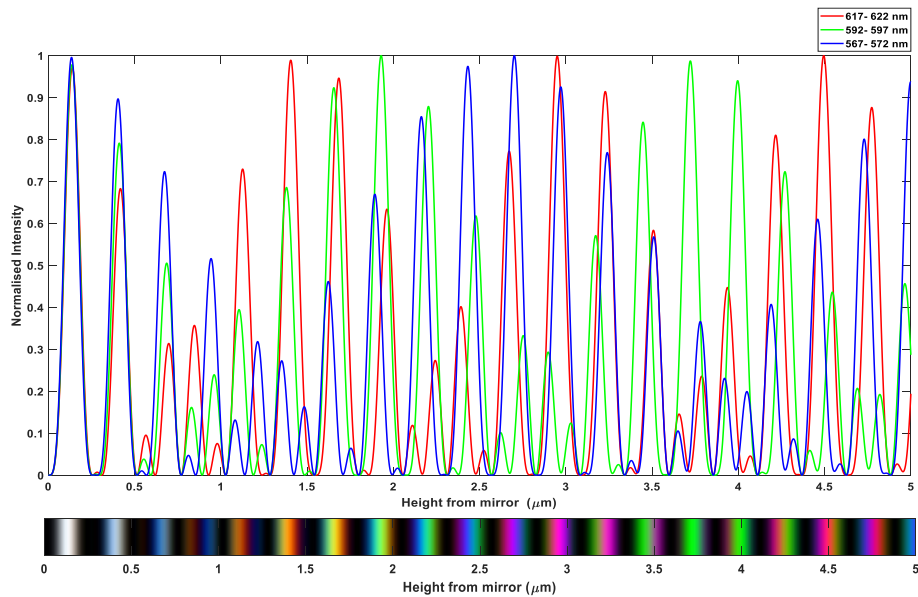


Figure 4.8 – A simulated TartanSW multi-emission normalised intensity profile over an axial range $z = 0\text{-}5\ \mu\text{m}$. Below a merged pseudo-coloured of the RGB image was generated using the simulated intensity profiles.

To verify experimentally, an $f = 48$ mm lens specimen was used to characterise the experimental conditions of the TartanSW multi-emission on an aluminum mirror (Laser 2000), Thorlabs dielectric mirror and a bare aluminum microscope slide. Images were linearly contrast adjusted in FIJI and a Gaussian blur of $\sigma = 2$ was applied in MATLAB. As before, to confirm the TartanSW multi-emission profiles, a bare aluminum microscope slide was used. Figure 4.9a-c showed the modulation effect which varied for each of the emission detection channels used. These images were merged to create an RGB composite image shown in Figure 4.9d. The resultant spectral signature from the merged image resembled the colour ordering of the simulated data in Figure 4.8. In addition, Figure 4.9e shows a radial intensity profile taken from the lens image which was converted to axial height from the mirror, using the known lens geometry (Eqn. 2.1). The intensity profiles for each channel of the bare aluminum microscope slide (Figure 4.9e) showed an intensity modulation which resembled the theoretical intensity profiles shown in Figure 4.8. Taken alongside the spectral signature, the experimental intensity profile and spectral signature observed had a modulation that became larger as the difference between the emission and excitation increased. To confirm that the intensity modulation observed was in agreement with the theoretical value, the experimental intensity modulation was obtained from Figure 4.9e. The intensity modulation was calculated for red, green and blue channels as 2600 nm, 1943 nm and 1592 nm which gave a percentage error when compared to the theoretical values of 1.41%, 2.37% and 5.49%, respectively.

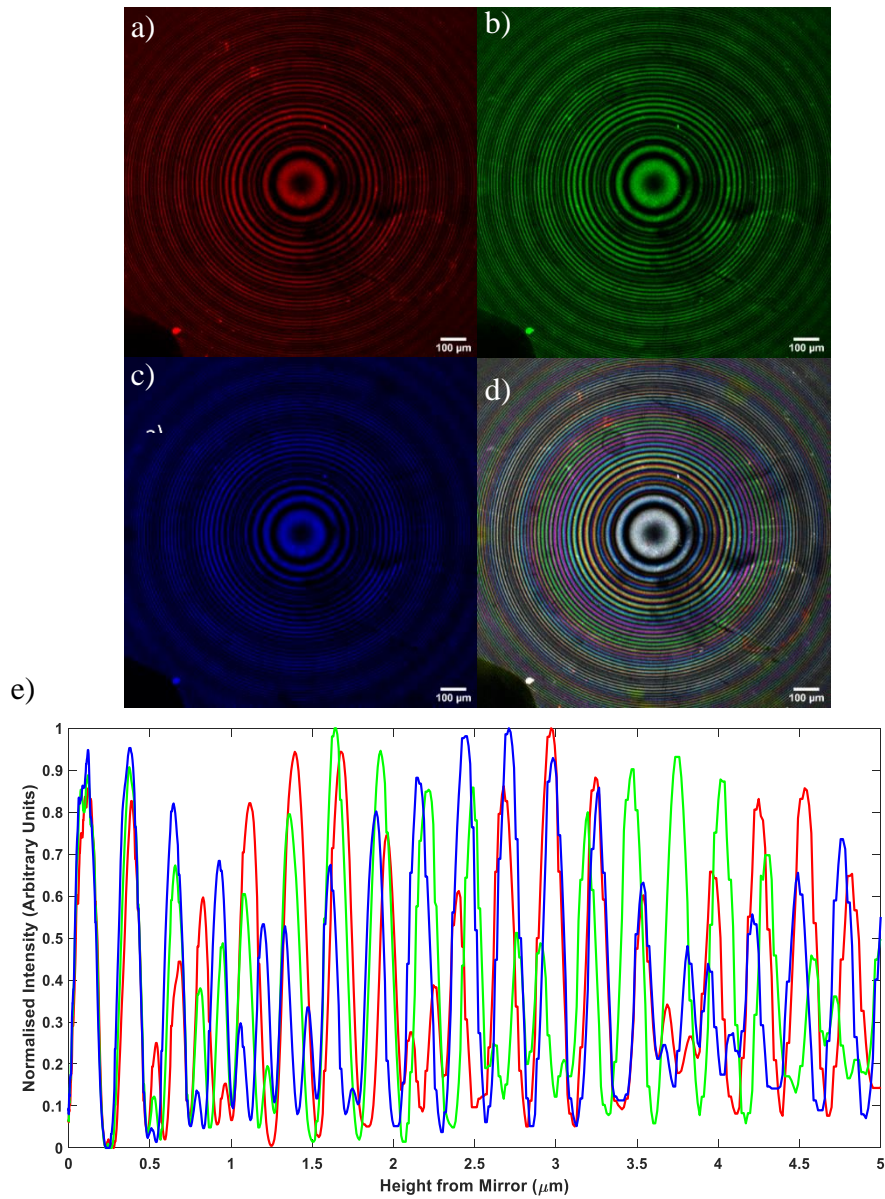


Figure 4.9 - TartanSW multi- emission images of an $f = 48$ mm lens specimen imaged on a bare aluminum microscope slide. An excitation wavelength of 514 nm was used with detection at a) 617-622nm, b) 592-597nm and c) 567-572 nm. d) A RGB image merge of images a-c resulting in a spectral signature. e) A normalised intensity profile from the centre of the image was then translated from radial distance to axial height from the mirror.

To test the effect of using an aluminum mirror and dielectric mirror for TartanSW multi-emission, a $f = 48$ mm fluorescent lens specimen was imaged. The resulting composite RGB merged images were shown in Figure 4.10a and c for the aluminum mirror and dielectric mirror, respectively. As with the TartanSW multi-excitation, the spectral signature for the TartanSW multi-emission observed was different for each of the reflective substrates used.

When the aluminum mirror was used, there was the presence of a shift in the spectral signature with the first anti-nodal plane missing in both the RGB image and line intensity plot as shown in Figure 4.10a and c. To quantify the axial shift, it was calculated in the same manner as in section 4.4.1, by comparing the bare microscope intensity plot (Figure 4.9e) with the aluminum mirror intensity plot (Figure 4.10c). As a result, the average axial shift was calculated as 285 ± 1 nm. Next, spatial frequency of the intensity modulation observed in Figure 4.10a and c was calculated using the normalised Intensity from Figure 4.10c. For the aluminum mirror, the spatial frequency of the intensity modulation was calculated as 2525 nm, 1774 nm and 1528 nm, with a percentage error of 4.25%, 6.53% and 1.25% when compared to the theoretical values.

A comparison of the dielectric mirror, again, showed a spectral signature that was different from the simulated and experimental data sets on the bare aluminum coverslip and aluminum mirror. The axial offsets were not immediately obvious, thus the first maxima of the intensity modulation values were determined in both the theoretical (Figure 4.8) and experimental (Figure 4.10d) intensity profiles. Next, the experimental and theoretical values were subtracted for each channel to determine the axial offset. The axial offsets were calculated as 195 nm, 816 nm, 70 nm for the red, green and blue pseudo-colour channels, respectively. The spatial frequency of the intensity modulations was calculated as 2699 nm, 1788 nm and 1546 nm. A percentage error when compared

to theory was calculated as 2.35%, 5.79% and 2.44%, which was in good agreement with the theoretical values.

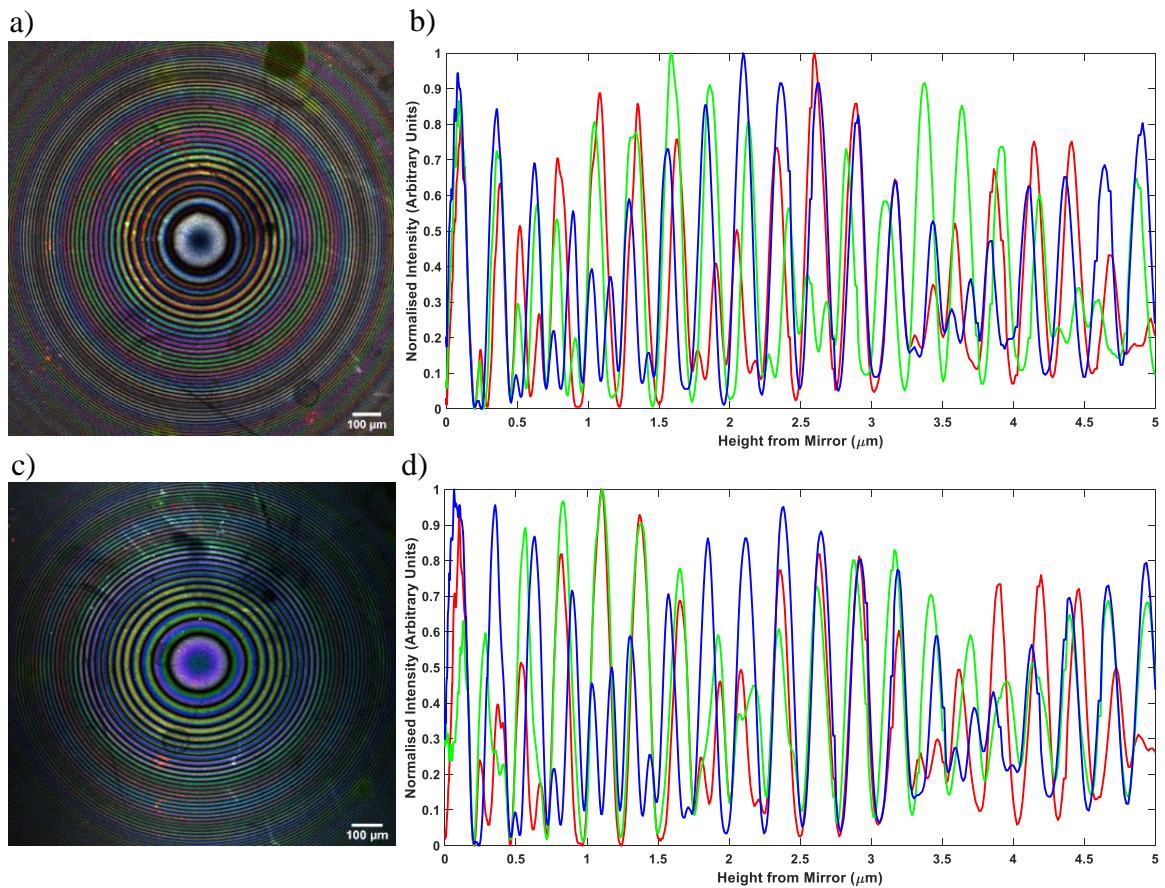


Figure 4.10 – TartanSW multi-emission images of a $f = 48$ mm lens specimen which used an emission detection channels of 567-548 nm, 592-597 nm and 617-622 nm which were pseudo-coloured blue, green and red, respectively. a) An aluminium mirror (Laser 2000) RGB composite image and b) is the normalised intensity profile of the lens specimen. c) Thorlabs dielectric mirror RGB composite image and b) is the normalised intensity profile of the lens specimen.

The results so far, showed that the theoretical models in Eqn. 4.4 had predicted the spectral signature captured with the bare aluminum microscope slide for both TartanSW methods. In particular, the effect of the emission SW on the modulation of the excitation SW, in both the TartanSW multi-excitation experimental and theoretical results, was not a trivial effect even with a 100 nm emission detection bandwidth. Next, the aluminum and dielectric mirrors were compared with the simulated and experimentally obtained bare aluminum microscope slide. It was noticed that the aluminum mirror had an axial offset that was consistent in the both TartanSW multi-excitation and multi-emission imaging methods. However, the comparison of the dielectric mirror showed a spectral signature which was not consistent with the theoretical and the experimentally TartanSW images captured with a bare aluminum microscope slide. The axial offsets calculated were different for each excitation or emission channel. Therefore, it was shown that the type of reflective substrate used effected the SW signature that was observed.

4.4.3 Confocal TartanSW multi-excitation and multi-emission imaging of red blood cells

The first application of TartanSW multi-excitation and multi-emission to a biological specimen was to use a RBC, due to its known biconcave structure. In this instance, an aluminum mirror was used as the reflective surface which the RBCs were adhered to.

TartanSW multi-excitation wavelength imaging of RBC was performed using 543 nm, 514 nm and 488 nm excitation wavelengths. Each image was then pseudo-coloured (red, green and blue) and merged to create an RGB composite image as shown in Figure 4.11a. It was clear from the merged image that there were spectral fringes. For each of the concentric rings, the colour order observed was such that the blue fringes correspond to the outer edge of the RBC, and the red fringes on the inner edge of the RBC. Interestingly, this colour order was the inverse of what was observed with the lens specimen. Figure

4.11b shows a radial intensity profile. Again, clear anti-nodal planes were observed for each excitation wavelength, with the red excitation leading the blue excitation towards the centre of the RBC concave surface.

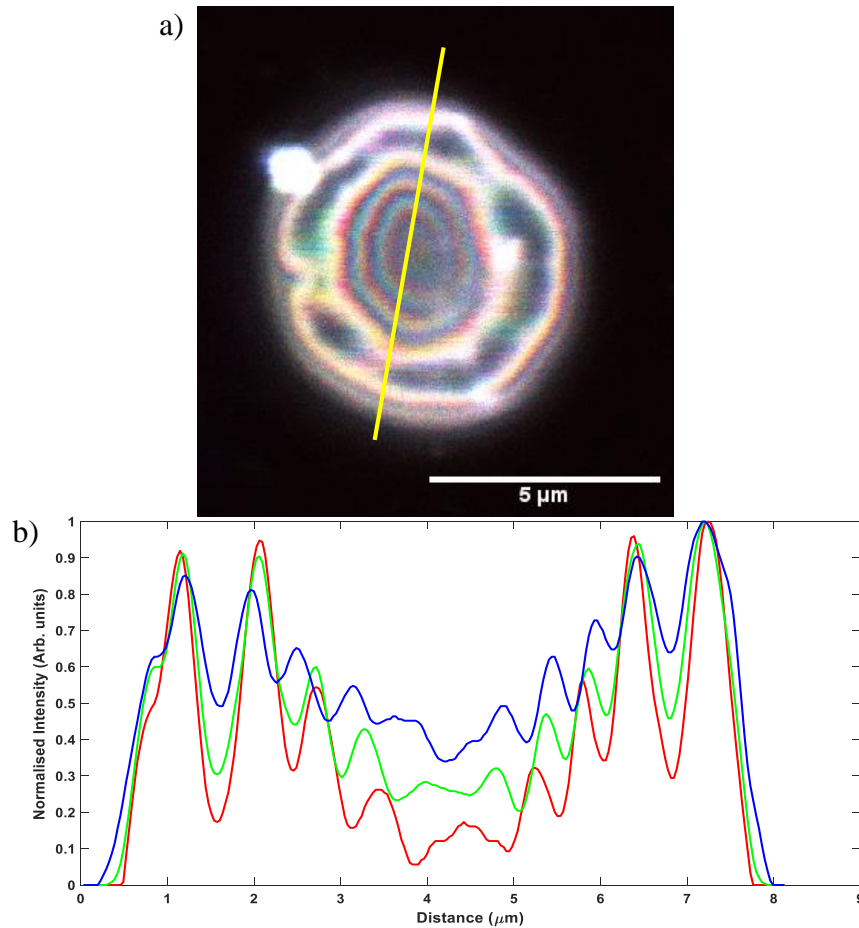


Figure 4.11 – A TartanSW multi-excitation image of a healthy RBC adhered to an aluminium mirror (Laser 2000) with the three excitation wavelengths images merged to create an RGB image in a). b) A normalised line intensity plot through the RBC shown for each of the excitation wavelengths - 543 nm (red), 514 nm (green) and 488 nm (blue).

Now, a RBC was imaged using the TartanSW multi-emission method with an excitation of wavelength of 514 nm and emission detection at 550-555 nm, 565-570 nm and 580-585 nm, respectively. Figure 4.12a a pseudo-coloured red, green and blue image which

were merged to create the RGB TartanSW multi-emission image for an RBC. However, the spectral fringes observed are very narrow and not as clear as the TartanSW multi-excitation RBC image in Figure 4.12a. This was apparent when comparing each detection channel in the intensity plot in Figure 4.12b, where there was very little spectral separation and intensity modulation between each of the TartanSW multi-emission channels.

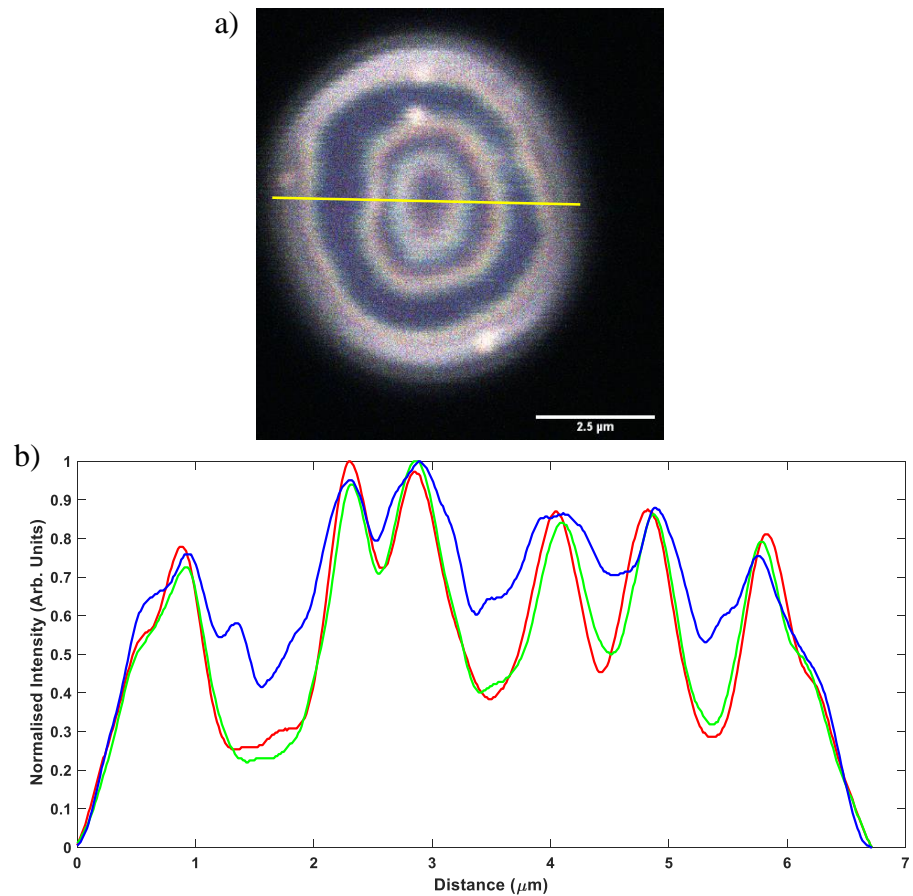


Figure 4.12 - A TartanSW multi-emission image of a healthy RBC adhered aluminium mirror (Laser 2000) with an 514 nm excitation wavelengths. Images were merged to create a merged RGB image in a). b) A normalised line intensity plot of the yellow line shown through the RBC each of the excitation wavelengths i.e. the 580-585 nm (red), 565-570 nm (green) and 550-555 nm (blue).

4.4.4 Confocal TartanSW multi-excitation and multi-emission imaging of MCF-7 cells

Next, I applied TartanSW multi-excitation and multi-emission imaging to a eukaryotic cell line; MCF-7 images were obtained using three excitation wavelengths at 543 nm, 514 nm and 488 nm. Here, it was possible to see the fringe structure created by each of the excitation wavelengths in the TartanSW images. I observed a fringe pattern around the outer edge of the cell, as each of the different excitation wavelengths intersected at different axial locations (Figure 4.13a). As before, each of the three channels were contrast adjusted and a lookup table of red, green and blue was applied to each image. The resultant merged RGB image had a spectral signature that resembled both the lens specimen and theoretical datasets. The normalised intensity plot taken through a region of the cell is shown in Figure 4.13b. It was observed that the banding structure for the SW anti-nodal planes in red, green and blue channels were spatially separated. Furthermore, notice that the spectral signatures began at the basal surface of the cell and the SW proceeds up the cell body, with loss in the spectral SW signature towards the centre of the cell body. Additionally, it was noticed that the spectral signature was observed on small cellular features. For example, at the outer edges basal surface, there were protrusions which were most likely to be the cell membrane around the filopodia.

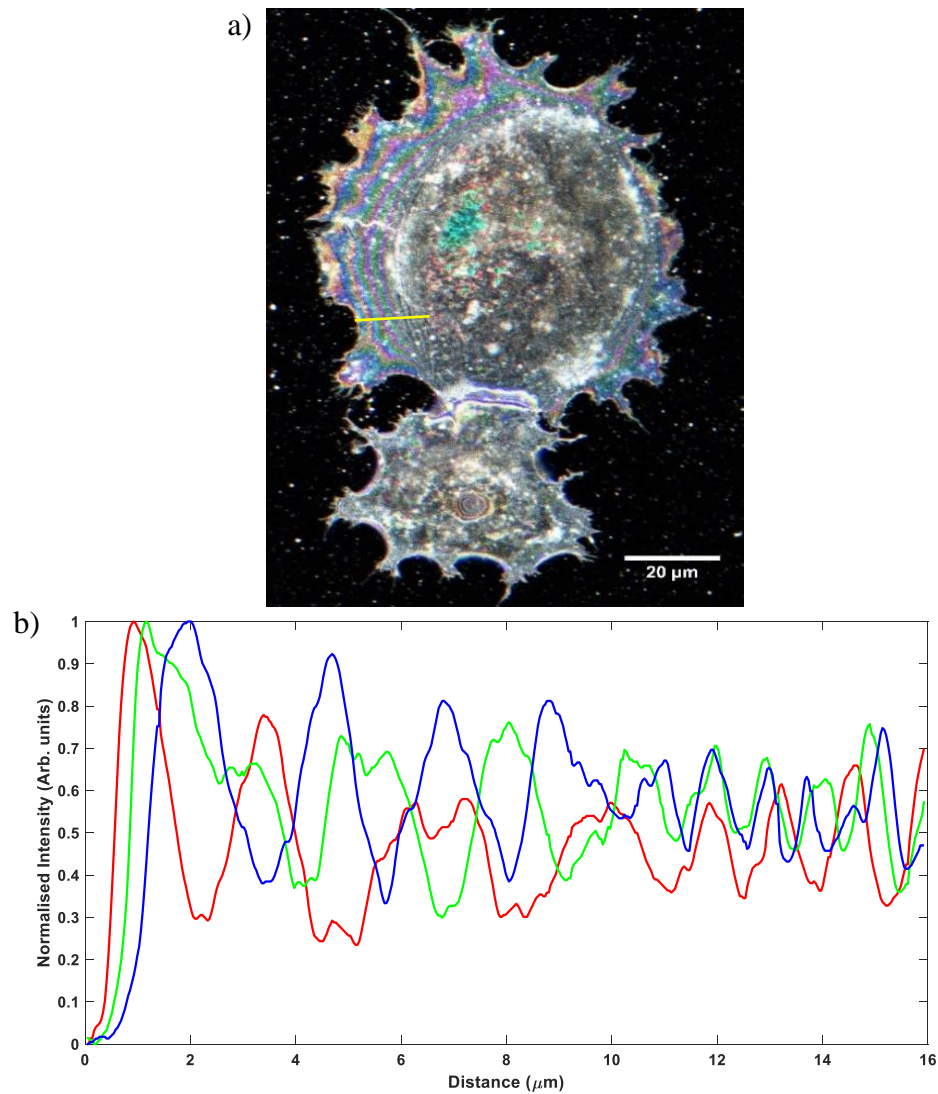


Figure 4.13 - A TartanSW multi-excitation image of a MCF-7 grown on an aluminium mirror (Laser 2000) with the three excitation wavelengths images merged to create a merged RGB image in a). b) A normalised intensity plot of the yellow line shown for each of the excitation wavelengths i.e. the 543 nm (red), 514 nm (green) and 488 nm (blue).

The application of TartanSW multi-emission was carried out on MCF-7 cells using an excitation wavelength of 514 nm with emission detection collected at 567-572 nm, 592-597 nm and 617-622 nm. Figure 4.14a the pseudo-coloured red, green and blue SW images were merged to create the RGB TartanSW multi-emission image of the MCF-7. Spectral banding was evident from the RGB MCF-7 image, also the spectral signature

appears to resemble the spectral signature of the simulated data (Figure 4.8b) and the lens specimen data (Figure 4.9d). However, in the intensity profile taken through a region of the cell (represented by the yellow line in Figure (4.14a), it was clear that the signal was very hard to differentiate from the background and saturated regions of DiI which is shown in Figure 4.14b. In addition, there was no notable intensity modulation that was expected in multi-emission imaging, despite the spectral signature observed in the RGB TartanSW multi-emission images shown in Figure 4.14a.

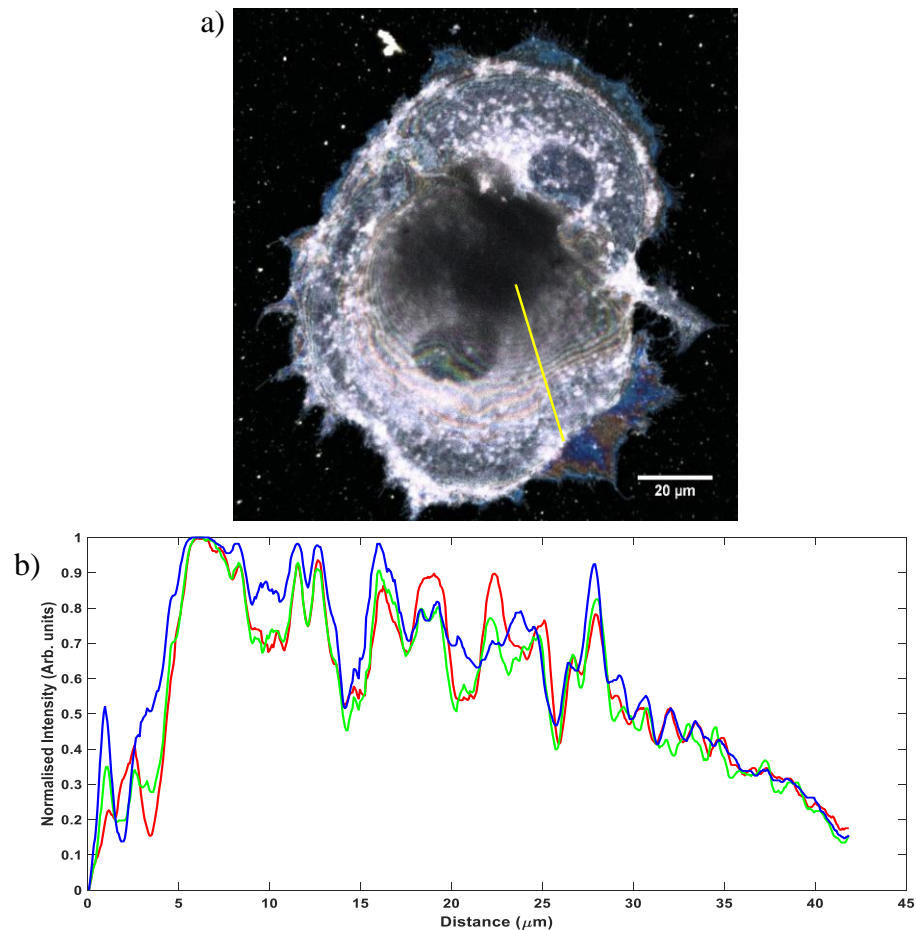


Figure 4.14 - A TartanSW multi-emission image of an MCF-7 cell grown on an aluminium mirror (Laser 2000) with a 514 nm excitation wavelength. Images were merged to create a merged RGB image in a). b) A normalised intensity plot of the yellow line which was shown for each of the emission wavelengths - 617-622 nm (red), 592-597 nm (green) and 567-572 nm (blue).

4.4.5 Simulated Difference SW method

Firstly, to characterise the DiffSW, I simulated SW excitation at 543 nm, 514 nm and 488 nm over the axial range of $z = 0$ to $5 \mu\text{m}$. To simulate the DiffSW method, I had taken the modulus of the difference, using Eqn. 4.7, between the 514-543 nm and 488-514 nm excitation wavelengths (MATLAB code shown in Appendix X). The result of the DiffSW method was an intensity profile shown in Figure 4.15. Note that the DiffSW intensity was minimal at points where the SW excitation wavelengths anti-nodal planes were near the mirror surface. This was because the relative excitation wavelengths were more in-phase. However, as the SW of green-red or blue-green became out-of-phase relative to one another, as in Figure 4.5b, the resultant DiffSW intensity becomes larger as shown in Figure 4.15. To quantify the FWHM of the DiffSW image, the *findpeaks* function was used in MATLAB and the theoretical FWHM for the blue-green and green-red was calculated as 79 nm and 84 nm, respectively.

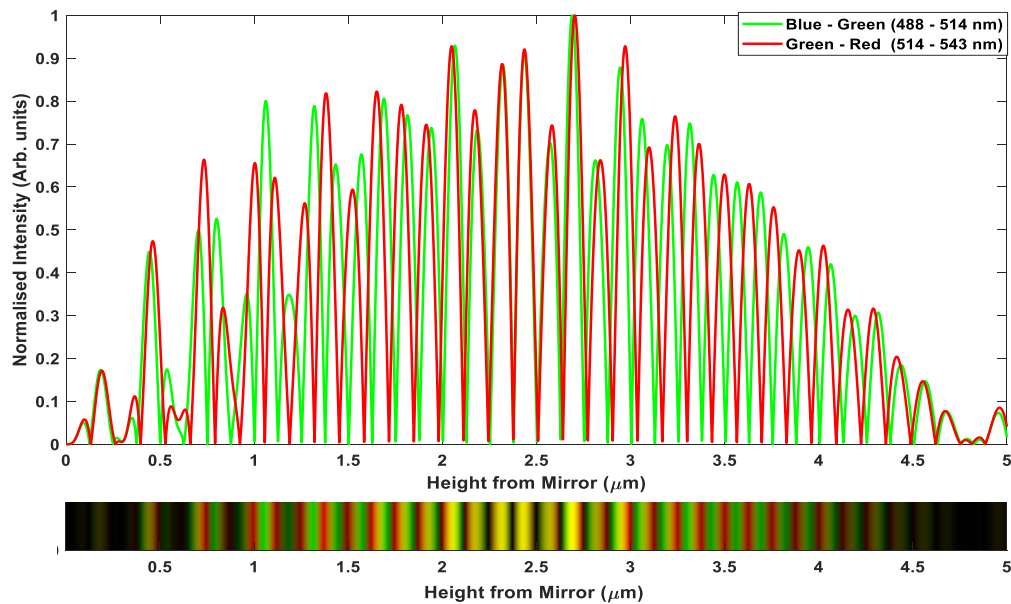


Figure 4.15 – The simulated DiffSW normalised intensity profile over an axial range of $z = 0$ - $5 \mu\text{m}$ for the green-red and blue-green DiffSW images. Below the merged pseudo-coloured red-green image generated using the TartanSW multi-excitation simulated intensity profile.

4.4.6 Application of the DiffSW method to experimental data

To verify the theoretical DiffSW, I used the TartanSW multi-excitation imaging of an $f = 48$ mm lens specimen, which was captured on a bare aluminum microscope slide at excitation wavelengths of 543 nm, 514 nm and 488 nm. In FIJI, each of the images was linearly contrast adjusted and a Gaussian blur of $\sigma = 2$ was applied. The absolute difference was taken using the image calculator in FIJI for the 514-543 nm (red) and 488-514 nm (green) channels which resulted in the images shown in Figure 4.16a and b, respectively. In the merged red-green (RG) image, the yellow regions corresponded to the locations where the anti-nodal planes from each SW difference image overlap. There are regions which corresponded to the greatest intensity difference between each channel (i.e. an anti-nodal plane overlapped with a nodal plane), which resulted in distinct red or green fringes. In Figure 4.16d, the DiffSW intensity profiles show very narrow and defined anti-nodal peaks with an amplitude modulation effect over the 5 μm axial range. This was also evident in the DiffSW images in Figure 4.16a-c. The FWHM of the anti-nodal planes was calculated for the experimental lens specimen as 79 ± 1 nm and 80 ± 3 nm, with a percentage error when compared to theory of 1% and 4% for the blue-green and green-red channels, respectively. Table 4.1 shows that the measured axial resolution in the 488 nm TartanSW multi-excitation provided a measured axial resolution of 126 ± 4 nm, which resulted in an ≈ 45 nm improvement in axial resolution using the DiffSW method.

Table 4.1 – A comparison of the measured axial resolution between the TartanSW multi-excitation and DiffSW methods. A $f = 48 \text{ nm}$ lens specimen was placed on a bare aluminum microscope slide and was the specimen used to obtain the axial resolution.

TartanSW multi-excitation	Axial Resolution (nm)	DiffSW	Axial Resolution (nm)
543 nm	153 ± 4	514-543 nm	80 ± 3
514 nm	143 ± 4	488-514 nm	79 ± 1
488 nm	126 ± 4		

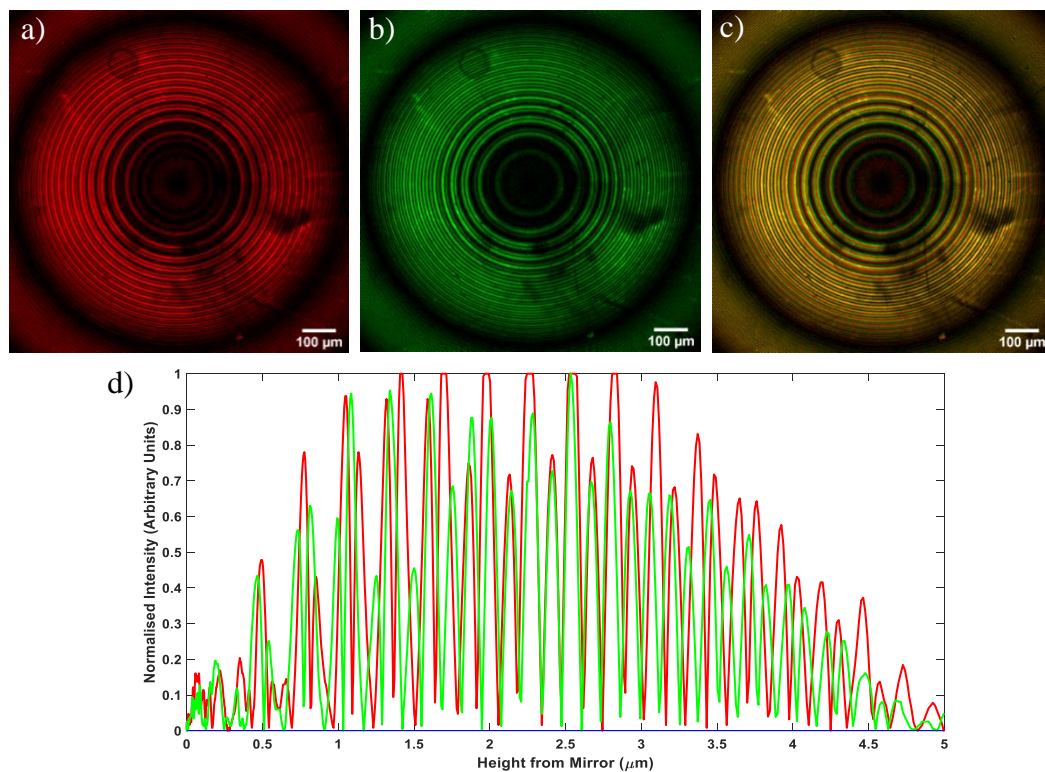


Figure 4.16 - DiffSW images of an $f = 48 \text{ mm}$ len specimen imaged on a bare aluminum microscope slide. Emission wavelengths were detected between 550-650 nm. In ImageJ, the absolute difference was calculated between the a) 514-543 nm, b) 488-514 nm and c) is the RG merged image of a) and c). d) An intensity profile from the centre of the image outwards was then translated from radial distance to axial height from the mirror.

Finally, DiffSW was applied to MCF-7 images captured at 543 nm, 514 nm and 488 nm excitation wavelengths. As with the lens specimen, the absolute difference was taken between the 514-543 nm and 488-514nm wavelengths to create a DiffSW image of the MCF-7 cell, as shown in Figure 4.17a and b. The merged RG DiffSW image of the MCF-7 was shown in Figure 4.17c. A very distinct fringe structure was observed. Additionally, much of the bright dye spots within the cell had been removed. Furthermore, a line intensity plot of the DiffSW through the MCF-7 is shown in Figure 4.17d. This demonstrated that DiffSW images produce very distinct SW peaks with much of the background signal removed when compared with TartanSW methods as shown in Figure 4.13b.

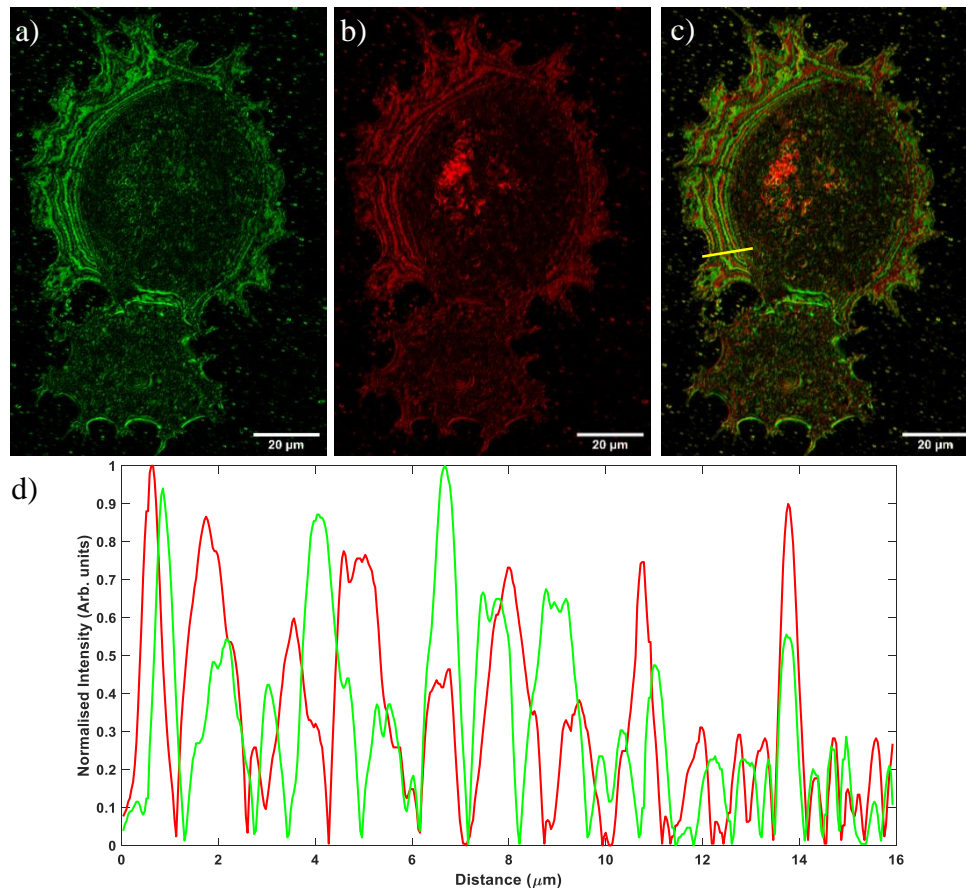


Figure 4.17 - DiffSW images of an MCF-7 imaged grown on an aluminium mirror (Laser 2000) with the emission wavelength was detected between 550-650 nm. In ImageJ the absolute difference between the a) 514-543 nm, b) 488-514 nm and c) A RG merged image of a) and c). d) An intensity profile was obtained from the yellow line.

4.5 Discussion

Previous SW methods utilised only a single wavelength to image the specimen of interest [13], [14], [72]–[74], [120], [122], [123], [145]. TartanSW is a method of SW imaging that can be utilised in two different distinct methods, multi-excitation and multi-emission imaging. To understand the theoretical behavior of the setup, I simulated the TartanSW multi-excitation with and without the contribution of the broad emission detection spectra (in this case 550-650 nm). It was observed that the banding SW structure had a modulation effect that was particularly evident with the 514 nm and 488 nm excitation, where the modulation occurred due to the presence of an emission SW. This modulation effect was not present in the simulation, where the emission contribution was not considered. The modulation effect was verified experimentally, using a bare aluminum microscope slide, where both the 514 nm and 488 nm excitation wavelengths showed the largest modulation effects. This modulation effect occurred at each axial locations where the fluorophore was excited. The modulation in intensity was observed due to the self-interference of the incident and reflected components of the emission wavelength [148]–[151]. However, this effect cancels out at axial locations far from the mirror surface when detected over a wide emission detection. In other words, the intensity distribution over all the emission wavelength components are spread out axially, reducing the modulation of the excitation SW intensity. [76].

TartanSW multi-excitation reduces the modulation gap because of the dependence of the relative phase relationship of the excitation wavelengths which intersect the specimen at different axial locations. The theoretically simulated data had a calculated modulation gap reduction of 34%, while the experimentally calculated modulation gap was 42%; an 8% difference. One reason for this disagreement, was that the simulation assumed homogenous fluorescence intensity over the emission detection range of 550-650 nm, which resulted in a larger intensity modulation in the final TartanSW multi-excitation simulation. In reality, the intensity of the light emitted by the fluorophore is

dependent on both the excitation and emission wavelengths selected in relation to the dye's spectra. As a consequence, it would be desirable to create a model which would account for the detection of fluorescent emission with intensity inhomogeneities, to produce a more accurate simulation of the TartanSW. The modulation gap could be further reduced by using a greater spectral separation between the excitation wavelengths, which would lead to quicker separation of the relative phases. However, the excitation wavelengths selected were limited to the excitation spectra available within the chosen fluorophore, and the excitation light sources available on the microscope system used. Therefore, it would be desirable to have a dye with a excitation spectrum that is as broad as possible. In contrast, for TartanSW multi-emission, there was no modulation gap reduction, this was due to only a single excitation wavelength being used, with the modulation in intensity which would only occur at regions within the anti-nodal planes generated by the excitation SW.

The TartanSW multi-emission approach utilised a narrow band emission wavelength detection which was simulated theoretically and compared to the experimental image captured using a bare aluminum microscope slide. It was observed that there was a strong beating pattern due to the intensity modulation, which is the difference between the stokes shift of the emission and excitation wavelength [72]. This was verified by comparison of the theoretical approach (Eqn. 4.4) which was a convolution of the excitation and emission SW [76], [77].

It was observed that with both the TartanSW multi-excitation and multi-emission, the mirrored substrate is a very important consideration when it comes to modelling the TartanSW method. Adjustments to the model would be require for the aluminum mirror (Laser 2000), which has a magnesium fluoride protective coating [152], which accounted for the average axial shift of $\Delta z \approx 285 \pm 1$ nm to the SW pattern. This offset is the spacer distance $\Delta z = nD$, where n is the refractive index of the spacer and D is the spacer thickness. In future, the spacer distance could be introduced into the theoretical model

as demonstrated by Swan et al. [148]. The Thorlabs broadband dielectric mirrors [153], resulted in a spectral signature which did not agree with the simulated TartanSW multi-excitation and multi-emission data sets. The axial offsets were different for each method that was used. Additionally, it was difficult to verify the spectral signature observed, due to the unknown materials and thickness used for the dielectric substrates.

The mirrored surface used was an important consideration to obtain an accurate simulation of the TartanSW methods. For both TartanSW methods, the aluminum mirror was a more suitable reflective surface, as the accuracy of inferring any quantitatively information extracted about a specimen's 3D geometry was dependent on the accuracy of the model TartanSW spectral signature. In contrast, the unknown structure of the dielectric mirror led to a spectral signature that could not be modelled, reducing the ability to extract meaningful axial height information. The ability to infer axial height directionality was evident with the TartanSW multi-excitation imaging of RBC, where there was a reversal in the red, green and blue ordering when compared to the model convex lens specimens, which is indicative of a concave surface. This may present an opportunity in future to utilise the spectral signatures to reconstruct a specimen without *a priori* knowledge. To do this, the relative spectral phase difference between the three excitation wavelengths could be used as a method to determine the axial height. Comparatively, the TartanSW multi-emission spectral intensity was not as prominent, this could be caused by the point spread function of the high NA objective lens used for RBC imaging. As a result of the high NA objective lens, the intensity modulation would not occur rapidly enough within the first three anti-nodal planes, and combined with the lack of separation between emission detection channels, the spectral signature would not be as apparent.

MCF-7 cells were utilised for eukaryotic cell imaging with our TartanSW method, which were stained with Dil, to obtain cell membrane information. Although the spectral radial data could not be translated to axial height, it was possible to use the spectral signature

to reveal qualitative axial height information about the cell structure for both TartanSW methods. However, the main advantage of TartanSW multi-excitation was the wide emission detection, which resulted in a higher intensity of fluorescent TartanSW signal captured. Whereas, the TartanSW multi-emission utilised only 5 nm wide detection channels, which resulted in poor contrast between the SW intensity and the background. As a result, it may be more difficult to utilise the TartanSW multi-emission to extract quantitative information about the specimen's geometry.

In previous studies, a excitation SW has been utilised to image between a reflective solid silicon and cell substrates to study cell adhesion in FLIC [76], [77]. Another method, SSIM, used a similar experimental set up, but detected the SWs generated over the range of the dye's emission spectrum. The SW emission intensity profile observed was dependent on the axial location of the fluorophore and a relative shift was observed in the emission profile at different axial heights. By calculating the axial shift at different lateral pixel locations over the detected emission wavelengths, the height of cell membrane from the substrate could be determined [148], [150], [151], [154]. However, these studies are confined to the basal surface of the cell, whereas the TartanSW method allows for the study of 3D information within the depth-of-field of the objective lens used.

SW microscopy has been used to contour map cell structure [72], [74], [120]. However, SW microscopy has not been used with the TartanSW multi-excitation approach which demonstrated a reduction in the modulation gap. Furthermore, the TartanSW technique allowed for the benefit of contour mapping of the cell and encodes additional information about the directionality of the cell geometry within the spectral signature. This could be particularly useful, as I had investigated if SW microscopy could detect morphological changes to the *P.berghei* iRBCs. However, due to the presence of the parasite within the RBC, the directionality of the iRBCs 3D geometry was ambiguous, and as a result difficult to extract. In future, TartanSW may provide a method to study the

iRBC and gain directional information about the 3D geometry that was not present when a single wavelength SW imaging was used.

DiffSW imaging is a method which can be used to improve the axial resolution of the TartanSW multi-excitation method. This has the benefit of being a post-acquisition technique which would require no additional setup to the existing TartanSW setup. DiffSW demonstrated a theoretical and experimental axial resolution of 79 nm, with a factor of ≈ 1.59 improvement over TartanSW multi-excitation imaging alone. DiffSW was also beneficial in that it removed any saturated intensities caused by fluorescent dye clumps which signals overlap in all the excitation wavelengths images, as they were subtracted out of the final DiffSW image. Furthermore, this has an additional benefit of removing the background signal that is homogenous over all excitation wavelengths. This resulted in a contrast improvement over the TartanSW multi-excitation method, which allows for better extraction of the intensity information than observed in the TartanSW images.

Previous work with RBCs in chapter 3, demonstrated that video-rate and time-lapse SW was possible using a wide-field epi-fluorescence setup. Therefore, it is possible to extend TartanSW and DiffSW methods to live cell imaging over time. This would be of particular interest to study dynamic events that cause morphological changes in the cell membrane over time, such as apoptosis [155], [156], cell migration [157] and mitosis [158], [159]. The application of TartanSW multi-excitation using a widefield epi-fluorescence setup, was faster and a more suitable method for live cell imaging, as a single colour SW image taking approximately 33 ms to capture. However, when using TartanSW multi-emission on widefield epi-fluorescence, this would require a complex multiple camera setup to collect all the desired emission wavelengths simultaneously. Or fluorescence emission dichroic filters would need to be changed in between each image, which would require a physical shift of the dichroic filters, either automatically or manually, producing slow multi-emission imaging. Furthermore, this would require that the cell events of interest

happen over the timescale of minutes rather than seconds for this to be a suitable technique. Using CLSM, both TartanSW methods were only suitable for capturing cell events that would be slower than 40s, due to the scanning nature of the CLSM. A three colour tartanSW multi-excitation image would take ≈ 2 minutes to capture and image, due to each image needing to be captured individually. Consequently, TartanSW multi-emission would be more suitable for capturing time lapse imaging using CLSM. This is due to the Leica SP5 CLSM which can simultaneously capture each multi-emission channel in a single image. As a result, it would take a third of the time to image using the TartanSW multi-emission method. However, the disadvantage of multi-emission over multi-excitation is the reduced fluorescent signal, due to the narrow band detection channels. As a result, higher excitation wavelength intensities would be required to increase fluorescence emission intensity compared to the multi-excitation method. Finally, there is still a need to develop a computational method which can utilise the spectral signature of the TartanSW multi-excitation method to create a 3D reconstruction of a specimen without *a priori* knowledge. This will be discussed in the next chapter.

4.6 Conclusion

In this chapter, I have compared the theoretical model for the TartanSW multi-excitation and multi-emission with a fluorescently label lens specimen placed on a bare aluminum microscope slide. The spectral signature observed was comparable between the theoretical model and experimental results. Furthermore, the spectral signature observed was dependent on the mirror surface used to generate the SW. This was due to the dielectric layer or protective coating on the mirrors surface which created an axial shift in the position of the anti-nodal planes position relative to the mirrored surface, and altered the spectral signature observed in the final TartanSW image. I demonstrated that a spectral signature was obtained by utilising both the TartanSW multi-excitation and multi-emission for imaging of both erythrocytes and eukaryotic cells stained with a

Dil. Lastly, by applying a post-acquisition technique on the TartanSW multi-excitation images, called DiffSW, the axial resolution of TartanSW multi-excitation method could be improved by ≈ 40 nm.

Chapter 5

A phase difference method for three-dimensional reconstruction of TartanSW multi-excitation images

In this chapter, I propose a phase difference method for the reconstruction of TartanSW multi-excitation data sets.

Firstly, I demonstrated that the simulated TartanSW multi-excitation data could be utilised to obtain axial height information from the phase difference between each of the excitation wavelengths used. The phase difference method was applied to 1D and 2D simulated lens specimen data to create an axial height reconstruction. The phase difference was calculated by extracting the phase angles with and without the implementation of a Hilbert transform. Next, the TartanSW multi-excitation data was captured using a lens specimen with a CLSM. This was done using two reflective surfaces, a bare aluminum microscope slide and a long pass filter (to suppress the emission components of the SW). When the phase difference reconstruction was applied to the experimental lens data, I demonstrated that for the bare aluminum microscope slide, the axial reconstruction was poor. This was thought to be because of the poor theoretical extraction of the phase difference relationship with respect to axial height. Lastly, a long pass filter was used, and the axial height reconstruction followed the profiles of the theoretical lens specimen. However, oscillations were present in the final reconstruction, which were thought to be due to Gibbs ringing from the application of a Hilbert transform to extract the wrapped phase angles.

5.1 Introduction

As shown in Chapters 2 and 3, multi-planar SW imaging was used to contour map specimens using a single wavelength of light to gain an insight in to the geometry of a specimen [72], [74]. However, single wavelength multi-planar SW microscopy led to ambiguity of the specimen geometry which made it difficult to extract geometric information without *a priori* knowledge of the specimen. In Chapter 4, I used TartanSW multi-excitation, with three different excitation wavelengths, which spectrally encoded information about the axial height of the specimen. In TartanSW multi-excitation microscopy, the TartanSW spectral signature observed was caused by the relative phase

relationship between each excitation wavelength along the optical axis (axial height). This phase method differs from the binarisation method on how it extracts axial information. For example, in binarisation, as the known axial locations from the SW profile were required to create a reconstruction, assumptions were made about the specimens geometry. By extracting the FWHM of the SW profile as was described in Chapter 3, a 3D reconstruction of the specimen could be created. However, *a priori* knowledge was required. In contrast, by using the TartanSW multi-excitation technique the phase relationship between each excitation wavelength could be used to give more precise axial height information about the specimen geometry over the whole SW intensity profile, and not just at the FWHM locations of the SW anti-nodal planes. As a result, the axial position would be dependent on the phase difference between the excitation wavelengths. Therefore, the spectral signature would be consistent for any modulation in the lateral (x,y) distance which would be observed due to the unknown specimen geometry. Lastly, as the fixed position of the mirror has the condition that for each wavelength the first nodal plane must occur at the mirrored surface ($x = 0$), this allows for a reference point that can be used to determine absolute axial height locations.

In this Chapter, I present a method which used the phase difference between the TartanSW multi-excitation wavelengths, as a method to reconstruct the height of a lens specimen without the application of *a priori* knowledge to the reconstruction. For waveforms that could be easily mathematically described, such as the theoretical SW, the phase information could be extracted. As a result, the theoretical phase difference was then calculated as a function of axial height. In contrast, to extract the phase information from the 2D projection of the TartanSW multi-excitation which has intersected an unknown geometry was more difficult. This was because the 2D projection of the SW waveform observed was dependent on the geometry of the unknown specimen. Thus, it was difficult to describe the unknown waveform

mathematically. As a result, this required a method to extract the phase of the SW waves in a 2D image without knowledge of the 3D structure.

5.1.1 Phase retrieval from known waveforms

Phase is a property of a wave that describes an (instantaneous) point in the position or time of a waveform over a cycle i.e. 0 to 2π radians [3]. In general, for two waves, with and without a $\pi/2$ phase shift, (Figure 5.1) could be defined as:

$$y = \sin(kz) \quad (5.1)$$

$$x = \sin\left(kz - \frac{\pi}{2}\right) = \cos(kz) \quad (5.2)$$

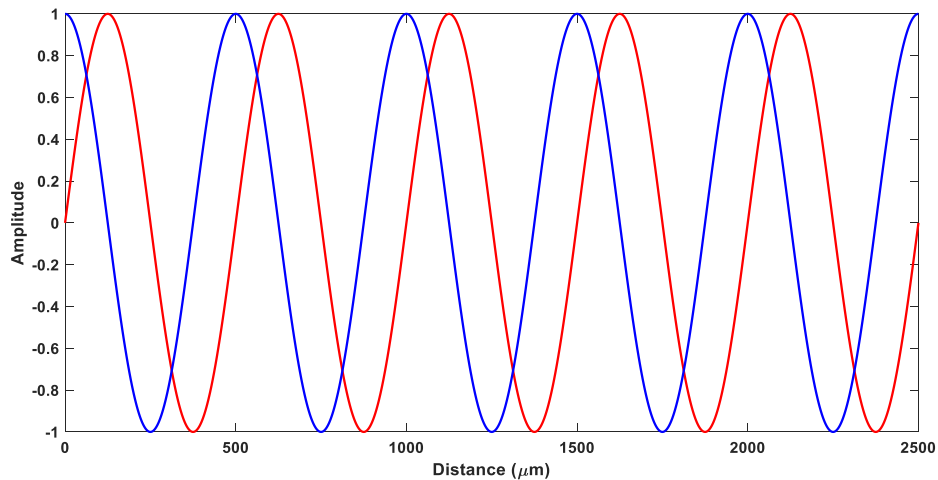


Figure 5.1 – This graphs shows the phase shift of $\pi/2$ which was introduced by creating an artificial phase shift. The red wave is defined as $\sin(kz)$ and the blue wave is $\cos(kz)$.

Now that two waves had a relative phase offset of $\pi/2$, it was possible to calculate the instantaneous phase angle (θ) of the waveform shown in red in Figure 5.2. By using the trigonometric relationship, the phase angle could be obtained mathematically from the two waveforms in Eqn. 5.1 and Eqn. 5.2, which gives:

$$\theta = \arctan2[x, y] \quad (5.3)$$

The arctan2 function was used to calculate the phase angle beyond the interval of $[-\pi/2, \pi/2]$ and thus over the full trigonometric range of a unit circle i.e. $[0, 2\pi]$ [160]. The result of Eqn. 5.3 is a wrapped phase angle, as shown in Figure 5.2a, where a sawtooth was formed with discontinuities of 2π . In principle, the unwrapping was achieved by looking for a region with $> \pi$ discontinuities, where a value of 2π was added onto the previous value to create an unwrapped phase angle [161]–[163]. By application of phase unwrapping to the wrapped phase in Figure 5.2a, the result is a linear function of the instantaneous phase of the waveform with position, as shown in Figure 5.2b. This approach is suitable for known waveforms which could be described theoretically, where a phase shift could be applied. However, for the TartanSW multi-excitation waveform which has an unknown mathematical description, due to the projection of the SW on to the 2D lateral plane, another method is required to calculate the instantaneous phase angle.

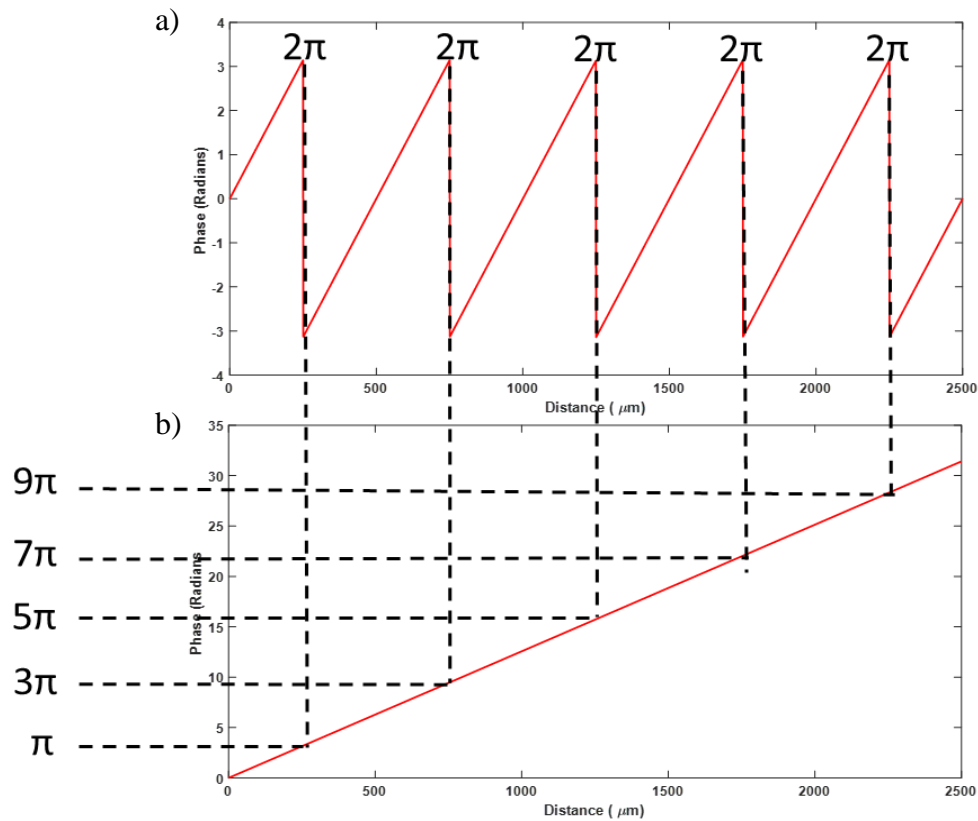


Figure 5.2 – The figure above shows the principle of phase unwrapping at phase discontinuities. a) A phase wrapped representation of the waveform in Figure 5.1. with discontinuities which correspond to 2π intervals. Thus, unwrapped was achieved by adding 2π to the previous known value resulted in a linear unwrapped phase as shown in b).

Phase unwrapping has been used in imaging and is common in digital holographic techniques. In digital holography techniques two images are obtained, a specimen and reference image, and from this the phase images could be extracted, which has the thickness of the specimen encoded within it [164]–[166]. This has been achieved using a single-wavelength to determine the thickness of a RBC [167]. However, to remove 2π phase ambiguity of the single wavelength approach, multiple wavelengths have been applied. The phase extracted images of each wavelength are subtracted to create a larger region of unambiguity [165]. This technique has been applied to test targets and spherical mirrors, as a method to characterise the height reconstructions [164]. In the

application of dual and multi-wavelength digital holography, it has been used to create height reconstruction from the phase images for onion cells [168], SKOV-3 ovarian cancer cells [165], KB cells [169] and WM-115 malignant melanoma cell line [170].

5.1.2 Hilbert transform for phase retrieval

The complex analytic signal was formalised by Gabor [171] for time-varying fields. However, the spatial domain was analogous to the time-varying analytical signal. Thus, the spatial analytical signal $z(x)$ is defined as:

$$z(x) = z_r(x) + iz_i(x) \quad (5.4)$$

where $z_r(x)$ is the real valued component and $z_i(x)$ is the imaginary component of the analytical signal. In particular, the relationship between the real and the imaginary parts of a complex analytic signal could be related through the Hilbert transform. Thus, the analytical signal is written as [172]:

$$z(x) = z_r(x) + i \frac{1}{2\pi} \int_{-\infty}^{\infty} \frac{z_r(x')}{x-x'} dx' \quad (5.5)$$

where, the integral $\frac{1}{2\pi} \int_{-\infty}^{\infty} \frac{z_r(x')}{x-x'} dx'$ describes the Hilbert transform of the real-valued component, $z_r(x)$, which resulted in an imaginary component z_i . Commonly, the analytical function is used to retrieve information about a signal such as: instantaneous amplitude, instantaneous frequency and instantaneous phase [171]. This is due to the inherent phase shift between the real and complex planes of $\pi/2$. Thus, the instantaneous phase φ , is calculated from the analytical signal using the following expression:

$$\varphi(x) = \tan^{-1} \frac{Im(z(x))}{Re(z(x))} \quad (5.6)$$

The result of eqn. 5.6 was a wrapped phase angle as shown in Figure 5.2. The Hilbert transform has been utilised in quantitative phase microscopy in the form of Hilbert phase microscopy (HPM) [172]–[174]. Hilbert phase microscopy has been used as a method to extract quantitative phase information by using an off-axis interferometric setup to

capture phase information in a single shot image. A Hilbert transform was utilised to extract the phase information and calculate the subsequent optical path length differences, using a Mach-Zehnder interferometric set up. Hilbert phase microscopy has been applied to RBC imaging [173], due to the relative homogeneity of the refractive index across the RBC. Therefore, the optical path lengths differences could be obtained from the phase information and in-turn the axial height of the specimen was calculated.

By the application of phase unwrapping algorithms alongside the Hilbert transform, the unwrapped phase angles for each TartanSW excitation wavelength could be obtained. As only a single SW intensity profile was needed for each of the excitation wavelengths, additional images shifted by $\pi/2$ were not required to obtain the wrapped phase angles. Thus, a Hilbert transform was a suitable method that could be applied to the TartanSW multi-excitation to retrieve the phase information, as this was a major requirement for the phase difference method to be applicable to specimens with unknown geometries.

5.2 Methods

5.2.1 Lens preparation and confocal imaging

The procedure for the preparation of Dil fluorescently coated lens specimens was carried out as described in Chapter 2.2.1. A $f = 48$ mm lens specimen was placed on two reflective substrates: a bare aluminum microscope slide (TS-AL-134, Dynasil) and a 550 nm long pass filter (FEL0550, Thorlabs) which transmitted the emission wavelength, thus preventing the formation of an emission SW. Images were captured using a Leica SP5 DM600 CLSM with a HCX PL FLUOTAR 5.0x 0.15 dry objective lens. Three excitation wavelengths were selected at 543 nm, 514 nm and 488 nm and the emission was collected between 550-650 nm. Images were captured with an image size of 2048 x 2048 pixels at a scan speed 100 Hz with a 3-frame average. A digital zoom of 2.01x was applied to the image during acquisition.

5.2.2 Phase method for three-dimensional reconstruction of line profile

The method proposed was as follows: Firstly, the data was simulated for an SW which was calculated using Eqn. 4.1 in MATLAB. This was done for the three excitation wavelengths of 543 nm, 514 nm and 488 nm. Next, a phase shift of $\pi/2$ was applied and implemented into the SW excitation equation as follows:

$$I_{ex}(z) = 1 - \cos\left(\frac{4\pi}{n\lambda_{exc}}z - \frac{\pi}{2}\right) \quad (5.7)$$

Using Eqn 5.7 and the *atan2* function a wrapped phase map was created. Next, phase unwrapping was done to generate a linear phase relationship from the wrapped phase map. This was achieved by using the *unwrap* function, which identified discontinuities of π jumps between the neighbouring phase angles and added a value of 2π to the corresponding phase angle, as was shown in Figure 5.2. For each of the three phase unwrapped excitation wavelengths, the absolute difference was calculated between the unwrapped phase angles for the 488-514 nm and the 514-543 nm. A first order polynomial fit was applied, as height as the function of absolute phase difference, and is given by:

$$z(\varphi) = m\varphi + c \quad (5.8)$$

where z is the axial height from the mirror, m is the gradient, c is the y-intercept and lastly φ is the absolute phase difference (MATLAB code shown in Appendix XI).

5.2.3 Phase method for three-dimensional reconstruction of line profile

An $f = 48$ mm specimen data set was simulated in MATLAB, using Eqn. 2.1., over a radial range of $R = -349 \mu\text{m}$ to $349 \mu\text{m}$. For the experimental lens specimen TartanSW multi-excitation RGB images, a line intensity from the centre outwards was taken using the

improfile in MATLAB, and each of the excitation wavelengths (543 nm, 514 nm and 488 nm) were stored in the red, green and blue channels of the RGB image.

For both the simulated and real lens specimen, the data was normalised from -1 to 1, due to the requirement of the *Hilbert* function within MATLAB. Next for an arbitrary waveform, an analytical signal was required, and was obtained using the *Hilbert* function. The *Hilbert* function works by implementing a fast Fourier transform (FFT) on the input values, and convolved the input data with a Heaviside step function to remove the negative frequencies. Then by taking the inverse FFT transform of the signal, the result was an analytical signal. Here, the analytical signal was represented by a real component and an imaginary component as in Eqn. 5.5. Due to the $\pi/2$ phase shift from the real and imaginary components, and by using the *atan2* function from eqn. 5.3, the wrapped phase angles were calculated. As before, phase unwrapping was required and done by using the *unwrap* function. The unwrapped angles were obtained and the phase difference was calculated between the 514-543 nm and 488-514 nm excitation wavelengths. The phase difference data was used to interpolated the axial height using Eqn. 5.8 (MATLAB code shown in Appendix XII).

5.2.4 Phase difference method for 3D Reconstruction of 2D simulated TartanSW multi-excitation data

As shown in Chapter 2.2.6, simulated 2D image data set for the theoretical excitation SWs of 543 nm, 514 nm and 488 nm was carried out. This was done over a radial range of $R = -349 \mu\text{m}$ to $349 \mu\text{m}$ for an $f = 48 \text{ nm}$ lens specimen.

For the 3D reconstruction of the 2D image data set, the phase shift was calculated in a similar method as section 5.2.2, but over the 2D image. For the Hilbert transformation of 2D simulated data sets, several changes were required. The *Hilbert* function had to be called twice, to create a Hilbert transform for the row and column of the image. This was achieved by transposing the matrix (' transpose operation in MATLAB) and a *Hilbert*

function was called within the another *Hilbert* function e.g. $Hilbert(Hilbert(\theta))'$. Next, the wrapped phase angles were unwrapped by calling the *unwrap* function twice. To unwrap the phase angles, the *unwrap* function had to be utilised for both the rows and columns of the matrix. For example, consider a phase angle matrix, θ , the *unwrap* function was called as follows: $unwrap(unwrap(\theta,[],2),[],1)$. This first calculates the unwrap along the rows, using the inner *unwrap* function then, again, for the columns using the outer *unwrap* function. The procedure to create a reconstruction was now repeated, as above, to generate a 3D reconstruction of the 2D simulated lens specimen using the phase difference method (MATLAB code shown in Appendix XIII).

To compare the interpolated axial height from the phase difference method, the difference between the theoretical lens reconstruction and the interpolated axial height was calculated. The mean axial height difference was calculated for the interpolated and theoretical the axial height values, along with the corresponding std. dev.

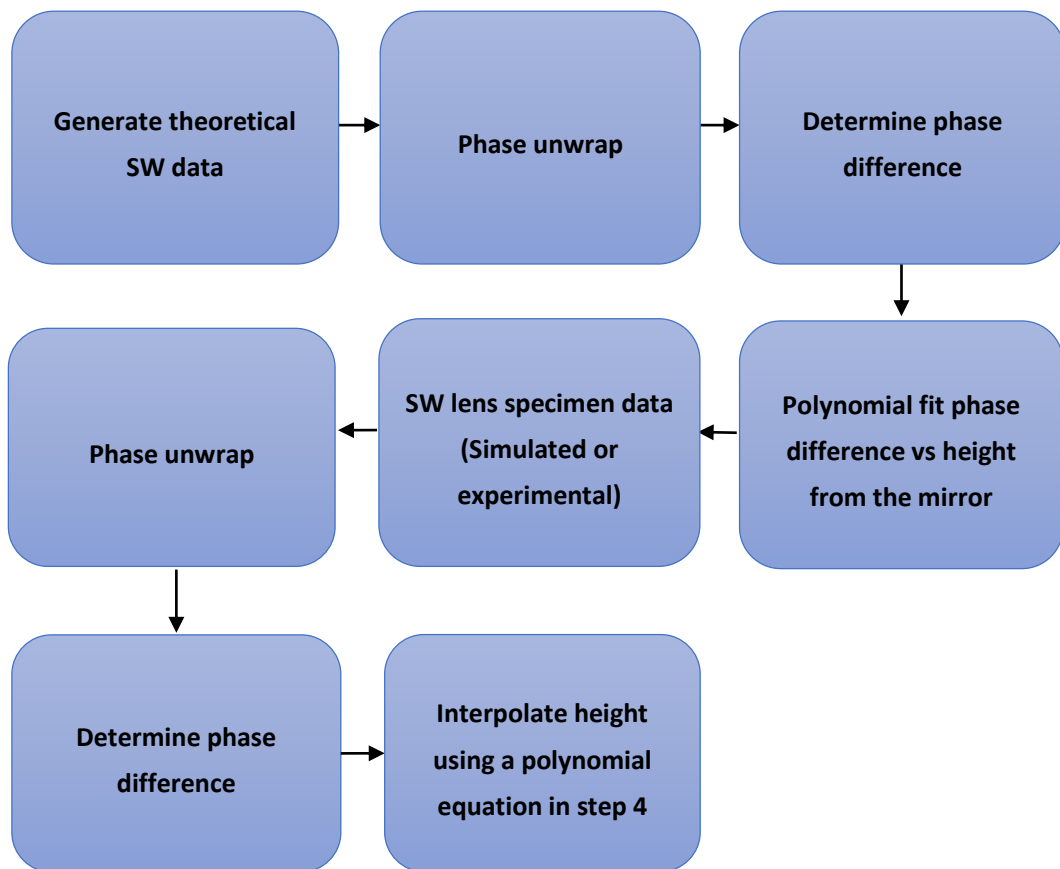


Figure 5.3 - A flowchart of the key computational step to reconstruct the TartanSW multi-excitation images using the phase difference method.

5.3 Results

5.3.1 A theoretical phase difference vs axial distance

Before the phase difference method could be applied, it was required that there was a method to interpolated axial height from the mirror surface as a function of phase difference between the 514-543 nm and the 488-514 nm wavelengths. This method was described in section 5.2.2. The three excitation SWs were generated, using Eqn. 4.1, Additionally, three excitation SW with a $\pi/2$ phase shift was simulated. The wrapped phase for each of the excitation SW wavelength, calculated using Eqn. 5.3, is shown in Figure 5.4. From Figure 5.4, it is shown that there was a relative phase relationship that changed between each excitation wavelength over the height range. As expected, once a 2π phase occurs within the SW propagation, there were discontinuities which created a sawtooth waveform over the axial distance.

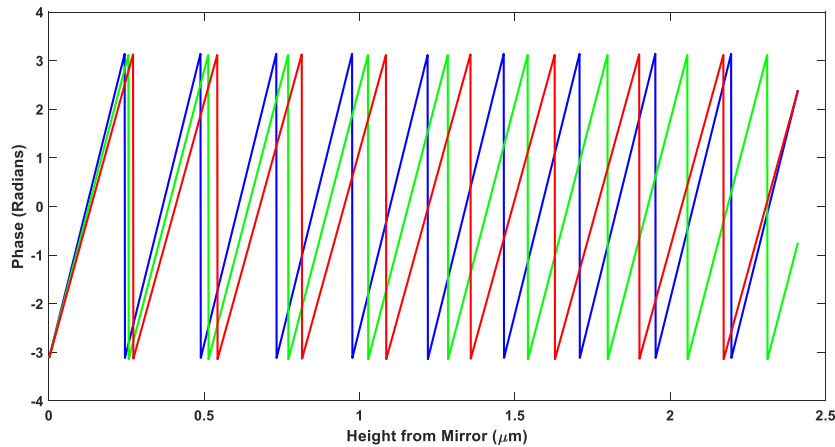


Figure 5.4 - Wrapped phase of simulated SW data for 543 nm, 514 nm, 488 nm excitation wavelengths used in the TartanSW data obtained using Eqn. 5.3.

Next, the wrapped phase needed to be unwrapped such that it was non-repeating. This was done in MATLAB using the *unwrap* function, which added additional phase of 2π at the discontinuities. In Figure 5.5a, a linear phase relationship was observed as a function of height from mirror. Where the shorter the excitation wavelength used, the steeper the gradient between the phase angle and height from the mirror. Thus, for each of the excitation wavelengths, the phase angle diverges from one another over the axial range. Next, the phase difference was calculated between 514-543 nm and the 488-514nm wavelengths, to produce an expression for two axial distance as a function of phase difference as shown in Figure 5.5b.

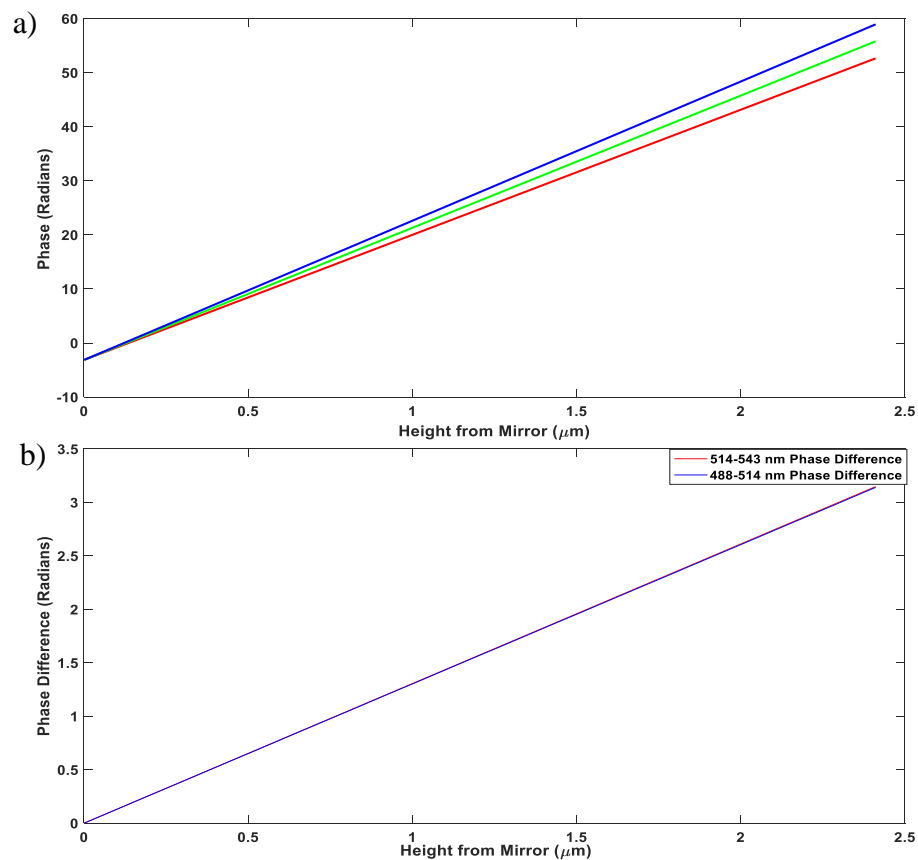


Figure 5.5- Simulated TartanSW data for - a) The phase unwrapped angles plotted against distance z from the mirrored surface using Eqn. 5.4. b) The phase difference between the 514-543 nm (red) and 488-514nm (blue) against axial distance from the mirror.

Finally, a linear fit was applied to the axial height vs phase difference, as shown in Figure 5.6. This resulted in an expression which was utilised to calculate the unknown axial distance for each of the 514-543 nm and 488-514 nm, using the known phase difference. The linear fit was given as, $Z(\varphi) = 77 \times 10^{-9} \varphi + 0$ for the 488-514 nm and this expression could be applied to simulated and experimental data for a $f = 48$ mm lens specimen. As a result, the axial height from the mirror was calculated using the phase difference values.

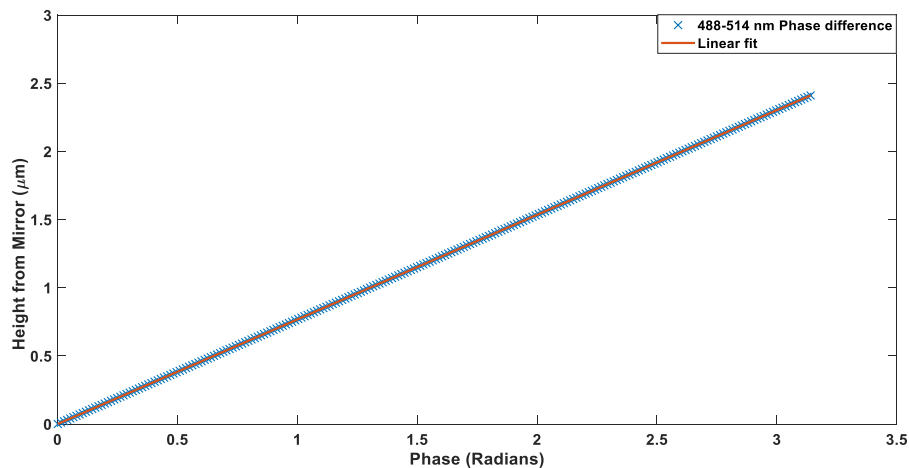


Figure 5.6 - Simulated TartanSW data with a linear fit applied to the phase difference method that interpolates the height from the mirror as a function of phase difference.

5.3.2 A 3D phase difference reconstruction of simulated $f = 48$ mm lens specimen

To test the phase difference reconstruction method, a data set was simulated for a $f = 48$ mm lens specimen. Three excitation wavelengths of 543 nm, 514 nm and 488 nm were simulated in MATLAB, using Eqn. 2.1. A radial dependent data set was simulated over a radial range of $-346 \mu\text{m}$ to $346 \mu\text{m}$. Now, a theoretical representation of the $f = 48$ mm lens specimen had been generated with a radial dependence, which was an idealised representation of the data that would be extracted from an experimental

TartanSW multi-excitation lens specimen data set. Using the methods outlined in section 2.2.1, the simulated radial TartanSW phase was determined using MATLAB's inbuilt function *Hilbert*, which calculated the Hilbert transform of the simulated data. The resultant real and imaginary components of the Hilbert transform was used to calculate the instantaneous phase angles which was shown in Figure 5.7a. The instantaneous angle was plotted against radial distance and there was a non-linear dependence on the radial distance, with the phase discontinuities at 2π phase boundaries, as was expected. Phase unwrapping was carried out on the data in Figure 5.7a, which resulted in unwrapped phase angles for the 543 nm, 514 nm and 488 nm wavelengths shown in Figure 5.7b. When compared with the Figure 5.5a, where there was a linear relationship, Figure 5.7b showed a relationship that was non-linear due to the radial dependence on the radius of curvature of the simulated lens.

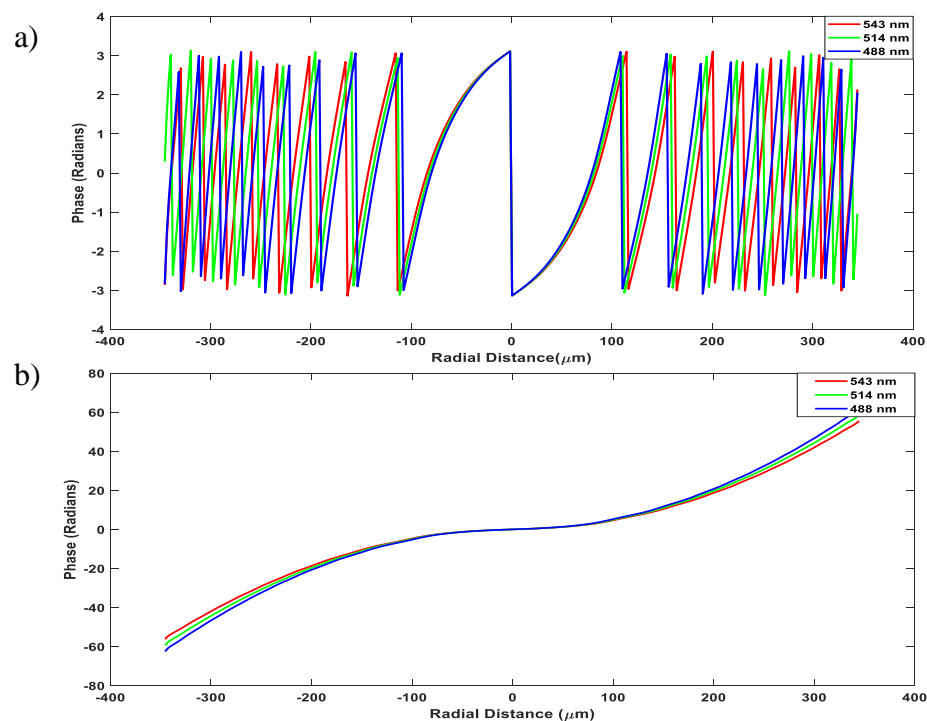


Figure 5.7 - Simulated $f = 48$ mm TartanSW data sets. a) The wrapped phase of the calculated using a Hilbert transform b) The unwrapped phase of which was determined using the *unwrap* function in MATLAB.

Now, using Eqn. 5.8, the absolute phase difference was calculated for the 488-514 nm and the 514-543 nm channels and shown in Figure 5.8. A convex profile was observed which resembled the profile of the lens specimen, with the presence of oscillations using the phase difference method.

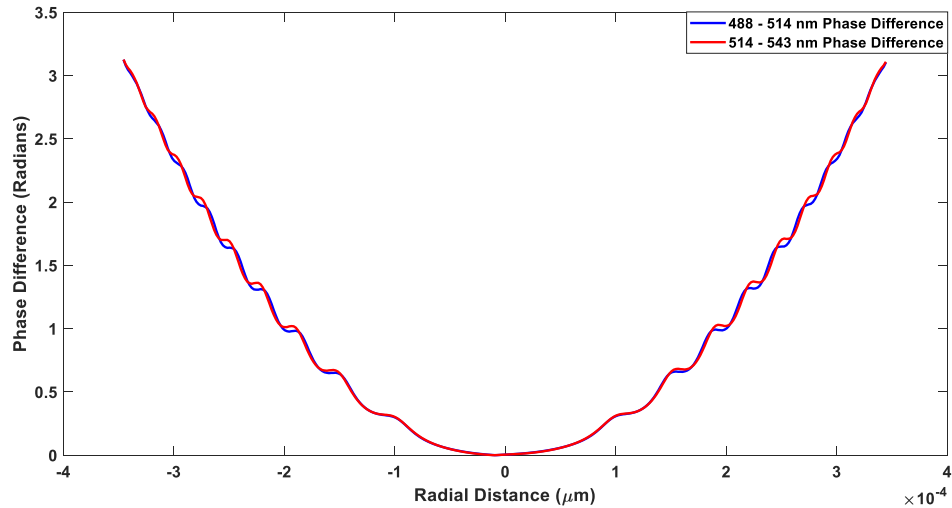


Figure 5.8 – The phase difference against radial distance applied for the two-colour phase difference of 514-543 nm and 488-514 nm.

Finally, to create a reconstruction of the simulated $f = 48$ mm lens specimen, Eqn. 5.6 which related the axial height to phase difference was used. Now, each of the phase difference locations for the 514-543 nm and 488-514 nm was interpolated using Eqn. 5.6. In Figure 5.9a and b, there were clear oscillations in the reconstruction of height from the mirror and radial distance. For both the 514-543 nm and 488-514 nm, the mean axial difference was calculated as 0.10 ± 24.34 nm and 0.04 ± 25.50 nm, respectively. These oscillations become less prominent at larger values above $1.5 \mu\text{m}$, and lower values below $0.25 \mu\text{m}$.

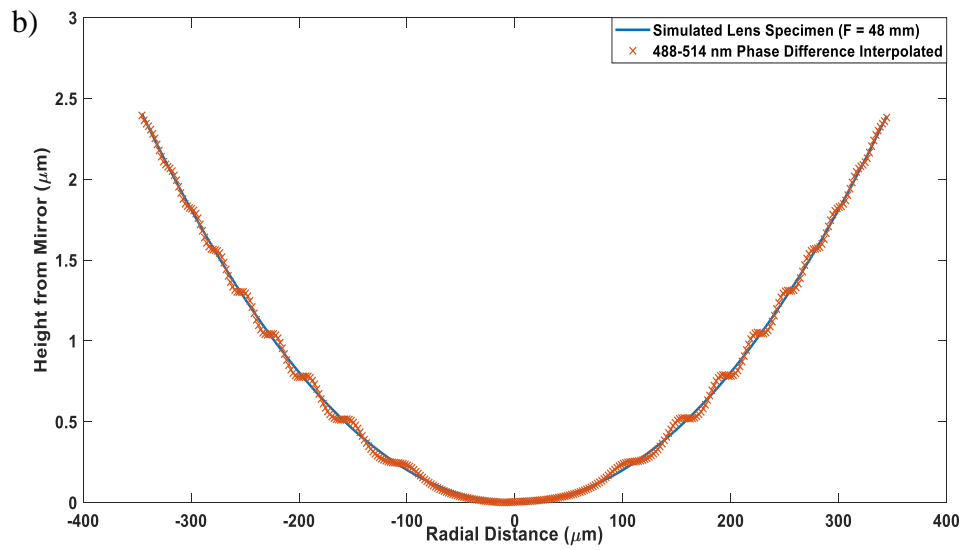
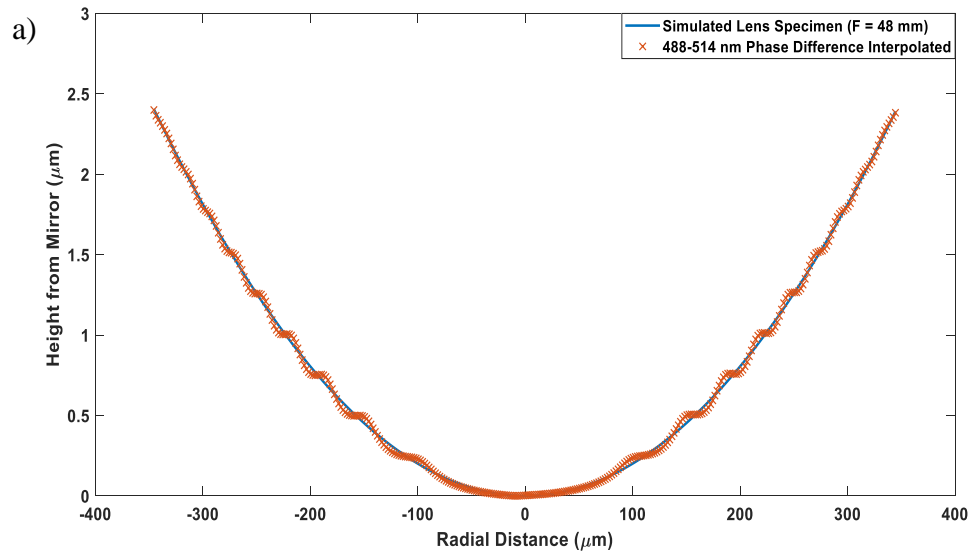


Figure 5.9 – An axial height from the mirror reconstruction for a simulated $f = 48$ mm phase difference method where the phase angles were extracted using the Hilbert transform for a) 488-514 nm and b) 514-543 nm.

To investigate the origin of the oscillations, the procedure above was repeated for simulated data. To achieve this, a $\pi/2$ phase shift was introduced to each of the excitation wavelengths. Therefore, in MATLAB, the Hilbert transform was not used to calculate the instantaneous phase, and instead Eqn. 5.3 calculated the instantaneous phase. The phase difference method was applied and the axial heights were interpolated using Eqn. 5.8. Figure 5.10 shows no oscillations were present when compared to the clear oscillations present in Figure 5.9a and b. As a result, it was apparent that the oscillations present were due to the application of the Hilbert transform to obtain the instantaneous phase angles of an arbitrary function.

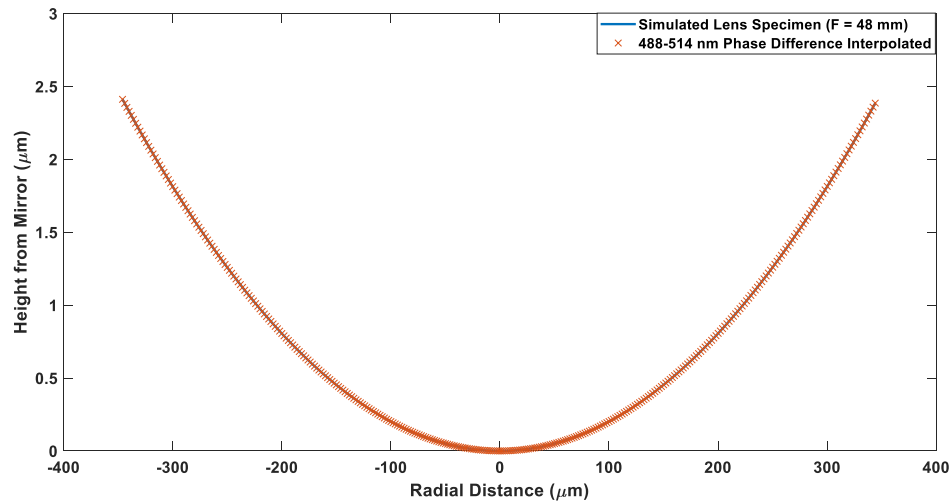


Figure 5.10 - A phase reconstruction of the axial height from the mirror using the radial distance of a $f = 48$ mm lens specimen. The phase angles were calculated using eqn. 5.3 opposed using a Hilbert transform.

Lastly, as it was clear the oscillations were present in the Hilbert transform data and not the phase shifted data. I demonstrated the effect of the Hilbert transform on a theoretical data set, where a 488 nm excitation wavelength was simulated over an axial range of 2.5 μm in MATLAB, using Eqn. 5.6, and the *hilbert* function was applied to the data. In Figure 5.11, the real and imaginary components of the Hilbert transform were plotted. It was observed that the effect of the Hilbert transform was that the imaginary

component (in orange) was shifted from the real valued wave (in blue). Furthermore, the imaginary component of the analytical signal was poor at the discontinuities of the boundaries of the waveform.

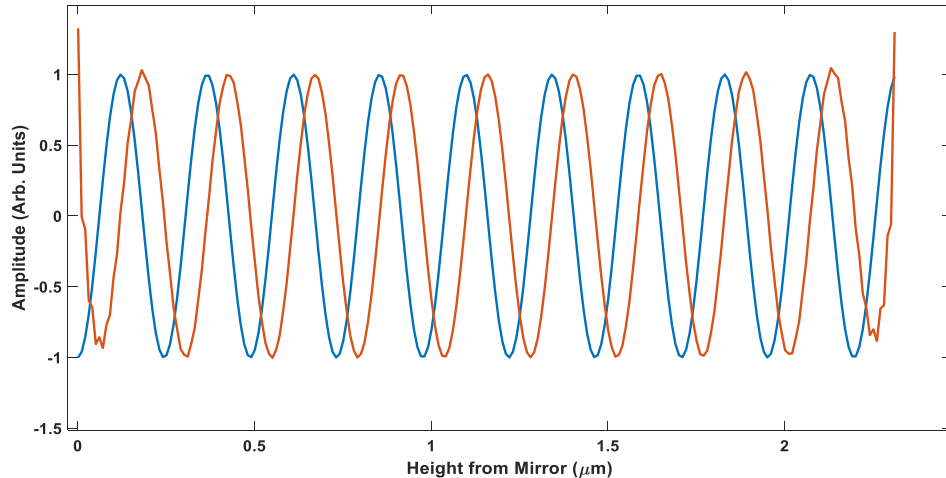


Figure 5.11 – A theoretical simulation of 488 nm excitation wavelength over an axial range of 2.5 μm . The real (blue) and imaginary (orange) components of a Hilbert transform was shown for the hilbert function applied in MATLAB.

5.3.3 A 3D phase difference reconstruction of simulated $f = 48$ mm lens specimen

To compare how effective the phase difference method was for a reconstruction of a 2D image, an $f = 48$ mm was simulated to produce a 2D image which was generated using Eqn. 2.1 as described in section 5.2.3. This was done for a phase difference between the 514-543 nm and the 488-514 nm excitation wavelengths.

Firstly, a comparison of the phase shift of $\pi/2$ was generated and the phase angles were calculated. The resulting phase map is shown in Figure 5.12a. The phase angle was represented in a greyscale map, where black is $-\pi$ and white is π . The regions where the white and black rings concede represent the phase boundaries with a 2π phase discontinuity. This was analogous to sawtooth profile of the wrapped phase of the

simulated lens specimen in Figure 5.7a. In the phase map, there were concentric fringes of repeating phase boundaries as shown in Figure 5.12a. Now, the unwrapped phase boundaries were calculated using the *unwrap* function, as described in section 5.2.4. The 2D unwrapped phase was shown in Figure 5.12b. A colourmap was applied to represent the unwrapped phase angle and it was observed that there was a smooth relationship between the 2D reconstruction of the phase angles from the centre outwards. The height from the mirror was interpolated using Eqn. 5.8, where a 3D reconstruction of the lens specimen was shown in Figure 5.12c, which was an accurate representation of the 3D theoretical lens specimen.

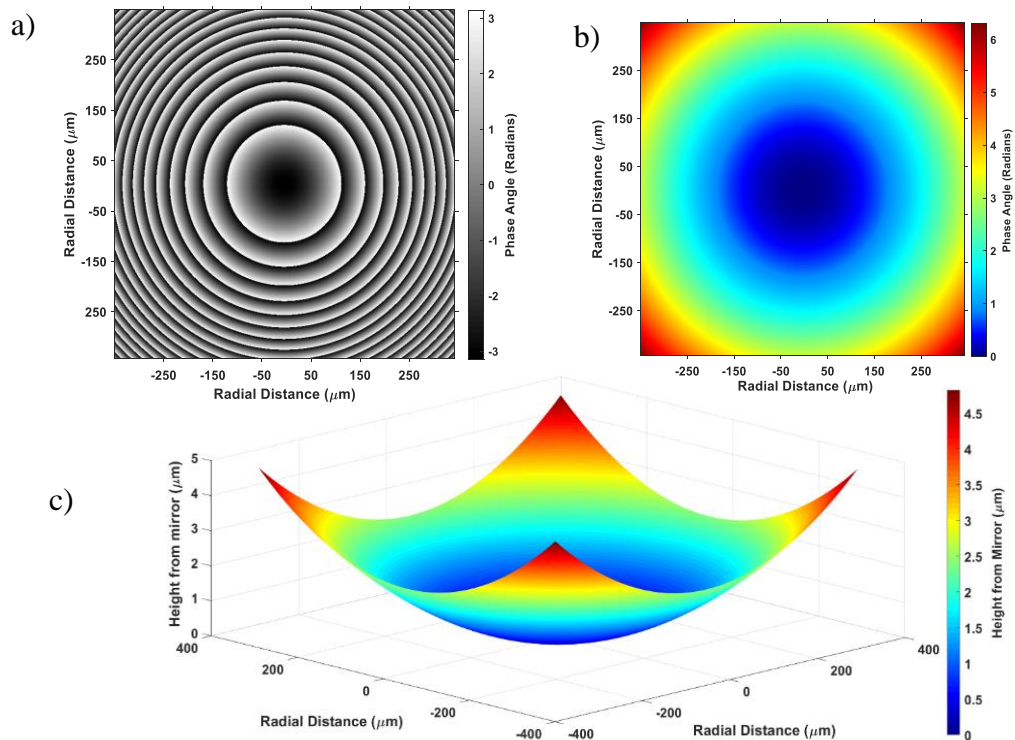


Figure 5.12 – The key steps in the phase extraction and 3D phase difference reconstruction when applied to a 2D simulated image. Here, a simulated function is offset by $\pi/2$ which utilised eqn. 5.3. a) A phase map of the result which shows the phase angle of each pixel. b) The phase difference from the 514-543 nm phase map. c) The 3D reconstruction of the lens specimen interpolating the axial height from the mirror using the theoretical phase difference.

Lastly, the Hilbert transform was applied to the lens specimen as a comparison between the simulated ideal data sets. This estimated how the 2D image would be reconstructed using the phase difference method to calculate the axial height. Figure 5.13a is the *hilbert* function extracted phase map reconstruction, using Eqn. 5.5, which resulted in a phase map of concentric rings. The 543 nm and 514 nm phase difference maps of the 2D image presented had oscillations within the phase difference angles along the x-axis at the centre angle at $x = 0 \mu\text{m}$, and along the x and y edge boundaries values = $-349 \mu\text{m}$ and $349 \mu\text{m}$ (Figure 5.13b). As a result, when the height from the mirror was calculated, it was observed there were oscillations clearly present in the 3D reconstruction (Figure 5.13c). Thus, a 3D reconstruction was created with oscillations present at the edge boundaries of the images when a Hilbert transform was used for the phase calculations. To quantify the effect of the oscillations, the axial height difference was calculated between the theoretical and simulated lens reconstruction for the 514-543nm and 488-514 nm which gave a phase difference of $0.45 \pm 132 \text{ nm}$ and $0.39 \pm 131 \text{ nm}$, respectively. The offset of the mean axial height was on average negligible ($< 1 \text{ nm}$). However, the mean axial height std. dev. was $\approx 130 \text{ nm}$, which was the oscillations observed in Figure 5.13c. As a result, the axial height reconstruction of a 2D image had shown a small mean height difference between the experimental and theoretical height values, but the Hilbert transform created large variability between the measured and theoretical axial height values.

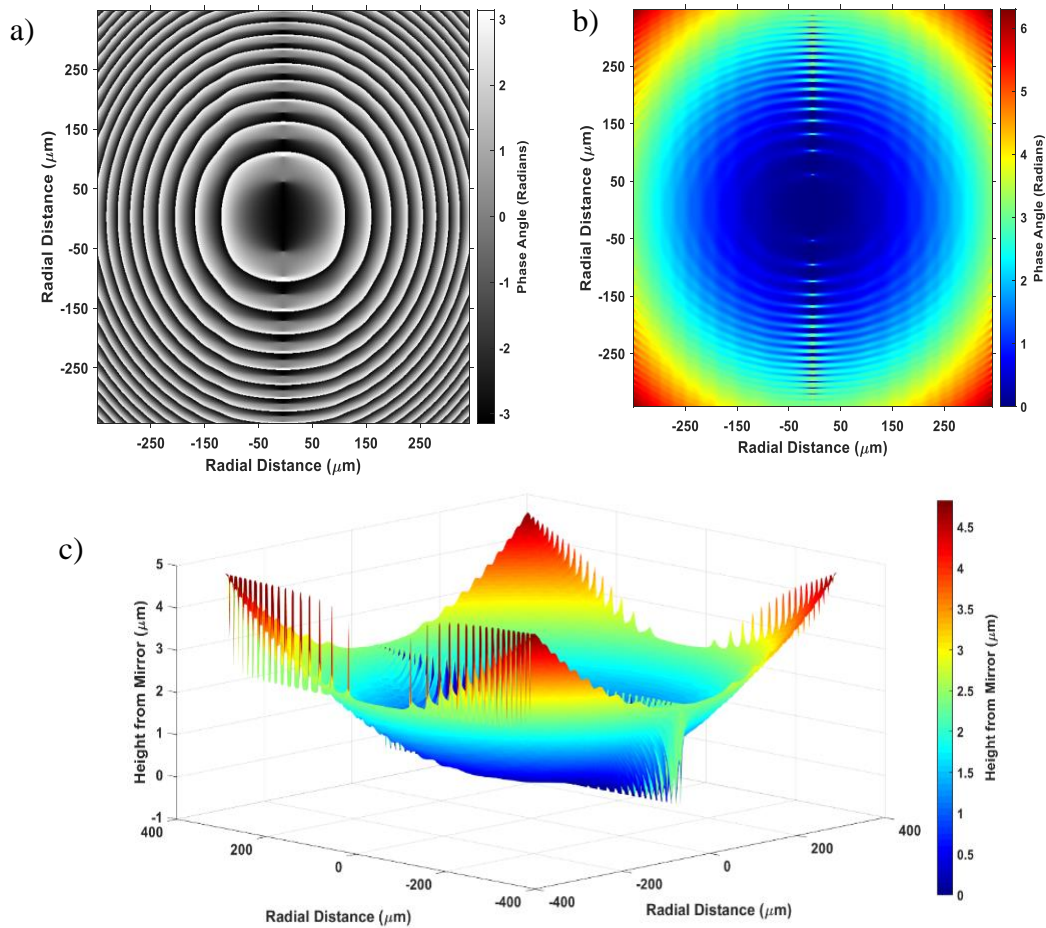


Figure 5.13 - The key steps in the phase extraction and phase difference 3D reconstruction when applied to a 2D simulated image. The simulated data above phase difference was generated using the Hilbert transform. a) A phase map of the result which shows each pixel value phase angle of the 543 nm excitation wavelength. b) The phase difference from the 514-543 nm phase map. c) A 3D reconstruction of the lens specimen interpolating the axial height from the mirror using the theoretical phase difference. It should be noted that there were oscillations present when a Hilbert transform was used to extract the phase angles which were not present with the theoretical phase extraction in Figure 5.12.

5.3.4 Phase difference reconstruction method of experimental $f = 48$ mm lens specimen data

To experimentally verify the phase difference method, a Dil stained $f = 48$ mm lens specimen was prepared using the protocol described in section 5.2.1, and was placed on a bare aluminum microscope slide and long pass filter. The lens specimen was imaged using a CLSM at excitation wavelengths of 543 nm, 514 nm and 488 nm. In FIJI, a Gaussian blur of $\sigma = 5$ was applied to the experimental lens data to remove the high frequency noise from the image.

In MATLAB, the theoretical axial height fit was generated using eqn. 4.1 and 5.7 over an axial height range of 0 to 3.5 μm . A line intensity plot was taken along the merged RGB TartanSW image and each SW excitation wavelength profile was individually normalised between -1 and 1. Next, a Hilbert transform was applied to the line intensity data and the phase angle was calculated, as shown in Figure 5.14a. This signal was then phase unwrapped, using the *unwrap* function, and the phase difference was calculated between the 514-543 nm (red) and the 488-514 nm (green) wavelengths. Then the axial height from the mirror was interpolated using polynomial fit of the theoretical data and shown in Figure 5.14b. It was apparent that at the radial distance 175 μm , the wrapped phase angles have poor phase wrapping. This resulted in poor reconstruction of the lens specimen beyond the radial distance of 175 μm .

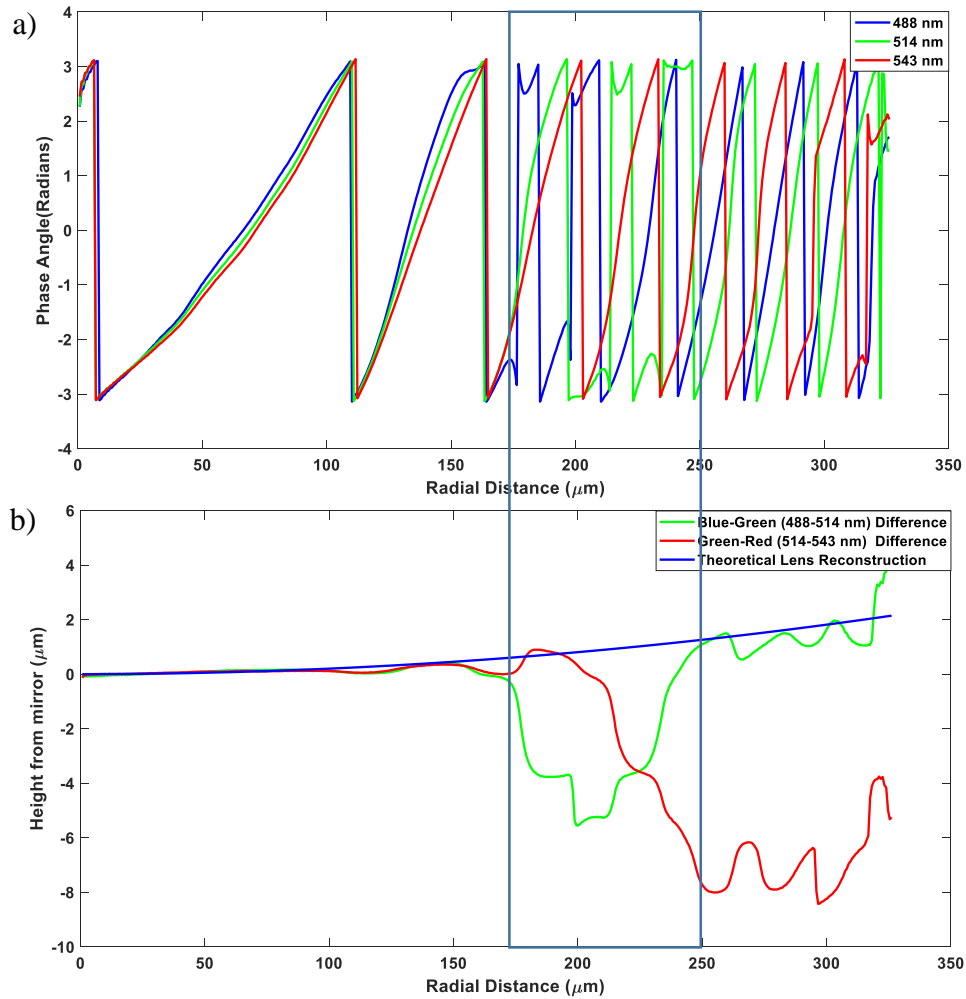


Figure 5.14 – Data extracted from a $f = 48$ mm lens specimen. a) The phase wrapped diagram for each of the 543 nm, 514 nm and 488 nm wavelengths. b) The reconstruction of the phase difference of the 488-514 nm (green) and 514-543 nm (red) data sets. The blue line was a theoretical representation lens specimen profile with radial distance against height from the mirrored surface.

To compensate for the poor phase wrapping, which caused the resulted in a poor reconstruction, I used the full theoretical expression for the TartanSW which included the effect of the emission detection over the 550-650 nm, using Eqn. 4.4. A $\pi/2$ phase shift was introduced, and using Eqn. 5.3, the wrapped phase angles were calculated and shown Figure 5.14. What resulted was a poor extraction of phase angles. The simulated

TartanSW wrapped phase data was unwrapped and used to generate a theoretical polynomial fit for each phase difference to axial height.

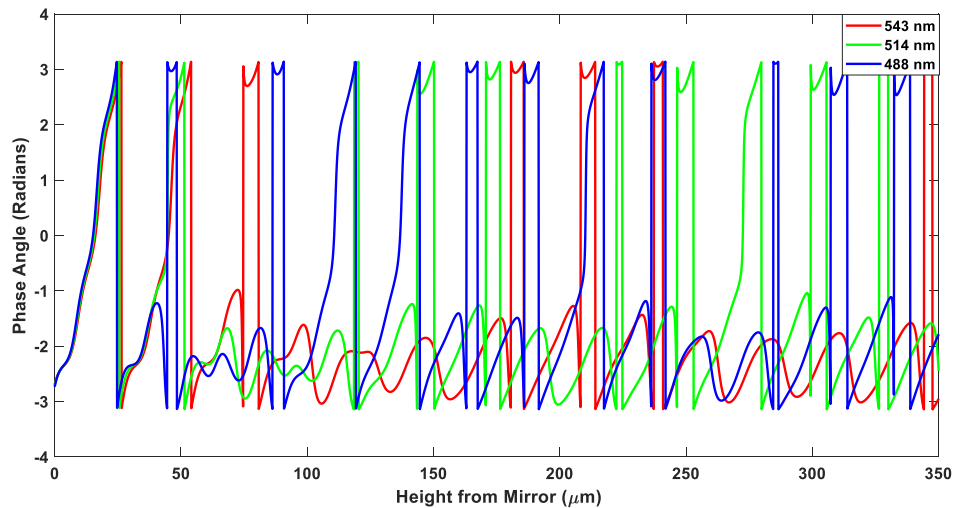


Figure 5.15 – The wrapped phases shown above for the theoretical expression for the model of SW with the emission contribution using eqn. 4.4.

By application of the hilbert transform to generate the wrapped phases which was shown in Figure 5.14. The phase unwrapping was applied and the phase difference was calculated. Using a linear polynomial fit from the theoretical data in Figure 5.15, the phase difference for the 488-514 nm and 514-543 nm experimental data was used to interpolate the axial height. However, in this case the full theoretical approach with the emission contribution was simulated. The result was shown in Figure 5.16, where a poor reconstruction of a lens specimen was observed which does not resemble the theoretical lens reconstructions of the convex profile. This was assumed to be because of the poor phase extraction of the regions which were heavily modulated by the theoretical SW emission contribution.

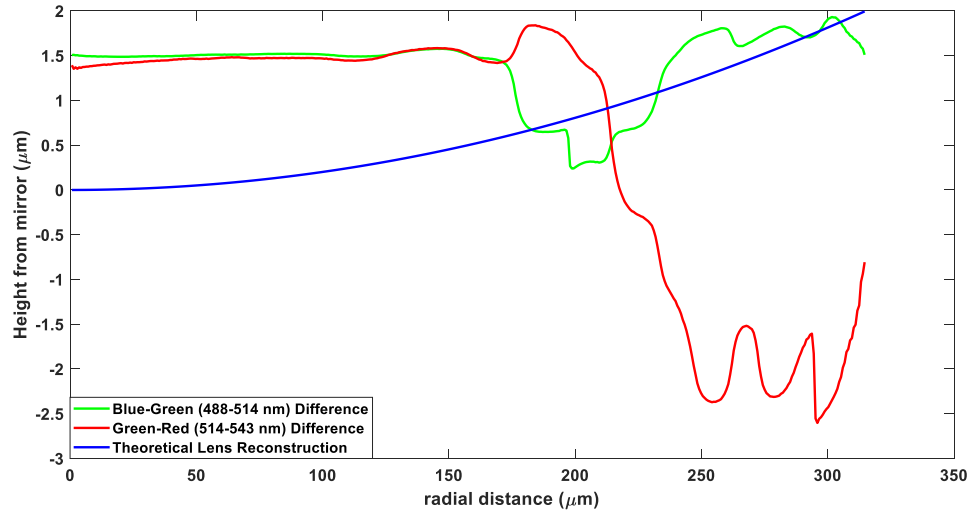


Figure 5.16 – The reconstruction of the line intensity plot taken from an experimental data set of a $f=48$ mm lens specimen. The axial height was interpolated from the phase difference of the 514-543 nm (red) and the 488-514 nm (green). The theoretical lens specimen was calculated using the lens specimens radius of curvature (shown in blue).

5.3.5 Phase difference reconstruction method of experimental $f = 48$ mm lens specimen data using a long pass filter as a substrate

To overcome the complexities of the emission contribution to the SW structure, which created poor reconstruction due to the theoretical phase wrapping. A 550 nm long pass filter was placed under the lens specimen to minimise the emission SW contribution. As a result, only the excitation light would have been reflected and a SW was formed due to only the excitation wavelengths. The result of the TartanSW $f = 48$ mm lens specimen image placed on a long pass filter is shown in Figure 5.17a. It was observed that a SW with colour ordering that was not comparable to the theoretical expression in Figure 4.5b or the bare aluminum microscope slide in Figure 4.6d. A line intensity profile was taken across the specimen that was only representative of the excitation wavelengths.

Notice that the emission contribution that was seen on the bare microscope slide in Figure 4.6, was not observed in the SW intensity profile in Figure 5.17a, when a specimen was placed on a long pass filter. However, there was an axial offset observed. In Figure 5.16a, it was shown that there was an additionally offset that was required to be accounted for and was calculated by $\phi_{offset} = \frac{2\pi z_{offset}}{\lambda_{exc}}$. By finding the first nodal plane position in the Figure 5.17b, the axial offset was determined as, 100 nm, 18 nm and 238 nm for the 543 nm, 514 nm and 488 nm excitation wavelengths, respectively. The theoretical SW with the offset was added in Eqn. 4.1, which gave an expression of $I_{ex}(z) = 1 - \cos\left(\frac{4\pi}{n\lambda_{exc}}z - \phi_{offset}\right)$ and with an $\pi/2$ phase shift included, eqn. 5.7 was now given as $I_{ex}(z) = 1 - \cos\left(\frac{4\pi}{n\lambda_{exc}}z - \phi_{offset} - \frac{\pi}{2}\right)$.

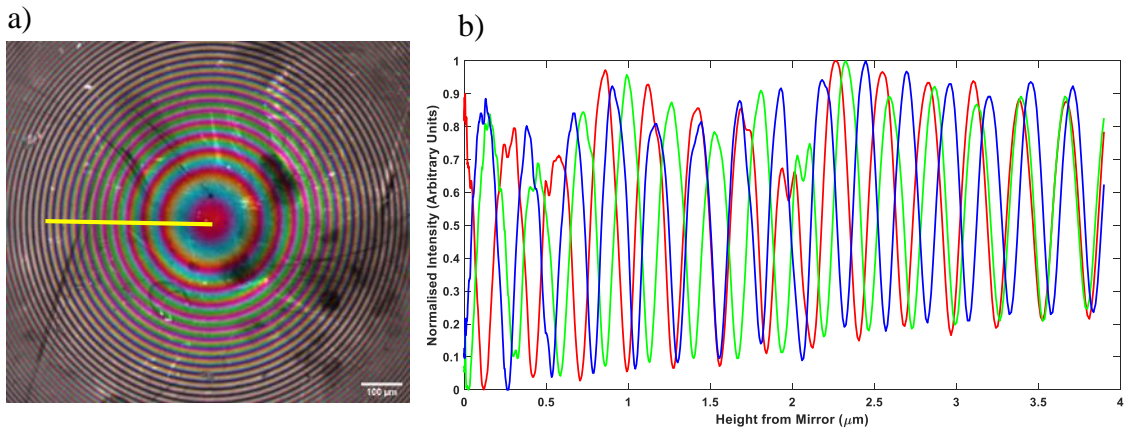


Figure 5.17- A TartanSW image of a $f = 48$ mm lens specimen placed on a 550 nm long pass filter (Thorlabs). Excitation wavelengths of 543, 514 and 488 nm were used and the emission was collected at 550-650 nm. a) The TartanSW multi-excitation RGB image. b) The intensity profile of each channel, which it was observed has minimal emission.

Next, a line intensity plot (shown in yellow line in Figure 5.17a) was taken through the specimen and using the Hilbert transform the wrapped phase was generated for the reconstruction. Figure 5.18a shows the wrapped phase map, notice how there was false wrapping at the beginning of the of the 488 nm. The phase difference reconstruction was

shown in Figure 5.18b, it was shown that the 514-543 nm followed the trend of the theoretical reconstruction with a mean difference of 551 ± 996 nm. However, the 488-514 nm phase difference reconstruction there was a clear offset with an axial mean difference of 4972 ± 526 nm.

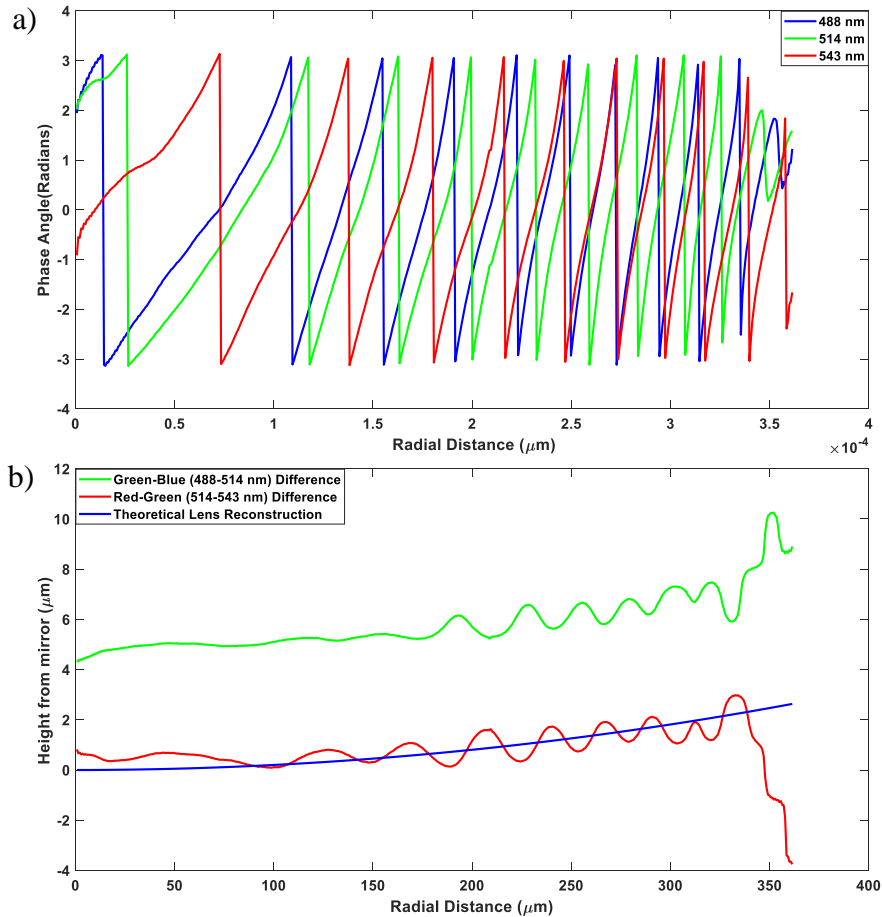


Figure 5.18 - Axial height reconstruction of axial height of a $f = 48$ mm lens specimen on a long pass filter a) The phase wrapped experimental data. b) The difference phase reconstruction which utilised the phase unwrapped data.

To overcome the phase unwrapping problems, a region of 25 data points was removed from the start and end regions of the intensity profile, where the discontinuities had occurred. The new phase wrapped phase excitation wavelengths was shown in Figure

5.19a, which now had removed the “false” wrapped phase. As with the previous experimental lens specimen data, the phase was unwrapped using the *unwrap* function in MATLAB and the axial heights were interpolated by Eqn. 5.7. The resultant reconstruction was shown in Figure 5.18b. Notice that the offset in the Figure 5.17b for the 488-514 nm (green line) was now removed in Figure 5.19b. The calculated mean axial difference between the experiment and theoretical data was 230 ± 315 nm. In the 514-543 nm phase reconstruction it was observed that it follows the trend of the theoretical lens reconstruction. The mean difference between the theoretical and experimental data was calculated as 375 ± 426 nm. In both cases, the phase difference reconstructions were improved, with the false phase wrapping removed in the 488-514 nm phase difference reconstruction.

In Figure 5.18c, in MATLAB a second order polynomial fit was applied to the 514-543 nm and 488-514 nm data to remove the oscillations around the theoretical lens specimen reconstruction. The result was a 488-514 nm (green) fit that followed the trend, but with a mean axial difference with a slight offset between the experimental and theoretical values of 74 ± 27 nm. Lastly, the 514-543 nm (red fit) demonstrated a curvature in the correct direction, but the curvature crosses the theoretical profile. This may be due to the initial offset at the beginning of the intensity profile which led to a bias in the fitting procedure. The axial mean difference was calculated to be 180 ± 207 nm between the theoretical and experimental axial height for the 514-543 nm using a second order polynomial fit.

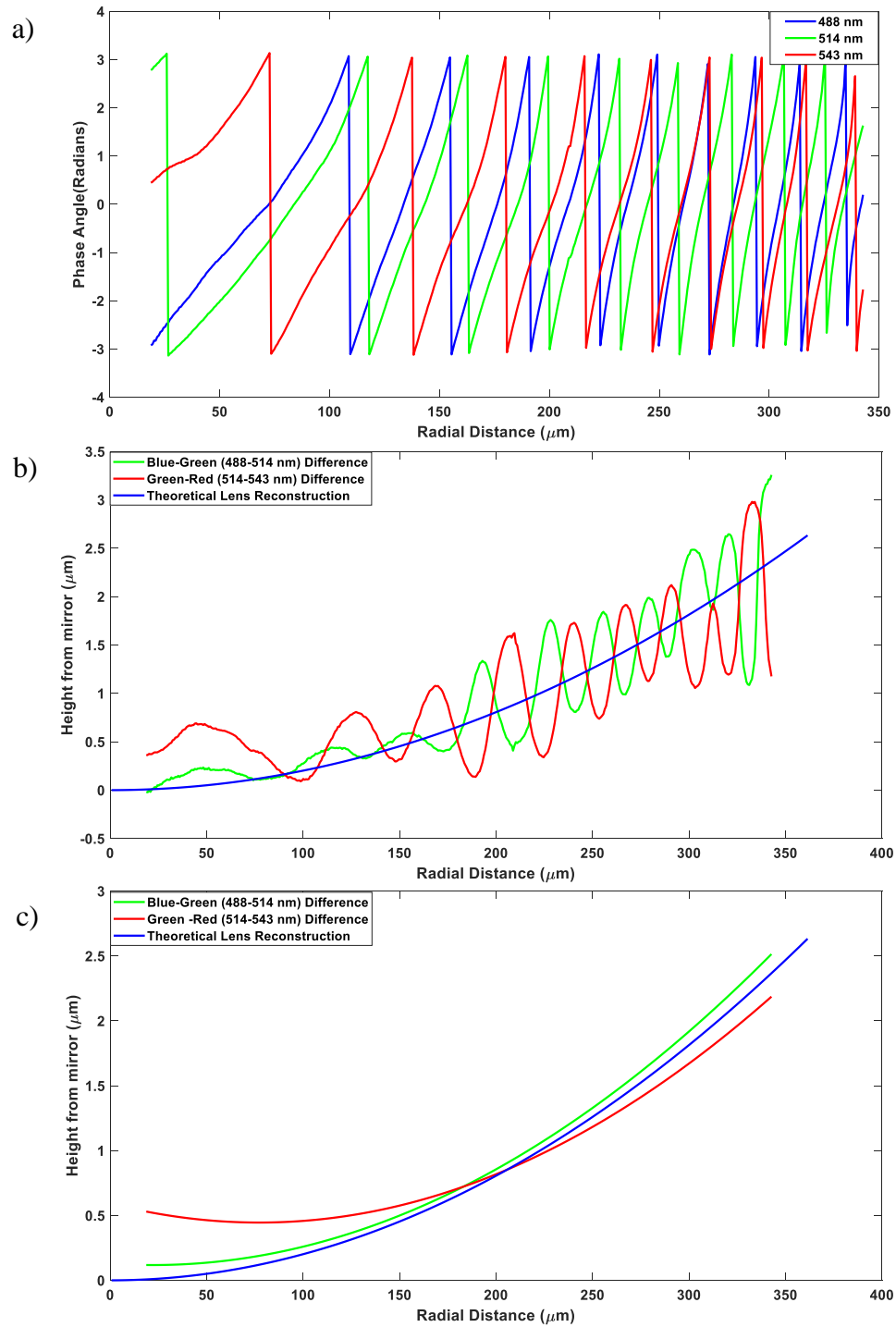


Figure 5.19 – Axial height reconstruction of a $f = 48 \text{ mm}$ lens specimen on a long pass filter with 25 data points removed from either side. a) The phase wrapped plot of the experimental data. b) The difference phase reconstruction which utilised the phase unwrapped data. c) A second order polynomial fit at the data lens reconstruction data in b).

5.4 Discussion

I developed a phase difference method and applied it to TartanSW which was used to reconstruct specimens without the requirement of *a priori* knowledge of the specimen geometry. To utilise the phase difference method, I used the three excitation wavelengths. Then I compared the phase difference at known axial location, based on the SW theory, and used this as a basis to interpolate unknown geometry as a function of phase difference. This was applied to the theoretically simulated and experimental data by using two phase retrieval methods: this could be done either by creating a $\pi/2$ phase shift or by application of a Hilbert transform. When the Hilbert transform was applied, this resulted in phase angles with the presence of oscillations (ringing), but this was not present when a $\pi/2$ phase shift was used on the theoretical SW data to calculate the phase angles. A possible explanation for this was the Gibbs phenomenon [175], [176], which was the presence of ringing in a function from determining a Fourier series occurring at a discontinuity [177]. In particular, this was prevalent because of the convolution between the real valued signal and the Heaviside step function. The Heaviside step function, which was used to remove the negative frequencies components in the Hilbert transform, has an amplitude of 0 at $x < 0$, a discontinuity at $x = 0$ and an amplitude which was equal to 2 at values of $x > 0$ [178]. However, it would exhibit oscillations when it had undergone a Fourier transform, at the regions of discontinuity ($x = 0$), as only a finite number of frequencies could be used to represent the Heaviside function [177]. The *hilbert* function in MATLAB created a Heaviside step function which was convolved with a Fourier transform of the real signal, before an analytical signal was obtained using an inverse Fourier transform [179]. This may have indicated why the ringing was observed in the Hilbert transform data, which introduced ringing to the complex component of the analytical signal, but not the simulated data which phase was shifted by $\pi/2$.

The Hilbert Transform extracted the phase from the simulated and experimental data sets using Eqn. 5.6. The phase was then used to calculate the unwrapped phase and the phase difference. It was observed that the ringing propagated through into the phase difference and final reconstruction. This was thought to be because the subtraction of the unwrapped phase angles which amplified the ringing present in the signal. Small deviation of the unwrapped angle, when subtracted, resulted in larger differences in the relative to the phase difference range. This was because the phase difference was measured over a smaller radian range, approximately 2π radians. Therefore, the phase difference oscillations were amplified over the small range which resulted in large oscillations in the final reconstruction. Additionally, the gradient of the linear fit of the theoretical SW data used for the final axial height interpolation, showed that a phase difference change of 0.1 radians resulted in an axial shift of ≈ 77 nm. Therefore, small variations in the phase difference would lead to large axial height deviations in the final axial height interpolation in the reconstructions.

The 3D reconstruction of the simulated 2D lens specimen SW data resulted in larger oscillations than was present in a line profile when a Hilbert Transform was used to extract the wrapped phase angles. I speculated that this was because the Hilbert transform was required to be applied twice over the 2D image which would have further amplified the oscillations. It should be noted that these large oscillations were more prevalent at the image edges (Figure 5.15b and c) i.e. the discontinuities of the simulated 2D image lens specimen data, which was consistent with the application of a Hilbert transform through all the data sets.

As in previous chapters, a Gaussian blur was applied to the experimental lens specimen data to remove as much of the high frequency noise components as possible. This was because even small differences created by noise could lead to shifts in the phase angle which would be amplified when the phase difference was calculated. This would have led to poorer axial height interpolation. Additionally, when phase unwrapping was

applied to noise or intensity fluctuations (due to poor fluorescent binding to the lens specimen surface), this would result in further phase discrepancies. This was due to noise with $> \pi$ phase angle causing the unwrapped phase angles to have an additional 2π added to its value at these locations. Although, this was not unexpected as phase unwrapping has been shown to be very sensitive to noise which could lead to artefacts in the unwrapped phase angles [180]–[182]. This was an inherent disadvantage to this method, as small variations in the experimental data were still present in the axial height reconstruction, even after noise filtering was applied.

Furthermore, it was observed that there was an axial offset of the initial starting position of the SW excitation waves when a long pass filter was used. In contrast, the bare aluminum microscope slide, no axial offset was present. This was most likely due to the dielectric substrate thickness of a long pass filter which created offset values for each of the excitation wavelengths. Oscillations in the reconstruction data were more prevalent in the long pass filter. I speculate this may have introduced artefacts at different offset values, as it appeared that the wrapped phases were different dependent on the initial axial offsets value. For example, the 488 nm wrapped phase had a 2π discontinuity (at a $\approx 0.1 \mu\text{m}$ radial distance in Figure 5.18a) that was not present in the 543 nm and 514 nm wavelengths. Thus, it created an offset in the 488-514 nm reconstruction. However, when this region was removed from the wrapped phase angles the 488-514 nm reconstruction was improved. Conversely, the false phase wrapping was not a problem when it was consistent over the three excitation wavelengths e.g. when a bare aluminum microscope slide was used. This was because the reconstruction method was based on the phase difference between each of the 514-543 nm and 488-514 nm wavelengths. As a result, as long as the false phase wrapping was consistent in each excitation wavelength, it would not affect the resultant axial height interpolation. This was an advantage of the phase difference technique, as it used the relative phase rather than absolute phase angle to reconstruct the height information. Therefore, it was not as

prone to systematic phase wrapping errors, if the errors were consistent across each of the SW excitation wavelengths.

Additionally, the bare aluminum microscope slide showed a good fit at the beginning of the phase difference reconstruction, when using the theoretical SW phase difference without any contribution from the emission SW. However, once the emission modulation was present in the experimental dataset, poor phase unwrapping occurred which led to a poor final reconstruction. To overcome this, the full theoretical SW theory was applied as described Chapter 4.2, by using eqn.4.4. However, this did not overcome the issues with trying to accurately model the intensity modulations due to the emission SW. I suspect that the theoretical SW waves amplitude modulation resulted in poor theoretical phase angle extraction (Figure 5.15) due to false phase wrapping. Thus, a method to computationally remove amplitude modulation over the full SW range is still required.

Several microscopy techniques use phase information, such as quantitative phase microscopy (QPI), to gain information about the 3D structure of a specimen. Quantitative phase microscopy is a label free method that can determine the optical path difference caused by the refractive index difference between the specimen and surrounding medium. By measuring the optical path difference, quantitative information about the specimen can be extracted [160], [183]. Quantitative phase methods can be broadly broken into two methods: phase shifting methods [100], [116]–[118], [160], which obtains the phase information from intensity images through temporal phase shifting with respect to a reference wave. From the multiple temporal images, the phase can be determined and used to calculate the optical thickness of a specimen. Off-axis techniques [172]–[174], have been used as method to extract phase information by using a spatial modulation in a single shot image. Again, this could be applied to imaging of biological specimens to obtain the thickness of the specimen from the phase information [183]. In comparison, the SW method had retrieved the phase measurements from the fluorescence signal of the periodic SW fringes that intersect the specimen. The fringe

pattern observed is projected in 2D and is dependent on 3D structure of the specimen being imaged. In other words, encoding the specimens 3D geometry in a 2D image. Standing wave microscopy required no additional components to a conventional microscope setup, other than a mirror underneath the specimen to generate the SW. However, unambiguous phase reconstruction was not possible in a single shot reconstruction method using single wavelength SW microscopy, unlike off-axis QPI techniques. Thus, to remove the geometric ambiguity in SW microscopy, multiple SW excitation wavelengths were required to calculate the relative phase dependence on axial height.

In future, the phase difference method could be applied to widefield SW TartanSW data which has the advantage of increased temporal resolution over CLSM and was suitable for fast long term imaging, using the video-rate SW imaging method as discussed in chapter 3. In chapter 3, it was shown that the exposure time for single wavelength image was ≈ 33 ms. Thus, to use three wavelength excitation to create a “single image” in widefield SW it would have taken ≈ 99 ms. Next, I applied the phase difference method to the 514-543 nm and 488-514 nm excitation wavelengths separately. This has shown that only two different SW excitation wavelengths were required to create the phase difference reconstruction. This would require less images than would be needed in phase-shifting QPI [183]. Additionally, TartanSW multi-excitation imaging time would be reduced by 33% using two excitation wavelengths over three excitation wavelengths for TartanSW imaging. However, if the three excitation wavelengths used in TartanSW multi-excitation imaging were combined, this could further extend the axial region of unambiguity of the specimen geometry that could be imaged. As a consequence, it would be a trade-off between the imaging speed and the axial region of the specimen which could be computational reconstructed without axial height ambiguity.

Overall, SW offers a much simpler set up that could be applied to an existing microscope, with the simple addition of a mirror, when compared to QPI and DHM techniques. Furthermore, with the addition of multiple wavelength that can be quickly switched between, fast topological imaging can be achieved which is not possible with QPI and DHM techniques. Lastly, the main advantage was that the TartanSW multi-excitation with the use of cellular membrane stains allows for the exact axial location of the fluorophores to be determined. This allows the specimen to be reconstructed more accurately. Whereas, QPI and DHM techniques can be susceptible to inaccuracies due to the varying refractive index differences within the cell membrane. Additionally, the presence of different organelles, nuclei and other sub cellular features within the cell, which have different thicknesses and refractive indices [183], make it difficult to reconstruct the thickness of the specimen accurately.

Future work would require more focus on removing the oscillations present in the complex component of the Hilbert transform, this could be somewhat suppressed by filtering out unwanted frequency components before applying the phase difference method. To achieve this, a low pass filter could be applied in conjunction with the Hilbert transform. Furthermore, the oscillations issue was more prominent in the 3D lens reconstruction of the simulated lens image than the 2D reconstructions. It should also be noted that larger amplitude oscillations were detected at discontinuities of the image edges. Lastly, a custom-built 2D Hilbert function may be required which would apply a 2D fast Fourier transforms (FFT), along with the additional filtering techniques, to the images data sets to calculate the 2D Hilbert transform. The aim would be to develop a more robust function than the in-built MATLAB *Hilbert* function. The end goal would be to apply this method to a 2D experimental lens specimen data sets to check the performance validity of the custom function.

The theoretical phase difference calculation could be simplified without the need of a linear fit, this would be achieved by the application of a theoretical phase difference

given as $z(\varphi) = \frac{1}{\Delta k} \Delta\varphi + \varphi_{offset}$. Where, Δk would be the difference in the excitation SW wave number, $\Delta\varphi$ would be phase difference and φ_{offset} would be the phase offset. The $\Delta\varphi$ from the experimental data would calculate the axial height, z , using the theoretical phase difference expression. It was clear that the linear fit in Eqn. 5.8, was analogous to the theoretical phase difference expression.

Previously, I had used RBCs as a biological analogue, due to its characteristic biconcave structure. In Chapter 4, a spectral signature reversal had been observed in the RBC compared to the lens specimen, thus it would be expected the phase method should detect this as change in direction of the curvature (convex or concave in shape). However, it would be desirable to have a geometric setup of a known concave surface which the TartanSW method could then be applied to (analogous to the plano-convex lens which offers a known geometric structure for a convex structure characterisation). This would provide comparative method to verify that the phase difference method would be able to detect specimens both convex and concave geometric structures using only the phase difference. Lastly, the application of the phase difference method to biological specimens, such as the eukaryotic and erythrocytes cell lines, would pose more of a problem due to the high background, more noise, and less defined structure in the resultant TartanSW Image. Therefore, this would require background correction and further image pre-processing before the phase difference method could be applied to the TartanSW images of the biological specimens.

5.5 Conclusion

In this chapter, I have shown that in principle the phase difference method was possible for simulated data with small oscillations due to the Hilbert transform. In the case of simulated line intensity data, it was possible to create an accurate reconstruction of the lens specimen. However, it created a larger ringing at regions of discontinuities in the 2D simulated lens specimen data. The phase difference method showed, in principle, that it was possible to extract the geometric shape of the object imaged using TartanSW multi-

excitation technique. However, the presence of large ringing effects in the experimental data needs to be addressed before applying it to more complicated datasets.

Chapter 6

Conclusion

6.1 Summary

In this thesis, I have presented work on multi-planar SW microscopy which encodes 3D information in a 2D image. This was applied to fluorescently labelled lens specimens, RBC and MCF-7s. I have developed computational methods and theoretical models to understand and extract 3D information from a single image for single wavelength excitation, Tartan SW multi-excitation and multi-emission techniques and DiffSW method.

In Chapter 2, I demonstrated that using a CLSM to capture SW RBC images of *P. berghei* and healthy RBC. In the SW images, a contour map of the bottom surface of RBCs which is in contact with the mirror surface could be observed and revealed morphological differences between the healthy and infected RBC cell membrane. To create 2D reconstructions of the SW images, I firstly used a Gaussian blur to remove any high frequency noise components from the SW images before the application of a local mean intensity threshold. This resulted in the segmentation of anti-nodal planes in the SW images, due to the variation in intensity between the nodal and anti-nodal planes. To confirm that the local mean threshold values applied to the image extracted as much of the anti-nodal data as possible, the percentage of the extracted anti-nodal planes in the threshold SW image was compared to the percentage of anti-nodal planes present in a simulation of a $f = 48$ mm lens specimen. I developed a computational method which could then be used to extract 2D position (x,y) and the pixel intensity information of the SW anti-nodal planes. This method was applied successfully to SW images of a lens specimen, RBC and iRBC to create a 2D reconstructions.

This 2D reconstruction method was further extended in Chapter 3. By using the 2D reconstruction method, it was possible to extract the anti-nodal plane information from a widefield SW RBC images. To verify the position and the assumptions made about the 3D SW PSF structure, I simulated the effect of the NA of the objective lens convolved with the SW pattern. I observed an intensity drop-off in the SW pattern over the axial

range was dependent on the NA. This revealed the presence of three SW planes when a 1.4 NA objective lens was used for imaging. The experimental widefield SW epifluorescence images of a fluorescently coated lens specimen in air and 4% BSA in PBS were compared to the theoretical anti-nodal spacing and FWHM, to verify the 3D structure of the SW. Next, the anti-nodal planes were then assigned axial height information using the assumptions made about the SW fringe pattern through *a priori* knowledge of a healthy RBC. At locations where I could not separate the anti-nodal planes, I developed a custom MATLAB function that interpolates the gaps in the nodal plane regions, and the resulting interpolated nodal image was subtracted from the original SW image to create separated anti-nodal planes. As a result, a 3D reconstruction was created for 981 out of 1000 SW RBC images captured at video-rate. This allowed for the extraction of 3D data from the 2D encoded RBC image along with visualisation of the 3D concave structure of the RBC.

In Chapter 4, I developed a theoretical model for TartanSW multi-excitation, multi-emission and DiffSW techniques. I experimentally confirmed that both the TartanSW multi-excitation and multi-emission, imaged on a bare aluminium microscope slide, showed a spectral signature that resembled the theoretical model. By application of different reflective substrate types, the spectral signature that was observed was dependent on the mirror surface type. The spectral signatures changes were caused by the dielectric layers, or protective coating on the mirrors surface. This created an axial shift in the position of the anti-nodal planes with respect to the bare aluminium microscope slide TartanSW images. TartanSW was then applied to both erythrocytes and eukaryotic cells stained with Dil. It was observed that the spectral signature resembled the theoretical and model lens specimen. It was apparent that the spectral signature could be used qualitatively, to infer more information about directionality of a cell's geometry. This was observed by the reversal of the TartanSW multi-excitation spectral signature ordering between the RBC and lens specimen, due to their respective concave and convex geometries. Lastly, a post-acquisition technique was applied to TartanSW

multi-excitation images called DiffSW, which improved the axial resolution of TartanSW multi-excitation method by ≈ 40 nm.

A method for reconstruction of TartanSW multi-excitation data was required that used the spectral signature to determine the axial height reconstruction of a specimen. In chapter 5, I proposed the use of the phase difference between each of the excitation wavelengths. In the case of simulated line intensity data, it was possible to create an accurate reconstruction of the lens profile, but small oscillations due to the Hilbert transform were present. Comparatively, large oscillations were observed at regions of discontinuities when the phase information was extracted using a Hilbert transform on the 2D simulated lens specimen data. In contrast, when the simulated waves were offset theoretically by $\pi/2$, no oscillation in the reconstruction were observed. The phase difference method showed, in principle, that it was possible to extract the geometric shape of the object when imaged using TartanSW multi-excitation technique. However, the presence of large ringing artefacts in the experimental data needs to be addressed before applying the phase difference method to 2D lens specimen and biological TartanSW multi-excitation images to create 3D reconstructions.

6.2 Future work

The application of multi-planar SW imaging techniques has been used for both upright CLSM and widefield epi-fluorescence microscopy to gain an axial super-resolution of ≈ 100 nm and contour map the specimens of interest. Standing wave microscopy is a simple technique that requires only the addition of a mirror under the specimen, and has been applied to a range of biological specimens. The application of different SW modalities such as TartanSW, which reduces the modulation gap present and the ambiguity of the specimen geometry, and DiffSW which further improves the axial resolution of TartanSW by ≈ 40 nm.

Widefield SW imaging has been shown to capture SW images at video-rate, which is currently being applied in the research group to study Dil stained MCF-7s images using

the TartanSW technique. The long-term goal of SW microscopy would be to study the 3D cell morphology of dynamical events such as mitosis, apoptosis and cell migration. Furthermore, it would be desirable to apply this technique to live cell imaging to study live actin behaviour, resulting in a contour of the cells cytoskeleton dynamics. The use of a single wavelength SW has the disadvantage of ambiguity of the structure of cells. This was evident when imaging *P. berghei* iRBC, which has a more complex concave structure due to the presence of the parasite in the iRBC, than was observed in healthy RBCs. In future, it would be desirable to apply TartanSW multi-excitation imaging to remove the ambiguity in the iRBC images, which in principle would allow for 3D reconstruction of the iRBC. This could be applied to study the morphology of iRBC at different stages of the parasites life cycle within the RBC, whilst using video-rate SW imaging to capture real time dynamical behaviour.

As SW 3D information is encoded within a 2D image of the specimen, it is important to develop computational methods to extract the SW data and provide quantitative analysis of the SW datasets. The long term goal would be to provide computational tools to analyse SW datasets that can be used by end-users that do not have expertise in developing or programming quantitative analysis tools. Currently, the computational methods available to extract the 3D information encoded within the 2D image of the specimen rely on *a priori* knowledge of the specimen. To overcome this, the phase difference method reconstructed the line intensity plots of a TartanSW lens specimens image without using *a priori* knowledge. Development is still ongoing with the phase difference reconstruction method which will require additional algorithms, such as custom-built phase extraction methods to help overcome the current challenges discussed in Chapter 5. The main challenge is overcoming the presence of oscillations from the Hilbert transform, which was particularly evident in the 2D SW images.

Machine learning has become more prominent in its use for segmentation of cells. For example, a pre-existing machine learning algorithm such as trainable WEKA [184] could

be used as a segmentation tool. Machine learning could be applied across SW datasets to extract the SW anti-nodal planes for complex cellular structures e.g. actin filaments or microtubules. This is particularly useful with large SW datasets, as it could be trained to detect SW anti-nodal planes against the background or nodal regions present in the SW datasets.

The overarching goal of the TartanSW methods will be to combine the long-term dynamical studies, with the computational algorithms available to create 3D reconstructions and extract quantitative analysis. This would then allow for quantification of the data present in the 3D reconstructions over time, e.g. quantify how the cell changes over time and measure 3D movements of the cell membrane and the associated morphological changes. Multi-planar SW microscopy would provide an axial super-resolution technique, using existing microscopes, which has shown promise as an imaging tool that could help in answering difficult biomedical questions.

References

- [1] C. Cremer and B. R. Masters, "Resolution enhancement techniques in microscopy," *Eur. Phys. J. H*, vol. 38, no. 3, pp. 281–344, Apr. 2013.
- [2] L. Schermelleh, R. Heintzmann, and H. Leonhardt, "A guide to super-resolution fluorescence microscopy," *J. Cell Biol.*, vol. 190, no. 2, pp. 165–175, 2010.
- [3] E. Hecht, *Optics*, Fourth Edi. Reading, Massachusetts, Massachusetts: Addison Wesley Longman, Inc, 2002.
- [4] R. Heintzmann and G. Ficz, "Breaking the resolution limit in light microscopy," *Methods Cell Biol.*, vol. 114, no. 4, pp. 525–544, 2013.
- [5] M. Born and E. Wolf, *Principle of Optics: Electromagnetic Theory of Propagation Intereference and Diffraction of Light*, Sixth. Peragamon Press, 1980.
- [6] X. Hao *et al.*, "From microscopy to nanoscopy via visible light," *Light Sci. Appl.*, vol. 2, 2013.
- [7] J. B. Pawley, *Handbook of Biological Confocal Microscopy*, Third. Springer, 2006.
- [8] R. Erni, M. D. Rossell, C. Kisielowski, and U. Dahmen, "Atomic-Resolution Imaging with a Sub-50-pm Electron Probe," *Phys. Rev. Lett.*, vol. 102, no. 9, p. 096101, Mar. 2009.
- [9] B. O. Leung and K. C. Chou, "Review of super-resolution fluorescence microscopy for biology.," *Appl. Spectrosc.*, vol. 65, no. 9, pp. 967–80, Sep. 2011.
- [10] J. G. G. White, W. B. B. Amos, and M. Fordham, "An evaluation of confocal versus conventional imaging of biological structures by fluorescence light microscopy.," *J. Cell Biol.*, vol. 105, no. 1, pp. 41–8, 1987.
- [11] K. Carlsson and N. Aslund, "Confocal imaging for 3-D digital microscopy.," *Appl. Opt.*, vol. 26, no. 16, pp. 3232–3238, 1987.
- [12] S. Hell and E. H. K. Stelzer, "Properties of a 4Pi confocal fluorescence microscope," *J. Opt. Soc. Am. A*, vol. 9, no. 12, p. 2159, 1992.
- [13] Lanni F, Taylor D, and Waggoner A, "Standing wave luminescence microscopy," A. S. US Patent No. 4,621,911, 1986.
- [14] B. Bailey, D. L. Farkas, D. L. Taylor, and F. Lanni, "Enhancement of axial resolution in fluorescence microscopy by standing-wave excitation.," *Nature*, vol. 366, no. 6450, pp. 44–8, 1993.
- [15] M. J. Rust, M. Bates, and X. Zhuang, "Stochastic optical reconstruction microscopy (STORM) provides sub-diffraction-limit image resolution," *Nat.*

Methods, vol. 3, no. 10, pp. 793–795, 2006.

- [16] E. Betzig *et al.*, “Imaging intracellular fluorescent proteins at nanometer resolution.,” *Science*, vol. 313, no. 2006, pp. 1642–1645, 2006.
- [17] S. T. Hess, T. P. K. Girirajan, and M. D. Mason, “Ultra-high resolution imaging by fluorescence photoactivation localization microscopy.,” *Biophys. J.*, vol. 91, no. 11, pp. 4258–72, 2006.
- [18] S. W. Hell and J. Wichman, “Breaking the diffraction resolution limit by stimulated emission: stimulated-emission-depletion fluorescence microscopy,” *Opt. Lett.*, vol. 19, no. 11, pp. 780–782, 1994.
- [19] T. A. Klar and S. W. Hell, “Subdiffraction resolution in far-field fluorescence microscopy,” *Opt. Lett.*, vol. 24, no. 14, pp. 954–6, 1999.
- [20] R. Hooke, *Micrographia: Or Some Physiological Descriptions of Minute Bodies Made by Magnifying Glasses. With Observations and Inquiries Thereupon*. London, 1667.
- [21] D. . Murphy, *Fundamentals of Light Microscopy and Electronic Imaging*, vol. 17, no. 5. 2002.
- [22] T. J. Fellers and M. W. Davidson, “Conjugate Planes in Optical Microscopy.” [Online]. Available: <http://www.microscopyu.com/articles/formulas/formulasconjugate.html>. [Accessed: 14-Jun-2016].
- [23] F. Zernike, “Phase Contrast *,” *Adv. Sci.*, vol. 121, no. 3141, pp. 345–349, 1955.
- [24] S. A. Johnson, “Chapter 1 – Phase Contrast Microscopy,” in *Biomedical Optical Phase Microscopy and Nanoscopy*, 2013, pp. 3–18.
- [25] R. D. Allen, G. B. David, and G. Nomarski, “The zeiss-Nomarski differential interference equipment for transmitted-light microscopy.,” *Zeitschrift fur wissenschaftliche Mikroskopie und mikroskopische Technik*, vol. 69, no. 4. pp. 193–221, 1969.
- [26] J. W. Lichtman and J. Conchello, “Fluorescence microscopy.,” *Nat. Methods*, vol. 2, no. 12, pp. 910–919, 2005.
- [27] G. G. Stokes, “On the Change of Refrangibility of Light,” *Philos. Trans. R. Soc. London*, vol. 143, no. January, pp. 463–562, 1852.
- [28] D. M. Jameson, *Introduction to Fluorescence*. Boston, MA: Taylor & Francis Group, 2014.
- [29] E. Coons, A. H. Creech, H. J., Jones, N. and Berliner, “The Demonstration of

- Pneumococcal Antigen in Tissues by the Use of Fluorescent Antibody," *J. Immunol.*, vol. 45, no. 3, pp. 159–170, 1942.
- [30] W. B. Amos and J. G. White, "How the Confocal Laser Scanning Microscope entered Biological Research," *Biol. Cell*, vol. 95, pp. 335–342, 2003.
- [31] H. Andersson, T. Baechi, M. Hoechl, and C. Richter, "Autofluorescence of living cells," *J. Microsc.*, vol. 191, no. 1, pp. 1–7, 1998.
- [32] A. C. Croce and G. Bottioli, "Autofluorescence spectroscopy and imaging: A tool for biomedical research and diagnosis," *Eur. J. Histochem.*, vol. 58, no. 4, pp. 320–337, 2014.
- [33] O. Shimomura, "Extraction , Purification and Properties of Aequorin , a Bioluminescent Protein from the Luminous," *J. Cell. Comp. Physiol.*, vol. 1353, no. 165, pp. 223–239, 1962.
- [34] R. Y. Tsien, "The Green Fluorescent," *Biochemistry*, vol. 67, no. 11, pp. 509–44, 1998.
- [35] N. C. Shaner, P. A. Steinbach, and R. Y. Tsien, "A guide to choosing fluorescent proteins.," *Nat. Methods*, vol. 2, no. 12, pp. 905–909, 2005.
- [36] B. N. G. Giepmans, S. R. Adams, M. H. Ellisman, and R. Y. Tsien, "The Fluorescent Toolbox for Assessing Protein Location and Function," *Science (80-.)*, vol. 312, no. April, pp. 217–224, 2006.
- [37] G. Piperno, M. Ledizet, and X. Chang, "Microtubules Containing Acetylated α -Tubulin in Mammalian Cells in Culture," *cell Biol.*, vol. 104, no. February, pp. 289–302, 1987.
- [38] R. M. Paredes, J. C. Etzler, L. T. Watts, and J. D. Lechleiter, "NIH Public Access," *Methods*, vol. 46, no. 3, pp. 143–151, 2009.
- [39] B. Hein, K. I. Willig, and S. W. Hell, *Optics*, vol. 105, no. 38. 2008.
- [40] R. Y. Tsien, "New Calcium Indicators and Buffers with High Selectivity against Magnesium and Protons: Design, Synthesis, and Properties of Prototype Structures," *Biochemistry*, vol. 19, no. 11, pp. 2396–2404, 1980.
- [41] I. Johnson, "Fluorescent probes for living cells.," *Histochem. J.*, vol. 30, no. 3, pp. 123–140, 1998.
- [42] J. Kapuscinski, "DAPI: a DNA-Specific Fluorescent Probe," *Biotech. Histochem.*, vol. 70, no. 5, pp. 220–233, 1995.
- [43] R. Rottenfusser, E. E. Wilson, and M. W. Davidson, "Fluorescence Microscopy." [Online]. Available: <http://zeiss->

campus.magnet.fsu.edu/articles/basics/fluorescence.html. [Accessed: 30-Jun-2016].

- [44] G. J. Brakenhoff, P. Blom, and P. Barends, "Confocal scanning light microscopy with high aperture immersion lenses," *J. Microsc.*, vol. 117, no. 2, pp. 219–232, 1979.
- [45] B. Amos, G. McConnell, and T. Wilson, "Confocal Microscopy," in *Handbook of Comprehensive Biophysics*, 2011, pp. 1–47.
- [46] J.-A. Conchello and J. W. Lichtman, "Optical sectioning microscopy.," *Nat. Methods*, vol. 2, no. 12, pp. 920–931, 2005.
- [47] T. Wilson, "Resolution and optical sectioning in the confocal microscope," *J Microsc*, vol. 244, no. 2, pp. 113–121, 2011.
- [48] S. Paddock, "Confocal reflection microscopy: The 'other' confocal mode," *Biotechniques*, vol. 32, no. 2, pp. 274–278, 2002.
- [49] W. B. Amos, "Instruments for Fluorescence Imaging," *Microscopy*. pp. 1–36, 2000.
- [50] D. Axelrod, "Cell-substrate contacts illuminated by total internal reflection fluorescence," *J. Cell Biol.*, vol. 89, no. 1, pp. 141–145, 1981.
- [51] A. L. Stout and D. Axelrod, "Evanescent field excitation of fluorescence by epi-illumination microscopy.," *Appl. Opt.*, vol. 28, no. 24, pp. 5237–5242, 1989.
- [52] D. Axelrod, "Total internal reflection fluorescence microscopy in cell biology," *Methods Enzym.*, vol. 361, no. 2, pp. 1–33, 2001.
- [53] D. Gingell, O. S. Heavens, and J. S. Mellor, "General electromagnetic theory of total internal reflection fluorescence: the quantitative basis for mapping cell-substratum topography.," *J. Cell Sci.*, vol. 87 (Pt 5), pp. 677–93, 1987.
- [54] M. G. L. Gustafsson, "Nonlinear structured-illumination microscopy: wide-field fluorescence imaging with theoretically unlimited resolution.," *Proc. Natl. Acad. Sci. U. S. A.*, vol. 102, no. 37, pp. 13081–13086, 2005.
- [55] J. Wilson and J. F. . Hawkes, *Laser: Principles and Application*. 1987.
- [56] S. W. Hell, "Far-Field Optical Nanoscopy," *Sci.* , vol. 316, no. 5828, pp. 1153–1158, 2007.
- [57] R. Heintzmann and C. G. Cremer, "Laterally modulated excitation microscopy: improvement of resolution by using a diffraction grating," *Proc.SPIE 3568, Opt. Biopses Microsc. Tech. III*, no. 185, pp. 185–196, 1999.
- [58] M. G. L. Gustafsson, "Surpassing the lateral resolution limit by a factor of two

- using structured illumination microscopy," *Microscopy*, vol. 198, no. January, pp. 82–87, 2000.
- [59] M. G. L. Gustafsson *et al.*, "Three-dimensional resolution doubling in wide-field fluorescence microscopy by structured illumination.," *Biophys. J.*, vol. 94, no. 12, pp. 4957–4970, 2008.
- [60] L. Schermelleh *et al.*, "Subdiffraction Multicolor Imaging of the Nuclear Periphery with 3D Structured Illumination Microscopy," *Microscopy*, vol. 320, no. 5881, pp. 1332–1336, 2010.
- [61] W. Moerner and L. Kador, "Optical detection and spectroscopy of single molecules in a solid," *Phys. Rev. Lett.*, vol. 62, no. 21, pp. 2535–2538, 1989.
- [62] A. Yildiz, "Myosin V Walks Hand-Over-Hand: Single Fluorophore Imaging with 1.5-nm Localization," *Science (80-.)*, vol. 300, no. 5628, pp. 2061–2065, 2003.
- [63] M. Bates, B. Huang, G. T. Dempsey, X. Zhuang, and T. Dempsey, "Multicolor Super-Resolution Imaging with Photo-Switchable Probes Fluorescent," *Science (80-.)*, vol. 317, no. 5845, pp. 1749–1753, 2007.
- [64] B. Huang, W. Wang, M. Bates, and X. Zhuang, "Three-dimensional Super-resolution Imaging by Stochastic Optical Reconstruction Microscopy," *Science (80-.)*, vol. 319, no. 5864, pp. 810–813, 2008.
- [65] G. Shtengel *et al.*, "Interferometric fluorescent super-resolution microscopy resolves 3D cellular ultrastructure.," *Proc. Natl. Acad. Sci. U. S. A.*, vol. 106, no. 9, pp. 3125–3130, Mar. 2009.
- [66] A. S. G. Curtis, "A Study by Interference Reflection Microscopy," *J. Cell Biol.*, vol. 20, no. 1, pp. 199–215, 1964.
- [67] V. a. Barr and B. S. C., "Interference Reflectance Microscopy," *Curr Protoc Cell Biol*, pp. 1–21, 2010.
- [68] H. Verschueren, "Interference reflection microscopy in cell biology: methodology and applications.," *J. Cell Sci.*, vol. 75, pp. 279–301, 1985.
- [69] S. W. Hell and E. H. K. Stelzer, "Fundamental improvement of resolution with a 4Pi-confocal fluorescence microscope using two-photon excitation," *Optics Communications*. 1992.
- [70] S. W. Hell, E. H. Stelzer, S. Lindek, and C. Cremer, "Confocal microscopy with an increased detection aperture: type-B 4Pi confocal microscopy.," *Opt. Lett.*, vol. 19, no. 3, p. 222, 1994.
- [71] M. Schrader, K. Bahlmann, G. Giese, and S. W. Hell*, "4Pi-Confocal Imaging in Fixed Biological Specimens," *Biophys. J.*, vol. 75, no. 4, pp. 1659–1668, 1998.

- [72] R. Amor, S. Mahajan, W. B. Amos, and G. McConnell, "Standing-wave-excited multiplanar fluorescence in a laser scanning microscope reveals 3D information on red blood cells.," *Sci. Rep.*, vol. 4, p. 7359, 2014.
- [73] F. Lanni *et al.*, "Excitation field synthesis as a means for obtaining enhanced axial resolution in fluorescence microscopes *," *Bioimaging*, vol. 1, no. 4, pp. 187–196, Sep. 1993.
- [74] F. Lanni, "Standing Wave Fluorescence Microscopy," in *Applications of fluorescence in the biomedical sciences*, 1986, pp. 505–521.
- [75] K. Elsayad *et al.*, "Spectrally coded optical nanosectioning (SpecON) with biocompatible metal-dielectric-coated substrates.," *Proc. Natl. Acad. Sci. U. S. A.*, vol. 110, no. 50, pp. 20069–74, 2013.
- [76] A. Lambacher and P. Fromherz, "Fluorescence interference-contrast microscopy on oxidized silicon using a monomolecular dye layer," *Appl. Phys. A Mater. Sci. Process.*, vol. 216, pp. 207–216, 1996.
- [77] A. Lambacher and P. Fromherz, "Luminescence of dye molecules on oxidized silicon and fluorescence interference contrast microscopy of biomembranes," *J. Opt. Soc. Am. B Opt. Phys.*, vol. 19, no. 6, pp. 1435–1453, 2002.
- [78] R. Gonzalez and R. Woods, *Digital Image Processing*, Third edit. Pearsons, 2008.
- [79] R. Garnett, T. Huegerich, C. Chui, and W. He, "With an Impulse Detector," *Image (Rochester, N.Y.)*, vol. 14, no. 11, pp. 1747–1754, 2005.
- [80] R. Gonzalez, R. Woods, and S. Eddins, *Digital Image Processing Using MATLAB*, Second Edi. McGraw Hill, 2010.
- [81] E. Meijering, "Cell Segmentation: 50 Years Down the Road," *IEEE Signal Process. Mag.*, vol. 29, no. 5, pp. 140–145, 2012.
- [82] N. Otsu, "A Threshold Selection Method from Gray-Level Histograms," *IEE Trans. Syst. Man, Cybernetics*, vol. SMC-9, no. 1, pp. 62–66, 1979.
- [83] P. D. Wellner, "Adaptive thresholding for the DigitalDesk," *Xerox, EPC1993-110*, pp. 1–19, 1993.
- [84] D. Bradley and G. Roth, "Adaptive Thresholding using the Integral Image," *J. Graph. GPU, Game Tools*, vol. 12, no. 2, pp. 13–21, 2007.
- [85] J. Sauvola and M. Pietikäinen, "Adaptive document image binarization," *Pattern Recognit.*, vol. 33, no. 2, pp. 225–236, 2000.
- [86] C. H. Wang and A. S. Popel, "Effect of red blood cell shape on oxygen transport in capillaries.," *Math. Biosci.*, vol. 116, no. 1, pp. 89–110, Jul. 1993.

- [87] M. Diez-Silva, M. Dao, J. Han, C.-T. Lim, and S. Suresh, "Shape and Biomechanical Characteristics of Human Red Blood Cells in Health and Disease.," *MRS Bull.*, vol. 35, no. 5, pp. 382–388, 2010.
- [88] L. Pauling, H. A. Itano, S. J. Singer, and I. C. Wells, "Sickle Cell Anemia, a Molecular Disease," *Science (80-.)*, vol. 110, no. 2865, 1949.
- [89] S. Eber and S. E. Lux, "Hereditary Spherocytosis - Defects in Proteins That Connect the Membrane Skeleton to the Lipid Bilayer," *Seminars in Hematology*, vol. 41, no. 2, pp. 118–141, Apr-2004.
- [90] A. F. Cowman and B. S. Crabb, "Invasion of red blood cells by malaria parasites," *Cell*, vol. 124, no. 4, pp. 755–766, 2006.
- [91] B. M. Cooke, N. Mohandas, and R. L. Coppel, "The malaria-infected red blood cell: Structural and functional changes," *Adv. Parasitol.*, vol. 50, no. 2, pp. 1–86, 2001.
- [92] T. Browicz, "Further observation of motion phenomena on red blood cells in pathological states," *Zbl Med. Wiss*, vol. 28, pp. 625–627, 1890.
- [93] H. Turlier *et al.*, "Equilibrium physics breakdown reveals the active nature of red blood cell flickering," *Nat. Phys.*, vol. 12, no. 5, pp. 513–519, 2016.
- [94] F. Brochard and J. F. Lennon, "Frequency spectrum of the flicker phenomenon in erythrocytes," *J. Phys.*, vol. 36, no. 11, pp. 1035–1047, 1975.
- [95] Y. Z. Yoon *et al.*, "Flickering analysis of erythrocyte mechanical properties: Dependence on oxygenation level, cell shape, and hydration level," *Biophys. J.*, vol. 97, no. 6, pp. 1606–1615, 2009.
- [96] N. T. Shaked, L. L. Satterwhite, M. J. Telen, G. A. Truskey, and A. Wax, "Quantitative microscopy and nanoscopy of sickle red blood cells performed by wide field digital interferometry," *J. Biomed. Opt.*, vol. 16, no. 3, p. 030506, 2011.
- [97] G. Popescu, Y. Park, W. Choi, R. R. Dasari, M. S. Feld, and K. Badizadegan, "Imaging red blood cell dynamics by quantitative phase microscopy," *Blood Cells, Mol. Dis.*, vol. 41, no. 1, pp. 10–16, 2008.
- [98] M. Abkarian, G. Massiera, L. Berry, M. Roques, and C. Braun-Breton, "A novel mechanism for egress of malarial parasites from red blood cells," *Blood*, vol. 117, no. 15, pp. 4118–4124, 2011.
- [99] K. Lee *et al.*, "Quantitative Phase Imaging Techniques for the Study of Cell Pathophysiology: From Principles to Applications," *Sensors*, vol. 13, no. 4, pp. 4170–4191, 2013.
- [100] J. Jung *et al.*, "Optical characterization of red blood cells from individuals with

- sickle cell trait and disease in Tanzania using quantitative phase imaging," *Sci. Rep.*, vol. 6, no. 1, pp. 1–9, 2016.
- [101] J. C. Waters, "Live-cell fluorescence imaging," *Methods Cell Biol.*, vol. 114, pp. 125–150, Jan. 2013.
- [102] H. E. Ives and T. C. Fry, "Standing Light Waves; Repetition of an Experiment by Wiener, Using a Photoelectric Probe Surface," *J. Opt. Soc. Am.*, vol. 23, no. 1, pp. 73–83, 1933.
- [103] F. Lanni, "Standing-Wave Fluorescence Microscopy," in *Applications of Fluorescence in the Biomedical Science*, D. L. Taylor, A. Waggoner, F. Lanni, B. Robert, and M. Robert, Eds. New York: Alan R. Liss, 1985.
- [104] D. Axelrod, "Carbocyanine dye orientation in red cell membrane studied by microscopic fluorescence polarization.," *Biophys. J.*, vol. 26, no. June, pp. 557–573, 1979.
- [105] S. Himbert *et al.*, "The Molecular Structure of Human Red Blood Cell Membranes from Highly Oriented, Solid Supported Multi-Lamellar Membranes," *Sci. Rep.*, vol. 7, p. 39661, 2017.
- [106] M. G. Honig and R. I. Hume, "DiI and DiO: versatile fluorescent dyes for neuronal labeling and pathway tracing," *Tins*, vol. 12, pp. 333–341, 1989.
- [107] Y. Li, Y. Song, L. Zhao, G. Gaidosh, A. M. Laties, and R. Wen, "Direct labeling and visualization of blood vessels with lipophilic carbocyanine dye DiI," *Nat. Protoc.*, vol. 3, no. 11, pp. 1703–1708, 2008.
- [108] M. G. Honig and R. I. Hume, "Fluorescent carbocyanine dyes allow living neurons of identified origin to be studied in long-term cultures," *J. Cell Biol.*, vol. 103, no. 1, pp. 171–187, 1986.
- [109] K. R. Hughes and A. P. Waters, "Rapid inducible protein displacement in *Plasmodium* in vivo and in vitro using knocksideways technology," *Wellcome Open Res.*, vol. 2, no. May, p. 18, 2017.
- [110] J. Schindelin *et al.*, "Fiji : an open-source platform for biological-image analysis," *Nat. Methods*, vol. 9, no. 7, pp. 676–682, 2012.
- [111] J. Zhang and P. A. Ney, "Reticulocyte mitophagy: Monitoring mitochondrial clearance in a mammalian model," *Autophagy*, vol. 6, no. 3, pp. 405–408, 2010.
- [112] G. Siciliano and P. Alano, "Enlightening the malaria parasite life cycle: Bioluminescent *Plasmodium* in fundamental and applied research," *Front. Microbiol.*, vol. 6, no. MAY, pp. 1–8, 2015.
- [113] A. S. Paul, E. S. Egan, and M. T. Duraisingh, "Host-parasite interactions that guide

- red blood cell invasion by malaria parasites," *Curr. Opin. Hematol.*, vol. 22, no. 3, pp. 220–226, 2015.
- [114] A. Esposito *et al.*, "Quantitative imaging of human red blood cells infected with *Plasmodium falciparum*," *Biophys. J.*, vol. 99, no. 3, pp. 953–960, 2010.
- [115] P. R. Gilson and B. S. Crabb, "Morphology and kinetics of the three distinct phases of red blood cell invasion by *Plasmodium falciparum* merozoites," *Int. J. Parasitol.*, vol. 39, no. 1, pp. 91–96, 2009.
- [116] J. Hur, K. Kim, S. Lee, H. Park, and Y. Park, "Melittin-induced alterations in morphology and deformability of human red blood cells using quantitative phase imaging techniques," *Sci. Rep.*, no. December 2016, pp. 1–10, 2017.
- [117] M. T. Rinehart, H. S. Park, K. A. Walzer, J. T. A. Chi, and A. Wax, "Hemoglobin consumption by *P. falciparum* in individual erythrocytes imaged via quantitative phase spectroscopy," *Sci. Rep.*, vol. 6, no. March, pp. 1–9, 2016.
- [118] H. S. Park, M. T. Rinehart, K. A. Walzer, J. T. Ashley Chi, and A. Wax, "Automated Detection of *P. falciparum* using machine learning algorithms with quantitative phase images of unstained cells," *PLoS One*, vol. 11, no. 9, 2016.
- [119] G. Deng and L. W. Cahill, "An adaptive Gaussian filter for noise reduction and edge detection," *IEEE Conf. Rec. Nucl. Sci. Symp. Med. Imaging Conf.*, pp. 1615–1619, 1993.
- [120] V. Krishnamurthi, B. Bailey, and F. Lanni, *Image processing in 3D standing wave fluorescence microscopy*, vol. 2655, no. 1. International Society for Optics and Photonics, 1996, pp. 18–25.
- [121] M. Nagorni and S. W. Hell, "Coherent use of opposing lenses for axial resolution increase. II. Power and limitation of nonlinear image restoration.," *J. Opt. Soc. Am. A. Opt. Image Sci. Vis.*, vol. 18, no. 1, pp. 49–54, 2001.
- [122] R. Freimann, S. Pentz, and H. Hörlner, "Development of a standing-wave fluorescence microscope with high nodal plane flatness.," *J. Microsc.*, vol. 187, no. Pt 3, pp. 193–200, 1997.
- [123] B. Bailey, V. Krishnamurthi, D. L. Farkas, D. L. Taylor, and F. Lanni, "Three-dimensional imaging of biological specimens with standing wave fluorescence microscopy," *SPIE Vol. 2184 Three-Dimensional Microsc.*, vol. 2184, pp. 208–213, 1994.
- [124] J. Canny, "A computational approach to edge detection.," *IEEE Trans. Pattern Anal. Mach. Intell.*, vol. 8, no. 6, pp. 679–698, 1986.
- [125] J. Dempster, D. L. Wokosin, K. D. McCloskey, J. M. Girkin, and A. M. Gurney,

“WinFluor: an integrated system for the simultaneous recording of cell fluorescence images and electrophysiological signals on a single computer system,” *Br. J. Pharmacol.*, vol. 137, pp. 146–146, 2002.

- [126] D. Fischer, “Radial Average.” 2014.
- [127] X. Yang *et al.*, “Mirror-enhanced super-resolution microscopy,” *Light Sci. Appl.*, vol. 5, no. 6, p. e16134, 2016.
- [128] F. H. C. Wong, J. S. Ng-Kamstra, N. L. H. Chen, and C. Fradin, “Localized photodamage of the human erythrocyte membrane causes an invagination as a precursor of photohaemolysis,” *J. Microsc.*, vol. 226, no. 1, pp. 6–17, Mar. 2007.
- [129] M. P. Sheetz and D. E. Koppel, “Membrane damage caused by irradiation of fluorescent concanavalin A.,” *Proc. Natl. Acad. Sci. U. S. A.*, vol. 76, no. 7, pp. 3314–7, 1979.
- [130] J. P. Pooler, “A New Hypothesis for the Target in Photohemolysis: Dimers of the Band 3 Protein,” *Photochem. Photobiol.*, vol. 43, no. 3, pp. 263–266, 1986.
- [131] Z. W. Zhang and B. Neu, “Role of macromolecular depletion in red blood cell adhesion,” *Biophys. J.*, vol. 97, no. 4, pp. 1031–1037, 2009.
- [132] B. Neu and H. J. Meiselman, “Depletion interactions in polymer solutions promote red blood cell adhesion to albumin-coated surfaces,” *Biochim. Biophys. Acta - Gen. Subj.*, vol. 1760, no. 12, pp. 1772–1779, 2006.
- [133] I. Todd, J. S. Mellor, and D. Gingell, “Mapping cell-glass contacts of Dictyostelium amoebae by total internal reflection aqueous fluorescence overcomes a basic ambiguity of interference reflection microscopy.,” *J. Cell Sci.*, vol. 89 (Pt 1), no. 1, pp. 107–14, Jan. 1988.
- [134] Y. Iwanaga, D. Braun, and P. Fromherz, “No correlation of focal contacts and close adhesion by comparing GFP-vinculin and fluorescence interference of Dil,” *Eur. Biophys. J.*, vol. 30, no. 1, pp. 17–26, 2001.
- [135] C. Monzel and K. Sengupta, “Measuring shape fluctuations in biological membranes,” *J. Phys. D. Appl. Phys.*, vol. 49, no. 24, p. 243002, 2016.
- [136] S. Chen, C. Li, and Y. Zhu, “Low-coherence wavelength shifting interferometry for high-speed quantitative phase imaging,” *Opt. Lett.*, vol. 41, no. 15, p. 3431, 2016.
- [137] N. T. Shaked, L. L. Satterwhite, N. Bursac, and A. Wax, “Whole-cell-analysis of live cardiomyocytes using wide-field interferometric phase microscopy,” *Biomed. Opt. Express*, vol. 1, no. 2, p. 706, 2010.
- [138] Y. Park *et al.*, “Metabolic remodeling of the human red blood cell membrane,” *Proc. Natl. Acad. Sci.*, vol. 107, no. 4, pp. 1289–1294, 2010.

- [139] Y. Park *et al.*, "Measurement of red blood cell mechanics during morphological changes.," *Proc. Natl. Acad. Sci. U. S. A.*, vol. 107, no. 15, pp. 6731–6, 2010.
- [140] M. Bouzin *et al.*, "Stimulated Emission Properties of Fluorophores by CW-STED Single Molecule Spectroscopy," *J. Phys. Chem. B*, vol. 117, no. 51, pp. 16405–16415, 2013.
- [141] M. Fernández-Suárez and A. Y. Ting, "Fluorescent probes for super-resolution imaging in living cells," *Nat. Rev. Mol. Cell Biol.*, vol. 9, no. 12, pp. 929–943, 2008.
- [142] T. Zhang *et al.*, "Structured illumination-based super-resolution optical microscopy for hemato- and cyto-pathology applications," *Anal. Cell. Pathol.*, vol. 36, no. 1–2, pp. 27–35, 2013.
- [143] S. Cho, S. Kim, Y. Kim, and Y. Park, "Optical imaging techniques for the study of malaria," *Trends Biotechnol.*, vol. 30, no. 2, pp. 71–79, 2012.
- [144] B. Huang, M. Bates, and X. Zhuang, "Super resolution fluorescence microscopy," *Annu. Rev. Biochem.*, vol. 78, pp. 993–1016, 2010.
- [145] V. C. Abraham, V. Krishnamurthi, D. Lansing Taylor, and F. Lanni, "The actin-based nanomachine at the leading edge of migrating cells," *Biophys. J.*, vol. 77, no. 3, pp. 1721–1732, 1999.
- [146] K. H. Drexhage, "Monomolecular layers and light," *Sci. Am.*, vol. 222, pp. 108–119, 1970.
- [147] K. H. Drexhage, "Interaction of light with monomolecular dye layers," in *Progress in Optics XII*, E. (ed. . Wolf, Ed. North-Holland, Amsterdam, 1974, pp. 165–231.
- [148] A. K. Swan *et al.*, "High-resolution spectral self-interference fluorescence microscopy," *Proc. SPIE - Int. Soc. Opt. Eng.*, vol. 4621, pp. 77–85, 2002.
- [149] H. Taniguchi, "Observation of reflection-induced light correlation," *Opt. Lett.*, vol. 19, no. 19, pp. 1565–1567, 1994.
- [150] a K. Swan *et al.*, "Towards nm-scale resolution in fluorescence microscopy using spectral self-interference," *J. Sel. Top. quantum Electron.*, vol. 9, no. 2, pp. 1–12, 2003.
- [151] M. Dogan *et al.*, "Spectral self-interference fluorescence microscopy for subcellular imaging," *IEEE J. Sel. Top. Quantum Electron.*, vol. 14, no. 1, pp. 217–225, 2008.
- [152] "aluminum-mirror-bk7-20mm-3mm-thick-10." [Online]. Available: <https://www.laser2000.co.uk/product/tfa-20c03-10/aluminum-mirror-bk7-20mm-3mm-thick-10>.

- [153] "BB1-E02 - Ø1" Broadband Dielectric Mirror, 400 - 750 nm." [Online]. Available: <https://www.thorlabs.com/thorproduct.cfm?partnumber=BB03-E02>. [Accessed: 05-Feb-2019].
- [154] L. Moiseev *et al.*, "Spectral self-interference fluorescence microscopy," *J. Appl. Phys.*, vol. 96, no. 9, pp. 5311–5315, 2004.
- [155] Y. Zhang, X. Chen, C. Gueydan, and J. Han, "Plasma membrane changes during programmed cell deaths," *Nat. Publ. Gr.*, vol. 28, no. 1, pp. 9–21, 2017.
- [156] O. T. Fackler and R. Grosse, "Cell motility through plasma membrane blebbing," *J. Cell Biol.*, vol. 181, no. 6, pp. 879–884, 2002.
- [157] K. Keren, "Cell motility : the integrating role of the plasma membrane," *Eur. Biophys. J.*, vol. 40, no. 9, pp. 1013–1027, 2011.
- [158] L. P. Cramer, "Investigation of the Mechanism of Retraction of the Cell Margin and Rearward Flow of Nodules during Mitotic Cell Rounding," *Mol. Biol. Cell*, vol. 8, no. 1, pp. 109–119, 1997.
- [159] L. Berre, M. Piel, and H. K. Matthews, "Exploring the Function of Cell Shape and Size during Mitosis," *Dev. Cell*, vol. 29, no. 2, pp. 159–169, 2014.
- [160] G. Popescu, *Quantitative phase imaging of cells and tissues*. McGraw Hill, 2011.
- [161] D. C. Ghiglia and L. A. Romero, "Robust two-dimensional weighted and unweighted phase unwrapping that uses fast transforms and iterative methods," *J. Opt. Soc. Am. A*, vol. 11, no. 1, pp. 107–117, 1994.
- [162] A. Baldi, "Two-dimensional phase unwrapping by quad-tree decomposition," *Appl. Opt.*, vol. 40, no. 8, pp. 1187–1194, 2001.
- [163] D. R. Burton, M. J. Lalor, and M. A. Gdeisat, "Fast two-dimensional phase-unwrapping algorithm based on sorting by reliability following a noncontinuous path," *Appl. Opt.*, vol. 41, no. 35, pp. 7437–7444, 2003.
- [164] J. Gass, A. Dakoff, and M. K. Kim, "Phase imaging without 2 π ambiguity by multiwavelength digital holography," vol. 28, no. 13, pp. 1141–1143, 2003.
- [165] A. Khmaladze, M. Kim, and C. Lo, "Phase imaging of cells by simultaneous dual-wavelength reflection digital holography," vol. 16, no. 15, pp. 900–911, 2008.
- [166] Y. Li, W. Xiao, and F. Pan, "Multiple-wavelength-scanning-based phase unwrapping method for digital holographic microscopy," *Appl. Opt.*, vol. 53, no. 5, pp. 22–24, 2014.
- [167] P. Rudent, J. E. A. N. A. T. Issot, B. E. R. Appaz, B. A. J. Avidi, G. E. T. Urcatti, and P. I. M. Arquet, "Quantification of stored red blood cell fluctuations by time-lapse

- holographic cell imaging,” vol. 9, no. 10, pp. 4714–4729, 2018.
- [168] D. Parshall and M. K. Kim, “Digital holographic microscopy with dual-wavelength phase unwrapping,” *Appl. Opt.*, vol. 45, no. 3, pp. 451–459, 2006.
- [169] A. Khmaladze, R. L. Matz, C. Zhang, T. Wang, M. M. B. Holl, and Z. Chen, “Dual-wavelength linear regression phase unwrapping in three-dimensional microscopic images of cancer cells,” *Opt. Lett.*, vol. 36, no. 6, pp. 912–914, 2011.
- [170] N. A. T. S. Haked, “Simultaneous three-wavelength unwrapping using external digital holographic multiplexing module,” *Opt. Lett.*, vol. 43, no. 9, pp. 1–4, 2018.
- [171] B. Gabor, “Theory of Communication,” *J. Institution Electr. Eng. - Part III Radio Commun.*, vol. 93, no. 26, pp. 429–441, 1946.
- [172] G. Popescu, R. R. Dasari, and M. S. Feld, “Hilbert phase microscopy for investigating fast,” *Opt. Lett.*, vol. 30, no. 10, pp. 1165–1167, 2005.
- [173] G. Popescu, C. A. Best, and M. S. Feld, “Erythrocyte structure and dynamics quantified by Hilbert phase microscopy,” *J. Biomed. Opt.*, vol. 10, no. 6, pp. 1083–12, 2005.
- [174] N. Lue *et al.*, “Tissue refractometry using Hilbert phase microscopy,” *Opt. Lett.*, vol. 32, no. 24, pp. 3522–3524, 2007.
- [175] J. W. Gibbs, “Fourier Series,” in *The collected works of J. Willard Gibbs*, New York: Layman-Greens, 1931, pp. 258–260.
- [176] M. L. Boas, “Fourier Series and Transforms,” in *Mathematical Methods for the Physical Sciences*, Third., Wiley, 2015, pp. 356–357.
- [177] W. J. Thompson, “Fourier series and the Gibbs phenomenon,” *Am. J. Phys.*, vol. 60, no. 5, pp. 425–429, 1992.
- [178] K. F. Riley, M. P. Hobson, and S. J. Bence, “Integral Transfrom,” in *Mathematical Methods for the Physical and Engineering*, Third., Cambridge University Press, 2006, p. 441.
- [179] “Hilbert Transform Matlab.” [Online]. Available: <https://uk.mathworks.com/help/signal/ug/hilbert-transform.html>. [Accessed: 11-Mar-2019].
- [180] J. Weng and Y. Lo, “Novel rotation algorithm for phase unwrapping applications,” *Opt. Express*, vol. 20, no. 15, pp. 3086–3105, 2012.
- [181] J. Weng and Y. Lo, “Integration of robust filters and phase unwrapping algorithms for image reconstruction of objects containing height discontinuities,” *Opt. Express*, vol. 20, no. 10, pp. 1246–1248, 2012.

- [182] V. V Volkov and Y. Zhu, "Deterministic phase unwrapping in the presence of noise," *Opt. Lett.*, vol. 28, no. 22, pp. 2156–2158, 2003.
- [183] Y. Park, C. Depeursinge, and G. Popescu, "Quantitative phase imaging in biomedicine," *Nat. Photonics*, vol. 12, no. October, 2018.
- [184] I. Arganda-carreras *et al.*, "Trainable Weka Segmentation : a machine learning tool for microscopy pixel classification," *Bioinformatics*, vol. 33, no. March, pp. 2424–2426, 2017.

Appendix I – Gaussian Blur signal to noise calculation

```
% Ross Scrimgeour (rcscimgeour@strath.ac.uk) -  
% This code generates radial plots for an across a line ROI. The user selects of an  
% input stack of different Gaussian blur images and compares the relative signal to %  
% noise from raw data with each Gaussian blurred image.  
clearvars;  
close all;  
  
%% creates radial and axial subplots alongside the theoretical plots  
% Image to microns scale  
scale = 1.368;  
addpath('!\Science\SIPBS\McConnellG\Ross                               Scrimgeour\PhD\MATLAB  
Code\SWFunctionToolbox');  
  
% Opens file explorer to load image file.  
% Stores the image file directory.  
% Reads in the image to the program.  
[filename, pathname, filterindex] = uigetfile({'*.jpg;*.tif;*.png;*.gif;*.tiff','All Image  
Files'});  
Filename = strcat(pathname,filename);  
info = imfinfo(Filename);  
imageStack = [];  
numOfImages = length(info);  
  
% Import image stack  
for k = 1:numOfImages  
    currentImage = imread(Filename, k, 'Info', info);  
    SWImage(:, :, k) = currentImage;  
end  
  
% Draw a line intensity plot allong the image  
imshow(SWImage(:, :, 1), []);  
title("Draw a line segement outwards")  
[cx,cy,Intensity(1,:),xi,yi] = improfile  
  
% if it is a stack of images this creates a matrix of the line intensity  
% image across all the stack  
for i = 2:numOfImages  
    Intensity(i,:) = improfile(SWImage(:, :, i),xi,yi)  
end
```

```
% Normalise intensity profiles
Intensity = mat2gray(Intensity);

% Convert the pixel number to distance
r_length = 1:length(Intensity(1,:));
Radial = (r_length./scale).*1e-6;

% Create a moving average along the intensity profile
MOV_MEAN = movmean(Intensity,21,2);
MOV_STD = movstd(Intensity,21,0,2);

% Calculate signal to noise and standard error
Sigtonoise = MOV_MEAN./MOV_STD;
SIGTONOISE = mean(Sigtonoise,2);
STDERROR = std(Sigtonoise,0,2)./sqrt(length(Sigtonoise));
```

Appendix II – Standing wave 2D reconstruction

```
% Author: Ross Scrimgeour (rcscimgeour@strath.ac.uk)
%

% Closes all Figures.
% Clears command window.
% Clears all variables.
close(Figure);
clc;
clearvars;

% Add path to the functions are saved
addpath('I:\Science\SIPBS\McConnellG\Ross Scrimgeour\Standing Wave paper\Matlab
Code\SWFunctionToolbox');

% Pixel to distance calibration
Scale = 22.71;

% Opens file explorer to load image file.
% Stores the image file directory.
% Reads in the image to the program.
[filename, pathname, filterindex] = uigetfile({'*.jpg;*.tif;*.png;*.gif;*.tiff','All Image
Files'});
Filename = strcat(pathname,filename);
info = imfinfo(Filename);
imageStack = [];
numOfImages = length(info);

for k = 1:numOfImages
    currentImage = imread(Filename, k, 'Info', info);
    imageStack(:, :, k) = currentImage;
end

% Normalise the intensity of the images
Normlnt = mat2gray(imageStack);

% Reads in the image size.
[h,w] = size(Normlnt(:, :, :));

for k = 1:numOfImages
```

```

[X,Y,Int] = CartGrid(NormInt(:,:,k),Scale);
I(:,:,k) = Int;

end
% Apply a Gaussian blur to image
I_GB = imgaussfilt(I,2);

for k = 1:numOfImages

    % Thresholds the image intensity using the adaptive threshold method.
    T = adaptthresh(I_GB(:,:,k),0.60,'NeighborhoodSize',25);
    BW(:,:,k) = imbinarize(I_GB(:,:,k),T);

end

% Create a colourmap for each image
for k = 1:numOfImages

    %% Determine the Cartesian coordinate values for the threshold image.
    X_Thres = X;
    Y_Thres = Y;

    X_Thres(~BW(:,:,k)) = 0;
    Y_Thres(~BW(:,:,k)) = 0;

    XX_Thres(:,:,k) = X_Thres;
    YY_Thres(:,:,k) = Y_Thres;

    %% Find the original image pixel intensity from the corresponding threshold image
    image_int(:,:,k) = I(:,:,k);
    image_int(~BW(:,:,k)) = 0;
    Thres_int(:,:,k) = image_int;

    % Creates a 3 X N colour map for the greyscale intensities
    Col_map=reshape(Thres_int(:,:,k),size(Thres_int(:,:,k),1)*size(Thres_int(:,:,k),2),1);
    Col_map2 = repmat(Col_map,1,3);
    Grey_int = cat(3, Thres_int(:,:,k), Thres_int(:,:,k), Thres_int(:,:,k));
    Col_map_final(:,:,k) = Col_map2;

end

```

```
% Save the images as a tiff
[FileName,PathName] = uinputfile({'*.tiff'});
for i = 1:numOfImages
    Savename = strcat(PathName,FileName);
    imwrite(Thres_int(:, :, i), Savename, 'WriteMode', 'append', 'Compression', 'none');
end
```

Appendix III- Custom polynomial fit function

```
function [Coeff,rsq,zq] = CustomPolfit3D(X,Y,Z,xq,yq,polydegree)
% A custom polynomial 3D fit using the pseudoinverse method for a 2nd,
% 3rd and 4th order polynomial and fits to the object boundary and not
% using a square surface as in the built in polyfit
% Inputs
% X,Y,Z is the input matrix for each coordinate to fit the polynomial
% equation to.
% xq and yq are the query points to interpolate from the polynomial
% equation
% polydegree is the polynomial equation degree (e.g. 1st, 2nd, 3rd)

% Outputs
% Coeff the coefficients of the polynomial equation
% rsq is the r-squared value
% zq is the interpolated z values .

% detailed explanation goes here
% Check x and y are vectors and converts to vectors if they are matrices
if isvector(xq) == 0
    xq = reshape(xq,size(xq,1)*size(xq,2),1);
else
end

if isvector(yq) == 0
    yq = reshape(yq,size(yq,1)*size(yq,2),1);
else
end

switch polydegree

case 2
    %% Create a matrix V for determining the coefficients
    V = zeros(length(X),6);

    % This loop fills the matrix V with all the values x and y for the polynomial equation
    for n = 1:length(X)
        V(n,:) = [1 X(n,1) Y(n,1) X(n,1).^2 X(n,1)*Y(n,1) Y(n,1).^2];
    end
```

```

% Create a matrix vq for interpolation
vq = zeros(length(xq),6);
% This loop fills the matrix vq with all the values xq and yq for the polynomial
equation
for n = 1:length(xq)
    vq(n,:) = [1 xq(n,1) yq(n,1) xq(n,1).^2 xq(n,1)*yq(n,1) yq(n,1).^2];
end

case 3
% Create a matrix V for determining the coefficients
V = zeros(length(X),10);

% This loop fills the matrix V with all the values x and y for the polynomial equation
for n = 1:length(X)
    V(n,:) = [1 X(n,1) Y(n,1) X(n,1).^2 X(n,1)*Y(n,1) Y(n,1).^2 X(n,1).^3 X(n,1).^2*Y(n,1)
X(n,1)*Y(n,1).^2 Y(n,1).^3];
end

% Create a matrix vq for interpolation
vq = zeros(length(xq),10);

% This loop fills the matrix V with all the values x and y for the polynomial equation
for n = 1:length(xq)
    vq(n,:) = [1 xq(n,1) yq(n,1) xq(n,1).^2 xq(n,1)*yq(n,1) yq(n,1).^2 xq(n,1).^3
xq(n,1).^2*yq(n,1) xq(n,1)*yq(n,1).^2 yq(n,1).^3];
end

case 4
% % Create a matrix V for determining the coefficients
V = zeros(length(X),15);

% This loop fills the matrix V with all the values x and y for the polynomial equation
for n = 1:length(X)
    V(n,:) = [1 X(n,1) Y(n,1) X(n,1).^2 X(n,1)*Y(n,1) Y(n,1).^2 X(n,1).^3 X(n,1).^2*Y(n,1)
X(n,1)*Y(n,1).^2 Y(n,1).^3 X(n,1).^4 X(n,1).^3*Y(n,1) X(n,1).^2*Y(n,1).^2
X(n,1)*Y(n,1).^3 Y(n,1).^4];
end

% Create a matrix vq for interpolation
vq = zeros(length(xq),15);

```

```

% This loop fills the matrix V with all the values x and y for the polynomial equation
for n = 1:length(xq)
    vq(n,:) = [1 xq(n,1) yq(n,1) xq(n,1).^2 xq(n,1)*yq(n,1) yq(n,1).^2 xq(n,1).^3
xq(n,1).^2*yq(n,1) xq(n,1)*yq(n,1).^2 yq(n,1).^3 xq(n,1).^4 xq(n,1).^3*yq(n,1)
xq(n,1).^2*yq(n,1).^2 xq(n,1)*yq(n,1).^3 yq(n,1).^4];
    end
end
% solves for the polynomial function to determine the coefficients
Coeff = V\Z;

% Calculates the line of best fit
zcalc = V*Coeff;

% Calculates the R-squared value
rsq = 1 - sum((Z - zcalc).^2)/sum((Z - mean(Z)).^2)

% interpolate query points vq for polynomial vit of choice
zq = vq*Coeff;
end

```

Appendix IV – Standing wave surface fit comparison

```
clearvars;
close all;

%% Simulate standing wave lens specimen image
% Define physical constants
% refractive index
n = 1;

% Excitation wavelength
lambdaex = 550*1e-9;

% Lens Radius of Curvature
R = 0.02481;

% calculate wavenumber
kex = 4*pi*n/lambdaex;

% Desired axial height in metres
Desired_z = 2.6*1e-6;

% Find max radial distance required for the desired axial height
maxr = ceil(sqrt(R.^2 -(R-Desired_z).^2)*1e6);

% setup the x,y,z and r (radial) data points
y = -maxr:4:maxr;
x = -maxr:4:maxr;
[X,Y] = meshgrid(x,y);
r2 = (sqrt(X.^2 + Y.^2)).*1e-6;
Z = (R-sqrt(R.^2-r2.^2));

% create the emission and excitation standing waves
SWex = mat2gray(1 - cos(kex.*Z));

%% Set up different x, y and z variables need for fitting

% Redefine X,Y and Z for SW simulation
X2 = X;
Y2 = Y;
Z2 = Z;
```

```

X3 = X;
Y3 = Y;
Z3 = Z;

% Remove nodal data positions from simulated data sets
X2(Z > 2.5*1e-6) = NaN;
Y2(Z > 2.5*1e-6) = NaN;
Z2(Z > 2.5*1e-6) = NaN;

X3(SWex < 0.5 | Z > 2.5*1e-6) = NaN;
Y3(SWex < 0.5 | Z > 2.5*1e-6) = NaN;
Z3(SWex < 0.5 | Z > 2.5*1e-6) = NaN;

%% Create a Gaussian offset to lens specimen data (comment out if no Gaussian offset
is desired)
% create an Gaussian function
Gauss = mat2gray(fspecial('gaussian', [71 71], 20));

Scaling_factor = 70;
% add to create a Gaussian offset
X3(41:111,41:111) = X3(41:111,41:111) - (Gauss.*Scaling_factor);
Y3(41:111,41:111) = Y3(41:111,41:111) - (Gauss.*Scaling_factor);

%% curve fitting to lens specimen

% create an x, y and z position vector
Xvector1 = reshape(X3,size(X3,1)*size(X3,2),1);
Yvector1 = reshape(Y3,size(X3,1)*size(X3,2),1);
Zvector1 = reshape(Z3,size(X3,1)*size(X3,2),1);

% remove NaNs
Xvector1(isnan(Xvector1) == 1) = [];
Yvector1(isnan(Yvector1) == 1) = [];
Zvector1(isnan(Zvector1) == 1) = [];

% Fit a polynoimal to lens data
[~,rsq2,z2] = CustomPolfit3D(Xvector1,Yvector1,Zvector1,X2,Y2,2);
[~,rsq3,z3] = CustomPolfit3D(Xvector1,Yvector1,Zvector1,X2,Y2,3);
[~,rsq4,z4] = CustomPolfit3D(Xvector1,Yvector1,Zvector1,X2,Y2,4);

z2 = reshape(z2,size(X2,1),size(X2,2));
z3 = reshape(z3,size(X2,1),size(X2,2));

```

```

z4 = reshape(z4,size(X2,1),size(X2,2));

% fit a cubic spline interpolation
% Interpolate SW image to create a 3D surface of the anti-nodal data points
minX = min(min(Xvector1));
MaxX = max(max(Xvector1));

% Setup a grid for each data point in the X and Y position
d = linspace(minX,MaxX,length(X2));
[xq,yq] = meshgrid(d);

% Create a X and Y grid for cubic interpolation
vqSurf = griddata(Xvector1,Yvector1,Zvector1,xq,yq,'cubic');

%% Plot Scatter and surface plots for each curve fitting procedure
% Create Figure
Figure1 = Figure('WindowState','maximized');

% Create axes
axes1 = axes('Parent',Figure1);
hold(axes1,'on');
Figure(1)
scatter3(Xvector1,Yvector1,Zvector1*1e6,'MarkerEdgeColor',[1 0 0],'Marker','x')
hold on
surf(X2,Y2,z2*1e6)
xlabel('Radial Distance (\mum)','FontSize',14,'FontWeight','bold')
ylabel('Radial Distance (\mum)','FontSize',14,'FontWeight','bold')
zlabel('Height from Mirror (\mum)','FontSize',14,'FontWeight','bold')
grid(axes1,'on');
% Set the remaining axes properties
set(axes1,'CameraPosition',...
    [-5316.74264273593 2698.06677257697 12.2776124321366],'FontSize',14,...
    'FontWeight','bold');

% Create Figure
Figure2 = Figure('WindowState','maximized');

% Create axes
axes1 = axes('Parent',Figure2);
hold(axes1,'on');
Figure(2)
scatter3(Xvector1,Yvector1,Zvector1*1e6,'MarkerEdgeColor',[1 0 0],'Marker','x')

```

```

hold on
surf(X2,Y2,z3*1e6)
xlabel('Radial Distance (\mum)','FontSize',14,'FontWeight','bold')
ylabel('Radial Distance (\mum)','FontSize',14,'FontWeight','bold')
zlabel('Height from Mirror (\mum)','FontSize',14,'FontWeight','bold')
grid(axes1,'on');
% Set the remaining axes properties
set(axes1,'CameraPosition',...
    [-5316.74264273593 2698.06677257697 12.2776124321366],'FontSize',14,...
    'FontWeight','bold');

% Create Figure
Figure3 = Figure('WindowState','maximized');

% Create axes
axes1 = axes('Parent',Figure3);
hold(axes1,'on');
Figure(3)
scatter3(Xvector1,Yvector1,Zvector1*1e6,'MarkerEdgeColor',[1 0 0],'Marker','x')
hold on
surf(X2,Y2,z4*1e6)
xlabel('Radial Distance (\mum)','FontSize',14,'FontWeight','bold')
ylabel('Radial Distance (\mum)','FontSize',14,'FontWeight','bold')
zlabel('Height from Mirror (\mum)','FontSize',14,'FontWeight','bold')
grid(axes1,'on');
% Set the remaining axes properties
set(axes1,'CameraPosition',...
    [-5316.74264273593 2698.06677257697 12.2776124321366],'FontSize',14,...
    'FontWeight','bold');

% Create Figure
Figure4 = Figure('WindowState','maximized');

% Create axes
axes1 = axes('Parent',Figure4);
hold(axes1,'on');
Figure(4)
scatter3(Xvector1,Yvector1,Zvector1*1e6,'MarkerEdgeColor',[1 0 0],'Marker','x')
hold on
surf(xq,yq,vqSurf*1e6)
xlabel('Radial Distance (\mum)','FontSize',14,'FontWeight','bold')
ylabel('Radial Distance (\mum)','FontSize',14,'FontWeight','bold')

```

```
zlabel('Height from Mirror (\(\mu\text{m}\))','FontSize',14,'FontWeight','bold')

grid(axes1,'on');
% Set the remaining axes properties
set(axes1,'CameraPosition',...
    [-5316.74264273593 2698.06677257697 12.2776124321366],'FontSize',14,...
    'FontWeight','bold');
```

Appendix V – Lens analysis

```
clc;
clearvars;

% Radius of Curvature of The lens specimen
R_lens = 0.02481

% Calibration factor for the pixels per distance(micron)
calib = 1.389;

% Opens file explorer to load image file
[filename, pathname, filterindex] = uigetfile({'*.jpg;*.tif;*.tiff;*.png;*.gif','All Image
Files'});
Filename = strcat(pathname,filename)
SWImage = imread (Filename);

% Reads in the image size
[h,w] = size(SWImage);

% checks if the image is square.
if w==h

    z = SWImage;

else
    if h > w
        h = w
    else if w > h
        w = h
    end
    end
    z = SWImage(1:h,1:w);
end

% Checks if the width and height are even or odd. If they are odd
% one is minus from the width and height values
if mod(w,2)==1;
    w2 = w-1;
else
    w2 = w;
end
```

```

if mod(h,2)==1;
    h2 = h-1;
else
    h2 = h;
end

% Sets the new squared image size
z = SWImage(1:h2,1:w2);
% Resultant squared image
Figure(4);imshow(z,[])

% sets the half width and half height values
half_height = h2/2;
half_width = w2/2;
m = half_height;

% Create a radial average of the lens specimen
[Zr,R] = radialavg(z,m);
R_average = R*half_height;
radial_average = (R_average*1e-6/calib);

% Normalise the the fluorescence signal
z_max = max(Zr);
z_min = min(Zr);
z_min2 = min(z_min);
z_max2 = max(z_max);
Zr_norm = (Zr- z_min2)/(z_max2-z_min2);

% Plots the Fluorescence Intensity vs Radial Distance
Figure(1);plot(radial_average,Zr_norm)
xlabel('Radial Distance (\mum)')
ylabel('Fluorescence Instensity (Arbitrary Units)')

% Translate the radial to axial height
L = (R_lens-sqrt(R_lens^2-radial_average.^2))*1e9;

% Plots Fluorescence Intensity vs Height from mirror
Figure(2);plot(L,Zr_norm,'r')
xlabel('Height from Mirror surface (nm)')
ylabel('Nomralised fluorescence intensity (Arb. units)')

```

hold on

% Finds the peaks and FWHM of for each standing wave.

```
[pks,locs,widths] =
```

```
findpeaks(Zr_norm,L,'MinPeakProminence',0.05,'annotate','extents');
```

%Determines the average FWHM of the standing wave planes

```
Average_FWHM = mean(widths)
```

```
widths = widths'
```

%Finds the size of the locs matrix

```
[x,num_pks] = size(locs);
```

%Calculates the anti-nodal-spacing for each peak

```
Anti_nodal_spacing = (locs(1,2:num_pks)-locs(1,1:num_pks-1));
```

```
Avg_anti_nodal_spacing = mean(Anti_nodal_spacing);
```

% % Plots Fluorescence Intensity vs Height from mirror with FWHM

```
Figure(3);findpeaks(Zr_norm,L,'MinPeakProminence',0.05,'annotate','extents')
```

```
xlabel('Height from mirror (nm)')
```

```
ylabel('Normalised fluorescence intensity (Arb. units)')
```

Appendix VI – Standing wave 3D reconstruction

```
% Author : Ross Scrimgeour (rcscimgeour@strath.ac.uk)
% Date : 09/2017
% This script will create a 3D reconstruction of a standing wave red blood
% cell for either a single image input or standing wave movie.

warning('off','all')
% Closes all Figures.
% Clears all variables.
close all;
clearvars;

%% Input Variables
% Pixel to distance calibration
Scale = 22.71;
% Gaussian Blur Standard Deviation
Std_dev = 2;
% Local Threshold Neighbourhood size and threshold sensitivity
Neighbourhood_size = 25;
Thresh_sensitivity = 0.6;
% Refractive index of cell suspension
n = 1.341;
% Excitation wavelengths used
Lambdaexc = 525*1e-9;

%% Input Image
% Opens file explorer to load image file.
% Stores the image file directory.
% Reads in the image to the program.
[filename, pathname, filterindex] = uigetfile({'*.jpg;*.tif;*.png;*.gif;*.tiff','All Image
Files'});
Filename = strcat(pathname,filename);
currentImage = imread(Filename);
info = imfinfo(Filename);
imageStack = [];
numOfImages = 1;

for k = 1:numOfImages
    currentImage = imread(Filename, k, 'Info', info);
    imageStack(:, :, k) = currentImage;
end
```

```

% Normalise the intensity of the images
NormInt = mat2gray(imageStack);

% Reads in the image size.
[h,w] = size(NormInt(:,:,:));

% Preallocate variables
T = zeros(size(NormInt,1),size(NormInt,2),numOfImages);
BW = zeros(size(NormInt,1),size(NormInt,2),numOfImages);
I = zeros(size(NormInt,1),size(NormInt,2),numOfImages);

% Create a Cartesian X and Y grid for image
for k = 1:numOfImages
    [X,Y,Int] = CartGrid(NormInt(:,:,k),Scale);
    I(:,:,k) = Int;
end

%% Application of Gaussian blur and intensity threshold
% Apply a Gaussian blur to image
I_GB = imgaussfilt(I,Std_dev);

for k = 1:numOfImages

    % Thresholds the image intensity using the adaptive threshold method.
    T =
    adapththresh(I_GB(:,:,k),Thresh_sensitivity,'NeighborhoodSize',Neighbourhood_size);
    BW(:,:,k) = imbinarize(I_GB(:,:,k),T);

end

% Plane separation
[SUB] = Antinodesep(BW,numOfImages,1);

% Plane separation check
[SUB2,time] = Nodal_SEP_Check(SUB);

% Create a new time variable
numOfImages2 = length(time);

% Create a time stamp
Timestamp = cell(numOfImages2,1);

```

```

Timestamp = {'Time (s) = '};
Timestamp2 = string(time);
Time_stamp = strcat(Timestamp, Timestamp2);

```

```

% Preallocate Variable

```

```

XX_Thres = zeros(size(NormInt,1),size(NormInt,2),numOfImages2);
YY_Thres = zeros(size(NormInt,1),size(NormInt,2),numOfImages2);
XX_edge = zeros(size(NormInt,1),size(NormInt,2),numOfImages2);
YY_edge = zeros(size(NormInt,1),size(NormInt,2),numOfImages2);
vqSurf = zeros(size(NormInt,1),size(NormInt,2),numOfImages2);
E_1 = zeros(size(NormInt,1),size(NormInt,2),numOfImages2);
E = zeros(size(NormInt,1),size(NormInt,2),numOfImages2);
vq = zeros(size(NormInt,1)*size(NormInt,2),1,numOfImages2);
Image_I = zeros(size(NormInt,1),size(NormInt,2),numOfImages2);
Col_map = zeros(size(NormInt,1)*size(NormInt,2),1,numOfImages2);

```

```

% Store the x and y coordinates of the threshold images

```

```

for k = 1:numOfImages2
    X_Thres = X;
    Y_Thres = Y;

    X_Thres(~SUB2(:, :, k)) = 0;
    Y_Thres(~SUB2(:, :, k)) = 0;

    XX_Thres(:, :, k) = X_Thres;
    YY_Thres(:, :, k) = Y_Thres;
end

```

```

end

```

```

%% Edge Detection

```

```

for k = 1:numOfImages2

    % Create a Canny edge detection for each standing wave image
    E_1(:, :, k) = edge(SUB2(:, :, k), 'canny');
    E(:, :, k) = bwmorph(E_1(:, :, k), 'clean');
end

```

```

end

```

```

% Determine the Cartesian coordinate values for the edge detection images.

```

```

for k = 1:numOfImages2

    X_edge = X;
    Y_edge = Y;
end

```

```

X_edge(~E(:,:,k)) = 0;
Y_edge(~E(:,:,k)) = 0;

XX_edge(:,:,k) = X_edge;
YY_edge(:,:,k) = Y_edge;

clear X_edge Y_edge I_GB T
end

%% Create a colour map
for k = 1:numOfImages2

    % Find the original image pixel intensity from the corresponding threshold image
    clear image_int
    image_int = I(:,:,k);
    image_int(~SUB2(:,:,k)) = 0;
    Image_I(:,:,k) = image_int;

    % Create row and column vectors from the X and Y threshold values
    Col_map(:,:,k) = reshape(Image_I(:,:,k),size(Image_I(:,:,k),1)*size(Image_I(:,:,k),2),1);

end

% Creates a 3 X N colour map for the greyscale intensities
Col_map2 = repmat(Col_map,1,3);

clear Col_map Image_I Image_int
%% Assign axial information to the SW planes
% Determine a vector with the axial FWHM values
z = RBCaxialHeight(Lambdaexc,n,4)*1e6;

XX = reshape(XX_edge,size(X,1)*size(X,2),1,numOfImages2);
YY = reshape(YY_edge,size(Y,1)*size(Y,2),1,numOfImages2);

X_Thres = reshape(XX_Thres,size(XX_Thres,1)*size(XX_Thres,2),1,numOfImages2);
Y_Thres = reshape(YY_Thres,size(YY_Thres,1)*size(YY_Thres,2),1,numOfImages2);

% Determine all X and Y anti-nodal data point positions
Xq = X_Thres;
Yq = Y_Thres;

for k = 1:numOfImages2

```

```
% Creates a unique ID for each edge detected ring.
```

```
[L,num] = bwlabel(E(:,:,k),8);
```

```
% Stores all the z values at the relevant FWHM axial positions based on each rings  
unique ID.
```

```
ZZ = L;
```

```
for i = 1:num
```

```
    ZZ(ZZ==i) = z(1,i);
```

```
end
```

```
% Creates column vector for all the ZZ matrix
```

```
ZZ = reshape(ZZ,size(X,1)*size(X,2),1);
```

```
% Finds the row and column positions in zz that is equal to zero.
```

```
[row, col] = find(ZZ == 0);
```

```
% set the X and Y coordinates to the current image
```

```
XX1 = XX(:,:,k);
```

```
YY1 = YY(:,:,k);
```

```
% Removes all the rows which in XX1, YY1 and ZZ where ZZ is equal to zero.
```

```
XX1(row) = [];
```

```
YY1(row) = [];
```

```
ZZ(row) = [];
```

```
% Find the length of each image
```

```
minX = min(min(X));
```

```
MaxX = max(max(X));
```

```
% Set up a x and y grid for each pixel in the image
```

```
d = linspace(minX,MaxX,length(X));
```

```
[xq,yq] = meshgrid(d);
```

```
% Interpolate SW image to create a 3D surface of the anti-nodal data points
```

```
vqSurf(:,:,k) = griddata(XX1,YY1,ZZ,xq,yq,'cubic');
```

```
% Interpolate SW image to create a 3D surface of the anti-nodal data points
```

```
vq(:,:,k) = griddata(XX1,YY1,ZZ,Xq(:,1,k),Yq(:,1,k),'cubic');
```

```

end

clear E E_1 d YY1 XX1 YY_Thres XX_Thres ZZ XX YY BW

if numOfImages2 == 1

    % Create Figure
    Figure1 = Figure('Color',[0 0 0],'units','normalized','outerposition',[0 0 1 1]);

    % Plot a 3D surface and scatter plot for each image that can be reconstructed
    S = 25;
    surf(xq,yq,vqSurf)
    hold on
    scatter3(Xq,Yq,vq,S,Col_map2,'MarkerFaceColor','flat','MarkerEdgeColor','none',...
        'Marker','square');
    hold off

    % Set the Figure axis/font sizes and colours
    set(gca,'FontSize',14,'GridAlpha',0.5,'GridColor',[1 1 1],...
        'GridLineStyle','--','LineWidth',1.5,'MinorGridAlpha',0.5,'Color','k')

    % Set the axes limits
    xlim([-4 4]);
    ylim([-4 4]);
    zlim([0 0.6]);

    % set axis labels
    xlabel('Lateral Distance \mum','position',[-0.8 -6.8 0])
    ylabel('Lateral Distance \mum','position',[-6.7 -0.27 0])
    zlabel('Axial Distance \mum')

    % Select the viewing angle
    view([305.56 70]);
    grid('on');

    % Set the Figure axis/font sizes and colours
    set(gca,'FontSize',14,'GridAlpha',0.5,'GridColor',[1 1 1],...
        'GridLineStyle','--','LineWidth',1.5,'MinorGridAlpha',0.5,'XColor',...
        [0.501960813999176 0.501960813999176 0.501960813999176],'YColor',...
        [0.501960813999176 0.501960813999176 0.501960813999176],'ZColor',...

```

```
[0.501960813999176 0.501960813999176 0.501960813999176])
```

```
% Add time stamp to Figure  
title(Time_stamp,'Color','w');
```

```
elseif numOfImages2 > 1
```

```
h = waitbar(0,'Creating Movie...');  
steps = numOfImages2;
```

```
for k = 1:numOfImages2
```

```
% Create Figure  
Figure1 = Figure('Color',[0 0 0],'units','normalized','outerposition',[0 0 1 1]);  
set(Figure1,'visible','off');
```

```
% Plot a 3D surface and scatter plot for each image that can be reconstructed  
S = 25;  
surf(xq,yq,vqSurf(:, :,k))  
hold on
```

```
scatter3(Xq(:, :,k),Yq(:, :,k),vq(:, :,k),S,Col_map2(:, :,k),'MarkerFaceColor','flat','MarkerEdgeColor','none',...  
        'Marker','square');  
hold off
```

```
% set the Figure axis/font sizes and colours  
set(gca,'FontSize',14,'GridAlpha',0.5,'GridColor',[1 1 1],...  
      'GridLineStyle','--','LineWidth',1.5,'MinorGridAlpha',0.5,'Color','k')
```

```
% Set the axes limits  
xlim([-4 4]);  
ylim([-4 4]);  
zlim([0 0.6]);
```

```
% set axis labels  
xlabel('Lateral Distance \mum','position',[-1.9 -5.6 0])  
ylabel('Lateral Distance \mum','position',[-5.7 -1.27 0])  
zlabel('Axial Distance \mum')
```

```
% Select the viewing angle  
view([305.56 70]);
```

```

grid('on');

% Aspect ratio of the reconstruction
daspect([1 1 1]);

% set the Figure axis/font sizes and colours
set(gca,'FontSize',14,'GridAlpha',0.5,'GridColor',[1 1 1],...
'GridLineStyle','--','LineWidth',1.5,'MinorGridAlpha',0.5,'XColor',...
[0.501960813999176 0.501960813999176 0.501960813999176],'YColor',...
[0.501960813999176 0.501960813999176 0.501960813999176],'ZColor',...
[0.501960813999176 0.501960813999176 0.501960813999176])

% Add time stamp to Figure
title(Time_stamp(1,k),'Color','w');

% store each Figure in a vector
drawnow
Frame(k) = getframe(gcf);
F = getframe(gcf);
im{k} = frame2im(F);
waitbar(k/ steps)

end
close (h);
end

% Save the images as a tiff
% [FileName,PathName] = uiputfile({'*.tif'});
t = Tiff('C:\Users\spb15144\Desktop\550 data 2.tif','w8');
tagstruct.ImageLength = 1314;
tagstruct.ImageWidth = 2552;
tagstruct.Photometric = Tiff.Photometric.RGB;
tagstruct.BitsPerSample = 8;
tagstruct.SamplesPerPixel = 3;
tagstruct.PlanarConfiguration = Tiff.PlanarConfiguration.Chunky;
tagstruct.Software = 'MATLAB';
tagstruct.SampleFormat = 1;

for k = 1:numOfImages2

t.setTag(tagstruct)
t.write(im{k});

```

```
    if k < numOfImages2
        t.writeDirectory();
    else
    end
end

t.close();
```

Appendix VII – Antinodal plane separation function

```
function [Antinodal_sep] = Antinodesep(BW,numOfImages,degint)
%This function uses the nodal regions of standing wave to separate the
%anti-nodal planes

%% Antinodal separation code for the function Antinodesep
for k = 1:numOfImages
    % Create an inverse of the image
    Inv_BW(:,:,k) = imcomplement(BW(:,:,k));

    % create nodal plane image
    [nodal(:,:,k),n] = bwlabel(Inv_BW(:,:,k));
end

% Create a single pixel thick nodal planes
for k = 1:numOfImages
    nodal2 = nodal(:,:,k);
    nodal2(nodal(:,:,k) == 1) = 0;
    thinnode(:,:,k) = bwmorph(nodal2,'thin',inf);
end

% Determine the width and half width of the image
half_width = (size(BW,1)/2)+0.5;
width = size(BW,1);

% Creates a square matrix of the x and y distances of the image.
N = size(BW,1);
[X,Y] = meshgrid(-1:2/(N-1):1);

% Calibrates the X and Y coordinates to the correct size for the image.
x1 = (X.*half_width);
y2 = (Y.*half_width);

% Calculates the radial distance for the centre of the image for each pixel
% Sets
[t2,r] = cart2pol(x1,y2);
r_line = r(half_width,half_width:length(r));
theta = ((1:degint:361)-1)';
SIZE = size(theta,1);
R_pos = repmat(r_line,SIZE,1,numOfImages);
```

```

% Preallocate matrices
s = zeros(size(BW,1),size(BW,2),numOfImages);
I_rot = zeros(SIZE,half_width,numOfImages);

% Creates matrices which rotates and stores each radial line for the x,y,z
% radial (r) and pixel intensity (S)
for i = 1:SIZE

    % rotates the image and stores each radial line from the centre to
    % right-hand edge
    s = imrotate(thinnode,-theta(i,1),'crop');

    for k = 1:numOfImages
        SE = strel('disk',2);
        s2 = imdilate(s(:,k),SE);
        s3 = bwmorph(s2,'thin',inf);

        % Stores the radial line for the rotated matrix
        I_rot(i,:,k) = double(s3(half_width,half_width:width));

    end
end

R_pos1(I_rot ~= 1) = 0;

% Creates matrices which rotates and stores each radial line for the x,y,z
% radial (r) and pixel intensity (S)
for k = 1:numOfImages
    clear rad_locations(i,:)

    for i = 1:SIZE
        Int_pos = I_rot(i,:,k);
        R_pos_temp = R_pos(i,:,k);
        R_pos_temp(Int_pos == 0) = [];

        if size(R_pos_temp,2) == 2
            R_pos_temp = padarray(R_pos_temp,[0 1],0,'post');

        elseif size(R_pos_temp,2) < 2
            R_pos_temp = [0, 0, 0];
        end
    end
end

```

```

elseif size(R_pos_temp,2) > 3
    R_pos_temp = [0, 0, 0];
end

rad_locations(i,:) = R_pos_temp;

end
r_locs(:,:,k) = rad_locations;
end

% Sorting code for the nodal planes
for k = 1:numOfImages
    try
        clear v_final V_interpt zerocheck Zerocheck2 Firstnonzero inrow

        r_location = r_locs(:,:,k);

        % Check that the first row contains a zero
        zerocheck = sum(r_location);
        Zerocheck2 = prod(zerocheck);

        % finds a new starting position if the first row contains a zero
        if Zerocheck2 == 0
            [rowz, colz] = find(zerocheck == 0);
            r_location(:,colz) = [];
            inrow = find(prod(r_location,2) ~= 0);
            Firstnonzero = inrow(1,1)-1;

            % if there is not a zero - set the second line as the first row.
        elseif Zerocheck2 ~= 0
            inrow = find(prod(r_location,2) ~= 0);
            Firstnonzero = inrow(1,1)-1;
        end

        % checks the number of nodal regions
        % sets up the sorting matrix v based on the first position of the
        % first nonzero row.
        nodenum = size(r_location,2);
        v = zeros(SIZE,nodenum);
        v(SIZE-(Firstnonzero-1):SIZE,1:nodenum) = r_location(1:Firstnonzero,:);
        v(1:(SIZE-Firstnonzero),1:nodenum) = r_location(Firstnonzero+1:SIZE,:);
        V1 = v;
    end
end

```

```
% sorts the numbers into the appropriate column based on the row above the
current row.
```

```
for i = 1:SIZE
```

```
clear Result
```

```
Check = V1(i,1:nodenum)./V1(i,1:nodenum);
Checkzero = sum(Check);
```

```
if isnan(Checkzero) == 1
```

```
    % Sets the 2 current rows to be compared as row vectors A2
    % and B2
```

```
    A = v(i-1,:);
```

```
    A(A == 0) = NaN;
```

```
    B = (V1(i,:));
```

```
    B(B == 0) = [];
```

```
    Result = zeros(1,nodenum);
```

```
    % Subtracts row A2 from B2 and finds the minimum value in
    % each column
```

```
    for j = 1:length(B)
```

```
        I1(1,:) = abs(A-B(:,j));
```

```
        minI1(:,j) = min(min(I1));
```

```
        if minI1(:,j) < 5
```

```
            % If the previous value is within 5 pixels it is set
            % the vale equal to the current value.
```

```
            [row, col] = find(I1 == minI1(:,j));
```

```
            Result(:,col) = B(:,j);
```

```
            % If the previous value is out with 5 pixels it is set
            % the vale equal to zero.
```

```
        elseif minI1(:,j) > 5
```

```
            [row, col] = find(I1 == minI1(:,j));
```

```
            Result(:,col) = 0;
```

```
        end
```

```
    end
```

```
    % Create a new sorted matrix v
```

```
    v(i,:) = Result;
```

```

else
    v(i,1:nodenum) = V1(i,1:nodenum);

end
end

% Sets any value to zero
v(v == 0) = NaN;

% Use interpolate to fill in the gaps any NaN values
for i = 1:nodenum
    V_interp(:,i) = interp1(theta,v(:,i),theta,'cubic');
end

% Re-sort the matrix comparing the original radial values to the interpolated
% radial values of the nodal planes to achieve better nodal plane
% sorting
for i = 1:SIZE

    clear Result

    Check = V1(i,1:nodenum)./V1(i,1:nodenum);
    Checkzero = sum(Check);

    if isnan(Checkzero) == 1
        % Sets the 2 current rows to be compared as row vectors A2
        % and B2
        A2 = V_interp(i-1,:);
        A2(A2 == 0) = NaN;

        B2 = (V1(i,:));
        B2(B2 == 0) = [];
        Result = zeros(1,nodenum);

        % Subtracts row A2 from B2 and finds the minimum value in
        % each column
        for j = 1:length(B2)
            l1(1,:) = abs(A2-B2(:,j));
            minl1(:,j) = min(min(l1));

            % If the previous value is within 5 pixels it is set

```

```

    % the vale equal to the current value.
    if minI1(:,j) < 5
        [row, col] = find(I1 == minI1(:,j));
        Result(:,col) = B2(:,j);

        % If the previous value is out with 5 pixels it is set
        % the vale equal to zero.
    elseif minI1(:,j) > 5
        [row, col] = find(I1 == minI1(:,j));
        Result(:,col) = 0;
    end
end
% Create a new sorted matrix v_final
v_final(i,1:nodenum) = Result;

else
    v_final(i,1:nodenum) = V1(i,1:nodenum);
end
end

clear I1 r_locs2

% remove the zero value with NaN's and store in a cell array
r_locs2(1:Firstnonzero,:) = v_final(SIZE-(Firstnonzero-1):SIZE,1:nodenum);
r_locs2(Firstnonzero+1:SIZE,:) = v_final(1:(SIZE-Firstnonzero),1:nodenum);
r_locs2(r_locs2 == 0) = NaN;
r_locs3{:,k} = r_locs2;

catch me1

end
end

% Setup a vector of angles that are separated by 1 degree intervals then
% convert to radians
rq = (0:1:360)';
theta_rad = (rq*(pi/180));

for k = 1:numOfImages
    try

        clear r_node
    
```

```

r_node = r_locs3{:, :, k};

for i = 1:(size(r_node,2))

    % interpolate nodal plane to fill in gaps for each nodal plane
    clear R1 R1outliers R11
    R1 = interp1(theta,r_node(:,i),rq,'cubic');
    R1outliers = isoutlier(R1,'median');

    % remove outliers and set to NaN
    R1(R1outliers == 1) = NaN;

    % Final interpolation of the nodal plane once outliers have been
    % removed
    R11 = R1(1:degint:361);
    R_final(:,i) = interp1(theta,R11,rq,'cubic');

end

% Obtain the x and y pixel location for each data point
% Round the data point values to whole numbers
[X_node1,Y_node1] = pol2cart(theta_rad,R_final);
X_nodal1(:, :, k) = round(X_node1,0)+round(half_width,0);
Y_nodal1(:, :, k) = (round(Y_node1,0).*-1)+round(half_width,0);

catch me2

end
end

% setup the bin for each data point
Bin = (1:361)';
Bin(1:361) = 1;

for k = 1:numOfImages
    try

        clear C M Nodal_Rings Nodal_rings r_node
        r_node = R_final;

        % create an image from each of the interpolated nodal regions
        for i = 1:(size(r_node,2))

```

```

M = zeros(size(BW(:,:,k)));
C = sub2ind(size(M),Y_nodal1(:,i,k),X_nodal1(:,i,k));
M(C) = Bin;
Nodal_rings(:,:,i) = imdilate(M,SE);

end

% Create a single image with all the interpolated nodal rings and subtract from
original threshold image
Nodal_Rings = sum(Nodal_rings,3);
Antinodal_sep(:,:,k) = BW(:,:,k) - Nodal_Rings;

catch me
end
end

% Removes negative values
Antinodal_sep(Antinodal_sep == -1) = 0;

```

Appendix VIII – TartanSW multi-excitation simulation

```
% Ross Scrimgeour 06/18
% TartanSW Multi-excitation simulation
clearvars;
close all;

%% Theoretical Intensity distribution
% Set refractive index of the medium
n = 1;
% Axial height in nanometres
z = (1:5000)*1e-9;

% Set excitation wavelength
lambdaexR = 543*1e-9;
lambdaexG = 514*1e-9;
lambdaexB = 488*1e-9;

% Calculate wavenumber
kexR = 4*pi*n/lambdaexR;
kexG = 4*pi*n/lambdaexG;
kexB = 4*pi*n/lambdaexB;

%% One dimensional excitation standing wave
SWexR = 1 - cos(kexR.*(z));
SWexG = 1 - cos(kexG.*(z));
SWexB = 1 - cos(kexB.*(z));

% integrate over all possible emission detection wavelengths
fun = @(lambda) (1-cos((4*pi*n/lambda).*(z)));
lemis = integral(fun,550*1e-9,650*1e-9,'ArrayValued',true);

% Theoretical convolution of excitation and emission standing waves
swpsfR = mat2gray(SWexR.*lemis);
swpsfG = mat2gray(SWexG.*lemis);
swpsfB = mat2gray(SWexB.*lemis);

% Create the spectral signature image
SWexcCol(:, :, 1) = swpsfR;
SWexcCol(:, :, 2) = swpsfG;
SWexcCol(:, :, 3) = swpsfB;
SWexcCol = repmat(SWexcCol, 300, 1);
```

```
% plot spectral signature
Figure(1);
imshow(SWexcCol)

% scale axial height to microns
z = z./1000;

% Plot TartanSW excitation
Figure(2);
plot(z,swpsfR,'r',z,swpsfG,'g',z,swpsfB,'b')
ylabel('Intensity (Arbitrary Units)')
xlabel('Height from Mirror (\mum)')
```

Appendix IX - TartanSW multi-emission simulation

```
% Ross Scrimgeour 06/18
% TartanSW Multi-emission simulation
clearvars;
close all;

% Set refractive index of medium
n = 1;

%excitation wavelength
lambdaex = 514*1e-9;

% Calculate wavenumber
kex = 4*pi*n/lambdaex;

%Set axial range
z = (1:5000).*1e-9;

% create the excitation standing waves
SWex = mat2gray(1 - cos(kex.*z));

% create the emission standing waves for each detection channel
fun = @(lambda) (1-cos((4*pi*n/lambda).*z));
SWemR = integral(fun,617*1e-9,622*1e-9,'ArrayValued',true);
SWemG = integral(fun,592*1e-9,597*1e-9,'ArrayValued',true);
SWemB = integral(fun,567*1e-9,572*1e-9,'ArrayValued',true);

% Calculate the resultant excitation emission standing wave
swpsfR = mat2gray(SWex.*SWemR);
swpsfG = mat2gray(SWex.*SWemG);
swpsfB = mat2gray(SWex.*SWemB);

% Create the spectral signature image
SWemCol(:, :, 1) = swpsfR;
SWemCol(:, :, 2) = swpsfG;
SWemCol(:, :, 3) = swpsfB;
SWemCol = repmat(SWemCol,300,1);

% plot spectral signature
Figure(1);
imshow(SWemCol)
```

```
% scale axial height to microns
z = z./1000;

%% create plots axial plots
Figure(1);
plot(z,swpsfR,'r',z,swpsfG,'g',z,swpsfB,'b')
ylabel('Intensity (Arbitrary Units)')
xlabel('Height from Mirror (\mum)')
```

Appendix X – Difference standing wave simulation

```
% Difference standing wave calculator image simulator
% Ross Scrimgeour 06/18
clearvars;

%% Theoretical Intensity distribution
% Set the NA objective and refractive index of the medium
n = 1.00;

% set excitation wavelength
lambdaexR = 543;
lambdaexG = 514;
lambdaexB = 488;

% calculate wavenumber
kexR = 4*pi*n/lambdaexR;
kexG = 4*pi*n/lambdaexG;
kexB = 4*pi*n/lambdaexB;

%set axial range
z = 1:5000;

% create excitation standing waves
SWexR = (1-cos(kexR.*(z)));
SWexG = (1-cos(kexG.*(z)));
SWexB = (1-cos(kexB.*(z)));

% integrate over all possible emission detection wavelengths
fun = @(lambda) (1-cos((4*pi*n/lambda).*(z)));
lemis = integral(fun,550,650,'ArrayValued',true);

% Theoretical convolution of excitation and emission standing waves
sw_psfR = SWexR.*lemis;
sw_psfG = SWexG.*lemis;
sw_psfB = SWexB.*lemis;

% calculate difference SW
DiffRG = mat2gray(abs(sw_psfR - sw_psfG));
DiffGB = mat2gray(abs(sw_psfG - sw_psfB));
```

```

% Create the sepctral signature image
SWexcCol(:, :, 1) = DiffRG;
SWexcCol(:, :, 2) = DiffGB;
SWexcCol(:, :, 3) = DiffGB.*0;
SWexcCol = repmat(SWexcCol, 300, 1);

% Plot spectral signature
Figure(1);
imagesc(z, 1:300, SWexcCol)
xlabel('Radial Distance (\mum)')
ylabel('Radial Distance (\mum)')

% Plot The intensity profile of the Difference SW's
Figure(2);
plot(z, DiffGB, 'g', z, DiffRG, 'r')
xlabel('Height from Mirror (\mum)')
ylabel('Nomralised fluorescence intensity (Arb. units)')

```

Appendix XI – Phase difference reconstruction of a simulated intensity profile of a lens specimen

```
% Phase difference reconstruction for line profile of simulated lens
% specimen
% Ross Scrimgeour 07/18
clearvars
clear all

%% IINEAR CURVE FITTING FOR PHASE DIFFERENCE METHOD FOR THEORETICAL SW
WAVES

% Theoretical Intensity distribution
% Set and refractive index of the medium
n = 1;
% set the radius of curvature
R = 0.02481;
% set excitation wavelength
lambdaexR = 543.*1e-9;
lambdaexG = 514.*1e-9;
lambdaexB = 488.*1e-9;

% wavenumber
kexR = 4*pi*n/lambdaexR;
kexG = 4*pi*n/lambdaexG;
kexB = 4*pi*n/lambdaexB;

% effective wavelength difference
effwave1 = (lambdaexR.*lambdaexG)./abs(lambdaexR-lambdaexG);
effwave2 = (lambdaexG.*lambdaexB)./abs(lambdaexG-lambdaexB);

% calculate the radial and axial distance of the effective wavelength
maxr = sqrt(R.^2 -(R-effwave2/4).^2)*1e6;
z = (1:10:(effwave2/4)*1e9-100)*1e-9;

%% One Dimensional standing wave
SWexR = 1 - cos(kexR.*(z));
SWexRnorm = 2*(SWexR - min(SWexR))./(max(SWexR) + min(SWexR)) - 1;

SWexG = 1 - cos(kexG.*(z));
SWexGnorm = 2*(SWexG - min(SWexG))./(max(SWexG) + min(SWexG)) - 1;
```

```

SWexB = 1 - cos(kexB.*(z));
SWexBnorm = 2*(SWexB - min(SWexB))./(max(SWexB) + min(SWexB)) - 1;

% Create a pi/2 phase shift in 1D standing wave
SWexRshift = 1 - cos((kexR.*(z))- pi/2);
SWexRnorm_shift = 2*(SWexRshift - min(SWexRshift))./(max(SWexRshift) +
min(SWexRshift)) - 1;

SWexGshift = 1 - cos((kexG.*(z))- pi/2);
SWexGnorm_shift = 2*(SWexGshift - min(SWexGshift))./(max(SWexGshift) +
min(SWexGshift)) - 1;

SWexBshift = 1 - cos((kexB.*(z))- pi/2);
SWexBnorm_shift = 2*(SWexBshift - min(SWexBshift))./(max(SWexBshift) +
min(SWexBshift)) - 1;

% Calculate phase angle from theory
% SWR = atan2(SWexRnorm,SWexRnorm_shift);
% SWG = atan2(SWexGnorm,SWexGnorm_shift);
% SWB = atan2(SWexBnorm,SWexBnorm_shift);
%
% PhaseR = (unwrap(SWR));
% PhaseG = (unwrap(SWG));
% PhaseB = (unwrap(SWB));

Figure(1);
plot(z*1e6,SWB,'b',z*1e6,SWG,'g',z*1e6,SWR,'r')
xlabel('distance z (\mum)')
ylabel('phase (radians)')

% Calculate the phase difference
diffRG = abs(PhaseG-PhaseR);
diffGB = abs(PhaseB-PhaseG);

%Interpolation linear fit the phase relationship to axial location
[PR,sR] = polyfit(diffRG,z,1);
zR = polyval(PR,diffRG,1);

[PG,sG] = polyfit(diffGB,z,1);
zG = polyval(PG,diffGB,1);

```

```

%% Simulated experimental data for convex surface
rc = (-maxr:2:maxr)*1e-6;
zc = (R-sqrt(R^2-rc.^2));

% Simulate standing waves
SWexRc = 1 - cos(kexR.*(zc));
SWexRnormc = 2*(SWexRc - min(SWexRc))./(max(SWexRc) + min(SWexRc)) - 1;

SWexGc = 1 - cos(kexG.*(zc));
SWexGnormc = 2*(SWexGc - min(SWexGc))./(max(SWexGc) + min(SWexGc)) - 1;

SWexBc = 1 - cos(kexB.*(zc));
SWexBnormc = 2*(SWexBc - min(SWexBc))./(max(SWexBc) + min(SWexBc)) - 1;

% create offset in standing wave (If needed for theoretical phase
% extraction
SWexRshiftc = 1 - cos((kexR.*(zc))- pi/2);
SWexRnormc_shift = 2*(SWexRshiftc - min(SWexRshiftc))./(max(SWexRshiftc) +
min(SWexRshiftc)) - 1;

SWexGshiftc = 1 - cos((kexG.*(zc))- pi/2);
SWexGnormc_shift = 2*(SWexGshiftc - min(SWexGshiftc))./(max(SWexGshiftc) +
min(SWexGshiftc)) - 1;

SWexBshiftc = 1 - cos((kexB.*(zc))- pi/2);
SWexBnormc_shift = 2*(SWexBshiftc - min(SWexBshiftc))./(max(SWexBshiftc) +
min(SWexBshiftc)) - 1;

% calculate pahse code from phase offset
% SWR = atan2(SWexRnormc_shift,SWexRnormc);
% SWG = atan2(SWexGnormc_shift,SWexGnormc);
% SWB = atan2(SWexBnormc_shift,SWexBnormc);

% PhaseRc = (unwrap(SWR));
% PhaseGc = (unwrap(SWG));
% PhaseBc = (unwrap(SWB));
%
% MinphaseR = min(PhaseRc) - 0;
% MinphaseG = min(PhaseGc) - 0;
% MinphaseB = min(PhaseBc) - 0;
%

```

```

% PhaseRc = PhaseRc - MinphaseR;
% PhaseGc = PhaseGc - MinphaseG;
% PhaseBc = PhaseBc - MinphaseB;

% Calculae the hilbert transform and phase unwrap
SWRc = hilbert(SWexRnormc);
angRc = angle(SWRc);
PhaseRc = phase_unwrap(angRc);

SWGc = hilbert(SWexGnormc);
angGc = angle(SWGc);
PhaseGc = phase_unwrap(angGc);

SWBc = hilbert(SWexBnormc);
angBc = angle(SWBc);
PhaseBc = phase_unwrap(angBc);

% Calculate the phase difference
diffRGc = abs(PhaseGc-PhaseRc);
diffGBc = abs(PhaseBc-PhaseGc);

%Interoplate axial height values for simulated lens specimen
zRc = polyval(PR,diffRGc);
zGc = polyval(PG,diffGBc);

```

Appendix XII – Phase difference reconstruction of simulated 3D lens specimen

```
% Difference standing wave calculator image simulator
% Ross Scrimgeour 07/18
clearvars
clear all

%% LINEAR CURVE FITTING FOR PHASE DIFFERENCE METHOD FOR THEORETICAL SW WAVES

% Theoretical Intensity distribution
% Set refractive index of the medium
n = 1;
% lens specimen radius of curvature
R = 0.02481;
% set excitation wavelength
lambdaexR = 543.*1e-9;
lambdaexG = 514.*1e-9;
lambdaexB = 488.*1e-9;

% wavenumber
kexR = 4*pi*n/lambdaexR;
kexG = 4*pi*n/lambdaexG;
kexB = 4*pi*n/lambdaexB;

% calculate effective wavelength
effwave1 = (lambdaexR.*lambdaexG)./abs(lambdaexR-lambdaexG);
effwave2 = (lambdaexG.*lambdaexB)./abs(lambdaexG-lambdaexB);

% calculate radial and axial
maxr = sqrt(R.^2 -(R-effwave2/4).^2)*1e6;
z = (1:10:(effwave2/4)*1e9-100)*1e-9;

% one dimensional standing wave
SWexR = 1 - cos(kexR.*(z));
SWexRnorm = 2*(SWexR - min(SWexR))./(max(SWexR) + min(SWexR)) - 1;

SWexG = 1 - cos(kexG.*(z));
SWexGnorm = 2*(SWexG - min(SWexG))./(max(SWexG) + min(SWexG)) - 1;
```

```

SWexB = 1 - cos(kexB.*(z));
SWexBnorm = 2*(SWexB - min(SWexB))./(max(SWexB) + min(SWexB)) - 1;

% Create a pi/2 phase shift for 1D standing wave
SWexRshift = 1 - cos((kexR.*(z))- pi/2);
SWexRnorm_shift = 2*(SWexRshift - min(SWexRshift))./(max(SWexRshift) +
min(SWexRshift)) - 1;

SWexGshift = 1 - cos((kexG.*(z))- pi/2);
SWexGnorm_shift = 2*(SWexGshift - min(SWexGshift))./(max(SWexGshift) +
min(SWexGshift)) - 1;

SWexBshift = 1 - cos((kexB.*(z))- pi/2);
SWexBnorm_shift = 2*(SWexBshift - min(SWexBshift))./(max(SWexBshift) +
min(SWexBshift)) - 1;

% Calculate phase angle
SWR = atan2(SWexRnorm_shift,SWexRnorm);
SWG = atan2(SWexGnorm_shift,SWexGnorm);
SWB = atan2(SWexBnorm_shift,SWexBnorm);

% Unwrap phase angle
PhaseR = (unwrap(SWR));
PhaseG = (unwrap(SWG));
PhaseB = (unwrap(SWB));

% Calculate the phase difference
diffRG = abs(PhaseG-PhaseR);
diffGB = abs(PhaseB-PhaseG);

%Interpolation linear fit the phase relationship to axial location
[PR,sR] = polyfit(diffRG,z,1);
zR = polyval(PR,diffRG,1);

[PG,sG] = polyfit(diffGB,z,1);
zG = polyval(PG,diffGB,1);

%% Two-dimensional reconstruction
% create a 2D x and y distance grid
r = (-maxr:1:maxr)*1e-6;
[y,x] = meshgrid(r,r);

```

```

% create mask
mask = ones(size(y));
mask(:,1:end/2) = -1;

% create an axial height grid based on x and y
r2 = sqrt(x.^2 + y.^2);
z2 = (R-sqrt(R^2-r2.^2));

% simulate 2D radial pattern due to len specimen
SWexR2 = (1-cos(kexR.*(z2)));
SWexRn2 = 2.*(SWexR2 - min(min(SWexR2)))/(max(max(SWexR2)) +
min(min(SWexR2))) - 1;
SWexR_shift = (1-cos(kexR.*(z2)-pi/2));
SWexRn_shift = 2.*(SWexR_shift - min(min(SWexR_shift)))/(max(max(SWexR_shift)) +
min(min(SWexR_shift))) - 1;

SWexG2 = (1-cos(kexG.*(z2)));
SWexGn2 = 2.*(SWexG2 - min(min(SWexG2)))/(max(max(SWexG2)) +
min(min(SWexG2))) - 1;
SWexG_shift = (1-cos(kexG.*(z2)-pi/2));
SWexGn_shift = 2.*(SWexG_shift - min(min(SWexG_shift)))/(max(max(SWexG_shift)) +
min(min(SWexG_shift))) - 1;

SWexB2 = (1-cos(kexB.*(z2)));
SWexBn2 = 2.*(SWexB2 - min(min(SWexB2)))/(max(max(SWexB2)) +
min(min(SWexB2))) - 1;
SWexB_shift = (1-cos(kexB.*(z2)-pi/2));
SWexBn_shift = 2.*(SWexB_shift - min(min(SWexB_shift)))/(max(max(SWexB_shift)) +
min(min(SWexB_shift))) - 1;

% Hilbert transform of 2D images
SWR2 = hilbert(hilbert(SWexRn2)).';
SWG2 = hilbert(hilbert(SWexGn2)).';
SWB2 = hilbert(hilbert(SWexBn2)).';

%% Non-hilbert wrapped phase angle calculation(uncommment if using)
% angR2 = atan2(SWexR_shift,SWexRn2);
% angG2 = atan2(SWexG_shift,SWexGn2);
% angB2 = atan2(SWexB_shift,SWexBn2);

angR2 = angle(SWR2).*mask;
angG2 = angle(SWG2).*mask;

```

```

angB2 = angle(SWB2).*mask;

% unwrap phase angle
PhaseR = unwrap(unwrap(angR2,[],2),[],1);
PhaseG = unwrap(unwrap(angG2,[],2),[],1);
PhaseB = unwrap(unwrap(angB2,[],2),[],1);

MinphaseR = min(min(PhaseR)) - 0;
MinphaseG = min(min(PhaseG)) - 0;
MinphaseB = min(min(PhaseB)) - 0;

PhaseR = (PhaseR - MinphaseR);
PhaseG = (PhaseG - MinphaseG);
PhaseB = (PhaseB - MinphaseB);

% phase difference calculation
diffRG2 = abs(PhaseG - PhaseR);
diffGB2 = abs(PhaseB - PhaseG);
%
% interpolate height of two dimensional image
zRc = polyval(PR,diffRG2);
zGc = polyval(PG,diffGB2);

% Create colorbar
colorbar;
%
```

Appendix XIII – Phase difference reconstruction of an experimental lens specimen

```
% Ross Scrimgeour 08/2018
% Read Lens specimen and extract and reconstruction in 3D using phase
% method
close all
clearvars
% Opens file explorer to load image file.
% Stores the image file directory.
% Reads in the image to the program.
[filename, pathname, filterindex] = uigetfile({'*.jpg;*.tif;*.png;*.gif;*.tiff','All Image
Files'});
Filename = strcat(pathname,filename);
SWImage = imread(Filename);

%% Read in line intensity plot from user
imshow(SWImage,[]);
c = improfile;

% pixel to radial distance scale (pixels/microns)
Scale = 1.389;

% Radius of curvature of lens specimen
R = 0.02481;

% store each excitation wavelength
SWRe = mat2gray(c(:,1,1))';
SWGe = mat2gray(c(:,1,2))';
SWBe = mat2gray(c(:,1,3))';

% Scale radial distance
r_length = 1:length(SWRe);
rc = (r_length./Scale)*1e-6;
z_lens = R - sqrt((R.^2 - rc.^2));

%% Theoretical Intensity distribution
% Theoretical Intensity distribution
% Set the NA objective and refractive index of the medium
n = 1;
% set excitation wavelength
```

```

lambdaexR = 543.*1e-9;
lambdaexG = 514.*1e-9;
lambdaexB = 488.*1e-9;

% calculate wavenumber
kexR = 4*pi*n/lambdaexR;
kexG = 4*pi*n/lambdaexG;
kexB = 4*pi*n/lambdaexB;

% effective wavelength
effwave1 = (lambdaexR.*lambdaexG)./abs(lambdaexR-lambdaexG);
effwave2 = (lambdaexG.*lambdaexB)./abs(lambdaexG-lambdaexB);

% axial height
z = linspace(0,effwave2*1e9/2,length(SWRe)).*1e-9;

%% IINEAR CURVE FITTING FOR PHASE DIFFERENCE METHOD FOR THEORETICAL SW WAVES

% Set up paramaters for the theorotical standing wave calculations
% refractive index of medium
n = 1;

% excitation wavelength
lambdaexR = 543.*1e-9;
lambdaexG = 514.*1e-9;
lambdaexB = 488.*1e-9;

% calculate wavenumber
kexR = 4*pi*n/lambdaexR;
kexG = 4*pi*n/lambdaexG;
kexB = 4*pi*n/lambdaexB;

%anitnodal spacing
anti-nodalR = lambdaexR/(2*n);
anti-nodalG = lambdaexG/(2*n);
anti-nodalB = lambdaexB/(2*n);

% Measured z-offset
% (To account for phase shifts from protective coating or dielectric mirror)
zoffsetR = 0;
zoffsetG = 0;

```

```

zoffsetB = 0;

% Calculate the path difference due to axial offset due to reflective
% substrate
Path_DiffR = (4*pi.*(zoffsetR)./lambdaexR);
Path_DiffG = (4*pi.*(zoffsetG)./lambdaexG);
Path_DiffB = (4*pi.*(zoffsetB)./lambdaexB);

% effective wavelength from phase difference method
effwave1 = (lambdaexR.*lambdaexG)./abs(lambdaexR-lambdaexG);
effwave2 = (lambdaexG.*lambdaexB)./abs(lambdaexG-lambdaexB);

maxr = sqrt(R.^2 -(R-effwave1/2).^2)*1e6;
z = (0:(effwave2/2)*1e9)*1e-9;
r = sqrt(R.^2 -(R-z).^2)*1e6;

% % one dimensional standing wave theory
SWexR = (1 - cos(kexR.*z - Path_DiffR));
SWexRnorm = 2*(SWexR - min(SWexR))./(max(SWexR) + min(SWexR)) - 1;

SWexG = (1 - cos(kexG.*z - Path_DiffG));
SWexGnorm = 2*(SWexG - min(SWexG))./(max(SWexG) + min(SWexG)) - 1;

SWexB = (1 - cos(kexB.*z - Path_DiffB));
SWexBnorm = 2*(SWexB - min(SWexB))./(max(SWexB) + min(SWexB)) - 1;

% Create a pi/2 phase shift form 1D theory
SWexRshift = (1 - cos((kexR.*z - Path_DiffR) - pi/2));
SWexRnorm_shift = 2*(SWexRshift - min(SWexRshift))./(max(SWexRshift) +
min(SWexRshift)) - 1;

SWexGshift = (1 - cos((kexG.*z - Path_DiffG) - pi/2));
SWexGnorm_shift = 2*(SWexGshift - min(SWexGshift))./(max(SWexGshift) +
min(SWexGshift)) - 1;

SWexBshift = (1 - cos((kexB.*z - Path_DiffB) - pi/2));
SWexBnorm_shift = 2*(SWexBshift - min(SWexBshift))./(max(SWexBshift) +
min(SWexBshift)) - 1;

% Calculate Phase angle
SWR = atan2(SWexRnorm_shift,SWexRnorm);
SWG = atan2(SWexGnorm_shift,SWexGnorm);

```

```

SWB = atan2(SWexBnorm_shift,SWexBnorm);

% unwrap phase
unwrapped_angR = unwrap(SWR);
unwrapped_angG = unwrap(SWG);
unwrapped_angB = unwrap(SWB);

% Calculate the phase difference
diffRG = (unwrapped_angG-unwrapped_angR);
diffGB = (unwrapped_angB-unwrapped_angG);

%Interpolation linear fit the phase relationship to axial location
[PRz,sR] = polyfit(diffRG,z,1);
zR = polyval(PRz,diffRG,1);

[PGz,sG] = polyfit(diffGB,z,1);
zG = polyval(PGz,diffGB,1);

%% Two-dimenisonal reconstruction
% normalise input intensities form lens image
SWexRnorm1 = 2*(SWRe - min(SWRe))./(max(SWRe) + min(SWRe)) - 1;
SWexGnorm1 = 2*(SWGe - min(SWGe))./(max(SWGe) + min(SWGe)) - 1;
SWexBnorm1 = 2*(SWBe - min(SWBe))./(max(SWBe) + min(SWBe)) - 1;

% Create a 2D hilbert transform which the real and imaginary parts can be
% used to calculate the phase angle
SWR2 = hilbert(SWexRnorm1);
SWG2 = hilbert(SWexGnorm1);
SWB2 = hilbert(SWexBnorm1);

% Calculate the phase angle
angR2 = angle(SWR2);
angG2 = angle(SWG2);
angB2 = angle(SWB2);

% Phase unwrap each channel using the inbuilt unwrap function
PhaseR2 = unwrap(angR2);
PhaseG2 = unwrap(angG2);
PhaseB2 = unwrap(angB2);

% Calculate the phase difference
diffRG2 = PhaseG2 - PhaseR2;

```

```
diffGB2 = PhaseB2 - PhaseG2;
```

```
% interpolate height of two dimensional image
```

```
zR = (polyval(PRz,diffRG2,1));
```

```
zG = (polyval(PGz,diffGB2,1));
```

```
% fitting of radial data
```

```
[PR,sR] = polyfit(rc,zR,2);
```

```
zRc = polyval(PR,rc);
```

```
[PG,sG] = polyfit(rc,zG,2);
```

```
zGc = polyval(PG,rc);
```